



Cape Peninsula  
University of Technology

***CUBESAT DEVELOPMENT: INTEGRATING THE CURRENT STATE-  
OF-THE-ART IN MANUFACTURING TECHNIQUES AND  
ENGINEERING ANALYSIS SOFTWARE***

by

**SHANE ALLAN HANDLEY MARTIN**

*Thesis submitted in fulfilment of the requirements for the degree*

**Master of Engineering:** Mechanical Engineering  
in the Faculty of Engineering and the Built Environment  
at the Cape Peninsula University of Technology

**Supervisor:** Professor Graeme Oliver

**Co-supervisors:** Donovan Cogan, Professor Oscar Philander

**Bellville, South Africa**

December 2020

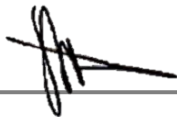
**CPUT copyright information**

*The dissertation/thesis may not be published either in part (in scholarly, scientific or technical journals), or as a whole (as a monograph), unless permission has been obtained from the University*

*The financial assistance of the National Research Foundation (NRF) towards this research is hereby acknowledged. Opinions expressed and conclusions arrived at, are those of the author and are not necessarily to be attributed to the NRF.*

## DECLARATION

I, *Shane Allan Handley Martin*, declare that the contents of this dissertation/thesis represent my own unaided work, and that the dissertation/thesis has not previously been submitted for academic examination towards any qualification. Furthermore, it represents my own opinions and not necessarily those of the Cape Peninsula University of Technology.



18 January 2021

---

**Signed**

**Date**

## ABSTRACT

With the advancements in technologies over the last decade, computational power, machine learning and artificial intelligence has revolutionized software, manufacturing capabilities and automation, amongst others. While the production industry has been experiencing the Fourth Industrial Revolution and Industry 4.0, engineering development can also experience a similar paradigm shift with the use of advanced software, to create digital twins for advanced simulations, and use advanced manufacturing methods, such as additive manufacturing, to optimise product design and assist in product development.

The aim of this research was to implement the current state-of-the-art in manufacturing techniques and engineering analysis software for CubeSat development. With Operation Phakisa underway, the development of CubeSat constellations is in focus at the African Space Innovation Centre (ASIC) at Cape Peninsula University of Technology (CPUT). To develop constellations efficiently, following the motivating force of Operation Phakisa, rapid prototyping and additive manufacturing was to be implemented. Methods and procedures were to be determined and implemented in using additive manufacturing to improve general CubeSat development. A CubeSat structure was to be designed to be suitable for additive manufacturing. The effect these additive manufacturing methods had on cost saving was to be determined. Advanced simulation software was to be used by developing a thermal digital twin of ZACube-2 CubeSat in the form of a finite element model and simulate the thermal orbital conditions to replicate that of the ZACube-2 orbit. The results of the simulation were to then be compared against actual data from ZACube-2, to validate the accuracy of the methods and model used for the digital twin.

With the constant development of additive manufacturing abilities and the advancements in CubeSat development, this research has shown how additive manufacturing can have a significant contribution towards CubeSat development by detecting design issues early on in the project, reducing costs, lead times and optimizing the design process. A 3D printed structure printed out of ULTEM 9085 was designed that met the structural and compatibility requirements. A finite element model of the structure was developed using orthotropic material properties to represent the 3D printed material characteristics. Finite element analysis on the structure, using both SOL101 and SOL103 Nastran solvers for static and harmonic analysis respectively, resulted in a maximum stress, 30% less than yield when subjected to the launch conditions loading and with a natural harmonic mode of 193 Hz, above the 100 Hz requirement. The structure was also designed to be compatible with commercial-off-the-shelf (COTS) components and proved to be more efficient to assemble and integrate by reducing the number of parts. The structure is also 14-39% lighter than COTS equivalents. The structure costs 57% more than manufacturing an aluminium structure when outsourced, however the lead time can be reduced from 3 weeks to 2 days. This cost would be significantly lower however, should the structure be 3D printed in-house.

Furthermore, the structure is lighter, easier to assembly and integrate and can be easily modified to suit the bus or payload needs.

Building a Concept Model, an accurate 3D printed replica with actual connectors and harnesses, as a new deliverable at the end of Phase B of a CubeSat mission, resulted in reducing the extra costs by 88% for the MDASat-1 CubeSat mission. This was achieved by identifying errors that were not picked up in CAD but discovered when conducting a trial assembly of the Concept Model. ASIC also saved significant time by identifying these issues early into the project rather than when building the engineering model (EM). Making use of the Concept Model saved costs towards the CubeSat mission as well as prepared and trained engineers for building the engineering and flight models of the CubeSats.

The current state-of-the-art in advanced engineering analysis software have made structural and thermal analysis more accessible and user friendly for design engineering. This allows for improved, optimised designs as well as the validation of the system and spacecraft design. The digital twin of ZACube-2 was developed by creating a simplified finite element model (FEM) of the CubeSat using 2D, and 1D elements. A simplified list of materials was used with accurate thermal and thermo-optical properties when defining the mesh of the FEM. A transient, orbital thermal simulation was conducted, replicating 15 orbits of ZACube-2, calculating the thermal radiation experienced by the CubeSat every 3 minutes. The digital twin showed to be very accurate when comparing the simulated results with temperature data acquired from ZACube-2, with a maximum variation at maximum and minimum temperatures of 2° C. Of the literature that was reviewed, none of the other researchers showed any form of validation of their results. Running the hypothetical dusk-dawn orbit simulation for ZACube-2 using the developed FEM showed that the satellite would be 15° C hotter in dusk-dawn than that of its current orbit. This would result in the overheating of components which could lead to catastrophic failure and finally mission failure. As part of this work a digital twin was developed for ASIC allowing them to better predict the thermal conditions the satellite components would be subjected to for a particular orbit. The methodologies developed in this research to create a thermal digital twin of a CubeSat could be applied to future missions or by other researchers to more optimally predict the thermal environment. Educated decisions can be made regarding orbit selections or contingency plans can be made to control the excess heat, such as passive heat control measures.

While Industry 4.0 is a term used predominantly in production and automation, some aspects of the revolution can be clearly seen to be implemented in the research and development engineering industry, with the advancements in additive manufacturing and the making use of the digital twin concept for engineering analysis, as demonstrated in this research.

## **ACKNOWLEDGEMENTS**

Firstly, I would like to thank the National Research Foundation (NRF) for their financial support towards my studies. Also, to the French South African Institute of Technology (F'SATI), specifically the director Professor Robert van Zyl for nominating me for the NRF bursary.

I would also like to thank my supervisor and co-supervisors, Professor Graeme Oliver, Prof Oscar Philander and Mr Donovan Cogan for their guidance with my research.

I would like to acknowledge the Product Lifecycle Management Competency Centre (PLMCC), for the use of the lab facilities.

Lastly, I would like to thank my friends and family for their constant support throughout my masters research.

## **DEDICATION**

To my mother and father who have always been there throughout my studies, supporting me and pushing me to follow my dreams.

## RESEARCH OUTPUTS

- Martin, S., Cogan, D., & Oliver, G. (2018). Additive Manufacturing for CubeSat Structures. *Mechanical, Manufacturing, Materials and Biomedical Engineering Conference* (pp. 59-60). South African Institution of Mechanical Engineering (SAIMEchE).
- Martin, S., Cogan, D., & van Zyl, R. (2020). CubeSat Thermal Modelling with On-Orbit Validation. *Paper submitted for publication.*
- Tadadjeu, S. I., Ngom, B. D., Martin, S., van Zyl, R. R., & Maaza, M. (2018). Ion Beams for Space Applications. In *Ion Beam Applications* (pp. 73-85). IntechOpen. doi:10.5772/intechopen.76993
- Wendland, A., Bumann, M., Martin, S., Nieman, J., & Bosman, S. (2020). Optimizing System Design Through Thermal Analysis with Cubesatellite as Case Study. *Systems, Software and Services Process Improvement. EuroSPI 2020. Communications in Computer and Information Science, vol 1251*. Springer. doi:10.1007/978-3-030-56441-4\_30

## TABLE OF CONTENTS

Declaration .....	ii
Abstract.....	iii
Acknowledgements.....	v
Dedication.....	vi
Research Outputs .....	vii
Table of Contents.....	viii
List of Figures.....	xii
List of Tables .....	xvii
Abbreviations.....	xviii
Symbols .....	xix
Glossary .....	xxi
1. Introduction.....	1
1.1. Background.....	1
1.1.1. CubeSats (CubeSats).....	1
1.1.2. African Space Innovation Centre .....	6
1.1.3. Space Mission Analysis and Design (SMAD).....	7
1.1.4. Rapid Prototyping / Additive Manufacturing .....	8
1.1.5. Industry 4.0 .....	10
1.2. Problem Statement .....	10
1.3. Aim .....	11
1.4. Objectives .....	11
1.4.1. Primary Objectives.....	11
1.4.2. Secondary Objectives .....	11
1.5. Limitations .....	12
1.6. Delineations .....	12
1.7. Research Methodology and Structure.....	12
2. Literature Review .....	16



2.1.	Industry 4.0 .....	16
2.2.	Additive Manufacturing in Space.....	17
2.3.	CubeSat Structure Designs.....	18
2.3.1.	Structural design for CXBN-2 2U CubeSat.....	18
2.3.2.	Additive Manufactured Structures.....	20
2.3.3.	Composite .....	23
2.4.	Engineering Analysis .....	24
2.4.1.	Thermal Analysis .....	24
3.	CubeSats .....	29
3.1.	CubeSat Structures .....	29
3.1.1.	CubeSat Standard .....	29
3.1.2.	Commercial-Off-the-Shelf (COTS).....	30
3.2.	CubeSat Design.....	32
3.2.1.	Launch Conditions .....	32
3.3.	Space Environment .....	33
3.3.1.	Thermal .....	33
3.3.2.	Radiation .....	36
4.	Additive Manufacturing .....	37
4.1.	Additive Manufacturing Types .....	37
4.1.1.	Vat Photopolymerization.....	37
4.1.2.	Powder Bed Fusion .....	37
4.1.3.	Binder Jetting .....	37
4.1.4.	Material Jetting .....	37
4.1.5.	Sheet Lamination .....	38
4.1.6.	Material Extrusion.....	38
4.1.7.	Direct Energy Deposition.....	39
4.1.8.	Hybrid .....	39
4.1.9.	Metal Additive Manufacturing .....	39

4.2.	Embedded Electronics in FDM .....	40
4.3.	Build Orientation Effects / Orthotropic .....	41
4.3.1.	Build Orientation Effects.....	41
4.4.	Effects on Design.....	41
4.5.	FDM Materials.....	43
4.5.1.	Polylactic Acid.....	43
4.5.2.	Acrylonitrile Butadiene Styrene .....	44
4.5.3.	Polycarbonate.....	44
4.5.4.	ULTEM.....	44
4.5.5.	Material Specifications.....	46
5.	Finite Element Method for Structural Analysis .....	48
5.1.	Finite Element Analysis .....	48
5.2.	Solid Elements for 3-D Problems.....	49
5.3.	Finite Element Equations .....	51
5.4.	Anisotropic Mechanics.....	52
5.5.	Orthotropy.....	54
6.	Results .....	57
6.1.	Structural Design for AM.....	57
6.1.1.	Design Objectives .....	57
6.1.2.	Material Selection .....	57
6.1.3.	Material Selection Discussion .....	58
6.1.4.	Discussion of Experiments .....	61
6.1.5.	Radiation Analysis .....	65
6.1.6.	Structure Design.....	67
6.1.7.	Discussion of Structure FEA.....	72
6.1.8.	Final Design Discussion .....	93
6.1.9.	Manufacturing .....	102
6.1.10.	Prototype.....	107

6.2.	AM Applications for CubeSat Development.....	111
6.2.1.	Rapid Prototyping for SMAD .....	111
6.2.2.	Infill Effects on Cost vs Performance.....	120
6.2.3.	Functional parts.....	129
6.2.4.	Discussion of AM applications for CubeSat development .....	133
6.3.	CubeSat Thermal Digital Twin .....	134
6.3.1.	Thermal Design and Analysis .....	134
6.3.2.	Material Properties .....	135
6.3.3.	Finite Element Model.....	136
6.3.4.	Thermal Results .....	139
6.3.5.	Thermal Discussion.....	144
6.4.	Final workflow chart.....	148
7.	Conclusion .....	151
7.1.	Structural Design for AM.....	151
7.2.	AM Applications for CubeSat Development.....	152
7.3.	The Effect of AM on Cost.....	153
7.4.	CubeSat Thermal Digital Twin .....	153
7.5.	Flow Chart for Managing CubeSat Development .....	155
8.	Recommendations.....	156
9.	Bibliography .....	157
	Appendix A.....	162
	Appendix B.....	163
	Appendix C.....	164

## LIST OF FIGURES

Figure 1-1: 1U to 3U CubeSats (Poghosyan & Golkar, 2017) .....	2
Figure 1-2: CubeSat launches since 2000 (Swartwout, 2015).....	3
Figure 1-3: EPS (Clyde Space Ltd, n.d.).....	3
Figure 1-4: OBC (Clyde Space Ltd, n.d.).....	4
Figure 1-5: Comms (ISISpace, 2015; Clyde Space Ltd, n.d.) .....	4
Figure 1-6: ADCS (CubeSat_Shop, n.d.) .....	5
Figure 1-7: Imager payload (CubeSat_Shop, n.d.).....	5
Figure 1-8: ZACube-2 (Martin et al., 2020).....	7
Figure 1-9: Space program development phases (Wertz & Larson, 1999).....	8
Figure 1-10: Thin vs thick layer build (Gibson et al., 2015) .....	9
Figure 1-11: Work flow processes to be developed as art of the research .....	13
Figure 2-1: Spacecraft bracket (Schiller, 2015).....	17
Figure 2-2: Exploded view of CXBN-2 (Dr.Wahidmurni, 2017).....	19
Figure 2-3: Tomsk-TPU-120 CubeSat (Anon, 2016).....	21
Figure 2-4: 1U PrintSat.....	21
Figure 2-5: UNSW-EC0 2U structure (Australian Centre for Space Engineering Research, n.d.) .....	22
Figure 2-6: 1U ABS structure (Piattoni et al., 2012).....	23
Figure 2-7: MkIII functional CubeSat structure (Keane, n.d.) .....	23
Figure 2-8: Carbon fibre 1U structure (Ball & Oliver, 2017).....	24
Figure 2-9: Dinh thermal physical properties (Dinh, 2012) .....	25
Figure 2-10: Dinh simulated absorbed heat flux( Dinh, 2012) .....	26
Figure 2-11: Dinh internal simulation results: hot (left), cold (right) (Dinh, 2012).....	26
Figure 2-12: MIST thermal model (Chandrashekar, 2017) .....	27
Figure 2-13: Payload temperatures for MIST at hot operational case (Chandrashekar, 2017) .....	28
Figure 3-1: ISIS 1U structure (ISISpace, 2015) .....	30
Figure 3-2: Pumpkin 1U structure (Pumpkin, 2015a) .....	31
Figure 3-3: Clyde Space 1U structure (Clyde Space Ltd, 2017) .....	31
Figure 3-4: View factor geometry (Martin et al., 2020).....	34
Figure 3-5: Spacecraft thermal environment (Martin et al., 2020) .....	35
Figure 4-1: ULTEM with embedded circuitry (Espalin et al., 2014).....	40
Figure 4-2: Embedded circuitry process (Espalin et al., 2014).....	40
Figure 4-3: FDM fibre orientation .....	41

Figure 4-4: Dogbone build orientation (left) and raster orientation (right) (Zaldivar et al., 2017) .....	42
Figure 4-5: Stress-strain curve for Zaldivar’s tensile tests (Zaldivar et al., 2017) .....	43
Figure 4-6: Raster orientations for primary axis 1 testing (left) and primary axis 2 testing (right) (El-Gizawy et al., 2011) .....	45
Figure 4-7: Raster Orientation for shear modulus properties (El-Gizawy et al., 2011) .....	45
Figure 5-1: A finite element .....	48
Figure 5-2: 3D coordinate system (Liu, 2002) .....	49
Figure 6-1: Material strength comparison .....	59
Figure 6-2: Thermal properties comparison .....	59
Figure 6-3: Material cost comparison .....	60
Figure 6-4: Tapped holes .....	61
Figure 6-5: Helical insert in the tapped hole .....	62
Figure 6-6: Test piece fasten to Perspex .....	62
Figure 6-7: Limiting torque results .....	63
Figure 6-8: TRIM material setup .....	66
Figure 6-9: Radiation depth in ULTEM at 14MeV .....	67
Figure 6-10: PC104 PC Board (Pumpkin Inc, 2003) .....	68
Figure 6-11: Clyde Space 1U side solar panel .....	68
Figure 6-12: Concept 1 .....	70
Figure 6-13: Concept 2 .....	70
Figure 6-14: Concept 3 .....	71
Figure 6-15: Concept 3 nut inserts .....	72
Figure 6-16: Concept 3 FEM .....	73
Figure 6-17: Rail FEM .....	74
Figure 6-18: Rods FEM .....	74
Figure 6-19: ULTEM shell FEM .....	75
Figure 6-20: Material orthotropy .....	76
Figure 6-21: RBE3 element definition .....	76
Figure 6-22: 1D element connector external view .....	77
Figure 6-23: 1D element connector internal view .....	77
Figure 6-24: Final FEM .....	78
Figure 6-25: Longitudinal analysis setup .....	79
Figure 6-26: Lateral analysis setup .....	80
Figure 6-27: Real Eigenvalue - Lanczos settings .....	81
Figure 6-28: Pumpkin structure FEM .....	82

Figure 6-29: Von Mises stress (left) and displacement (right) .....	82
Figure 6-30: Von-Mises stress under longitudinal loading .....	83
Figure 6-31: Deflection under longitudinal loading .....	84
Figure 6-32: Stress concentration for longitudinal loading .....	85
Figure 6-33: Maximum stress in ULTEM under longitudinal loading .....	86
Figure 6-34: Von Mises stress under lateral loading .....	86
Figure 6-35: Deflection under Later loading.....	87
Figure 6-36: Stress concentration for lateral loading .....	87
Figure 6-37: Maximum stress in ULTEM under lateral loading .....	88
Figure 6-38: First four harmonic modes.....	89
Figure 6-39: Von Mises stress for Pumpkin structure .....	89
Figure 6-40: Stress concentration in Pumpkin structure.....	90
Figure 6-41: Deflection in Pumpkin structure.....	90
Figure 6-42: Final design shell.....	93
Figure 6-43: Weight reduction in base and lid .....	94
Figure 6-44: Final design exploded view .....	95
Figure 6-45: Mass comparison structures .....	96
Figure 6-46: Final design base with rods .....	97
Figure 6-47: Final design PCB stacking.....	98
Figure 6-48: Final design shell mounted.....	99
Figure 6-49: Final design rails mounted.....	100
Figure 6-50: Final design assembled.....	101
Figure 6-51: Fortus 400mc 3D printer .....	102
Figure 6-52: STL import into Repitier Host.....	103
Figure 6-53: Layer 1 of sliced 3D Print .....	103
Figure 6-54: Sliced 3D model.....	104
Figure 6-55: Sliced ULTEM shell.....	104
Figure 6-56: Sliced ULTEM shell up to layer 150.....	105
Figure 6-57: Ultra-low profile screws .....	106
Figure 6-58: 3D printed prototype base .....	108
Figure 6-59: Prototype shell 3D print in progress .....	108
Figure 6-60: 3D printed prototype shell .....	109
Figure 6-61: Helical inserts in 3D printed prototype.....	110
Figure 6-62: Assembled prototype structure .....	111
Figure 6-63: ZACube-2 CAD concept (left) and ZACube-2 3D printed concept.....	112

Figure 6-64: Concept Model development process .....	113
Figure 6-65: Real vs simplified CAD of UTRXC .....	114
Figure 6-66: UTRXC Concept Model.....	114
Figure 6-67: Concept Model connectors .....	115
Figure 6-68: Sliced UTRXC board .....	116
Figure 6-69: 3D printed UTRXC .....	116
Figure 6-70: Assembly of UTRXC CM.....	117
Figure 6-71: Helical insert tool .....	117
Figure 6-72: Concept Model assembly process.....	118
Figure 6-73: Assembled Concept model .....	119
Figure 6-74: Assembled Concept Model.....	119
Figure 6-75: Type I specimen profile.....	121
Figure 6-76: Axial and transvers strains for applied load.....	122
Figure 6-77: Typical stress-strain curve .....	123
Figure 6-78: Toe compensation .....	124
Figure 6-79: PLA 100% printing .....	125
Figure 6-80: PLA tensile test .....	125
Figure 6-81: Three broken 80% PLA tensile test specimens.....	126
Figure 6-82: Three broken 100% PLA tensile test specimens.....	127
Figure 6-83: PLA Specimen cross section view 100% (left) 80% (right) .....	127
Figure 6-84: Stress-strain graph for PLA .....	128
Figure 6-85: Cost-performance ratio comparison for PLA .....	129
Figure 6-86: "Potted" fastener.....	130
Figure 6-87: Adhesive dispenser CAD .....	130
Figure 6-88: 3D printed adhesive dispenser.....	131
Figure 6-89: Solar panel mount in position.....	131
Figure 6-90: Solar panel mount.....	132
Figure 6-91: 3D printed solar panel mount .....	132
Figure 6-92: ZACube-2 exterior mesh .....	136
Figure 6-93: ZACube-2 interior mesh.....	137
Figure 6-94: Simulation results – hot.....	140
Figure 6-95: Simulation results – cold .....	140
Figure 6-96: Simulated vs actual UTRX temperatures.....	141
Figure 6-97: Simulated vs actual EPS temperatures.....	142
Figure 6-98: Simulated vs actual BAT temperatures .....	142

Figure 6-99: Battery cold (left) and hot (right) results ..... 143  
Figure 6-100: Battery heater telemetry ..... 144  
Figure 6-101: Dusk-dawn orbit..... 145  
Figure 6-102: Dusk-dawn temperature over time - entire satellite ..... 146  
Figure 6-103: Dusk-dawn temperatures ..... 147  
Figure 6-104: Flow chart for improved CubeSat development by integrating the current state-of-the-art  
in manufacturing techniques and engineering analysis software ..... 150



## LIST OF TABLES

Table 1-1: ZACube-2 orbital parameters .....	6
Table 2-1: CXBN-2 vibration test parameters (Dr.Wahidmurni, 2017) .....	20
Table 2-2: LEO thermal environment (Dinh, 2012).....	24
Table 3-1: Ariane 5 vibration qualification levels .....	32
Table 3-2: Launch vehicle fundamental frequencies .....	32
Table 4-1: Build orientation effects (Zaldivar et al., 2017) .....	43
Table 4-2: ULTEM 9085 Properties (El-Gizawy et al., 2011) .....	46
Table 4-3: FDM material specs .....	47
Table 6-1: Helical insert limiting torque .....	63
Table 6-2: ULTEM 9085 Mechanical Properties .....	72
Table 6-3: 3D printing build details .....	105
Table 6-4: Bill of Materials.....	106
Table 6-5: PLA Tensile Test Results .....	127
Table 6-6: Specimen printing statistics .....	128
Table 6-7: Harness costs .....	133
Table 6-8: ZACube-2 minimum and maximum subsystem temperatures .....	134
Table 6-9: Thermal material properties.....	135
Table 6-10: PCB material properties.....	135
Table 6-11: ZACube-2 subsystem masses .....	137
Table 6-12: Subsystem heat loads.....	138
Table 6-13: Workflow details .....	148

## **ABBREVIATIONS**

1D .....	One Dimensional
3D .....	Three Dimensional
ABS .....	Acrylonitrile Butadiene Styrene: Thermoplastic
AM .....	Additive Manufacturing
AMTL.....	Advanced Manufacturing Technology Laboratory
ASIC.....	African Space Innovation Centre
ASTM.....	American Society for Testing and Materials
CAD.....	Computer Aided Design
CAE.....	Computer Aided Engineering
cc .....	Close Corporation
CDS .....	CubeSat Design Specification
CM.....	Concept Model
CNC.....	Computer Numerical Control
COTS.....	Commercially Off the Shelf
CPUT.....	Cape Peninsula University of Technology
CTE .....	Coefficient of Thermal Expansion
EM.....	Engineering Model
EQM .....	Engineering – Qualification Model
ERB .....	Earth Radiation Belt
ESA .....	The European Space Agency
F’SATI.....	French South African Institute of Technology
FDM .....	Fused Deposition Modelling

FEA .....Finite Element Analysis

FM.....Flight Model

FEM.....Finite Element Model

HSTXC.....Commercial high-speed S-Band Transmitter

UTRXC.....Commercial Ultra high frequency Transceiver

g.....Acceleration due to gravity ( $1g = 9.81 \text{ m/s}^2$ )

HDT.....Heat Deflection Temperature

ISIS .....Innovations Solutions in Space

LEO .....Low Earth Orbit

LTAN .....Local Time of the Ascending Node

NASA .....The National Aeronautics' and Space Administration

PC .....Polycarbonate

PCB .....Printed Circuit Board

PLA .....Polylactic Acid

P-POD .....Poly-Picosatellite Orbital Deployer

SMA .....Subminiature version A

SMAD .....Space Mission Analysis and Design

SRB .....Solid Rocket Booster

STL .....Stereolithography – Geometry file for 3D printing

UK.....United Kingdom

UTS .....Ultimate Tensile Strength

**SYMBOLS**

\$.....Dollars

$\sigma_y$ .....Yield Stress  
 $\text{€}$ .....Euro  
 1U (2U,3U, etc.) .....One Unit  
 C .....Celsius  
 E or  $E$ .....Modulus of Elasticity  
 eV .....electron-volt  
 G or  $G$  .....Modulus of Rigidity  
 g.....Acceleration due to gravity ( $1g = 9.81 \text{ m/s}^2$ )  
 Hz .....Hertz – Unit for frequency  
 N.....Newton  
 Nm.....Newton-Meter  
 P.....load  
 Pa.....Pascal – Unit for pressure, stress and strength  
 R .....Rand  
 $T_g$ .....Glass transition temperature  
 U .....displacement  
 W .....Watts  
 $B$  .....Strain-displacement matrix  
 $C$  .....Elasticity Matrix  
 $F$  .....Force  
 $H$  .....Displacement interpolation matrix  
 $K$  .....Stiffness Matrix  
 $\varepsilon$ .....Strain

$\nu$ .....Poisson's Ratio

$\tau$ .....Shear Stress

## **GLOSSARY**

Carbon Fibre..... A type of composite material using woven fibres and resins

Coefficient of Thermal Expansion ..... The coefficient of thermal expansion (CTE) is defined as the change in the size of an object with its change in temperature.

CubeSat..... A nanosatellite that has a standard form factor of 100x100x113 mm.

Degree of Freedom (DoF)..... The DoF of an object or system is the number of parameters of its motion and may vary independently. 6DoF is the freedom of movement of a rigid body in a 3-dimensional space. It allows for the free movement forward or backwards, left or right, up or down in 3 perpendicular axes, x, y, and z as well as the rotation around these axes. This rotation is known as roll, pitch and yaw in aerospace terms.

Fundamental Frequency..... The lowest frequency of the waveform

Glass Transition Temperature ..... Glass transition temperature ( $T_g$ ) is the temperature at which a material transitions between A brittle, "glass" state into a softer or rubbery state.

Heat Deflection Temperature ..... Heat deflection temperature (HDT) is the temperature at which a plastic starts to deform under certain loading conditions.

Local Time of the Ascending Node ..... The Local Time of the Ascending Node (LTAN) is the local time at which the spacecraft crosses the equator on the ascending branch of its orbit.

Modulus of Elasticity ..... The ratio of tensile stress to tensile strain: The ease at which a material deforms due to tension

Moment of Inertia ..... The moment of inertia is the ability for an object to resist rotation.

Natural Frequency .....	The frequency where a system oscillates without any external load
Octave Rule .....	The resonant frequency of a structure must be twice of its supporting structure.
Orthotropic .....	Three perpendicular planes of elastic symmetry
Poisson's Ratio .....	The ratio of the proportional lateral reduction in width to the increase in the length of a material in tension
Resonant Frequency.....	The frequency of a vibrating body excited by another, at which the amplitude response is maximum
Shear Modulus.....	The ratio of shear stress to shear strain: The ease at which a material deforms due to shearing
Slice .....	To create a layered model of specific geometry for 3D printing
Stiffness .....	Stiffness is the ability for an object to resist deformation based on an applied load and is defined as the ratio of the applied force over the resulting deflection.
Young's Modulus .....	Also known as the modulus of elasticity, Young's Modulus is the ability for a material to change in length when subjected tensile or compressive stress.

## ***CHAPTER ONE***

### **1. INTRODUCTION**

#### **1.1. Background**

##### **1.1.1. CubeSats (CubeSats)**

CubeSat missions and projects are becoming increasingly popular around the world. More universities and commercial industries are using CubeSats to demonstrate or test new technologies. They are also being more widely used for educational purposes by schools and universities. (Poghosyan & Golkar, 2017)

The first small satellite dates as far back as 1957, which was the launch of the first-ever satellite, Sputnik-1. Since then, technology has come a long way, with the first high school to launch a satellite in 2013 (Swartwout, 2013).

Initially, only large space agencies that were backed by governments had the capabilities to develop satellites. The development of the satellites would require large engineering teams and facilities which were too expensive for academic facilities or private industries. Space agencies such as the National Aeronautics and Space Administration (NASA) and the European Space Agency (ESA) each launched massive crafts between 5 and 8 tons between 1990 and 2000. These heavy satellites were extremely expensive to build and therefore, over the next decade there was an interest in developing smaller crafts. (Poghosyan & Golkar, 2017)

Over the years, as technology improved, this enabled agencies to develop smaller and cheaper components that could be commercially bought off-the-shelf. This is where the CubeSat, a standard developed by Stanford and California Polytechnic State University (Cal Poly), came about. (Poghosyan & Golkar, 2017)

The CubeSat is a standard of a nanosatellite developed specifically to be compatible with the Poly-Picosatellite Orbital Deployer (P-POD). The P-POD is a standard launch interface also developed by Stanford and Cal Poly to safely house and launch the CubeSats. The P-POD has the dimensions of 13 cm x 16 cm x 40 cm which can house up to three 1U CubeSats or one 3U. CubeSats are dimensioned at a standard 1U of 10 cm x 10 cm x 11cm and are not to exceed 1.33 kg. It is, however, possible to have a 2U or 3U CubeSat which adds multiple 1U CubeSat dimensions to create a larger configuration (Swartwout, 2013). See Figure 1-1 below.

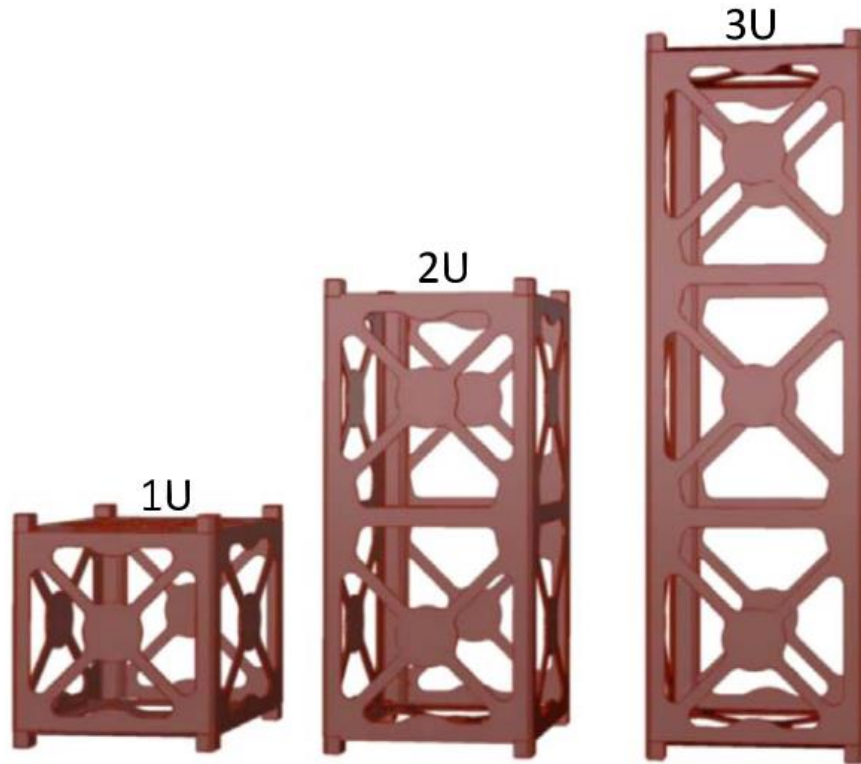


**Figure 1-1: 1U to 3U CubeSats** (Poghosyan & Golkar, 2017)

From the year 2000 through to 2017, 679 CubeSats have been launched (Swartwout, 2015). See Figure 1-2 on the following page that shows the trend in CubeSat launches during that period. The new off-the-shelf availability of components to build CubeSats allowed not only national space agencies the opportunity to launch satellites but also universities, private commercial companies and even schools (Poghosyan & Golkar, 2017). CubeSats are perfect tools for testing technologies, earth imaging, communications, scientific data collection and of course for educational purposes (Swartwout, 2015).

They gave universities a relatively cheap means of educating academics and students in real-life space mission scenarios. They could develop their own satellite to test new technologies and ideas at a price that was more affordable.



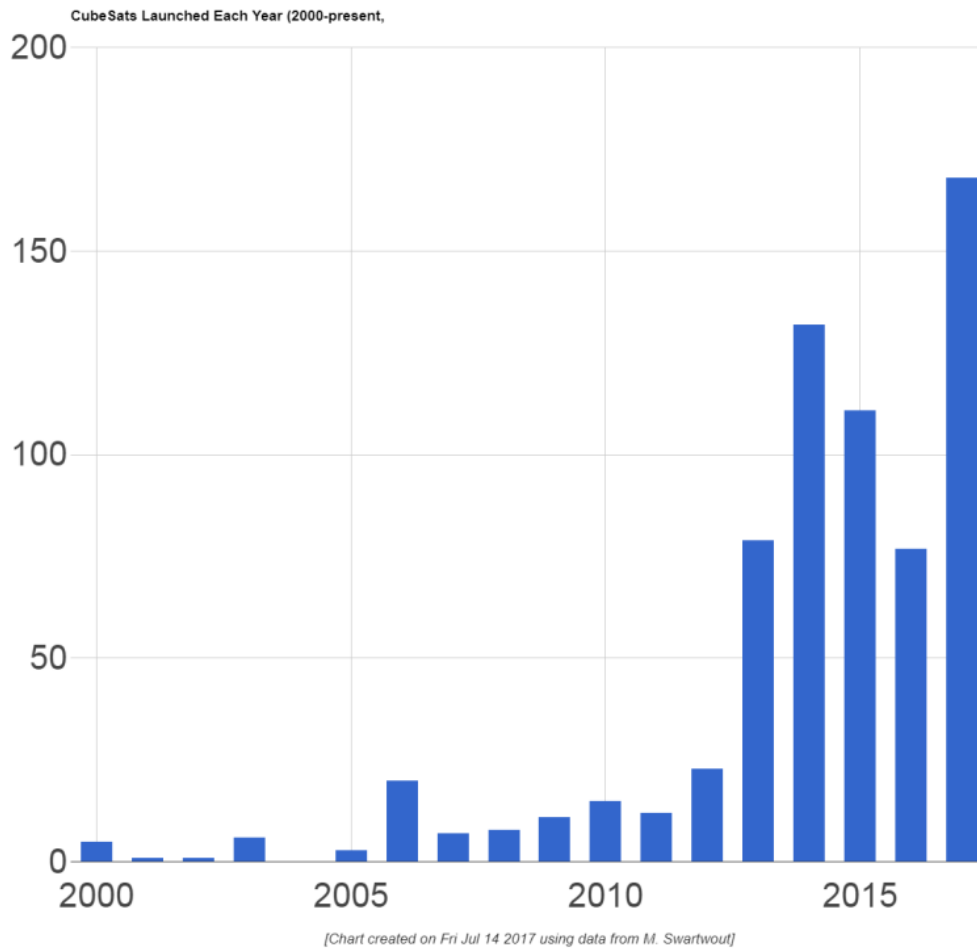


**Figure 1-2: CubeSat launches since 2000** (Swartwout, 2015)

#### 1.1.1.1. CubeSat Components

Power Module: The power module consists of the electronic power system (EPS), as seen in Figure 1-3, the solar panels and lithium-ion batteries. The components all control the power of the CubeSat which allows it to operate.

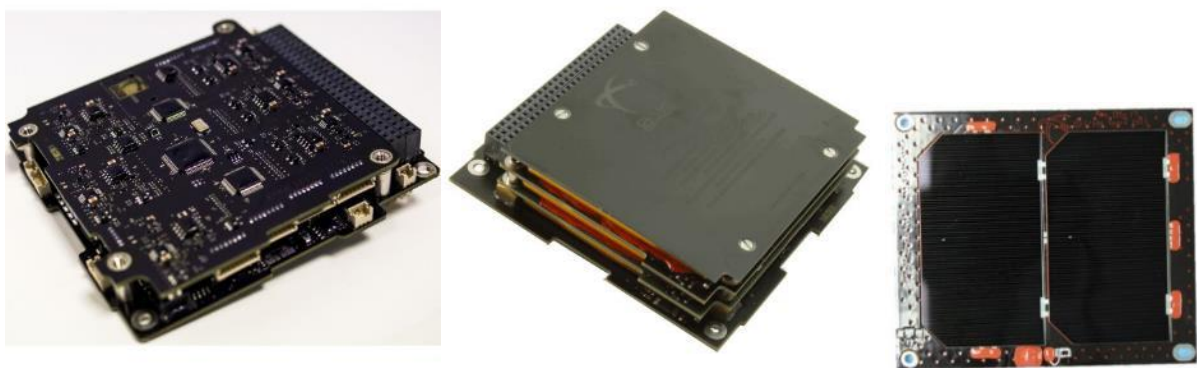


**Figure 1-3: EPS** (Clyde Space Ltd, n.d.)

**On-Board Computer (OBC):** The OBC, shown in Figure 1-4, is the component that controls everything that happens on the CubeSat. It governs what the payloads are doing and controls how data is sent to and from the ground station on earth.



**Figure 1-4: OBC** (Clyde Space Ltd, n.d.)

**Communication Module:** The communication module consists of receivers, transmitters and antennas to communicate to and from Earth. Figure 1-5 shows an example of a very high frequency (VHF) and ultra-high frequency (UHF) transceiver which uses deployable antennas to communicate to and from Earth.

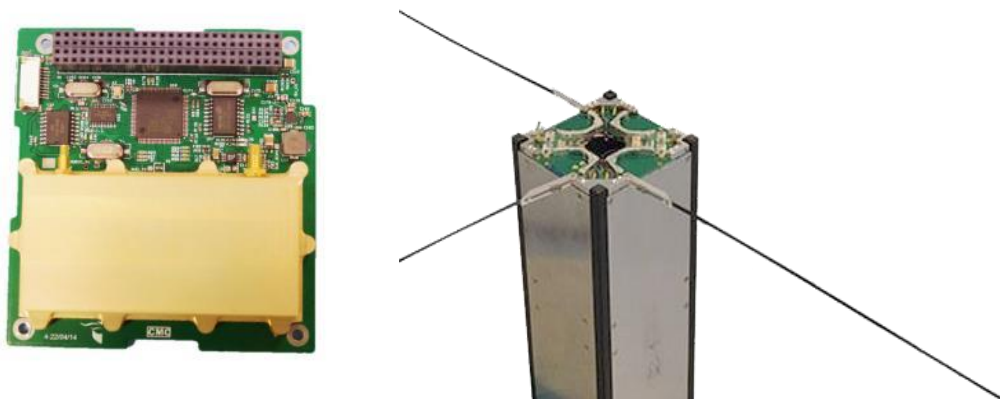


**Figure 1-5: Comms** (ISISpace, 2015; Clyde Space Ltd, n.d.)

**Attitude Determination and Control System (ADCS):** ADCS systems use magnetometers, magnetorquers, momentum and reaction wheels to determine the attitude and control the aim of the satellite, as can be seen in Figure 1-6. These systems are usually used when an imager is used as a payload that needs to be aimed towards Earth or for the pointing of antennas.

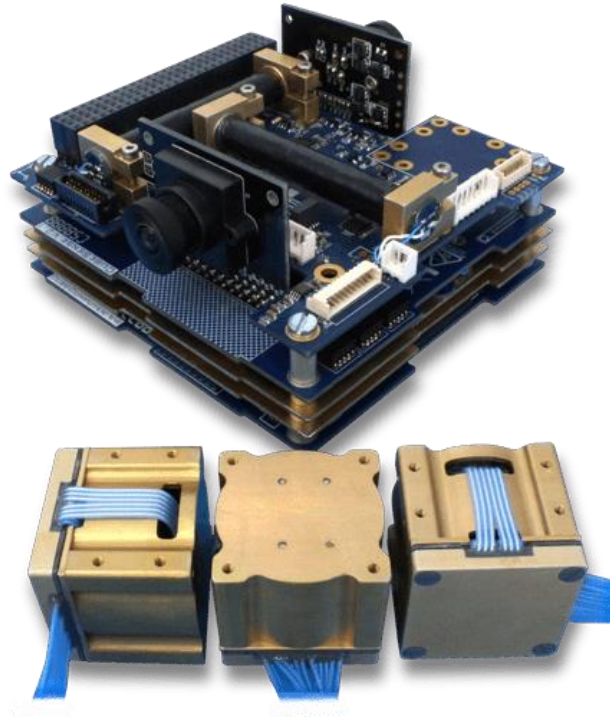


**Figure 1-6: ADCS** (CubeSat\_Shop, n.d.)

Heat control: Some CubeSats require heat control methods to control the heat within the CubeSat. This is achieved by active or passive heat control methods, although passive heat control methods such as heat straps or pipes are most commonly used in CubeSats (Fortescue et al., 2011).

Payloads: Different CubeSats have different payloads depending on the flight mission. An example of a primary payload for a CubeSat can be an imager for taking images and videos of Earth as seen in Figure 1-7.



**Figure 1-7: Imager payload** (CubeSat\_Shop, n.d.)

### 1.1.2. African Space Innovation Centre

The African Space Innovation Centre (ASIC) is an innovation hub of graduate students and engineers developing nano-satellite technologies. The centre is housed at the F’SATI at CPUT.

In 2013 CPUT launched its first CubeSat, ZACUBE-1. This CubeSat was developed through CPUT’s nanosatellite programme which is hosted by F’SATI and ASIC (Anon, 2017).

ZACUBE-1 is a 1U CubeSat with a primary payload of a high-frequency radio beacon. The primary mission is to characterize the Super Dual Auroral Radar Network (SuperDARN) radar array which is situated at the South African Antarctic Station. The mission is in collaboration between CPUT, Stellenbosch University and the South African National Space Agency (Van Zyl et al., 2013).

In December 2018, CPUT launched its second CubeSat, ZACUBE-2. The satellite is a 3U CubeSat with a Software Defined Radio (SDR) and a novel near infra-red imager as its primary payloads.

#### 1.1.2.1. ZACube-2

ZACube-2’s primary mission objective was to serve as a technology demonstration for its ship tracking payload for ocean vessel detection through AIS using the SDR. It is in a sun-synchronous orbit between 500 and 600km in altitude. Further orbital parameters can be seen in Table 1-1.

**Table 1-1: ZACube-2 orbital parameters**

<b>Orbit type</b>	Sun-synchronous
<b>Orbit period (s)</b>	5746.5
<b>Max Altitude (km)</b>	577
<b>Inclination (°)</b>	97.6
<b>Eccentricity</b>	0.002
<b>Argument of periapsis (°)</b>	124.5
<b>LTAN</b>	11:30

ZACube-2 weighs approximately 3.4kg with inhouse developed communications platforms to support the payloads. The communication platforms include and X and S Band transmitter as well as an ultra-high frequency transceiver (UTRX). The attitude of the satellite is controlled by magnetorquers and

reaction wheels as a part of a 3-axis stabilized attitude determination and control system (ADCS) (Villiers & Zyl, 2015). Figure 1-8 shows the external and internal view of ZACube-2.



**Figure 1-8: ZACube-2** (Martin et al., 2020)

#### 1.1.2.2. Operation Phakisa and MDASat

Operation Phakisa is the fast track by the South African government of the implementation of development in ocean economy and e-health. This is achieved by the monitoring of the ocean economy around the South African coast using Automated Information Service (AIS) and VHF Data Exchange Service (VDES). (Anon, 2017)

A constellation of CubeSats will be implemented to facilitate South Africa Maritime Domain Awareness (MDA). The SDR that was flown and proven on ZACUBE-2 will be the primary payload of each satellite to carry out the mission objectives. By making use of a constellation of satellites, the re-visit time to the South African Exclusive Economic Zone (EEZ) is reduced. (Anon, 2017)

Phase one of Operation Phakisa and MDASat is the development of a constellation of 3 2U CubeSats. These satellites are currently in development at the ASIC. This will be the first time multiple satellites will be built simultaneously at ASIC.

#### 1.1.3. Space Mission Analysis and Design (SMAD)

When a new space mission is started, the methodologies that are defined in SMAD are usually followed. One of these methodologies from a systems engineering aspect is the space mission lifecycle as defined by space program development phases that are followed for space mission designs.

Different space agencies have slight variations, but all follow a similar flow as can be seen in Figure 1-9 below. At CPUT's ASIC for developing CubeSats, the ESA lifecycle is followed. At the end of each phase, the phase is concluded by reviewing that particular phase. For example, at the end of Phase B, there is a Preliminary Design Review (PDR) to conclude the phase. At the end of some phases, there are physical deliverables, for example during phase C, an Engineering Model (EM) and Qualification Model (QM) of the spacecraft are built. These units are for testing the spacecraft's systems. The EM is for testing that all subsystems work within the entire spacecraft system while the QM undergoes tough environmental testing to replicate the launch conditions and verify these satellites subsystems will survive. In some cases, to reduce costs only one Engineering-Qualification Model (EQM) is built. This model is used as the EM and QM. The final model which is built during Phase D is the Flight Model (FM). This is the model that will then be launch and used to carry out the mission objectives (Wertz & Larson, 1999).

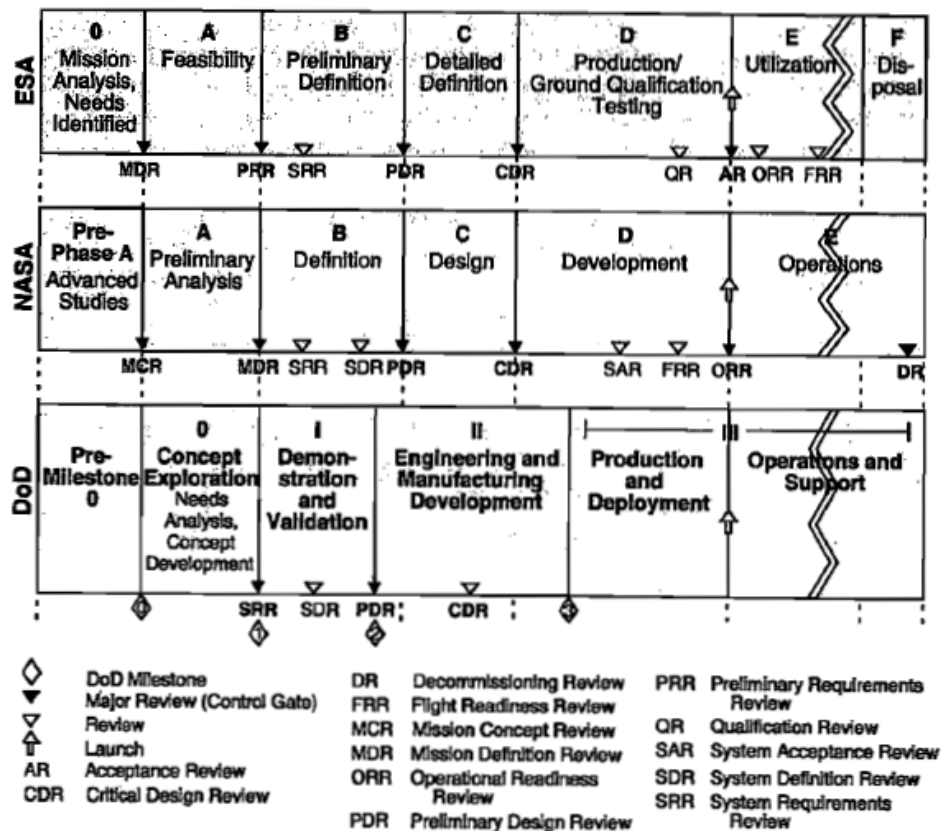


Figure 1-9: Space program development phases (Wertz & Larson, 1999)

#### 1.1.4. Rapid Prototyping / Additive Manufacturing

Rapid Prototyping was the term given to additive manufacturing (AM) when it was originally adopted. This was because manufacturers used to use the technology to rapidly produce prototypes of their products. The term rapid prototyping has mostly fallen away as AM has developed significantly by its improved accuracy and material properties thus becoming a manufacturing method used for testing, tooling  
Shane Martin

and production, not only for prototyping. A technical committee within ASTM international officially adopted the term additive manufacturing to replace that of the older rapid prototyping. (Gibson et al., 2015). Rapid Prototyping today refers to the method of producing a quick artefact of a design or concept.

Unlike conventional subtractive manufacturing methods such as CNC milling, additive manufacturing (AM) produces parts by adding material. Parts are fabricated with little, to no process planning based on a three-dimensional (3D) computer-aided design (CAD). AM allows for a simple way of producing complex 3D parts without having to determine process orders, cutting tools, etc. AM works in such a way that the part is generated by the material being layered upon itself to form the part based on the data from the CAD model. The quality of the part depends on the size of these layers, the thinner the layer, the better the accuracy and the closer it will be to the original model. In Figure 1-10 below, the comparison of a thick versus a thin layer build can be seen. AM machines to date all use the same layer-based methods however vary in the materials they use, how these layers are made and how they are bonded. All of these variances affect the final outcome of the product, its accuracy to the original model or material and mechanical properties of the part. (Gibson et al., 2015)



**Figure 1-10: Thin vs thick layer build** (Gibson et al., 2015)

With the advancements in AM, 3D printing is becoming increasingly popular in developing advanced structures while keeping an excellent strength to weight ratio. Some major manufacturing companies

making use of AM include Michelin, Nike, General Motors, BMW, amongst hundreds of other aerospace and automotive manufacturers (Duann Scott, 2017).

### **1.1.5. Industry 4.0**

Industry 4.0 or also known as the fourth industrial revolution is a continuation of the third industrial revolution with the adoption of computers and automation and progressing further to smart machinery and autonomous systems that function on data and machine learning. Industry 4.0 is being used to develop smart factories, which uses virtual environments including the Internet of Things, Big Data, Cloud Computing, etc., to interact with the physical environments which include autonomous robots and additive manufacturing. (Dilberoglu et al., 2017). According to Rodič, 2017, the key technologies and developments in Industry 4.0 include (Rodič, 2017):

- Green IT
- Big data and analytics
- Autonomous systems
- Horizontal and vertical system integration through new standards
- Cybersecurity
- Augmented reality
- The industrial Internet of Things
- Additive manufacturing
- The cloud
- Simulation modelling

The Digital Twin concept defines the use of simulation modelling throughout the product lifecycle, from development and testing a virtual environment and making use of previous product lifecycle data. “Combining the real life data with the simulation models from design enables accurate productivity and maintenance predictions based on realistic data.” (Rodič, 2017)

## **1.2. Problem Statement**

With the advancements in technologies over the last decade, computation power, machine learning and artificial intelligence has revolutionized software, manufacturing capabilities and automation, amongst others. While the production industry has been experiencing the Fourth Industrial Revolution and Industry 4.0, engineering development can also experience a similar paradigm shift with the use of advanced software to create digital twins for advanced simulations and use advanced manufacturing methods such as additive manufacturing to optimise product design and assist in product development.

As product development continues, components for CubeSats are becoming increasingly powerful. With this increase in power, comes heat. It is therefore becoming a requirement to accurately predict the



thermal conditions that a CubeSat will experience in orbit. This has been difficult to accurately predict in the past due to the complexity of the simulations required and the computational power needed.

While developing and building CubeSats is relatively affordable for space engineering, it still has extremely high costs. Developing ways of reducing these costs therefore is critical for CubeSat development. Reducing costs makes it more affordable for institutions and research facilities as well as allowing for continued research and development. CubeSat structures are most commonly purchased as an off-the-shelf item as it has flight heritage and is a simple design to accommodate most satellite configurations. These off-the-shelf structures, however, are expensive and limit the CubeSat design to suit the structure. For this reason, in-house built structures can be developed to overcome these limitations (Swartwout, 2015). Using additive manufacturing methods an in-expensive alternative structure for education facilities and industries could be designed. Additive manufacturing could also be used to assist in the development phase of a CubeSat mission as well as creating tools and jigs as mechanical support equipment, this could have significant cost savings by reducing materials costs, avoiding additional costs by identifying issues early in the mission and optimizing workflow.

### **1.3. Aim**

The aim of this research is to show how CubeSat development can be optimised by integrating the current advancements in manufacturing in the form of additive manufacturing. Advanced analysis software will also be used to develop finite element models for optimizing CubeSat structural and thermal design through simulations and analysis.

### **1.4. Objectives**

#### **1.4.1. Primary Objectives**

- Design CubeSat structure suitable for additive manufacturing.
- Determine and implement methods of using additive manufacturing to improve general CubeSat development.
- Determine if these methods have cost saving effect.
- Develop a thermal digital twin of a ZACube-2 CubeSat in the form of a finite element model. Conduct thermal simulations on the digital twin, analyse results and compare against actual data.

#### **1.4.2. Secondary Objectives**

- To review previous literature concerning CubeSats, additive manufacturing, structure design and thermal analysis.
- Discuss the results of the three primary objectives.

- Conclude findings and give recommendations for further research or improvement.

### **1.5. Limitations**

- No funding has been specifically allocated to the research topic for testing and/or prototyping.
- The CPUT Fortus 400mc 3D printer was only available for use after mid-2019
- Tensile testing facilities data acquisition were limited to strain by displacement.

### **1.6. Delineations**

- Since CPUT has fused deposition modelling (FDM) type 3D printers and the lack of budget for the project, only FDM type of additive manufacturing would be considered for the research.
- F'SATI, the research centre at which the research project is being conducted focuses on the development of CubeSats. Therefore, rapid prototyping, additive manufacturing and analysis for CubeSat development is the focus of the study. Structural design will be focused specifically on 1U structures.

### **1.7. Research Methodology and Structure**

The research will be looking at approaches to improve CubeSat mission development through advanced manufacturing and engineering analysis software. First a literature survey will be conducted to determine what research has been previously done and where improvements can be made. ASIC has developed workflow processes for CubeSat development throughout the years with the development of ZACube-1, ZACube-2 and MDASat-1 CubeSats. Figure 1-11 shows these workflow processes that were implemented to integrate the state-of-the-art in manufacturing and engineering analysis into CubeSat development for a given mission. The various aspects of CubeSats and their missions will be investigated, identifying where and which workflow processes need to be developed to improve process efficiency and the quality of the final product. The design of a 3D printed structure is then discussed showing how additive manufacturing can optimise CubeSat design. This is followed by how additive manufacturing can be used during a CubeSat mission improving the workflow and efficiency of the mission phases by making use of prototypes and 3D printed functional parts. By making use of advanced thermal simulation as a thermal digital twin to replicate and predict the thermal conditions of a ZACube-2 CubeSat then shows its significance and how it can be used to optimise the mission design. To conclude the research, it is then shown how these methods can be implemented into CubeSat development to improve the overall design process.

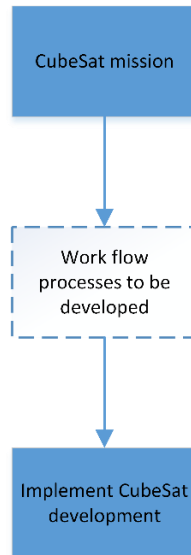


**Figure 1-11: Work flow processes to be developed as art of the research**

Below is a breakdown of the research structure of this thesis.

### ***Chapter One – Introduction***

In this chapter, the research problem, aim, objectives, as well as the background of the research, are discussed. This covers the background of CubeSats and its significance at CPUT, where they began and what they are, as well as what additive manufacturing and Industry 4.0 is. The research structure and methodology for conducting this research is also shown.

### ***Chapter Two – Literature Review***

In this chapter previous literature that has been published related Industry 4.0 and the Fourth Industrial Revolution is discussed, followed by the use of additive manufacturing for space, CubeSat structures design and CubeSat thermal analysis.

### ***Chapter Three – CubeSats***

In this chapter, the theory behind CubeSats is discussed. This includes the theory behind the CubeSat structure, what its specifications are as well as what current designs are available as off-the-shelf components. The procedures and consideration that are needed for the designing of a spacecraft are then discussed. This includes what conditions the CubeSat will experience during the launch as well as the space environment once in space.

#### ***Chapter Four – Additive Manufacturing***

This chapter discusses what additive manufacturing is, how it works and the different types. The effect additive manufacturing has on the design process is also discussed as well as the typical materials that would be available for FDM type additive manufacturing.

#### ***Chapter Five – Finite Element Method for structural analysis***

The concepts, definitions, and methods used in structural Finite Element Analysis (FEA) and orthotropic materials are discussed in this chapter. The theory covers basic first principles of finite elements and how they are used in FEA software. Also covered, is the theory behind the stiffness matrixes and anisotropic mechanics used for the properties required for the defining of orthotropic materials for FEA software.

#### ***Chapter Six – Results***

This chapter discusses the results and findings attaining to the primary research objectives. First the structure design objectives, procedure, concepts, tests and analyses are discussed. The chapter begins with the methods used to select the appropriate material for use on the structure. The testing methods required to acquire the mechanical properties of the chosen material as well as fastening method is then discussed. Following this section is the discussion of how the structure is designed using finite element analysis to validate design decisions. This starts with the Finite Element Model (FEM) setup and design considerations for the various simulations. The results of the FEA are then shown followed by a discussion of the results. The concepts that were developed and analysed as well as the design considerations that lead to the final design are then discussed. This section references the FEA results previously discussed in the chapter and how it was used to optimise the structure and reach the final design. This final design is then discussed. The following section discusses the recommended manufacturing method that would be used in the manufacturing of the structure followed by a Bill of Materials (BoM) and costing for the entire structure.

The results of the second primary objective are then discussed, showing the impact additive manufacturing can have on space mission analysis and design and how creating concept model prototypes can have a systems-level contribution towards Cube and Nanosatellite development. The use of an affordable 3D printer for prototyping and functional part manufacturing is then discussed showing the effects the infill density can have on cost versus the performance of the part. Various functional parts that aid in the integration and assembly procedure of CubeSats are then discussed and how they save on cost and time during development.

Finally, the results of the final primary objective are discussed. How thermal design of a CubeSat is carried out and the methods used in developing the digital twin in the form of a finite element model.

The analysis setup and simulation results are discussed comparing to actual data taken from the ZACube-2 CubeSat. A further simulation is discussed showing the importance of an accurate thermal digital twin and how it impacts mission and CubeSat design.

***Chapter Seven and Eight – Conclusion and Recommendations***

In Chapter Seven and Eight, a conclusion is made based on the results discussed in Chapter 6. The conclusion is made by comparing and concluding the results based on the original research problem, aim and objectives. Future work recommendations and improvements are then discussed in the following Chapter Eight.

## 2. LITERATURE REVIEW

### 2.1. Industry 4.0

The fourth industrial revolution is forcing companies to re-examine the way research and business is conducted. It is bringing new jobs that require new skills that allow rapid adaptation, innovation and entrepreneurship (Rodič, 2017). Simulation has developed from an analytical and optimisation orientation to integrating simulation models into decision support tools to be used recurrently (Rodič, 2017).

Simulation has developed since the 1960s where it was only accessible by mathematical and computing experts to a standard tool used by engineers. Simulation allows for validation and testing of systems in the form of model based systems (Rodič, 2017). With the introduction of Industry 4.0, modelling of a manufacturing and other systems in a virtual environment using artificial intelligence for process control with autonomous adjustment is required (Rodič, 2017). This new simulation modelling paradigm can be surmised by the concept “Digital Twin”. The Digital Twin concept defines the use of simulation modelling throughout the product lifecycle, from development and testing a virtual environment and making use of previous product lifecycle data. “Combining the real life data with the simulation models from design enables accurate productivity and maintenance predictions based on realistic data.” (Rodič, 2017)

Using the Digital Twin for product development, making use of the system design approach allows for the integration into the final product for training, optimisation and further development. Simulation software allows for engineers to construct a virtual prototype of a design, directly from CAD and integrate it as a Digital Twin on a real time platform as a functional mock-up unit (Rodič, 2017). Using a digital twin to identify issues early in the design process can save costs and further design optimisation.

AM will become a key technology used in the fabricating of new customized products. This mass customization is necessary for Industry 4.0 as a non-traditional manufacturing method with its ability to create complex, sophisticated objects in the form of new materials and geometries. There are still some doubts about AM application in mass production however it is already extremely popular in the aerospace, biomedical and manufacturing industries. Its ability to create accurate, optimised objects in an efficient manner could see it replacing conventional manufacturing methods in the near future. (Dilberoglu et al., 2017)

## 2.2. Additive Manufacturing in Space

AM fit with the aerospace industry very well, especially in the space side. Typically, products for space are not high rate products. The parts are also usually complex, suiting a very specific requirement leading to complex geometries and structures. AM allows for the production of single units at a relatively low cost and completely change the business approach. (Schiller, 2015)

The complex geometries of aerospace parts lead to a dramatic increase in manufacturing costs when using existing subtractive manufacturing. These complex geometries, however, are one of the strengths of AM machines. AM can easily produce these complex parts, allowing parts to be optimally designed with complexities while not dramatically increasing the manufacturing costs. (Schiller, 2015)

When optimizing designed parts using topology optimisation, the tool shows areas of a part that can have material removed without affecting the structural integrity. In traditional manufacturing methods it would be quite complex and expensive to manufacture the part with the optimised geometry however with additive manufacturing it is easily achieved. In Figure 2-1 below, a comparison of a bracket made with traditional manufacturing methods versus additive manufacturing can be seen. (Schiller, 2015)

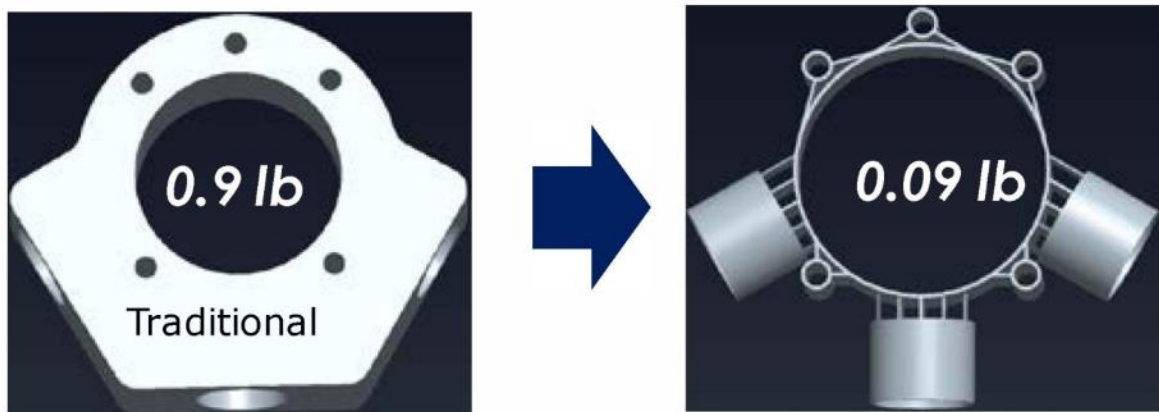


**Figure 2-1:** Spacecraft bracket (Schiller, 2015)

According to Davies, S, an additive manufacturing company named, Made in Space, has been using 3D printing on the ISS in what's called the Additive Manufacturing Facility (AMF). The facility has been printing parts out of ABS and polyethylene but was planning to start printing using PEI/PC material also known as ULTEM 9085 which has a significantly higher tensile strength. The idea was to be able to produce tools, spares for extravehicular as well as intravehicular activities. Satellite structures could also be created on-site if there is a demand. (Davies, 2017)

According to Grunewald, S, United Launch Alliance (ULA) developed and is using a duct system in the Atlas V rockets environmental control system ductwork. This ductwork is made from ULTEM 9085

and printed using the Stratasys Fortus 900mc FDM 3D printer. The ductwork is responsible for delivering nitrogen to parts of the rocket booster during the launch sequence. By using additive manufacturing, ULA reduced part costs by 57%. ULA also expects to include over 100 3D printed parts on their next generation of Atlas rockets. (Grunewald, 2015)

Other commercial space companies have also been using 3D printing for space use. SpaceX uses an entirely 3D printed rocket engine, SuperDraco printed using an EOS metal laser sintering 3D printer (Sher, 2019). The NASA crew from Crew Dragon of SpaceX used 3D printed face helmets which are believed to have been 3D printed using FDM type 3D printing (M, 2020).

Relativity Space, an additive manufacturing company has Stargate, the world's largest 3D printer. The purpose of this printer is to be able to 3D print an entire rocket, intending to launch into low earth orbit. Similar to SpaceX they also have developed a 3D printed rocket engine, Aeon (Salmi, 2019).

### **2.3. CubeSat Structure Designs**

#### **2.3.1. Structural design for CXBN-2 2U CubeSat**

Byeloborodov, 2017 focused their thesis on the design of a 2U structure for the CXBN-2 CubeSat carrying two CZT detectors as its payload. The objective was to develop all subsystems in-house while still adhering to the guidelines as stipulated in the CDS.

Byeloborodov made use of 3D printing for prototyping of the CubeSat concept. Making use of the 3D printed model allowed for the variation of the design. It was also used to check that deployment systems work as they are meant to. The models of the 3D printed components could also be used for clearance checks while waiting for machined parts. The 3D printed model could also be used to check cable lengths and routing before manufacturing the actual cables and harnesses.

Because this structure design was for a specific mission, the subsystems could be integrated into the assembly along with the structure. This was useful for applying mass to the CAD models of the subsystems for determining the centre of gravity of the CubeSat.

One of the objectives of the structure design was to reduce the number of parts for the structure re simplifying manufacturing and assembly. Less parts reduce the chances of failure, number of fasteners required and machining cost. The structure was to consist of two side panels, three crossmembers, two payload brackets, an antenna place, solar panels and deployment system. Figure 2-2 shows an exploded view of the entire CXBN-2 CubeSat. All structural members were machined out of 6061-T6 aluminium.



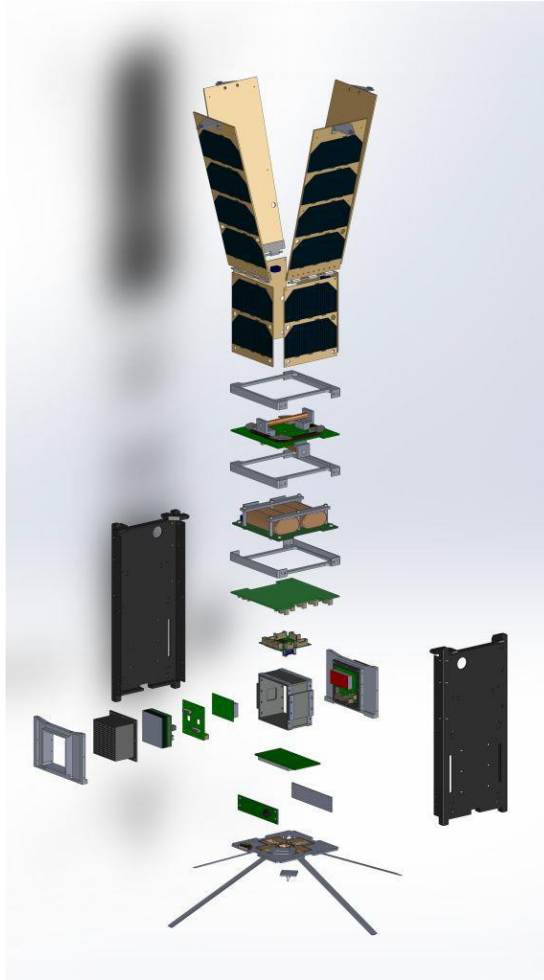


**Figure 2-2: Exploded view of CXBN-2** (Dr.Wahidmurni, 2017)

Byeloborodov listed several issues that were found with the CubeSat, many of which required the complete disassembly of the satellite, most of the subsystems and the payload encountered issues that needed to be solved, the structure itself was not grounded sufficiently which was believed to be due to the anodizing layer on the inside of the frame. This was solved by removing some of the anodizing with oven cleaner. Other structural issues included clearance and fitment issues with parts not fitting and disconnecting from one another. It was noted that most of these issues were discovered with the engineering model (EM) of the satellite so that the issues were solved for the flight model (FM).

Vibration testing was done on the satellite to meet the flight acceptance test requirements for the battery packs as shown in Table 2-1. It was reported that both EM and FM passed the vibration testing inspection post vibration.

**Table 2-1: CXBN-2 vibration test parameters** (Dr.Wahidmurni, 2017)

Frequency (Hz)	ASD (G <sup>2</sup> /Hz)	dB/Octave	G <sub>rms</sub>
20.00	0.028800	*	*
40.00	0.028800	0.00	0.76
70.00	0.072000	4.93	1.43
700.00	0.072000	0.00	6.89
2000.00	0.018720	-3.86	9.65

Byeloborodov concluded that the structure design needed to be “more universal”, implying that the design needed to be more versatile by having multiple mounting holes for subsystem positioning. It was also concluded that the machining quality is very important, and a compromise must be made between cost, lead time and machining quality. The budget for the structure was approximately \$31,673 per structure, which equates to R528,261 at the current R16.95 to the dollar. Excluding labour costs, the total material costs per structure was approximately \$3333 which equates to R55,579.

While Byeloborodov concluded that the structure did finally fit and pass the vibration testing, no other testing or analysis were shown to be done on the satellite or structure. Static gravitational loading, which has the greatest stress induced on a structure was not shown to be considered. Neither was the natural harmonic mode of the satellite or structure considered. There was also no discussion of any thermal analysis done on the satellite, although this may have been excluded from the scope of the research. Environmental simulation is highly important for structural and thermal design to simulate the conditions that the satellite will experience and should not be neglected in a structure or CubeSat design.

### 2.3.2. Additive Manufactured Structures

Typically, the aluminium structures are used for CubeSat missions however alternative structures have been developed and some tested. There have been three recorded missions where CubeSats are making use of a 3D printed structure including a Tomsk-TPU-120, PrintSat and QB50 UNSW EC0. An Italian group of engineers from the University of Bologna also developed a 1U CubeSat out of ABS however only a prototype was manufactured and not launched. There is limited published information regarding these designs, however, the fact that there have been previous attempts shows the potential for success.

#### 2.3.2.1. Tomsk-TPU-120

Tomsk-TPU-120, the 3U CubeSat developed by Russian Tomsk Polytechnic University (TPU) was the first spacecraft to have a 3D Printed structure in orbit when it was deployed into orbit in August 2017. The CubeSat, shown in Figure 2-3, was launched from Russia to the International Space Station (ISS)

in March 2016 where it was later deployed via a Russian spacewalker. (Tomsk Polytechnic University, 2017)

Unfortunately, no technical data about the CubeSat could be found.



**Figure 2-3: Tomsk-TPU-120 CubeSat** (Anon, 2016)

#### 2.3.2.2. PrintSat

PrintSat, shown in Figure 2-4, is a 1U CubeSat developed by Montana State University. The CubeSat was constructed using Selective Laser Sintering which is a form of 3D printing. The structure was made out of a polyamide-based, carbon fibre filled material called Windform XT. (Anon, n.d.)

Unfortunately, the PrintSat was lost in a launch failure in November 2015.

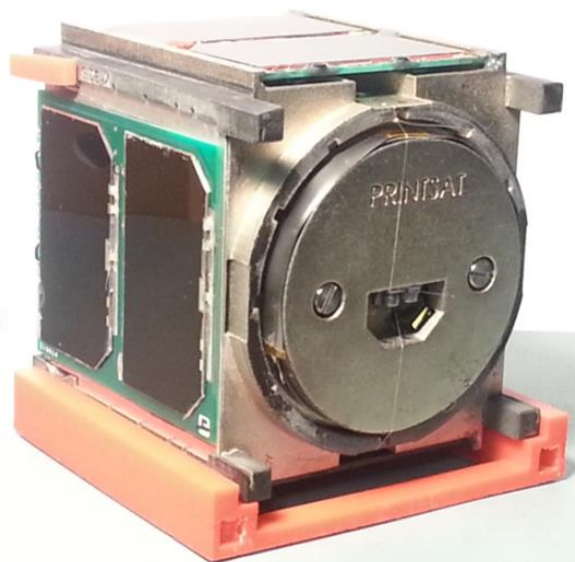


**Figure 2-4: 1U PrintSat**

### 2.3.2.3. QB50 UNSW EC0

The Australian university, University of New South Wales (UNSW) developed and built a Satellite named Educational CubeSat Zero (EC0) to be a part of the QB50 network of 50 CubeSats that were launched in April 2017 (The Australian Centre for Space Engineering Research, 2016).

The CubeSat, shown in Figure 2-5, also makes use of additive manufacturing, unfortunately again no technical data could be found, other than that the material used is a thermoplastic called Polyether ether ketone (PEEK). (The Australian Centre for Space Engineering Research, 2016)

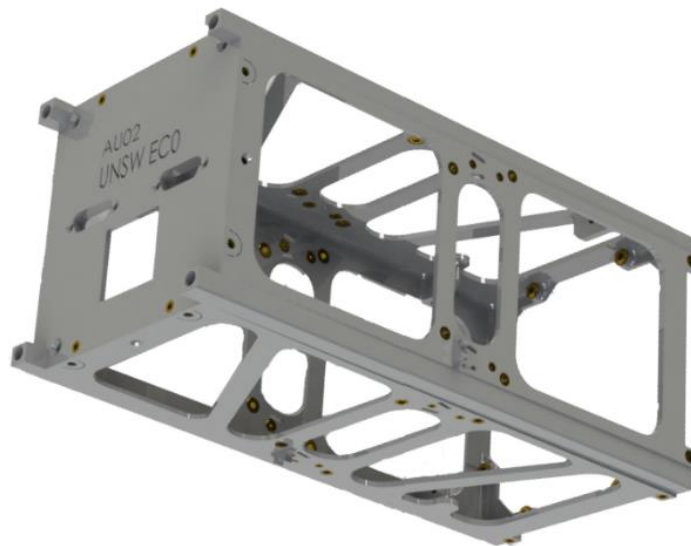


**Figure 2-5: UNSW-EC0 2U structure** (Australian Centre for Space Engineering Research, n.d.)

### 2.3.2.4. Plastic CubeSat

The Italian University of Bologna and a group of students and academics have developed a 1U CubeSat, as shown in Figure 2-6, which has a structure made from ABS using FDM additive manufacturing. Various tests were done on the prototype of the CubeSat and showed great potential for further improvement. The prototype has not had any mission heritage however and no mission launches have been documented (Piattoni et al., 2012).

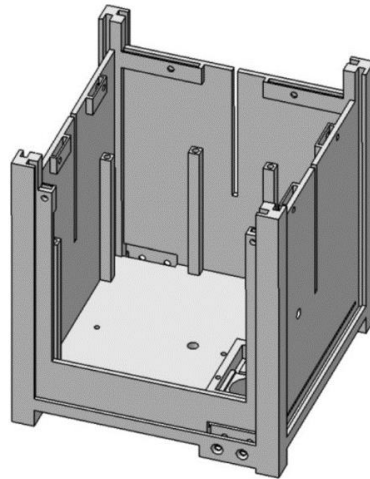


**Figure 2-6: 1U ABS structure** (Piattoni et al., 2012)

#### 2.3.2.5. The Mk III Functional CubeSat Structure

The Mk III is the third design that private engineer Phillip Keane has developed during his studies. The structure which is shown in Figure 2-7, has only been developed for research purposes however and not implemented into any missions at this stage. The structure was printed out of ULTEM 9085 using a Fortus 450mc printer. Keane states that ULTEM is up to 50% lighter than some types of aluminium and functions as better shielding when compared with aluminium. (Keane, n.d.)

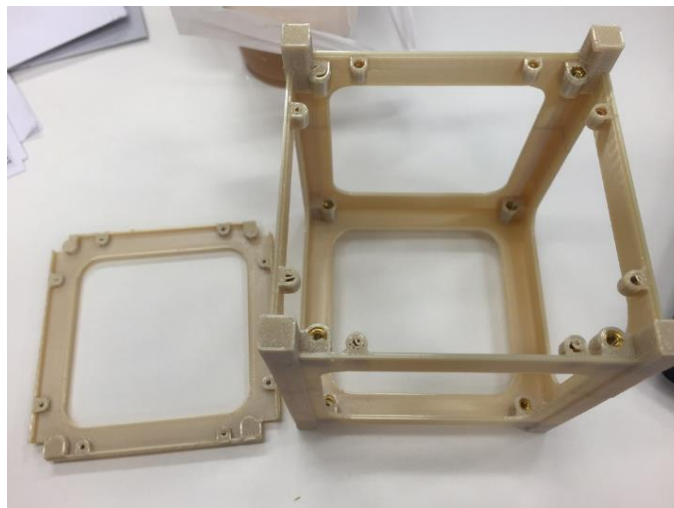


**Figure 2-7: MkIII functional CubeSat structure** (Keane, n.d.)

#### 2.3.3. Composite

Jeffrey Ball from CPUT looked at using a multifunctional composite (MFC) structure for use in a CubeSat. He used carbon-fibre composite materials for the main structure and this allowed for an integration of electrical circuitry within the material. A prototype of the CubeSat was manufactured and tested and showed that the use of MFC has a potential for further development and could be a viable alternative to the standard aluminium structure. See Figure 2-8 below. (Ball & Oliver, 2017)

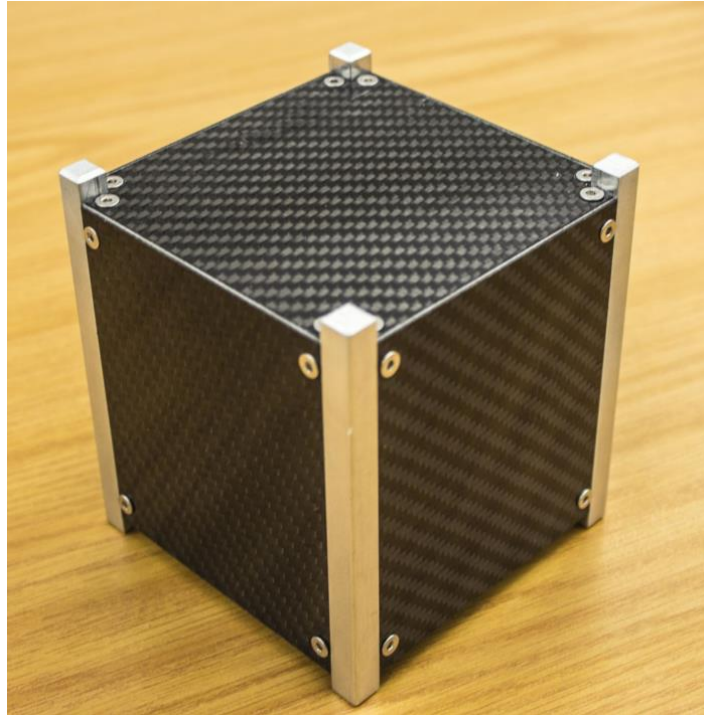


**Figure 2-8: Carbon fibre 1U structure** (Ball & Oliver, 2017)

## 2.4. Engineering Analysis

### 2.4.1. Thermal Analysis

Satellites that operate in the near-earth environment have three primary sources of thermal radiation, radiation heat from the sun, planetary heating from earth (black body radiation) and the albedo (the reflection of solar radiation). (Dinh, 2012)

Dinh tabulated the thermal radiation impact on a satellite at Low Earth Orbit (LEO) which can be seen in Table 2-2 below.

**Table 2-2: LEO thermal environment** (Dinh, 2012)

	<b>Perihelion</b>	<b>Aphelion</b>	<b>Mean (Hot Case)</b>	<b>Eclipse</b>	<b>Eclipse (Cold Case)</b>
Direct Solar	1414 W/m <sup>2</sup>	1323 W/m <sup>2</sup>	1371 W/m <sup>2</sup>		0
Albedo (Average)	0.30 +/- 0.01	0.30 +/- 0.01	0.30 +/- 0.01		0.25
Planetary IR (Average)	234 +/- 7 W/m <sup>2</sup>	234 +/- 7 W/m <sup>2</sup>	234 +/- 7 W/m <sup>2</sup>		220 W/m <sup>2</sup>

#### 2.4.1.1. 1U Thermal analysis using Ansys Icepak and Thermal Desktop

Dinh performed a thermal study of a 1U CubeSat with a Pumpkin CubeSat kit structure. The main subsystems included a hysteresis antenna, radio communication system, battery and solar cells and other various electrical hardware for power distribution, data handling, communication and control. The study looked at the thermal modelling of the internal components of the CubeSat in a circular orbit at an altitude of 400km and an inclination angle of 56.1°.

Dinh simplified the entire model with three material surface thermo-optical properties; anodized aluminium, solar cells and DuPont™ Tedlar white. The absorbance and emittance for each material surface was (0.14, 0.84), (0.40, 0.45) and (0.39, 0.87) respectively.

Dinh conducted two separate studies, one on the internal components and their heat distribution using Ansys Icepak and the other determining the external heat radiation using Thermal Desktop. Dinh assumed that the internal and external heating would not affect one another and that individual, separate studies would suffice.

Dinh conducted a study on a BeagleBoard to validate the modelling methods and material properties used. Figure 2-9 shows the properties that were used for the study. The board was simplified significantly to only consist of the board and heat source. While no further information was given how the materials were used in the simulation, Dinh concluded from his study that the simulation deviated from the actual results by approximately 2° C.

Description/Composition	Cond. [W/in/K]	Density [kg/in <sup>3</sup> ]	Cp [J/kg/K]
Aluminum (Alloy 2024-T6)	4.489*	0.04539	873.372*
FR4 2 oz Copper	0.44958	0	0
OMAP Chip	0	0.0327741	837.32

Note: \* indicates property is temperature dependent.

**Figure 2-9: Dinh thermal physical properties** (Dinh, 2012)

To simulate the external thermal heating due to radiation, the CubeSat was modelled as a simplified model with only external surfaces and simulated using Thermal Desktop. It was unclear how the finite element model was defined and what material and optical properties were used where. Figure 2-10 shows the total absorbed heat flux based on the simulation results of the external surface of the satellite. It is unclear how this data was used and whether it was used for setting up the internal analysis.

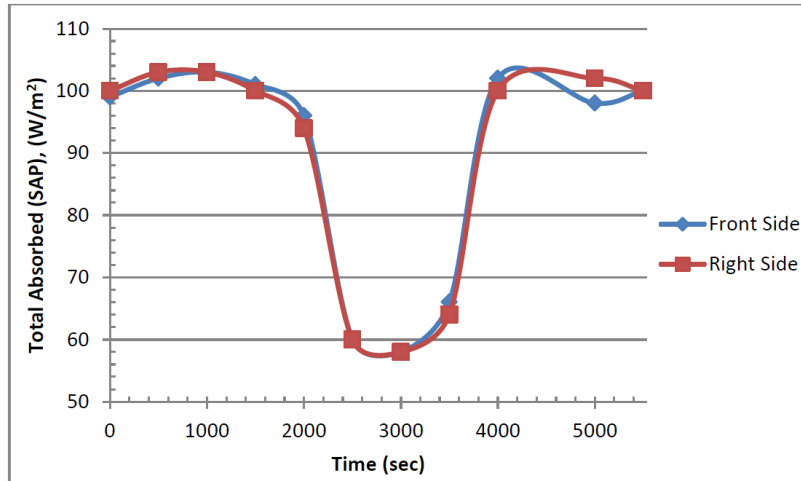


**Figure 2-10: Dinh simulated absorbed heat flux( Dinh, 2012)**

Dinh then conducted an internal analysis of the CubeSat components with various heat loads taken from the satellites power budget. To represent the space environment, the simulation was constrained by “turning off the “flow” option in Icepak, and a very low thermal conductivity value was assigned to the ambient computation domain” (Dinh, 2012). The simulation was run for a “hot case” and “cold case”, although it was unclear how these cases differentiated from one another, whether the data from the external radiation analysis was used somehow. Figure 2-11 show the hot and cold case results for the internal simulation with the hot case reaching a maximum temperature of approximately 40° C with an average temperature across the boards of approximately 25° C. For the cold case the maximum temperature was found to be approximately -20° C with an average board temperature of approximately -45° C.

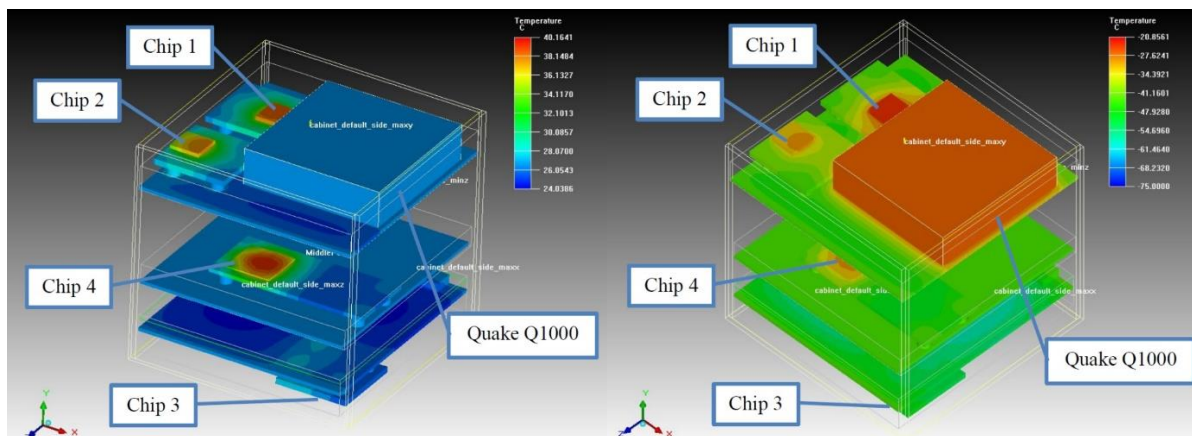


**Figure 2-11: Dinh internal simulation results: hot (left), cold (right) (Dinh, 2012)**



Dinh concluded that for a system with low power components like in this study, none of the components overheated however thermal control systems might be required for higher power systems (Dinh, 2012). He also noted that heaters might be needed for some components.

While Dinh had some interesting results and findings it seemed like his research was limited by software availability. Lots of information regarding the setup of the finite element model and what materials and properties were used was omitted. It was also unclear whether the external radiation effects were implemented into the internal simulation. The phrase, “This decoupled analysis approach assumed that the external heating did not cause any changes to the internal environment and vice-versa.” leads one to believe that the two simulations were separate. This significantly reduces the accuracy of the simulated results. The results given by Dinh were also not validated against any recorded data.

#### 2.4.1.2. Thermal modelling of MIST CubeSat

Chandrashekar, 2017 conducted a thermal analysis of a 3U CubeSat, MIST using Systema-Thermica software. MIST consisted of batteries, power supply unit, on-board computer, transceiver, magnetorquer, antenna system and various payloads. Using Systema-Thermica, first the Geometrical Model Management (GMM) was defined building up the geometry of the satellite and meshing the geometry in nodes. The Thermal Model Management was then created which includes the mathematical model in the form of capacitances and conductive couplings for each of the nodes as well as a dissipation profile for each component. The mesh shapes used to model MIST were simplified to square plates, boxes, cylinders and discs. See Figure 2-12 showing the thermal model for MIST. All components were modelled to be in direct contact with one another. The materials used were assumed and a custom material for the PCBs was made using an average of the materials that made up the PCB (Chandrashekar, 2017).

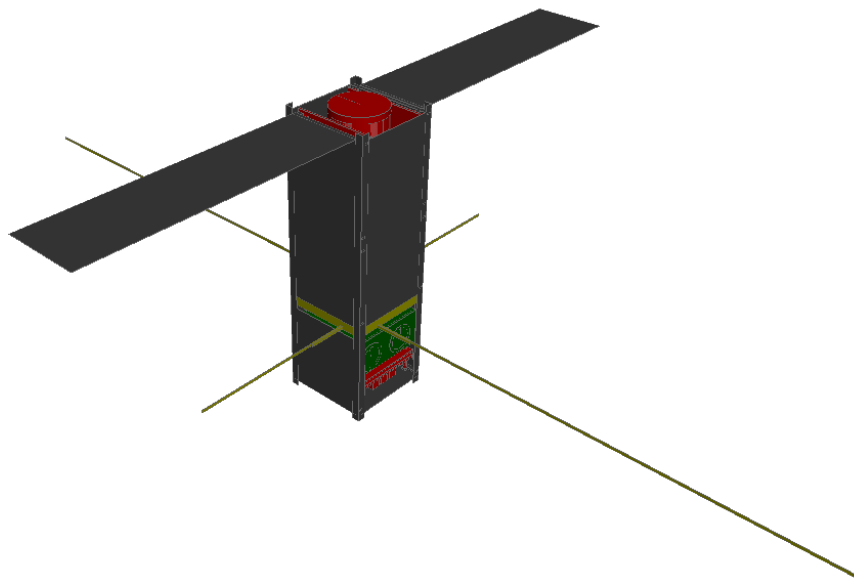


**Figure 2-12: MIST thermal model** (Chandrashekar, 2017)

Figure 2-13 shows the simulated temperatures at hot operational case versus the required temperatures. It can be seen how several of the payloads are showing to operating below the required temperature ranges.

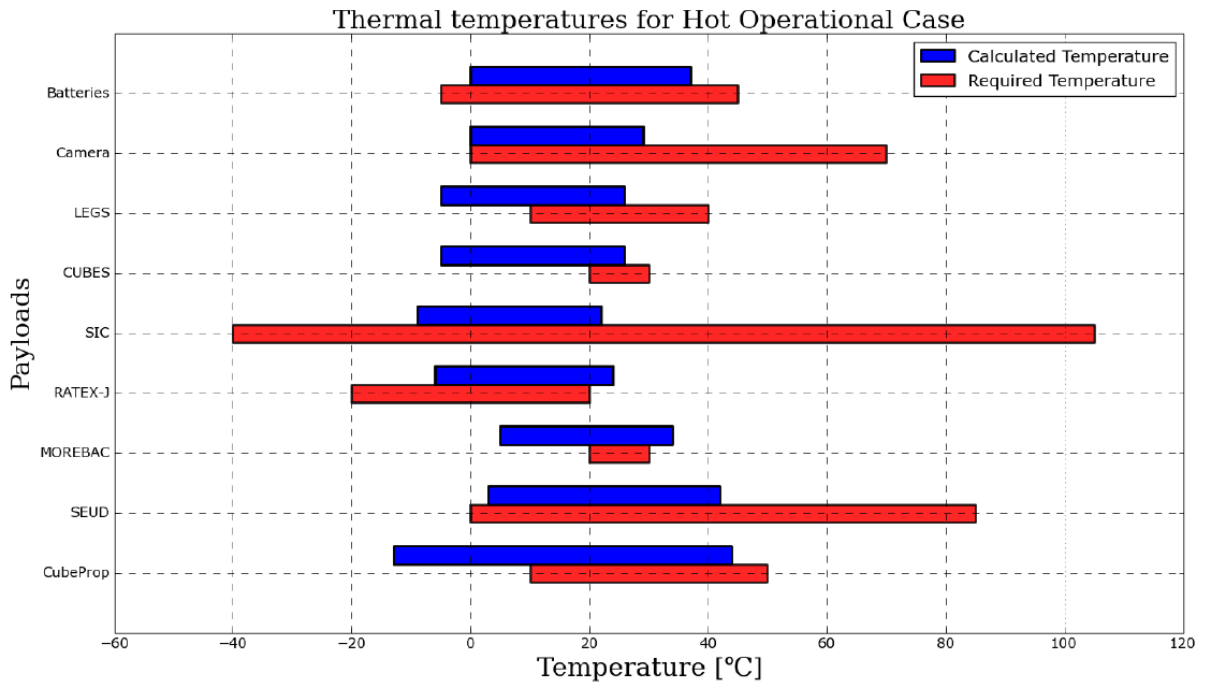


**Figure 2-13: Payload temperatures for MIST at hot operational case (Chandrashekar, 2017)**

Chandrashekar concluded that heat control measures and design changes would need to be made to the satellite to ensure the payloads operate within their required temperature range. It was also recommended that some of the materials that were assumed needed to be updated along with their optical properties. The simulation also reflected cold results which could have been due to an error with the LTAN used for the simulation.

Like Dinh’s study, Chandrashekar’s also did not have any means of validating that the simulated results are accurate. Validation of the thermal model is critical to ensuring that the thermal model is simulating accurate, reliable results for CubeSat design.

## ***CHAPTER THREE***

### **3. CUBESATS**

#### **3.1. CubeSat Structures**

##### **3.1.1. CubeSat Standard**

In 1999, Cal Poly and Stanford University collaboratively developed the CubeSat Standard. With that standard came the CubeSat Design Specification (CDS). The CDS is a document that states the requirements of a CubeSat design to suit the original standard. These specifications are to ensure that the CubeSat design fits and matches the requirements of the P-POD as well as being suitable for space deployment. This is to ensure the safety of the launch vehicle and other CubeSat's being deployed by the P-POD. (CalPoly, 2014)

The document has an extensive list of requirements that need to be met which cover general requirements to mechanical, dimensional, electrical and operational. The CDS needs to be referred to for any design regarding a CubeSat. For mechanical design, the following aspects are highlighted from the document.

1. From the "General Requirements" section (CalPoly, 2014)
  - 1.1. Materials used on the CubeSat must satisfy the low out-gassing requirements of a Total Mass Loss (TML) of less than or equal to 1.0% and a Collected Volatile Condensable Material (CVCM) of less than or equal to 0.1%). Approved low out-gassing materials can be found from a NASA approved list online.
2. From the "Mechanical Requirements" section (CalPoly, 2014)

All requirements under the mechanical section must be adhered to for mechanical design. The full list can be found in Appendix A1 while some structure related points are highlighted below.

  - 2.1. Physical dimensions for CubeSat's being launched from a P-POD must adhere to the dimensions shown in Appendix A1.
  - 2.2. Rails must have a surface roughness of less than 1.6  $\mu\text{m}$
  - 2.3. The maximum masses for 1U, 1.5U, 2U and 3U are 1.33 kg, 2 kg, 2.66 kg and 4 kg respectively.
  - 2.4. The CubeSat's centre of gravity shall be within 2 cm, 3 cm, 4.5 cm and 7 cm from its geometric centre in the Z direction for the different respective sizes.
  - 2.5. Structure and rails are to be made of Aluminium 7075, 6061, 5005 or 5052. If other materials are used, the developed must submit a DAR and adhere to the waiver process.

Any organisation that wants to design their own CubeSat must follow the specification of the CDS form.

### 3.1.2. Commercial-Off-the-Shelf (COTS)

Several organisations have developed designs for CubeSats however, three stand out for their heritage of successful space missions. The Dutch organization Innovations Solutions in Space (ISIS), is one of these three organizations. ISIS offers several products ranging from communications systems to the CubeSat structures themselves. They offer structures of configurations up to a 16U as well as other auxiliary components. Their 1U structure has a flight heritage since 2012 and is used widely in the CubeSat market. The majority of the structure is made out of high strength aluminium weighing in at 110 grams and is designed according to the CDS (ISISpace, 2015). The price of a 1U structure ranges from €2,150 – €2,500 which in Rand at the current exchange rate would be a maximum of R37,200 (Excluding shipping costs) as of September 2018. See Figure 3-1 below of a typical 1U structure.



**Figure 3-1: ISIS 1U structure** (ISISpace, 2015)

Another organization that has successful flight heritage since 2003 is the American organization, Pumpkin Space Systems. They also offer several products including CubeSat Structures, like ISIS they use high strength aluminium and the structure weighs in at an estimated 140 grams. This structure also adheres to the CDS document. The price of a 1U structure is roughly \$1,725 - \$3,150 which in Rand at the current exchange rate would be a maximum of R41,000 (Excluding shipping costs) (Pumpkin, 2015b) See Figure 3-2 below of a typical 1U structure.

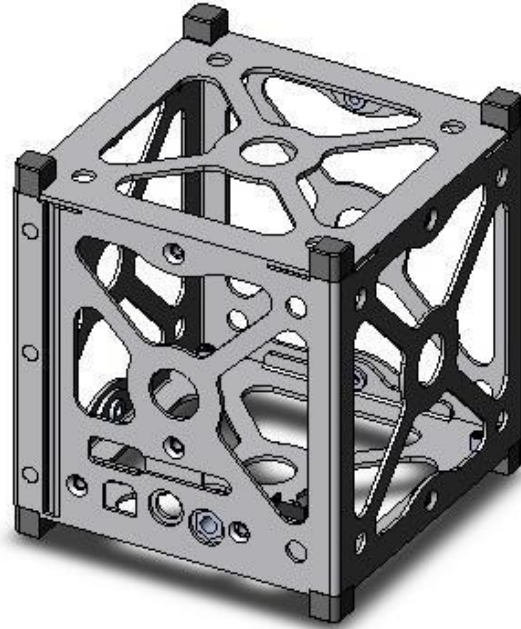


**Figure 3-2: Pumpkin 1U structure** (Pumpkin, 2015a)

The third organisation that also follows the CDS with its aluminium structure is the UK company Clyde Space. Their design weighing in at 155 grams. The structure can be purchased for \$4,600 which in Rand at the current exchange rate would be R60,000 (Excluding shipping costs). See Figure 3-3 below of a typical 1U structure. (Clyde Space Ltd, 2017)

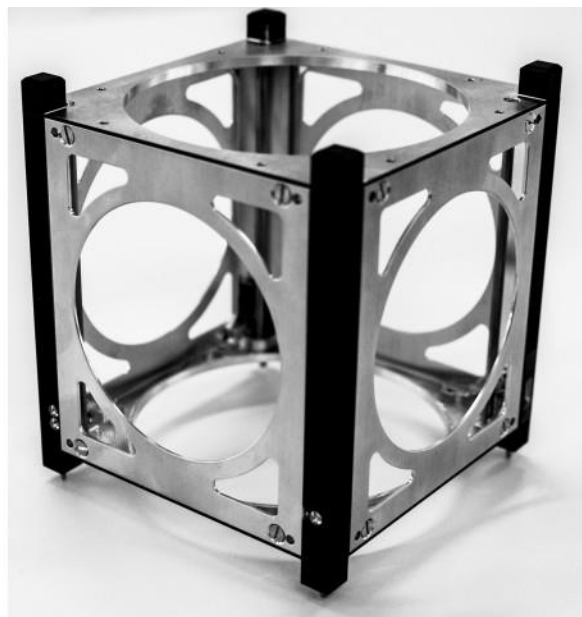


**Figure 3-3: Clyde Space 1U structure** (Clyde Space Ltd, 2017)

### 3.2. CubeSat Design

After meeting the requirements of the CDS, the structure must also be able to survive the launch as well as the environment in space.

#### 3.2.1. Launch Conditions

During the launch of the rocket carrying the CubeSat, the sat will experience the highest strain. This is due to high gravitational forces pushing down on the Sat as well as extreme vibrations through the rocket. These vibrations are caused by Solid Rocket Boosters (SRBs) which propel the launch vehicle towards space. Various other sources continue to provide dangerous vibrations after the initial vibrations induced by the SRBs. When designing CubeSats, engineers need to test the satellites based on the launch providers specifications. Fortescue stated that for qualification for the Ariane 5, the spacecraft must meet the following Sine vibration levels seen in Table 3-1 below; (Fortescue et al., 2011).

**Table 3-1: Ariane 5 vibration qualification levels**

Frequency Range (Hz)	Qualification Level
2-5	12.4 mm
5-50	1.25 g
50-100	1g

Fortescue et al. also stated that the natural frequency of a lightweight spacecraft must be greater than that of the launch vehicle fundamental frequency. (Fortescue et al., 2011) Table 3-2 below shows the fundamental frequencies for various launch vehicles.

**Table 3-2: Launch vehicle fundamental frequencies**

Launch Vehicle	In Lateral Axis	In the longitudinal axis (thrust direction)
Dnepr	$\geq 15$ Hz	20 Hz – 45 Hz
Delta II 7320	$> 12$ Hz	$> 35$ Hz
H-IIA	$> 10$ Hz	$> 30$ Hz
PSLV	$> 18$ Hz	$> 40$ Hz
Soyuz Spacecraft	$> 12$ Hz	$> 27$ Hz
Soyuz Spacecraft + adapter	$> 15$ Hz	$> 35$ Hz
Zenit 2 SLB	$> 16$ Hz	$> 20$ Hz

The acceleration of the launch vehicle during launch causes high forces on the CubeSat. The acceleration varies between -4.55 and 2.5 g's in the longitudinal direction and between -2 and +2 g's in the lateral direction. The forces that these accelerations cause are used to analyse the strength of the structure using FEA software (Fortescue et al., 2011).

### 3.3. Space Environment

#### 3.3.1. Thermal

Due to the vacuum in LEO, the only thermal interaction a spacecraft experiences is through conduction and radiation. Convection is so minimal that it can be considered negligible (Fortescue et al., 2011).

##### 3.3.1.1. Conductive heat transfer

For the thermal conduction through a body, the material is assumed to be homogeneous with constant thermal conductivity. When considering a spacecraft of  $n$  isothermal nodes (Fortescue et al., 2011), the conductive heat flow rate  $Q_C$ , from the  $i^{th}$  to the  $j^{th}$  node is given by

$$Q_{cij} = h_{ij}(T_i - T_j) \quad (3.1)$$

Where  $h_{ij}$  is the effective heat conductance between nodes  $i$  and  $j$ .  $T_i$  and  $T_j$  are the temperatures for the  $i^{th}$  and  $j^{th}$  nodes respectively.

##### 3.3.1.2. Radiative heat transfer

Radiative heat transfer between two surfaces is defined by three parameters, the surface properties, the radiative view factors,  $F$ , and the surface temperatures,  $T$ . The radiative view factor  $F_{ij}$  for radiation leaving surface  $i$  and being intercepted by  $j$  is defined the fraction of the respective radiation (Fortescue et al., 2011).

The view factor calculation between surface 1 and 2 or  $A_{i,j}$ , Equation 3.2 (Fortescue et al., 2011) is used, where  $s$  and  $\phi_{i,j}$  define the geometry relationship between the surfaces which can be seen in Figure 3-4.

$$F_{ij} = \frac{1}{A_i} \int_{A_i} \int_{A_j} \frac{\cos\phi_i \cos\phi_j}{\pi s^2} dA_i dA_j \quad (3.2)$$

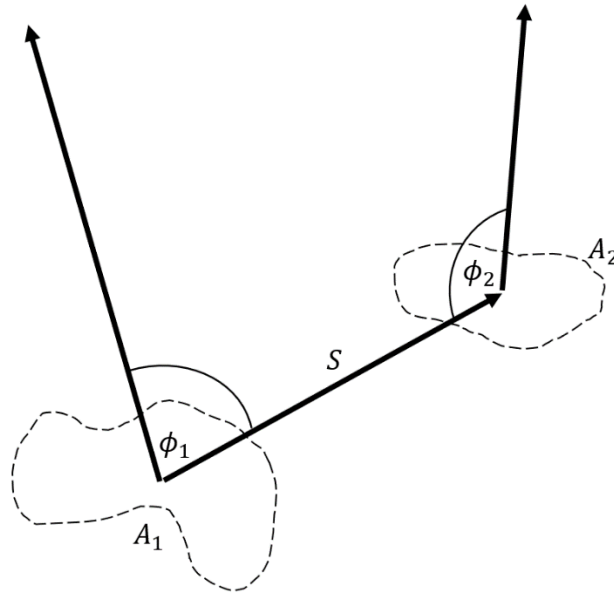


**Figure 3-4: View factor geometry** (Martin et al., 2020)

To calculate the amount of heat radiation,  $Q_r$  leaving a diffuse surface  $i$  and absorbed by  $j$  Equation 3.3 (Fortescue et al., 2011) can be used.

$$Q_{rij} = A_i F_{ij} \varepsilon_{ij} \sigma (T_i - T_j) \quad (3.3)$$

Where  $A_i$  is the surface area of  $i$ ,  $F_{ij}$  is the view factor of  $j$  seen by  $i$ ,  $\varepsilon_{ij}$  is the effective emittance and  $\sigma$  is the Stefan-Boltzmann constant of  $5.67 \times 10^{-8} W \cdot m^{-2} \cdot K^{-4}$ . Effective emittance that are separated by a distance small relative to their surface area, between two surfaces for two parallel diffuse surfaces can be calculated with a simplified equation as given in Equation 3.4 (Fortescue et al., 2011).

$$\varepsilon_{ij} = \frac{\varepsilon_i \varepsilon_j}{\varepsilon_i + \varepsilon_j - \varepsilon_i \varepsilon_j} \quad (3.4)$$

### 3.3.1.3. Thermal radiation

The thermal radiation experienced by spacecrafts in orbit can be broken up into the following different types (Fortescue et al., 2011) as displayed in Figure 3-5.



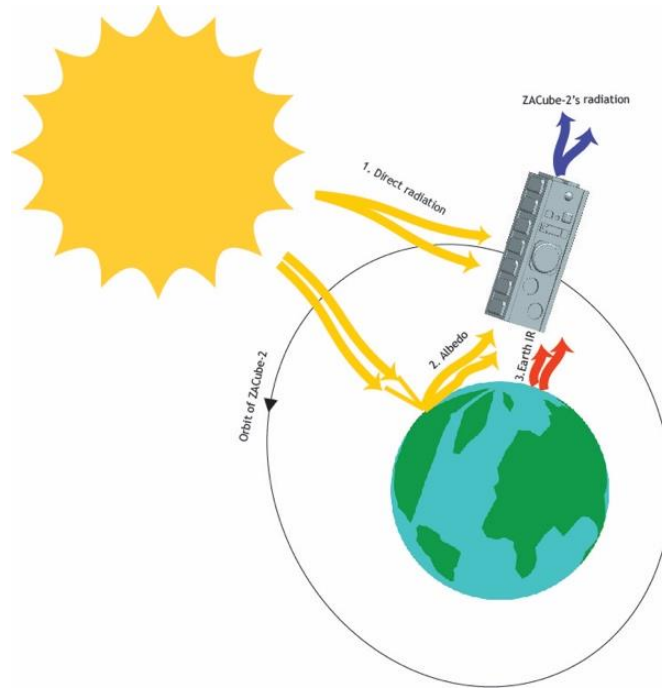


**Figure 3-5: Spacecraft thermal environment** (Martin et al., 2020)

1. Direct solar radiation: The radiation experienced directly from the sun and can be assumed as a constant value of  $Q_{solar} = 1379 \text{ W/m}^2$  at Earth's average distance from the sun.
2. Albedo radiation: The radiation that is reflected off the Earth's surface and can be assumed as  $Q_{albedo} = 0.3Q_{solar}$
3. Planetary radiation: The radiation emitted by the Earth itself which has an average intensity of  $Q_{Earth} = 237 \text{ W/m}^2$
4. Spacecraft radiation: Radiation that the spacecraft emits to deep space. It can be defined as shown in Equation 3.5 (Fortescue et al., 2011).

$$Q_{space} = \sigma \epsilon A_{space} T^4 \quad (3.5)$$

Where  $A_{space}$  is the effective area of the spacecraft with an unobstructed view of space.

#### 3.3.1.4. Heat transfer equations

The thermal energy balance of a spacecraft can be written as (Fortescue et al., 2011):

$$Q_{external} + Q_{internal} = Q_{space} + Q_c + Q_r \quad (3.6)$$

Where

$$Q_{external} = Q_{solar} + Q_{albedo} + Q_{planetary} \quad (3.7)$$

And  $Q_{internal}$  is the internal heat dissipation and  $Q_c$  and  $Q_r$  is the conductive and radiative heat transfer respectively as defined in Equation 3.1 and 3.3.

When considering a spacecraft defined by discretized nodes, the process of net heat change at nodes  $(i, j)$  can be given by (Fortescue et al., 2011):

$$m_i C_i \frac{dT_i}{dt} = Q_{external_i} + Q_{internal} - Q_{space} - \sum_{j=1}^n h_{ij}(T_i - T_j) - \sigma \sum_{j=1}^n A_i F_{ij} \epsilon_{ij} (T_i^4 - T_j^4) \quad (3.8)$$

Where  $m_i$  is the mass and  $C_i$  is the specific heat for that node.

For transient analysis, the left side of the equation is changed as:

$$m_i C_i \frac{T_i, \delta_t - T_{i,0}}{\delta_t} \quad (3.9)$$

The heat inputs and temperatures are replaced by their average over the time interval  $\delta_t$ . Values of  $T_{i,0}$  are then replaced by the newly calculated values of  $T_i, \delta_t$  and repeating the calculation then provides the temperature history at consecutive time intervals  $\delta_t$  (Fortescue et al., 2011).

### 3.3.2. Radiation

Satellites that orbit at LEO are exposed to a belt of radioactive ions and electrons in the form of a belt known as Van Allen radiation belt. There can also be fluxes of heavy ions such as helium, nitrogen and oxygen depending on the solar and geomagnetic activity. Proton and electron energies range from 0.01 to 400 MeV and 0.4 to 4.5 MeV with fluxes from  $10^8$  to  $600/\text{cm}^2 \text{ s}$  and  $4 \times 10^8$  to  $100/\text{cm}^2 \text{ s}$  respectively. A region known as the South Atlantic Anomaly is a region when spacecrafts can experience higher radiation effects due to the radiation belt being brought to lower altitudes. This is due to the offset and tilt of the geomagnetic axis relative to the Earth's rotation axis (Fortescue et al., 2011).

Trapped particles due to radiation can cause single-event upsets in electronic parts which could cause damage to the parts resulting in catastrophic failure. Electronic components are therefore often shielded with aluminium cases to protect against radiation.

## ***CHAPTER FOUR***

### **4. ADDITIVE MANUFACTURING**

As mentioned in Section 1.1.4, the term rapid prototyping has been replaced by additive manufacturing due to its advancements in technology. AM is now used in multiple industries and is at the forefront of the fourth industrial revolution.

#### **4.1. Additive Manufacturing Types**

Additively manufactured parts quality and mechanical properties depend on the type of manufacturing method used. There are numerous different manufacturing types to date, each with their advantages and disadvantages (Jones & Coates, 2015).

##### **4.1.1. Vat Photopolymerization**

A vat of liquid photopolymer is converted to a solid part through polymerization where the resin is cured through selective exposure to light. Typical methods include SLA, DLP, 3SP and CLIP. The advantages of this type of AM include a high level of accuracy and complexity, smooth surface finish and can accommodate large build areas. Typical Materials used are UV-Curable Photopolymer Resins

##### **4.1.2. Powder Bed Fusion**

Powdered materials are combined to form the part using a heat source such as a laser or electron beam. The powder surrounding the part acts as support material for the overhanging features. Typical methods include SLS, DMLS, SLM, EBM, SHS and MJF. Its advantages include a high level of complexity, the excess powder acts as support material, has a wide range of materials. The materials available include plastics, metals, ceramic powders and sand.

##### **4.1.3. Binder Jetting**

Parts are built layer by layer by applying liquid bonding agents onto thin layers of powdered material. Metal and ceramic parts are typically fired in a furnace after printing. Typical methods include 3DP, ExOne and VoxelJet. The advantages include being able to print in full colour, high productivity and can use a wide range of materials. The materials that are available include powdered plastic, metal ceramics, glass and sand.

##### **4.1.4. Material Jetting**

Parts are made by depositing droplets of the material layer by layer. Common varieties include jetting thermally molten materials that then solidify at ambient temperatures, as well as jetting photocurable

resin and curing it with UV light. Methods include Polyjet, SCP, MJM and Projet. The advantages include high levels of accuracy, prints in full colour as well as the ability to have multiple materials in a single part. Materials used include photopolymers, polymers, and waxes.

#### **4.1.5. Sheet Lamination**

Parts are formed by sheets of material being stacked and laminated together. Regions that are not needed are cut out layer by layer after the object is built. Typical methods include LOM, SDL and UAM. The advantages of sheet lamination include high volumetric build rates, relatively low cost, and allows for metal foils including embedding components. Materials used include paper, plastic sheets and metal foils/tapes.

#### **4.1.6. Material Extrusion**

Molten material is extruded out a nozzle to form a part of multiple layers. The most common method being Fused Deposition Modelling (FDM) which extrudes molten thermoplastic. The advantages of material extrusion type AM include being inexpensive and economical, allows for the use of multiple colours, can be used in an office environment and the parts have good structural properties. Another method being FFF. Materials used include thermoplastic filaments and pellets, liquids and slurries.

Fused Deposition Modelling is a trademarked name for the method of 3D printing originally developed by Stratasys, the same company that builds the Fortus machines. The FDM process involves a filament that is fed through a heating chamber to liquefy polymer. An extrusion pressure is generated by a tractor wheel arrangement that pushes the filament into the chamber. The material is then extruded onto the build platform through a nozzle in a build pattern that would have been previously programmed. The material will then cool and bond onto any adjoining material. The head of the machine will then move upwards, the filament height and add the next layer. The strength of the part being made depends on the build pattern and orientation that the part is being made. For example, a part being made in a vertical orientation versus a part being made on a side orientation will have different mechanical properties. (Ziemian et al., 2012)

FDM is the most popular form of AM as it is compatible with a range of materials and results in parts having impressive mechanical properties. When considering polymer-based AM, FDM made parts are amongst the strongest. A possible disadvantage to the AM method is that its build speed is relatively slow, for some applications this could become a drawback, but it all depends on the application. (Gibson et al., 2015)

The quality and strength of the part, of course, depend on the material selected. Different materials have different mechanical properties, which in conjunction with the build orientation determines the strength of the material. Different materials also are only compatible with certain nozzle tips; these tips also

determine the slice height which in turn affects the resolution of the part. A finer resolution means a smoother finish and higher accuracy.

#### **4.1.7. Direct Energy Deposition**

An energy source such as a laser or electron beam is used as it is fed into a melt pool on the surface of the part to adhere powder or wire to underlying layers. The benefits of this method are that it is not limited by direction or axis, it's effective for repairs or adding features and can have multiple materials in a single part. Methods used in include, LMD, LENS and DMD. Materials include metal wire or powder and ceramics.

#### **4.1.8. Hybrid**

A hybrid machine known as AMBIT makes use of CNC machining as well as laser metal deposition which incorporates both subtractive as well as additive manufacturing to create parts. Parts made with these machines have strengths from both forms of manufacturing. They have a good surface finish, high productivity as well as the geometrical and material freedoms from the laser metal deposition.

#### **4.1.9. Metal Additive Manufacturing**

The AM industry has been trying to perfect the use of metal additive manufacturing to substitute conventional metal manufacturing methods. Metal is the most common and widely used material in manufacturing and therefore if it can be perfected for additive manufacturing, this would be a huge step forward for Industry 4.0. Some of the most common metals in AM include aluminium, titanium and stainless steel. SLS, a powder bed fusion type of AM is used to create the metal parts. This method, however, has displayed issues related to the microstructure resulting in cracking, warping and high residual stresses. Once these issues have been overcome, metal AM will become extremely popular, especially as a key in Industry 4.0. (Dilberoglu et al., 2017)

#### 4.2. Embedded Electronics in FDM

Espalin et al. conducted a study on embedding electronic circuitry into an FDM part as a module of a CubeSat subsystem. The FDM process was enhanced by the addition of micromachining and laser ablation to embed the circuitry. In Figure 4-1 below, a two-axis gyroscope with an IIC-based SPA-1 which was embedded into the UTLEM thermoplastic part can be seen (Espalin et al., 2014).

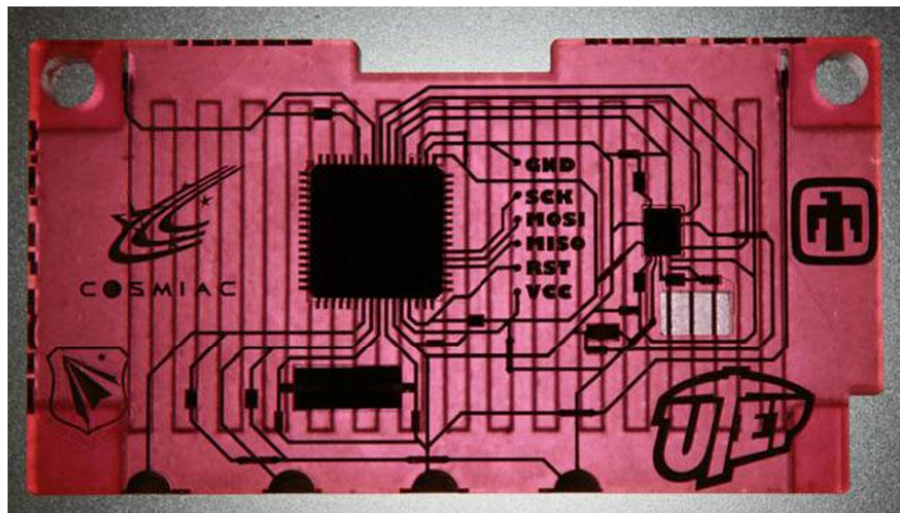


**Figure 4-1:** ULTEM with embedded circuitry (Espalin et al., 2014)

In Figure 4-2 below, the steps of the process of making the CubeSat module can be seen.

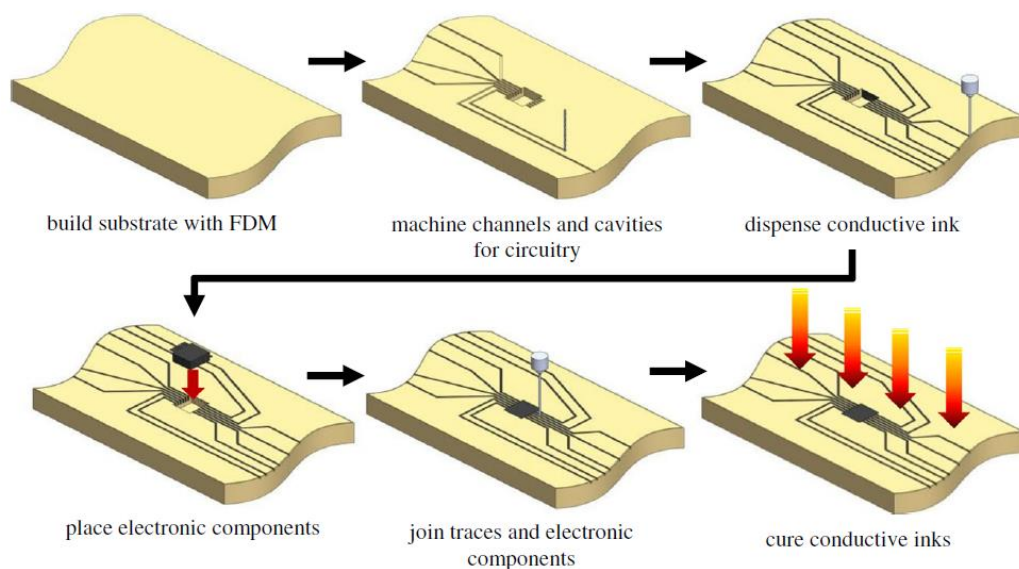


**Figure 4-2:** Embedded circuitry process (Espalin et al., 2014)

Applying this technique of embedding electronic circuitry and subsystems into a CubeSat structure could dramatically improve the volumetric efficiency of the CubeSat. (Espalin et al., 2014)

### 4.3. Build Orientation Effects / Orthotropic

#### 4.3.1. Build Orientation Effects

FDM parts are built by layers of molten filament being stacked and fused upon each other. Each layer consists of the molten filament being layered in a raster pattern to fill the layer to create the desired shape. The mechanical properties of the final part depend on the way the part was orientated with respect to the build direction and raster pattern. Several researchers have found the correlation between build orientation and these mechanical properties for parts printed using FDM. Parts displayed a degradation of mechanical strength when tested perpendicularly to the direction of layer construction. (Zaldivar et al., 2017)

Ahn et al. showed that these mechanical properties can, however, be improved by modifying the build parameters such as the layer thickness, raster angle, raster width, air gap, and chamber temperature. (Ahn et al., 2002)

FDM parts represent orthotropic materials which mean their mechanical properties are dependent on their fibre orientation. These orientations refer to the X, Y and Z coordinate directions and represented as directions 1, 2 and 3 respectively. An orthotropic material can be defined when  $E_1 \neq E_2 \neq E_3$  (Roylance, 2000) where E is the Modulus of Elasticity. Figure 4-3 below shows the fibre orientation regarding the three coordinate directions, X, Y and Z.

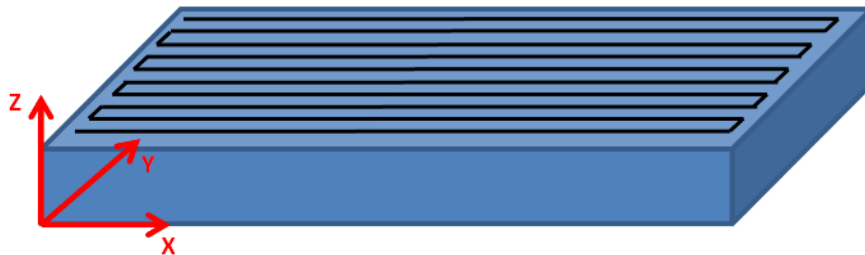


**Figure 4-3: FDM fibre orientation**

#### 4.4. Effects on Design

When designing parts that are going to experience mechanical stress, these parts are analysed using Finite Element Analysis software to simulate the loading conditions. For the FEA software to be accurate, the finite element model must accurately represent the real-life model. This comes down to two factors: the model's mesh and its material properties. For a study of a part made using FDM, the part presents orthotropic material properties. Orthotropic materials require 9 mechanical constants to make

up the stiffness matrix used by the FEA software. The constants include 3 moduli of elasticity, 3 Poissons ratio and 3 moduli of rigidity. These are to cover the mechanical properties in the three mutually perpendicular axes.

Zaldivar et al carried out a study on the print orientation effects on the mechanical and thermal properties of ULTEM 9085 using a Stratasys Fortus 400mc FDM 3D printer. FDM parts are known to have orthotropic mechanical properties, having different strengths based on the applied load vs build direction. To study the mechanical properties, six different dogbone test specimens were printed in accordance with the ASTM standard for plastic tensile testing D638. Figure 4-4 (left) below shows a visual representation of the six orientations that the dogbones are printed. In Figure 4-4 (right) a more detailed look can be seen of the raster orientation with respect to the axial direction of the dogbone.

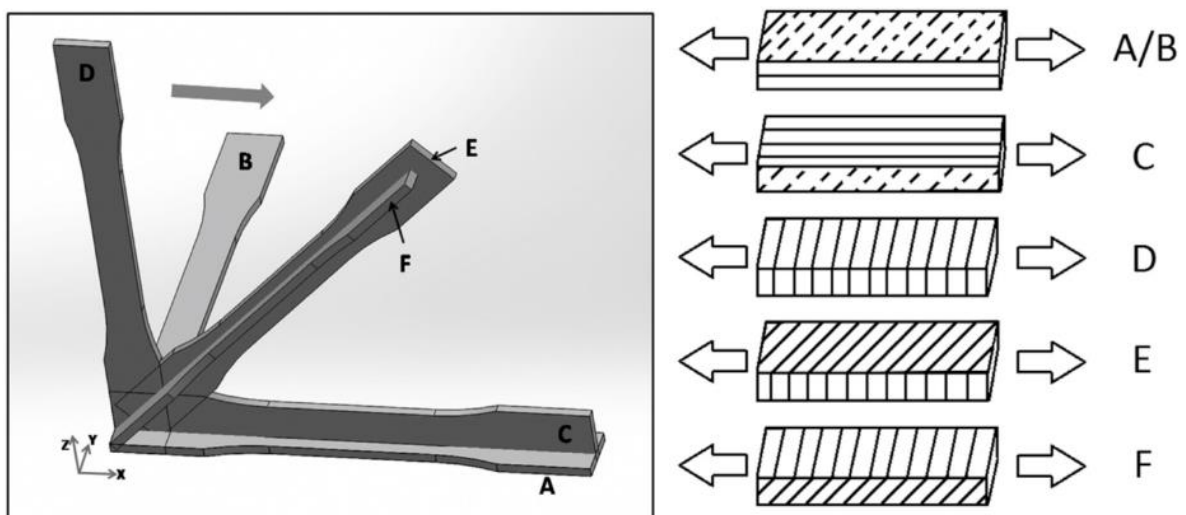


**Figure 4-4: Dogbone build orientation (left) and raster orientation (right) (Zaldivar et al., 2017)**

For the thermal study, a Thermal Mechanical Analyser (TMA) was used to determine the coefficient of thermal expansion for each build orientation and for their three primary directions. The specimens were tested with a temperature that ramped from 25 up to 150 degrees at 5 deg/min.



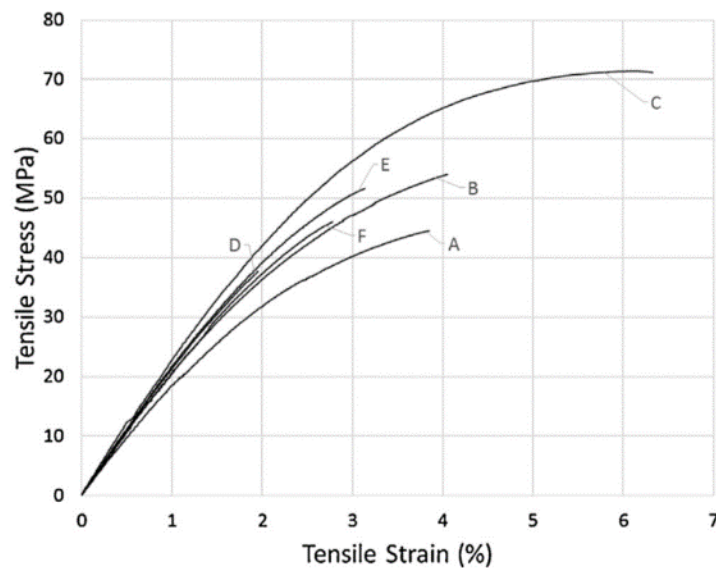
In

Table 4-1 and Figure 4-5 below, the results of the tensile tests of the various different dogbone specimens can be seen. Sample C showed the highest tensile strength of approximately 71 MPa.

**Table 4-1: Build orientation effects** (Zaldivar et al., 2017)

Mechanical Properties of 3D ULTEM® Dogbones as a function of Build Orientation.

Sample	Build Orientation	Tensile strength (MPa)	Strength Utilization (FDM/Injection Molded) (%)	Modulus (GPa)	Strain-to failure (%)
A	X- flat, 0°	46.83 ± 5.3%	56.5%	2.01 ± 7.9%	4.03 ± 9%
B	Y- flat, 0°	55.79 ± 2.7%	67.4%	2.28 ± 16.9%	4.72 ± 15%
C	X- edge, 0°	71.03 ± 2.6%	85.8%	2.48 ± 7.7%	7.38 ± 12%
D	Z - up, 0°	38.48 ± 9.7%	46.5%	2.03 ± 9.8%	2.03 ± 9%
E	X- edge, 45°	47.52 ± 11.3%	57.4%	1.77 ± 8.2%	2.79 ± 12%
F	X- flat, 45°	42.97 ± 13.7%	51.9%	2.12 ± 1.9%	2.55 ± 14%



**Figure 4-5: Stress-strain curve for Zaldivar’s tensile tests** (Zaldivar et al., 2017)

## 4.5. FDM Materials

### 4.5.1. Polylactic Acid

Polylactic Acid (PLA) is the low-cost option for fast prototyping of parts. The plastic is renewable and biodegradable with the ability to be printed translucent or opaque. PLA had good tensile strength and is stiffer in comparison to ABS. It has a low melting point which results in lower required power and heat for extrusion. PLA is effective for concept verification and design validation.

#### **4.5.2. Acrylonitrile Butadiene Styrene**

Acrylonitrile Butadiene Styrene (ABS) is the most commonly used thermoplastic and has been the foundation for FDM for many years. ABS materials have developed significantly over the years and have several variations, each suitable for different applications. ABS is excellent for creating models, prototypes, patterns, tools as well as end-use parts.

ABS-M30 variant produces stable and durable parts, capable of been printed in multiple colours. It makes use of soluble support material which allows for easy finishing parts. It has a medically approved variant, ABS-M30i which meets the necessary standards to be in contact with skin, food and medications. Another variant of ABS, ABS-ESD7 allows for the dissipation for electrostatic charge. This makes the material ideal for electrical applications. ABSi is a variant that has the advantage of being a translucent colour which makes it popular for lighting applications while maintaining its advantageous mechanical properties.

#### **4.5.3. Polycarbonate**

PC or polycarbonate is the most widely used industrial thermoplastic. Parts are accurate, very durable and are stable. It has very good mechanical properties with the second-highest tensile strength of FDM materials as well as a high heat deflection temperature. It's very tough and is suitable for functional testing, tooling or production.

PC also has variations including PC-ABS and PC-ISO. PC-ABS is a blend of ABS and PC which gives it a combination of desirable properties from both thermoplastics. It has the good mechanical properties of PC while also having the good flexural strength, feature definition and surface finish of ABS. It also offers soluble support. Like ABS-M30i, PC-ISO is compatible with medical pharmaceutical and food industries. PC-ISO has 33-59% higher tensile and flexural strength as well as heat deflection temperature.

#### **4.5.4. ULTEM**

ULTEM 9085 is one of the most well-rounded materials available on the market. It has good mechanical thermal and chemical properties as well as being fire, smoke and toxicity rated. ULTEM 9085 also meets the aerospace requirements making it NASA certified plastic. ULTEM 1010, another variant has the lowest coefficient of thermal expansion of any FDM material. It also has very high tensile strength and chemical resistance.

El-Gizawy et. al. conducted a study to determine the orthotropic properties of ULTEM 9085 printed with a Stratasys Fortus 400mc FDM 3D printer. To find the orthotropic material properties two build directions were used, flat and vertical. The printer was set to use its default settings other than creating a custom raster infill to maintain the raster orientation throughout the print. Tests were done using an

MTS System tensile machine which tested the specimens at 5mm/min and measuring strain along 0°, 45° and 90°. Tensile tests and specimens were done in accordance with the ASTM standard D638(El-Gizawy et al., 2011).

In Figure 4-6, it can be seen how the modulus of elasticity along the primary axis 1 and 2 was found. The raster orientation was set along the axis of tension to acquire the axis 1 properties and the orientation was perpendicular to the axis of tension to acquire the axis 2 properties(El-Gizawy et al., 2011).

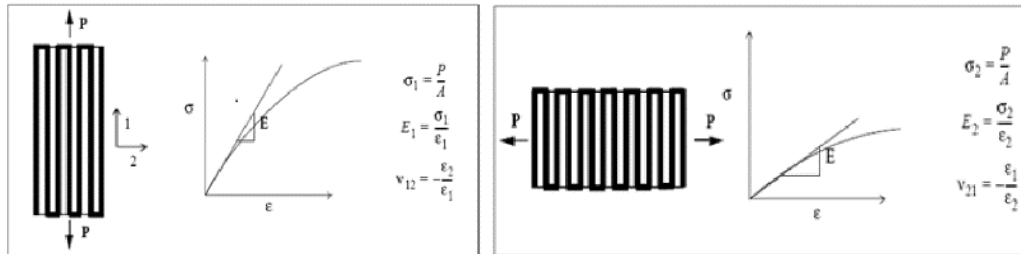


**Figure 4-6: Raster orientations for primary axis 1 testing (left) and primary axis 2 testing (right)** (El-Gizawy et al., 2011)

The shear modulus properties were found by using the stiffness properties found in a 45° raster test using the equation as displayed below.

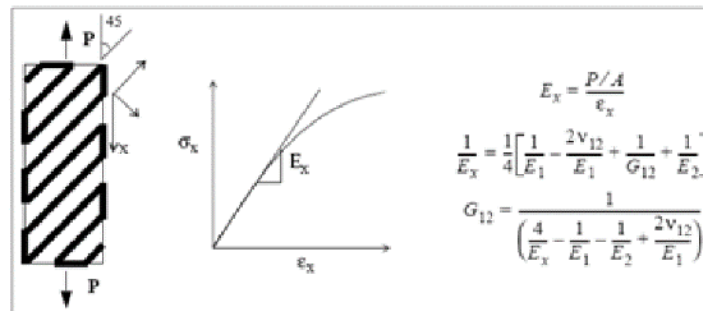


**Figure 4-7: Raster Orientation for shear modulus properties** (El-Gizawy et al., 2011)

Further properties E3, V31 and V32 were found using upright samples printed with 0° and 90° rasters.

Multiple tests were conducted and the stiffness properties for ULTEM 9085 were found as tabulated in Table 4-2. Tensile strength was found to vary depending on build direction and raster orientation. For flat specimens, the highest UTS was found to be 78.6 MPa for 0° raster and the lowest UTS of 45.7 MPa for 90°. For vertical specimens, the UTS remained relatively constant at around 50 MPa. This is due to the tension axis being transverse to the raster orientation, therefore, having a small impact on its UTS (El-Gizawy et al., 2011).

**Table 4-2: ULTEM 9085 Properties** (El-Gizawy et al., 2011)  
Stiffness Properties of ULTEM 9085

Property	Value
E <sub>1</sub>	2539.4 MPa
E <sub>2</sub>	2327.9 MPa
E <sub>3</sub>	2159.6 MPa
$\nu_{12}$	0.46
$\nu_{13}$	0.39
$\nu_{23}$	0.40
G <sub>12</sub>	635.5MPa
G <sub>13</sub>	635.5MPa
G <sub>23</sub>	582.82MPa

Zaldivar et.al did similar tests using a Fortus 400mc printer and the ASTM D638 tensile test method. For these tests, the prints were set to use the default raster orientation of 45°. For these tests, the UTS for flat specimens was found to be approximately 50 MPa. The strongest UTS was found by printing the specimens on their edge displaying 71 MPa. The weakest UTS was found for the vertical specimen at 38.5 MPa. The modulus of elasticity found for the 1,2 and 3 axes was found to be 2 GPa, 2.3 GPa, and 2 GPa respectively. Poissons Ratio  $\nu_{12}$  ,  $\nu_{13}$  was found to be 0.37 and 0.39 respectively. (Zaldivar et al., 2017)

Bagsik et.al also did the same tests with the same methods as Zaldivar et.al and found a UTS of 46 MPa for flat specimens, 63 MPa for specimens on their edge and 41 MPa for vertical specimens. Modulus for elasticity for axis 1 and 3 was also found to be approximately 2 GPa. (Bagsik et al., 2010)

Stratasys published their own data for ULTEM 9085 with the UTS for on edge and vertical to be 69 and 42 MPa respectively and modulus of elasticity as 2.15 GPa and 2.27 GPa respectively.

#### 4.5.5. Material Specifications

The table below lists the important material properties for the above-mentioned materials. This includes the mechanical properties such as the density, tensile strength and tensile modulus as well as the thermal properties such as the heat deflection temperature (HDT), glass transition temperature (Tg) and coefficient of thermal expansion (CTE). Finally, the cost per 1500cc of filament is also listed. It should be noted that the cost for PLA is significantly lower as it is not compatible with the Fortus 400mc printer which was used for this research however has been included as a reference.

In Table 4-3 below, a max and min tensile strength can be seen. This relates to the build orientation of the part. Max strength is along the layered direction (X and Y) while min strength is along the build direction (Z). The materials properties for the materials were acquired from the specification sheets in

2017 which are available on the Stratasys web page while the prices of filament from the 3DXTech webpage price lists in 2019 (3DXTech Advanced Materials, 2019)(Stratasys Ltd., 2017).

**Table 4-3: FDM material specs**

	<b>PLA</b>	<b>ABS</b>	<b>PC</b>	<b>PC-ABS</b>	<b>ULTEM 9085</b>
<b>Density (g/cc)</b>	1.24	1.04	1.2	1.1	1.34
<b>Tensile Strength Max (MPa)</b>	61	32	57	41	69
<b>Tensile Strength Min (MPa)</b>	43	28	42	41	42
<b>Tensile Modulus Max (MPa)</b>	3400	2230	1944	1900	2270
<b>Tensile Modulus Min (MPa)</b>	2800	2180	1957	1900	2150
<b>HDT (°C)</b>	80	96	138	110	153
<b>Tg (°C)</b>	62	108	161	125	186
<b>CTE (um/m-k)</b>	68	159	68.4	73.8	65.27
<b>Cost /1500 cc (\$)</b>	90	360	413	413	716

## CHAPTER FIVE

### 5. FINITE ELEMENT METHOD FOR STRUCTURAL ANALYSIS

#### 5.1. Finite Element Analysis

When analysing a body using FEA, the body is broken up into small pieces known as finite elements. This is illustrated in Figure 5-1. Each finite element consists of mass and stiffness terms that attached to grid points known as nodes. These mass and stiffness terms represent the mass and stiffness of the body and can be modelled as elements such as beams, plates or trusses. Several nodal points are associated with each element, at which adjacent elements are linked together. (Zaidi, 2017)

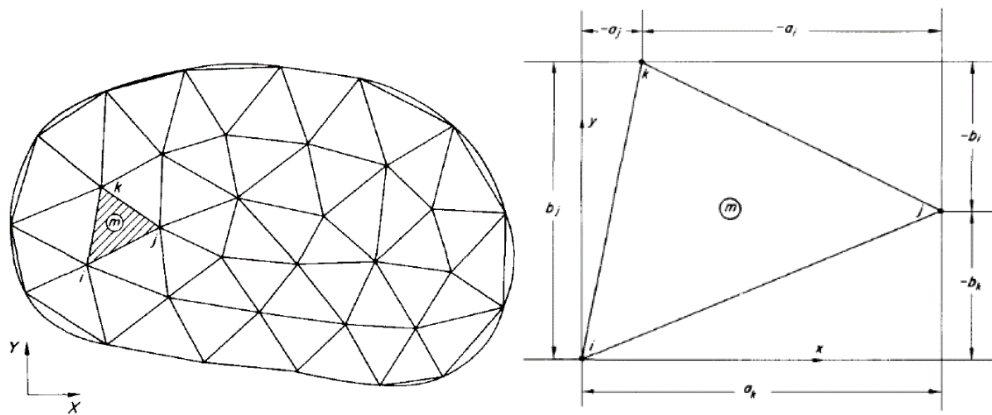


Figure 5-1: A finite element

Equations of statics or dynamics are written at each of these nodes in each direction. Each node is connected by multiple *springs*. At each node there are generally 6DoF, each equation for each *spring* is assembled in a matrix and solved. The solution gives the deflection calculated at nodes and stress over each element for a given load condition in each *spring*, etc. The smaller the elements making up the body, the more accurate the analysis is. (Zaidi, 2017)

### 5.2. Solid Elements for 3-D Problems

For elements of a body in a 3-dimensional Cartesian space, the elements have certain characteristics to determine, stresses, strains, deflections, etc. In Figure 5-2 the coordinate system can be seen for 3-D solid elements. (Liu, 2002)

Stresses:

$$\sigma = \{\sigma\} = \begin{Bmatrix} \sigma_x \\ \sigma_y \\ \sigma_z \\ \tau_{xy} \\ \tau_{yx} \\ \tau_{xz} \\ \tau_{zx} \end{Bmatrix}; \text{ or } [\sigma_{ij}] \quad (5.1)$$

Strains:

$$\varepsilon = \{\varepsilon\} = \begin{Bmatrix} \varepsilon_x \\ \varepsilon_y \\ \varepsilon_z \\ \gamma_{xy} \\ \gamma_{yx} \\ \gamma_{xz} \\ \gamma_{zx} \end{Bmatrix}; \text{ or } [\varepsilon_{ij}] \quad (5.2)$$

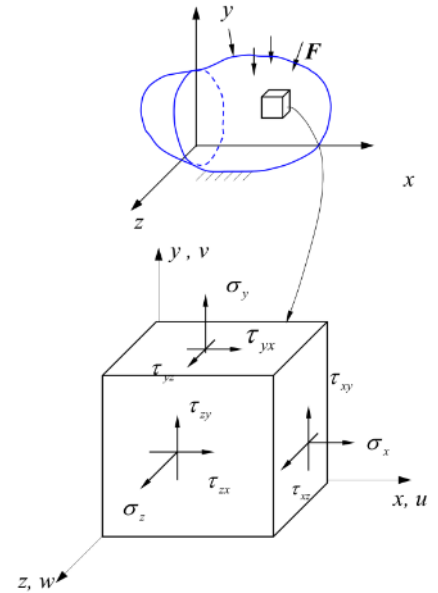


**Figure 5-2: 3D coordinate system**  
(Liu, 2002)

Stress-strain relationship for isotropic material:

$$\begin{Bmatrix} \sigma_x \\ \sigma_y \\ \sigma_z \\ \tau_{xy} \\ \tau_{yx} \\ \tau_{xz} \\ \tau_{zx} \end{Bmatrix} = \frac{E}{(1+\nu)(1-2\nu)} \begin{bmatrix} 1-\nu & \nu & \nu & 0 & 0 & 0 \\ \nu & 1-\nu & \nu & 0 & 0 & 0 \\ \nu & \nu & 1-\nu & 0 & 0 & 0 \\ 0 & 0 & 0 & \frac{1-2\nu}{2} & 0 & 0 \\ 0 & 0 & 0 & 0 & \frac{1-2\nu}{2} & 0 \\ 0 & 0 & 0 & 0 & 0 & \frac{1-2\nu}{2} \end{bmatrix}$$

Or

$$\sigma = E\varepsilon \quad (5.3)$$

*Displacement:*

$$u = \begin{Bmatrix} u(x, y, z) \\ v(x, y, z) \\ w(x, y, z) \end{Bmatrix} = \begin{Bmatrix} u_1 \\ u_2 \\ u_3 \end{Bmatrix} \quad (5.4)$$

*Strain-displacement relationship:*

$$\begin{aligned} \varepsilon_x &= \frac{\partial u}{\partial x}, \varepsilon_y = \frac{\partial v}{\partial y}, \varepsilon_z = \frac{\partial w}{\partial z}, \\ \gamma_{xy} &= \frac{\partial v}{\partial x} + \frac{\partial u}{\partial y}, \gamma_{yz} = \frac{\partial w}{\partial y} + \frac{\partial v}{\partial z}, \gamma_{xz} = \frac{\partial u}{\partial z} + \frac{\partial w}{\partial x} \end{aligned} \quad (5.5)$$

or

$$\varepsilon_{ij} = \frac{1}{2} \left( \frac{\partial u_i}{\partial x_j} + \frac{\partial u_j}{\partial x_i} \right), \quad (i, j = 1, 2, 3)$$

Or in tensor notation

$$\varepsilon_{ij} = \frac{1}{2} (u_{i,j} + u_{j,i})$$

*Equilibrium Equations:*

$$\begin{aligned} \frac{\partial \sigma_x}{\partial x} + \frac{\partial \tau_{xy}}{\partial y} + \frac{\partial \tau_{xz}}{\partial z} + f_x &= 0, \\ \frac{\partial \tau_{yx}}{\partial x} + \frac{\partial \sigma_y}{\partial y} + \frac{\partial \tau_{yz}}{\partial z} + f_y &= 0, \\ \frac{\partial \tau_{zx}}{\partial x} + \frac{\partial \tau_{zy}}{\partial y} + \frac{\partial \sigma_z}{\partial z} + f_z &= 0, \end{aligned} \quad (5.6)$$

Or

$$KU = F$$

Where  $K$  is the stiffness matrix of the structure,  $U$  is the global displacements and  $F$  the forces that can be used to solve for the unknown DOF vector  $U$ .

$K$  can be obtained by the summation of the element stiffness matrices. (Bathe, 2016)

$$K = \sum K^i$$

*Boundary Conditions (BC's):*

$$U_i = \bar{u}_i, \quad \text{on } \Gamma_u \text{ (specified displacement)}$$



$$t_i = \bar{t}_i \quad \text{on } \Gamma_\sigma \text{ (specified traction)}$$

$$\text{(traction } t_i = \sigma_{ij}n_j)$$

*Stress Analysis:*

Solving equations (5.3), (5.5) and (5.6) under the BC's in (5.7) gives the stress, strain, and displacement. To study a structure that has been idealized in an assemblage of finite elements, three phases are required. (Bathe, 2016)

1. Calculation of the system matrices. For static analysis of orthotropic materials, these are K and C.
2. Solution of equilibrium equations.
3. Evaluation of element stresses.

### 5.3. Finite Element Equations

The general governing finite element equations are discussed below based on a three-dimensional body as seen in Figure 5-2 (Bathe, 2016). The displacements within the element are measured in the local coordinate system  $x, y, z$  as a function of the displacements at the  $N$  finite element nodal points. Therefore, for element  $m$ ,

$$u^{(m)}(x, y, z) = H^{(m)}(x, y, z)\hat{U} \tag{5.8}$$

Where the superscript  $m$  denotes element  $m$ , the  $H^m$  is the displacement interpolation matrix and  $\hat{U}$  is a vector for the global displacement components  $U_i, V_i, W_i$ , at all nodal points where  $\hat{U}$  is a 3 dimension vector as seen with Equation 5.9,

$$\hat{U}^t = [U_1, U_2, U_3, \dots U_n] \tag{5.9}$$

Where  $U_i$  can correspond to any local coordinate system, not limited to  $x, y$  and  $z$ .  $\hat{U}$  includes displacements at supports of the element assemblage, therefore at a later stage the values of  $\hat{U}$  must be imposed prior to solving for the unknown nodal displacements.

Although all nodal point displacement are listed in  $\hat{U}$ , it should be noted that only the displacements at the nodes of the specific element will affect the displacement and strain distributions within that element. With the assumptions on the displacements in Equation 5.8, the corresponding element strains can now be evaluated,

$$\varepsilon^{(m)}(x, y, z) = B^{(m)}(x, y, z)\hat{U} \quad (5.10)$$

Where  $B^{(m)}$  is the strain-displacement matrix, the rows of  $B^{(m)}$  are obtained by differentiating and combining rows of the matrix  $H^{(m)}$ . By making use of Equation 5.8 and 5.10 in the principle of virtual displacements will lead to an effective assemblage process of all element matrices into governing structure matrices. This process is referred to as the direct stiffness method.

Element strains and initial stresses are used to relate to the stresses in a finite element using,

$$\tau^{(m)} = C^m \varepsilon^m + \tau^{I(m)} \quad (5.11)$$

Where  $C^m$  is the elasticity matrix of an element  $m$  and  $\tau^{I(m)}$  are the given initial stresses. The material law for  $C^m$  can apply to an isotropic, orthotropic or anisotropic material and can vary from element to element.

From the assumption on displacements within each finite element as seen in Equation 5.8, equilibrium equations can be derived that correspond to the nodal point displacements of an assemblage of finite elements.

#### 5.4. Anisotropic Mechanics

The general linear elastic equation, also known as the generalized Hooke Law for anisotropic materials take the form;

$$\varepsilon_{ij} = E_{ijkl}^{-1} \sigma_{kl} \quad \sigma_{ij} = E_{ijkl} \varepsilon_{kl} \quad (5.12)$$

Where the fourth-rank elasticity tensors, stiffness  $E_{ijkl}$  or compliance  $E_{ijkl}^{-1}$  are defined by 81 components. Derived from each indices  $i, j, k, l$  running through 1, 2 and 3. Stiffness and compliance tensors are symmetric with respect to the change of indices in the pairs of  $i, j$ , and  $k, l$ . This is due to the symmetry of the stress  $\sigma_{kl} = \sigma_{lk}$  and strain  $\varepsilon_{ij} = \varepsilon_{ji}$ .

$$E_{ijkl} = E_{jikl} = E_{ijlk} \quad E_{ijkl}^{-1} = E_{jikl}^{-1} = E_{ijlk}^{-1} \quad (5.13)$$

Furthermore, the symmetry with respect to the change of indices between  $ij$  and  $kl$  must hold due to the property of positive definiteness of strainer energy or complementary energy.

$$E_{ijkl} = E_{klij} \quad E_{ijkl}^{-1} = E_{klij}^{-1} \quad (5.14)$$

These symmetry conditions lead to only 21 of the stiffness or compliance tensors being independent. To describe the generalized Hooke's law by use of vector-matrix Voigt's notation the stress and strain tensors are written as columnar vectors. For tensor  $i, j = 1, 2, 3$  and vectors  $k = 1$  through 6:

$$\begin{array}{ccccccc} ij & 11 & 22 & 33 & 23,32 & 31,13 & 12,21 \\ & \downarrow & \downarrow & \downarrow & \downarrow & \downarrow & \downarrow \\ k & 1 & 2 & 3 & 4 & 5 & 6 \end{array}$$

From the above Voigt's description, we can obtain the stress and strain tensors:

$$[\sigma_{ij}] = \begin{bmatrix} \sigma_{11} & \sigma_{12} & \sigma_{23} \\ & \sigma_{22} & \sigma_{23} \\ & & \sigma_{33} \end{bmatrix} \rightarrow \begin{bmatrix} \sigma_1 & \sigma_6 & \sigma_5 \\ & \sigma_2 & \sigma_4 \\ & & \sigma_3 \end{bmatrix} \rightarrow \begin{Bmatrix} \sigma_1 \\ \sigma_2 \\ \sigma_3 \\ \sigma_4 \\ \sigma_5 \\ \sigma_6 \end{Bmatrix} \quad (5.15)$$

$$[\varepsilon_{ij}] = \begin{bmatrix} \varepsilon_{11} & \varepsilon_{12} & \varepsilon_{23} \\ & \varepsilon_{22} & \varepsilon_{23} \\ & & \varepsilon_{33} \end{bmatrix} \rightarrow \begin{bmatrix} \varepsilon_1 & \varepsilon_6 & \varepsilon_5 \\ & \varepsilon_2 & \varepsilon_4 \\ & & \varepsilon_3 \end{bmatrix} \rightarrow \begin{Bmatrix} \varepsilon_1 \\ \varepsilon_2 \\ \varepsilon_3 \\ \varepsilon_4 \\ \varepsilon_5 \\ \varepsilon_6 \end{Bmatrix} \quad (5.16)$$

Analogous scheme is applied to the first and second pairs of indices of stiffness and compliance tensors where appropriate factors 2 or 4 are applied.

$$E_{ijkl} = E_{mn}, \quad E_{ijkl}^{-1} = E_{mn}^{-1} \text{ if } m \text{ or } n \text{ go through } 1, 2, 3 \quad (5.17)$$

$$2E_{ijkl} = E_{mn}, \quad 2E_{ijkl}^{-1} = E_{mn}^{-1} \text{ if } m \text{ or } n \text{ go through } 4, 5, 6$$

$$4E_{ijkl} = E_{mn}, \quad 4E_{ijkl}^{-1} = E_{mn}^{-1} \text{ if both } m \text{ and } n \text{ go through } 4, 5, 6$$

For an example of axial strain  $\varepsilon_{11}$  the transformation becomes:

$$\begin{array}{cccccccc} \varepsilon_{11} & = & E_{1111}^{-1}\sigma_{11} & + & E_{1122}^{-1}\sigma_{22} & + & E_{1133}^{-1}\sigma_{33} & + & 2E_{1123}^{-1}\sigma_{23} & + & 2E_{1113}^{-1}\sigma_{13} & + & 2E_{1112}^{-1}\sigma_{12} \\ \downarrow & & \downarrow & & \downarrow & & \downarrow & & \downarrow & & \downarrow & & \downarrow \\ \varepsilon_1 & = & E_{11}^{-1}\sigma_1 & + & E_{12}^{-1}\sigma_2 & + & E_{13}^{-1}\sigma_3 & + & E_{14}^{-1}\sigma_4 & + & E_{15}^{-1}\sigma_5 & + & E_{16}^{-1}\sigma_6 \end{array} \quad (5.18)$$

Considering shear strain  $\varepsilon_{23}$ :

$$\begin{aligned}
 \varepsilon_{23} &= E_{2311}^{-1}\sigma_{11} + E_{2322}^{-1}\sigma_{22} + E_{2333}^{-1}\sigma_{33} + 2E_{2323}^{-1}\sigma_{23} + 2E_{2313}^{-1}\sigma_{13} + 2E_{2312}^{-1}\sigma_{12} \\
 \downarrow \quad \downarrow \quad \downarrow \quad \downarrow \quad \downarrow \quad \downarrow \quad \downarrow \\
 2\varepsilon_4 &= 2E_{2311}^{-1}\sigma_1 + 2E_{2322}^{-1}\sigma_2 + 2E_{2333}^{-1}\sigma_3 + 4E_{2323}^{-1}\sigma_4 + 4E_{2313}^{-1}\sigma_5 + 4E_{2312}^{-1}\sigma_6 \\
 \downarrow \quad \downarrow \quad \downarrow \quad \downarrow \quad \downarrow \quad \downarrow \quad \downarrow \\
 \gamma_4 &= E_{41}^{-1}\sigma_1 + E_{42}^{-1}\sigma_2 + E_{43}^{-1}\sigma_3 + E_{44}^{-1}\sigma_4 + E_{45}^{-1}\sigma_5 + E_{46}^{-1}\sigma_6
 \end{aligned} \tag{5.19}$$

Finally, the generalized Hooke's Law in vector-matrix notation is as follows:

$$\begin{aligned}
 \varepsilon_i &= E_{ij}^{-1}\sigma_j \quad (i = 1,2,3; j = 1,2, \dots,6) \\
 \gamma_i &= E_{ij}^{-1}\sigma_j \quad (i = 4,5,6; j = 1,2, \dots,6)
 \end{aligned} \tag{5.20}$$

Or

$$\{\varepsilon\} = [E^{-1}]\{\sigma\} \text{ or equivalently } \{\sigma\} = [E]\{\varepsilon\} \tag{5.21}$$

Where  $E$  or  $E^{-1}$  represent the elastic stiffness or compliance tensors.  $\varepsilon$  and  $\sigma$  representing the columnar vectors of stress and strain respectively. (Skrzypek & Ganczarski, 2015) When the columnar vectors of stress and strain and elasticity matrices are used, Hooke's Law is compiled as:

$$\begin{Bmatrix} \varepsilon_1 \\ \varepsilon_2 \\ \varepsilon_3 \\ \gamma_4 \\ \gamma_5 \\ \gamma_6 \end{Bmatrix} = \begin{bmatrix} E_{11}^{-1} & E_{12}^{-1} & E_{13}^{-1} & E_{14}^{-1} & E_{15}^{-1} & E_{16}^{-1} \\ E_{21}^{-1} & E_{22}^{-1} & E_{23}^{-1} & E_{24}^{-1} & E_{25}^{-1} & E_{26}^{-1} \\ E_{31}^{-1} & E_{32}^{-1} & E_{33}^{-1} & E_{34}^{-1} & E_{35}^{-1} & E_{36}^{-1} \\ \hline E_{41}^{-1} & E_{41}^{-1} & E_{43}^{-1} & E_{44}^{-1} & E_{45}^{-1} & E_{46}^{-1} \\ E_{51}^{-1} & E_{51}^{-1} & E_{53}^{-1} & E_{54}^{-1} & E_{55}^{-1} & E_{56}^{-1} \\ E_{61}^{-1} & E_{61}^{-1} & E_{63}^{-1} & E_{64}^{-1} & E_{65}^{-1} & E_{66}^{-1} \end{bmatrix} \begin{Bmatrix} \sigma_1 \\ \sigma_1 \\ \sigma_1 \\ \tau_1 \\ \tau_1 \\ \tau_1 \end{Bmatrix} \tag{5.22}$$

### 5.5. Orthotropy

Most materials used in the engineering environment exhibit specific symmetry which can lead to a reduction in elastic modulus. When material directions of a specific material are defined in such a way that cause the compliance matrix to transform to the given structural symmetry frame, this, in turn, leads to the bottom left and top right blocks of the compliance matrix becoming a zeroth population. The nine Rabinovich  $\eta_{(i)jk}$  and three Chencov  $\eta_{ij(kl)}$  modules are also equal to zero, therefore the coupling between shear stresses and elongation does not exist and shear strains are only produced by stresses at the

same planes. The symmetry named orthotropy is in the form of three mutually perpendicular axes, (1,2 & 3) which determine the three material orthotropy planes. (Skrzypek & Ganczarski, 2015)

Below, the compliance matrix  $C$  or  $E^{-1}$  can be seen.

$$E^{-1} = \left[ \begin{array}{ccc|ccc} \frac{1}{E_{11}} & -\frac{\nu_{21}}{E_{22}} & -\frac{\nu_{31}}{E_{33}} & & & \\ \frac{\nu_{12}}{E_{11}} & \frac{1}{E_{22}} & \frac{\nu_{32}}{E_{33}} & & & \\ \frac{\nu_{13}}{E_{11}} & -\frac{\nu_{23}}{E_{22}} & \frac{1}{E_{33}} & & & \\ \hline & & & \frac{1}{G_{23}} & 0 & 0 \\ & & & & \frac{1}{G_{13}} & 0 \\ & & & & & \frac{1}{G_{12}} \end{array} \right] \quad (5.23)$$

The following conditions apply to the compliance matrix above:

$$\frac{\nu_{21}}{E_{11}} = \frac{\nu_{12}}{E_{22}} ; \frac{\nu_{13}}{E_{33}} = \frac{\nu_{31}}{E_{11}} ; \frac{\nu_{23}}{E_{33}} = \frac{\nu_{32}}{E_{22}} \quad (5.24)$$

This results in for a case of orthotropy, nine independent material constants, three generalized Hooke's modules  $E_{11}, E_{22}, E_{33}$ , three generalized Kirchhoff's modules  $G_{12}, G_{23}, G_{31}$  and three generalized Poisson's ratios  $\nu_{21}, \nu_{23}, \nu_{31}$ . (Skrzypek & Ganczarski, 2015)

The stiffness matrix,  $K$ , for orthotropic materials can be found from the inverse of the compliance matrix in Equation 5.23,

$$K = \left[ \begin{array}{ccc|ccc} \frac{1 - \nu_{23}\nu_{32}}{E_{22}E_{33}\Delta} & \frac{\nu_{21} + \nu_{23}\nu_{31}}{E_{22}E_{33}\Delta} & \frac{\nu_{31} + \nu_{21}\nu_{32}}{E_{22}E_{33}\Delta} & & & \\ \frac{\nu_{12} + \nu_{13}\nu_{32}}{E_{33}E_{11}\Delta} & \frac{1 - \nu_{13}\nu_{31}}{E_{11}E_{33}\Delta} & \frac{\nu_{32} + \nu_{12}\nu_{31}}{E_{11}E_{33}\Delta} & & & \\ \frac{\nu_{13} + \nu_{12}\nu_{23}}{E_{11}E_{22}\Delta} & \frac{\nu_{23} + \nu_{13}\nu_{21}}{E_{11}E_{22}\Delta} & \frac{1 - \nu_{12}\nu_{21}}{E_{11}E_{22}\Delta} & & & \\ \hline & & & G_{23} & & \\ & & & & G_{13} & \\ & & & & & G_{12} \end{array} \right] \quad (5.25)$$

Where,

$$\Delta = \frac{1 - \nu_{12}\nu_{21} - \nu_{23}\nu_{32} - \nu_{31}\nu_{13} - 2\nu_{12}\nu_{23}\nu_{31}}{E_x E_y E_z} \quad (5.26)$$

The following conditions apply to the stiffness matrix;

$$\begin{aligned} \frac{\nu_{21} + \nu_{23}\nu_{31}}{E_{22}E_{33}\Delta} &= \frac{\nu_{12} + \nu_{13}\nu_{32}}{E_{33}E_{11}\Delta} \\ \frac{\nu_{32} + \nu_{12}\nu_{31}}{E_{11}E_{33}\Delta} &= \frac{\nu_{23} + \nu_{13}\nu_{21}}{E_{11}E_{22}\Delta} \\ \frac{\nu_{31} + \nu_{21}\nu_{32}}{E_{22}E_{33}\Delta} &= \frac{\nu_{13} + \nu_{12}\nu_{23}}{E_{11}E_{22}\Delta} \end{aligned} \quad (5.27)$$

## ***CHAPTER SIX***

### **6. RESULTS**

#### **6.1. Structural Design for AM**

##### **6.1.1. Design Objectives**

- The structure must meet all the spacecraft design requirements applicable to CubeSat structures as was discussed in Section 3.2.
- The structure must be lighter or as light as other COTS structures.
- The structure design should show a benefit over using COTS alternatives;
  - It can allow for more versatility when it comes to payload configuration than the current COTS structures, as discussed in Section 3.1.2, implementing modular design to improve integration.
  - Could improve the assembly process of the CubeSat.
  - Could be a cheaper structure alternative for universities, small organisations and research stations to develop CubeSats.

##### **6.1.2. Material Selection**

Material selection is based on several different constraints. Firstly, the material must be a material that is available for the Fortus 400mc. This material must be strong enough to withstand the conditions that the CubeSat will experience. The materials also need to be able to withstand the harsh conditions of space, including heat, radiation, and outgassing. NASA has specific outgassing requirements that the materials need to meet. Secondary constraints include the cost of the material, the cost of producing a product using that specific material. It is also important to ensure that the materials are available in South Africa.

The initial materials that will be considered will be all materials that are compatible with the Fortus machine. These materials will then be shortlisted by the constraints until only the materials that meet all the criteria are left. From these materials left, a final selection can be made.

The following criteria will be discussed when selecting a suitable material for the CubeSat Structure:

- **Strength and weight:** The material must meet or exceed the minimum requirements to survive launch. While meeting these requirements, the materials should not be heavy. It is therefore important that the materials have a good strength to weight ratio.

- Suitability for space use: This includes the outgassing requirements by NASA. These are extremely important because without meeting the outgassing requirements, the CubeSat will not be allowed into space. The other important aspect to consider for space suitability is the thermal properties of the material. How the material will respond to the harsh thermal conditions in space.
- Space Heritage: This is whether the material has been used successfully previously in a space mission. If so, it shows that the material has a successful heritage and should work again.
- Cost: The cost of the material when compared to its other properties must be considered.

### **6.1.3. Material Selection Discussion**

In Section 4.5 the various materials and their specifications were discussed. Each of these materials that were compatible with the Fortus 400mc had various advantages and disadvantages however the most important factor was whether the material would survive in space.

Polylactic Acid (PLA), while having good mechanical properties is a bioplastic that degrades significantly over time. This degradation means that it would not be suitable for space use, especially in the harsher space environment (Rogers, 2015). PLA also has a low glass transition temperature (T<sub>g</sub>) of only 62° C, therefore, it would not be able to withstand the thermal conditions in space. Because of these factors, PLA will not be considered as a potential material for use for producing CubeSat structures.

The four thermoplastics that were compared and discussed were ABS, PC, PC-ABS and ULTEM 9085.

#### **6.1.3.1. Strength and Weight**

When considering the strength of the FDM materials, it is important to note that these materials strengths depend on the build orientation. In Section 4, Table 4-3 showed the material properties of the various materials showing a max and min tensile strength as well as the tensile modulus. While overall strength is important the tensile modulus is also as this defines how brittle/flexible the part will be. Ideally, one wants a part with high tensile strength and Young's modulus to ensure high part strength and rigidity.

Figure 6-1 shows the comparison between the strength-to-weight ratios of the various materials can be seen (Stratasys Ltd., 2017). The weight was defined as the material density per unit volume. It can be seen how ULTEM and PC have similar values with ULTEM just 6% above that of PC.



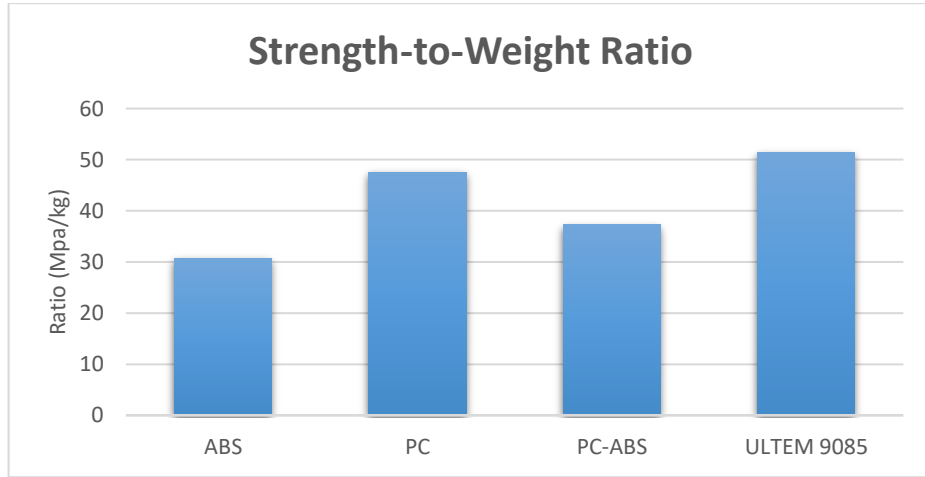


**Figure 6-1: Material strength comparison**

6.1.3.2. Suitability for Space

When it comes to material outgassing properties, three of the four materials are certified and meet the NASA outgassing requirements as stipulated in the CDS. The only material that has not been certified being the PC-ABS blend material, ruling it out as a potential material.

As mentioned previously the thermal properties of a material are crucial when it comes to the selection of a suitable material. If a material cannot withstand high temperatures, the part can lose its structural rigidity and compromise the design. In Figure 6-2 (Stratasys Ltd., 2017), the comparison of the thermal properties of the materials can be seen (High HDT and  $T_g$  values while low CTE values are preferable). ULTEM shows the highest thermal stability of all the materials, quite significantly greater than PC and ABS. It shows how ULTEM will hold its shape up to very high temperatures while also expanding the least under and temperature change.

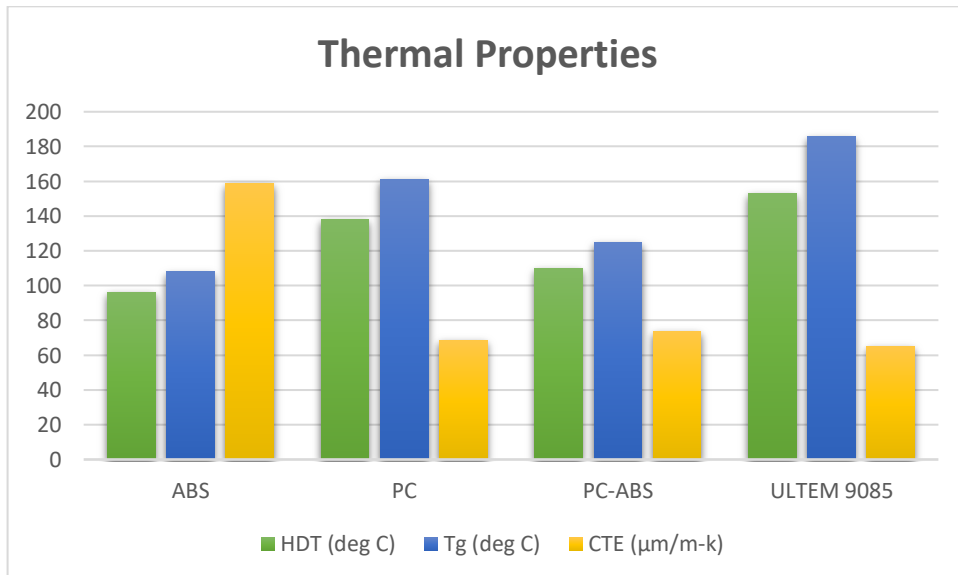


**Figure 6-2: Thermal properties comparison**

### 6.1.3.3. Space Heritage

In Section 2.2 various additive manufactured parts for space were discussed. This included parts made of ABS and ULTEM on the ISS as well as an ULTEM duct for a rocket booster. As of yet, there are no reports of the performance of any 3D printed component exposed directly to the space environment.

### 6.1.3.4. Cost

In Figure 6-3, the comparison of the cost for a 1500cc FDM canisters can be seen in dollars. These prices were taken from 3DXTech Advanced Materials online shop (3DXTech Advanced Materials, 2019). It can be seen how ABS, PC, and PC-ABS cost about the same per canister while ULTEM 9085 is almost double the price. This is due to the high quality and high-performance specs of the ULTEM material which can be seen in the previous points.

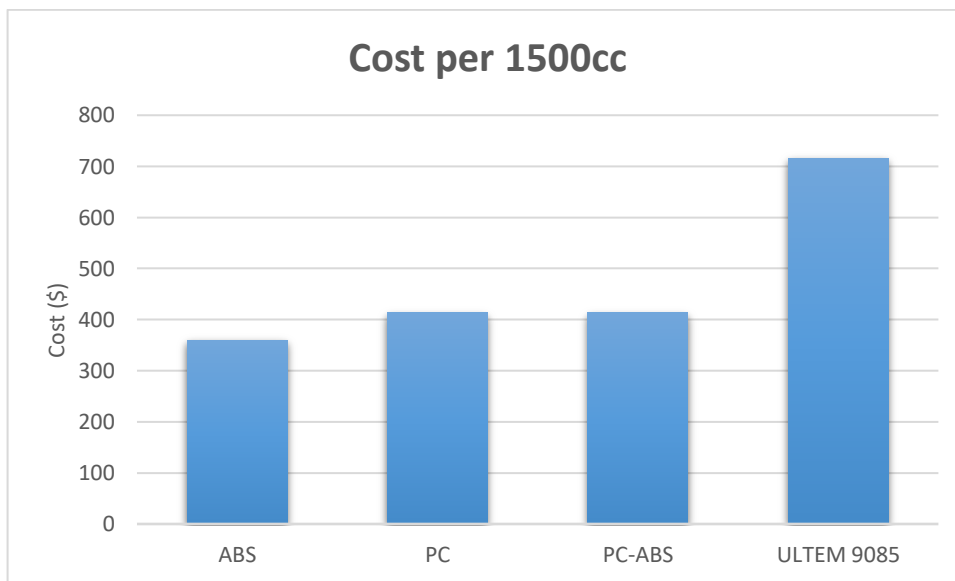


**Figure 6-3: Material cost comparison**

### 6.1.3.5. Final Material Selection

Based on the criteria that were discussed in the previous points, both PC and ULTEM 9085 showed promising capabilities for use to manufacture a CubeSat structure. While ULTEM did have a significantly higher cost, the overall potential performance of the material outweighs that of PC. ULTEM also has more heritage in space use as it is specifically made for the aerospace industry.

ULTEM 9085 was also one of the materials that CPUT had in stock which made acquiring the material easier. For these reasons, ULTEM 9085 was chosen as the material for the design on the CubeSat Structure.

#### 6.1.4. Discussion of Experiments

##### 6.1.4.1. Helical Insert Test

##### 6.1.4.1.1. Helical Insert Test Setup

One of the design considerations for the final design was the type of fastening method used to fasten the structure together. To test whether helical inserts were viable, tests and analyses were done on M3 inserts to ensure that these inserts were capable of holding the structure together. COTS CubeSat structures that make use of M3 fasteners are to be fastened at 0.3 Nm of torque. This was also confirmed by Cogan, D who was the lead mechanical engineer for ZACube-2

Hand tests were carried out by tightening an M3 screw through a Perspex sheet into the helical insert that had been inserted into a sample piece of PLA. This would be done with a torque driver to control the amount of torque applied to the fastener. PLA is a more basic form of thermoplastic, not nearly as strong as ULTEM. The 3D printer used to print the sample pieces was also a basic office 3D printer, without the precision and reliability of industrial printers such as the Fortus 400mc. This means that the sample piece is much weaker than that of the designed structure so if the tests pass with the PLA, the inserts are guaranteed to work in the ULTEM.

First, the samples were printed with the 3D printer in two orientations, flat, and on edge. This was to test the variation in the strength of the insert depending on the build orientation. The printer was set to a layer thickness of 0.2mm with the infill density set to 100% to ensure that the part was completely solid.

Next, the holes were drilled to size and tapped with the tools given in the helical insert kit. In Figure 6-4, it can be clearly seen that the quality of the thread in the plastic is not good. The thread can be seen to be inconsistent and rough.



**Figure 6-4: Tapped holes**

The insert tool could then be used to insert the helical inserts into the plastic as seen in Figure 6-5.



**Figure 6-5: Helical insert in the tapped hole**

Once this was done the test was set up by screwing an M3 socket screw through a Perspex sheet and into the insert as can be seen in Figure 6-6.

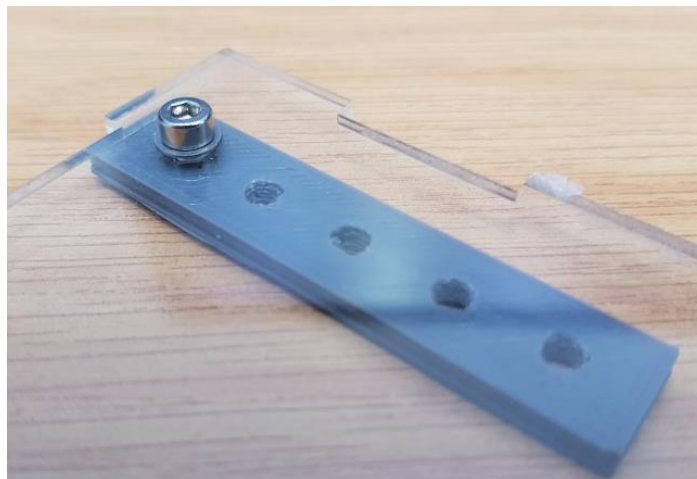


**Figure 6-6: Test piece fasten to Perspex**

A mark was made on the test sample where the end of the helical insert is positioned. This way it could be seen if the insert started to rotate as the thread strips. The test was carried out by torquing the screw at the torque driver's lowest torque of 0.3 Nm. If the torque driver slipped, the fastener had been successfully torqued to 0.3 Nm. If the driver did not slip, this meant that the thread was stripping. This was checked by watching for movement in the insert and its alignment with the mark. The torque was then increased by a single increment on the driver and re-tested until there was proof of the insert stripping or deforming. This torque was recorded as the inserts limit. The test was repeated several times for both the flat and on edge samples and the average limiting torque found.

#### 6.1.4.1.2. Helical Insert Test Results

In the previous section, the methodology of conducting the helical insert tests was discussed by making use of a torque driver. 5 tests were conducted for each sample orientation. It was found that both flat and on-edge samples met the required clamping torque of 0.3 Nm which qualified that helical inserts for use in the structure. The flat samples displayed the lowest average limiting torque of 0.37 Nm while the on-edge samples displayed an average of 0.47 Nm. The test results can be seen in Table 6-1 and Figure 6-7 below.

Table 6-1: Helical insert limiting torque

Test Number	Flat Limiting Torque	On-Edge Limiting Torque
<b>1</b>	0.35	0.4
<b>2</b>	0.35	0.3
<b>3</b>	0.4	0.45
<b>4</b>	0.3	0.7
<b>5</b>	0.45	0.5
<b>Average</b>	0.37 ( $\sigma = 0.05$ )	0.47 ( $\sigma = 0.132$ )

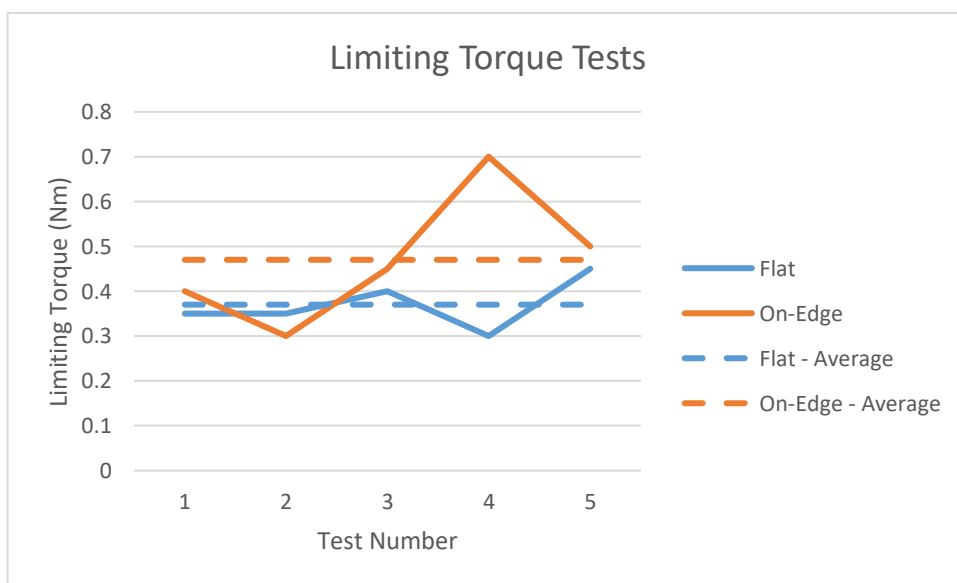


**Figure 6-7: Limiting torque results**

To identify the bolt tension induced in the fastener due to the applied torque, the below equation could be used.

$$T = kDF$$

$$\therefore F = \frac{T}{kD} \quad (6.1)$$

Where;

*F: Force (N)*

*T: Torque (Nm)*

*k: Bolt constant*

*D: Nominal bolt diameter*

For a stainless steel M3 fastener, the required applied torque (T) is 0.3 Nm with a bolt constant of 0.2 and a nominal diameter of 3 mm.

Therefore;

$$F = \frac{0.3}{0.2 \times 0.003}$$
$$= 500 \text{ N}$$

Applying a 0.3 Nm torque to the fastener results in a bolt preload force of 500 N. Applying the limiting torque of 0.37 Nm would result in a bolt preload force of 617 N.

#### 6.1.4.1.3. Helical Insert Test Discussion

The results seen previously showed that for 3D printed PLA, the limiting torque for M3 threaded inserts was 0.37 Nm and 0.47 Nm for flat and on-edge specimens respectively. It should be noted again that these tests were done using specimens printed in PLA using a basic office 3D printer. These printers are by no means industrial level such as that of the Fortus 400mc. PLA also does not have structural properties like that of ULTEM 9085. Regardless of these two factors, the tests were still conclusive in that the 3D printed specimens with helical inserts could survive the required preloading torque for the fasteners. The results also showed that at the limiting torque of 0.37 Nm, the induced bolt preloaded tension

would be approximately 617 N this is 117 N greater than the required 0.3 Nm which would induce 500 N of preload.

For the ULTEM structure, M2.5 fasteners would be used for fastening the rails and solar panels onto the structure. M2.5 screws require a preloading torque of 0.25 Nm which also results in 500 N of preload. It can be assumed that M2.5 helical inserts would also be capable of limiting torque of 0.37 Nm as the pitch size difference between the M2.5 and M3 is only 0.1 mm and the limiting factor is mainly the material itself. This means that each M2.5 fastener can handle an additional 117 N of axial loading.

The only scenario that could cause axial loading, also known as pull out force, on the fasteners would be the force of the solar panels under the 20 g of load. According to Innovation Solution in Space (ISIS), a 1U solar panel weighs approximately 50 grams. Therefore, the maximum load this would induce on each of the four fasteners would be only approximately 2.5 N at 20 g of loading.

It is therefore clear that the use of M2.5 fasteners with helical inserts inserted into the ULTEM would be feasible and sufficiently strong for fastening the structure together.

#### 6.1.4.2. Material Testing

Currently, there are no standard testing methods allocated to AM materials however in previous studies plastic and composite testing methods have been used. A study was also done by Forster which examined all possible testing methods for AM parts. In this study he identified that both ASTM D3039 and ASTM D638 test would be suited for the testing of tensile properties of an AM part (Forster, 2015). Stratasys the suppliers of the FDM material known as ULTEM 9085 make use of the ASTM D638 testing method. Therefore, the same method should be used in tests done toward the satellite structure.

Material testing of ULTEM 9085 was not in the scope of this research but would be recommended for further research.

#### 6.1.5. Radiation Analysis

One of the advantages of aluminium structures is the shield it functions as for particle radiation. Aluminium is often used as shielding for high priority electronic components as it stops most electron and proton particles from penetrating the electronic chips and causes damage and errors to the circuitry. The aluminium structure itself, therefore, acts as additional shielding for the entire structure. An analysis was therefore conducted to identify the radiation shielding effects of an ULTEM structure and compare it to that of aluminium.

##### 6.1.5.1. Expected Radiation in LEO

Satellites in LEO such as CubeSats are exposed to several radiation types including trapped particles from Van Allen's Earth Radiation Belts (ERBs), solar cosmic radiation, and cosmic rays.

OMERE space environment software was used to identify the flux of electrons and protons over an energy range of 0.04 to 300 MeV. It was found that low energy particles had the highest flux compared to high energy particles.

OMERE and TRIM were used to identify that 2 typical layers of 2mm of Aluminium can block protons with energy up to approximately 19 MeV.

To identify the stopping ability of ULTEM for protons, TRIM was setup with ULTEM input as the target layer for radiation. ULTEM was defined as 2 mm of PEEK which has a chemical formula of  $(C_{37}H_{24}O_6N_2)_n$ , as seen in Figure 6-8 below. The simulation was then run radiating the target material with hydrogen at various energies to determine the limit of 2 mm of ULTEM. In Figure 6-9 it could be seen the energy limit of 14 MeV as shown by the target depth of the particles into the materials. This showed that ULTEM has 26% lower radiation protection versus aluminium.

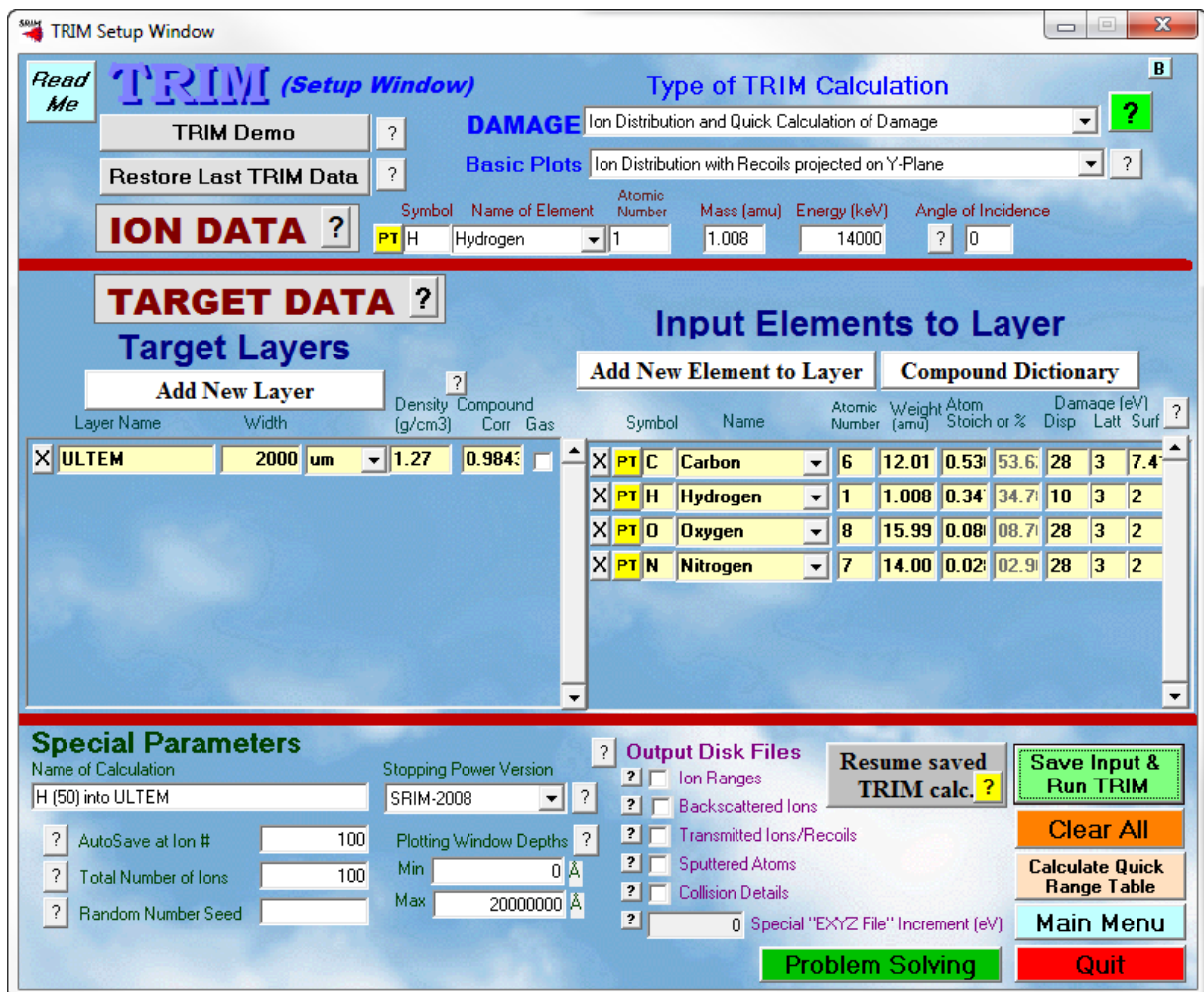
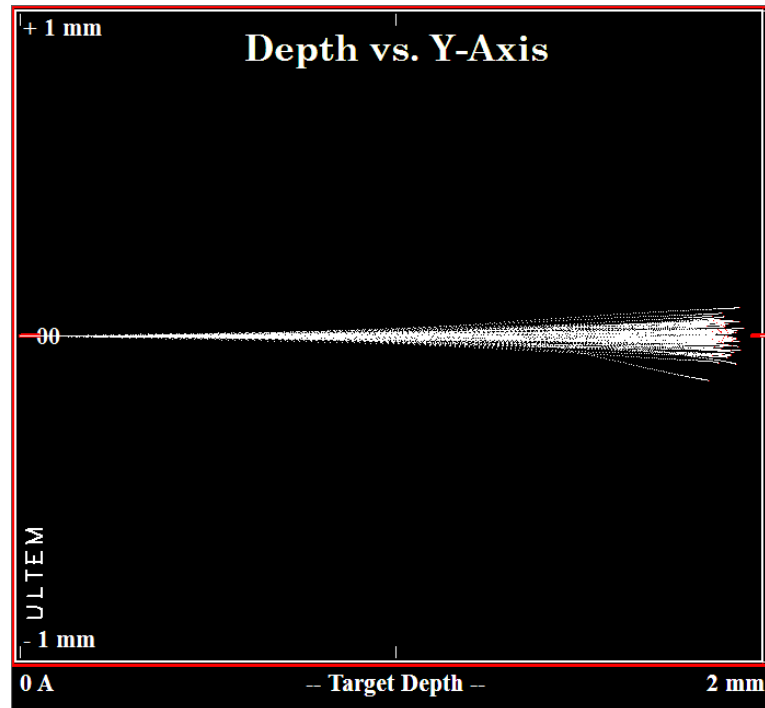


Figure 6-8: TRIM material setup





**Figure 6-9: Radiation depth in ULTEM at 14MeV**

### 6.1.6. Structure Design

Designs for the structure were done using Siemens NX software. The student version of NX offers powerful Computer-Aided Design (CAD) and Computer-Aided Engineering (CAE). NX uses the Nastran structural solver as its FEA tool. The advantage of using NX and its Nastran solver is that you can switch seamlessly between the CAD and CAE contexts allowing one to make geometry changes while working on the finite element model (FEM). This offers improved designing efficiently over exporting and importing between software.

#### 6.1.6.1. Design Considerations

##### 6.1.6.1.1. Structure Qualification

When designing a structure for a CubeSat, there are three considerations for qualifying for use. Does it meet the requirements stipulated in the CDS? Will it survive the launch? And, will it survive in space? More detail on these requirements was discussed in Section 3. These are the primary objectives for designing a CubeSat structure to qualify it for use, however, to design an optimised structure more must be considered.

##### 6.1.6.1.2. Commercial Use

The structure must be appealing to the commercial market, therefore it should be designed with commercial use in mind. Almost all CubeSats make use of payloads that follow the PC-104 spec. This must

be considered when designing the structure to ensure that the rods are aligned to suit the PC-104 spec. Figure 6-10 below shows an image of a typical PC104 board.

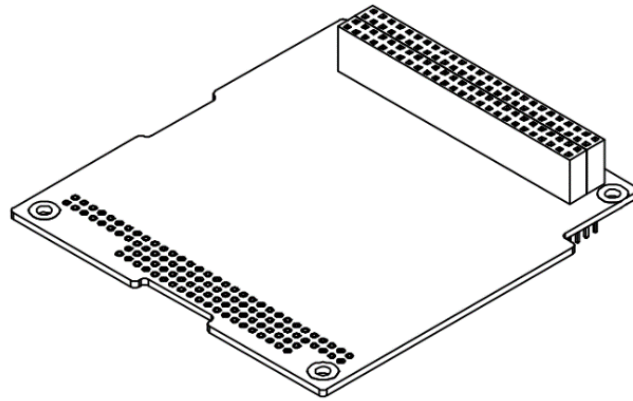


Figure 6-10: PC104 PC Board (Pumpkin Inc, 2003)

The design must also accommodate the mounting of COTS solar panels which have a specific bolt arrangement. For this design, the ClydeSpace 1U side solar panels were used as a reference for the bolting pattern. See Figure 6-11 below of the 1U side solar panel.

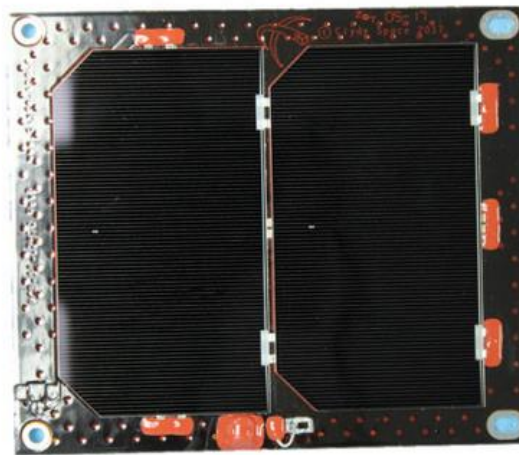


Figure 6-11: Clyde Space 1U side solar panel

Another important factor to consider when designing a structure for the commercial market is the ease of assembling. When assembling a CubeSat, extreme care must be taken to ensure nothing is bumped, scratched or jammed. Therefore, assembling the structure of the CubeSat should be as easy as possible. It should also be easy to stack the payloads and components onto the structure.

#### 6.1.6.1.3. Fastening Method

Selecting the method of fastening the structure together was crucial in the final design of the structure. Originally there were four options; tapping and screwing straight into the plastic, using threaded inserts, using nuts or using helical inserts.

Tapping into the plastic would result in the least amount of post-processing and would not require extra hardware. The concern with this, however, would be when assembling and disassembling the structure, screwing in and out of the plastic thread could damage the thread over time and lead to the thread stripping.

To overcome this issue, a threaded insert or nut can be used. The problem with using a nut or threaded insert is that it requires at least 4mm of material thickness which clashes with the rods and stand-offs of the structure.

Helical inserts offer a hybrid between the tapped plastic and threaded inserts. They are very small, only 2.5mm long which lets them fit without interfering with the rods and stand-offs. The helical inserts significantly strengthen the thread in the plastic while also preventing fatigue in the thread due to constant assembling and disassembling. In Section 6.1.4.1.3 the results of experiments and FEA analysis to verify the strength of using helical inserts can be seen.

#### 6.1.6.2. Concepts

When developing concepts, the first step is to identify the overall dimensions of the structure. These dimensions can be taken straight from the CDS. The spec for a 1U is 100x100x113.5 mm with aluminium rails of a square cross-section of 8.5 mm. The rail ends are chamfered by 1mm and the outer edge of the rail has a rounded radius of 1 mm. See Appendix A for a detailed drawing of the 1U dimensions.

The rails must be a separate part as they must be aluminium so they cannot be printed. The rods that the CubeSat's components slide onto will also be metal so will be separate from the 3D printed structure.

With this information the various concepts were deployed, improving the design with each revision.

##### 6.1.6.2.1. Concept 1

The first concept was more to get a working concept that met the requirements of the CDS. This concept could be used as a starting point to innovate further. This structure had too many separate parts as can be seen in Figure 6-12. The 3D printed faces were split up into 6 panels with the four rails split up into a long section with a separate rail end. This design also resulted in far too many fasteners which would make the assembling process tedious. This design also did not make use of the benefits of 3D printing as each side was a separate component.

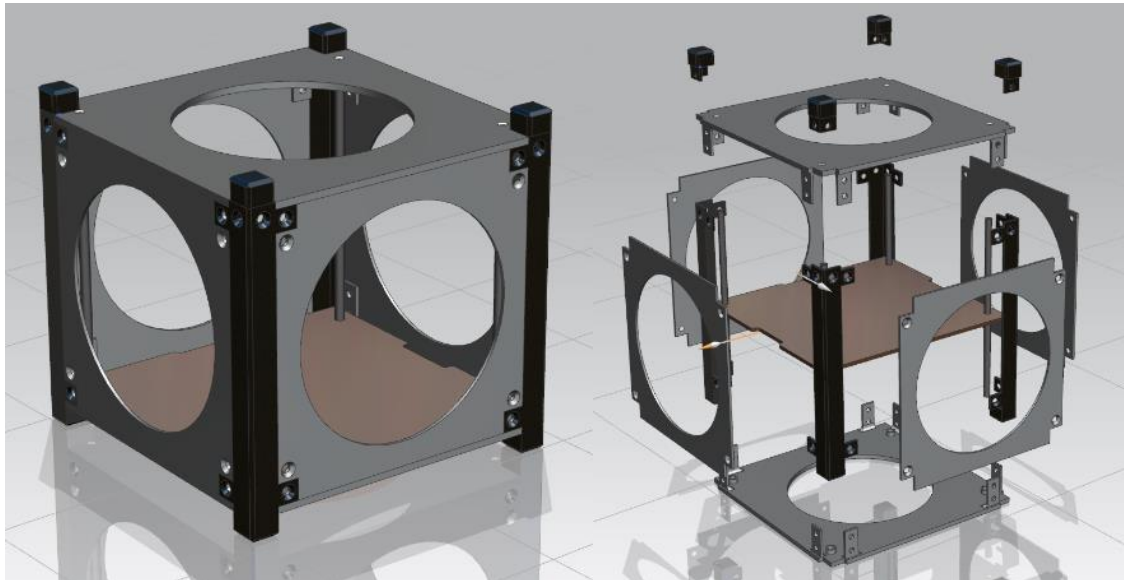


**Figure 6-12: Concept 1**

6.1.6.2.2. Concept 2

Concept 2 made slight changes to the original concept. One of the main changes was having the aluminium rail ends split into three parts, the rail ends which now were positioned on the inside of the structure allowing the screws to screw into the aluminium. The structure also made use of a different geometric weight reduction shape on the panels as can be seen in Figure 6-13. This concept still had a large number of fasteners and separate parts making the assembly process tedious.

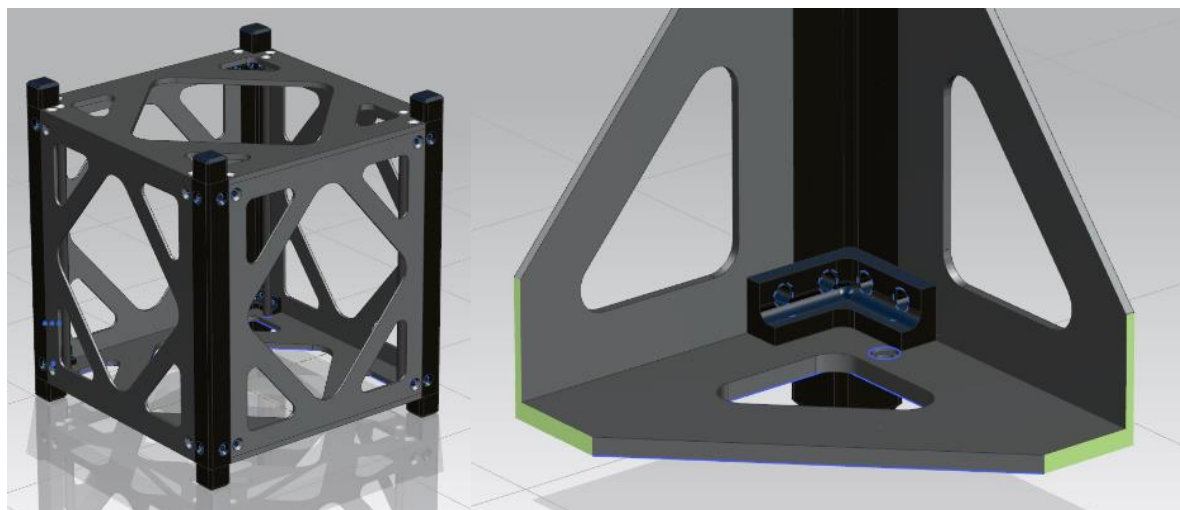
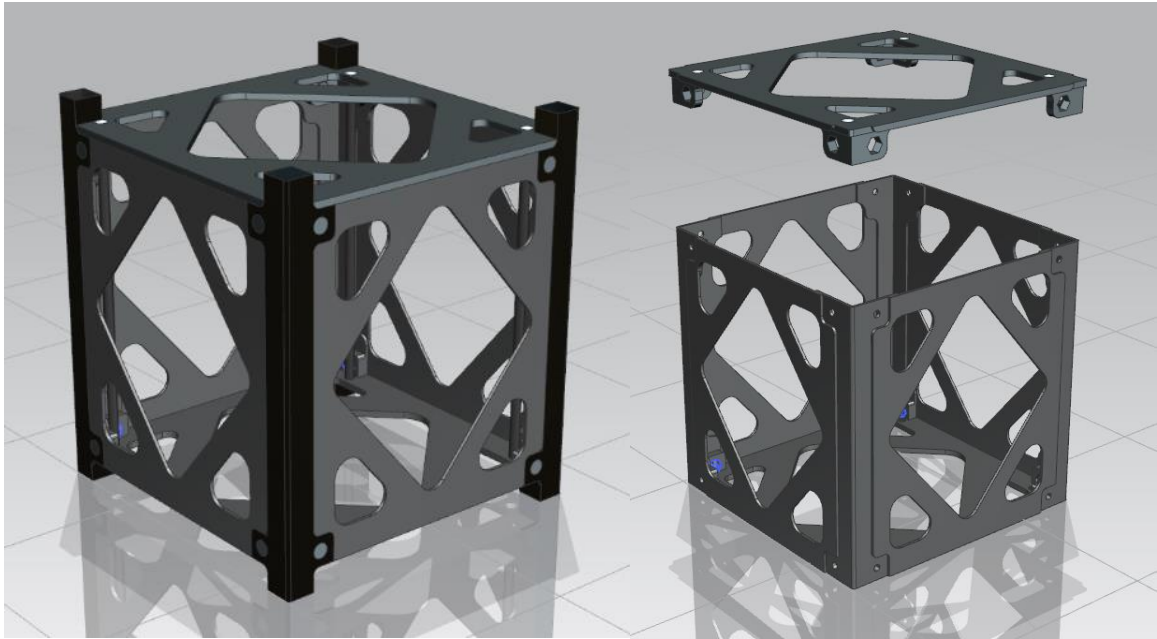


**Figure 6-13: Concept 2**

6.1.6.2.3. Concept 3

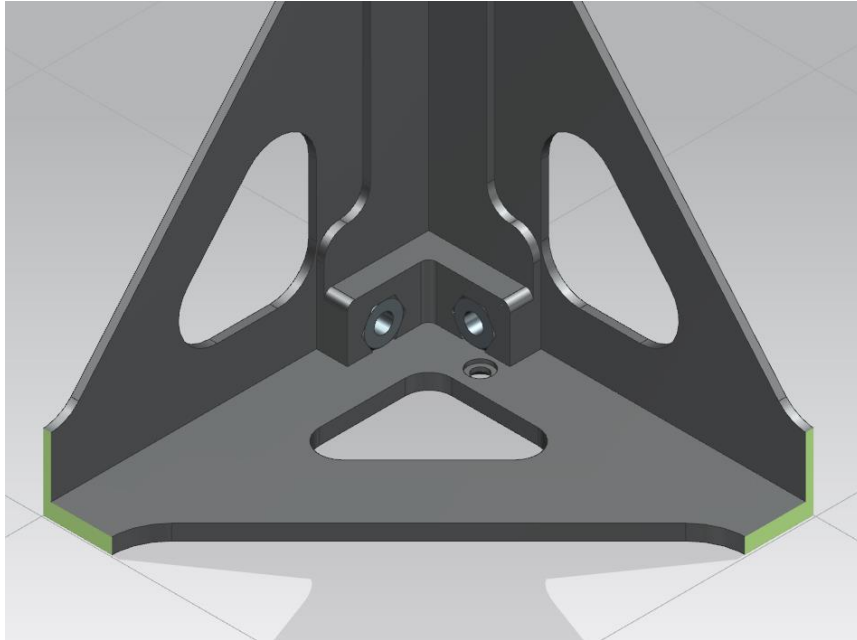
The third concept was approached to improve the design to make it more suitable for 3D printing and reduce the number of parts. For this design, the rails were one solid part and the main shell of the structure was reduced to only two parts reducing the number of structural components from 18 to only 6. In  
Shane Martin

Figure 6-14 the main shell of the structure can be seen as two separate parts, a shell body with a lid. This allows for the 3D printing of the shell in only two parts which allow them to both fit on the 3D printer bed at one allowing for the entire shell to be printed in one run.



**Figure 6-14: Concept 3**

This concept makes use of inserting M2.5 nuts into the structure for the screw to fasten onto as can be seen in Figure 6-15. This ensures no stripping of tapped plastic threads. Ideally, threaded inserts would be used however due to the limitation of space between the outer limits of the structure and the position of the internal rods threaded inserts would be too long.



**Figure 6-15: Concept 3 nut inserts**

### 6.1.7. Discussion of Structure FEA

#### 6.1.7.1. Setup

##### 6.1.7.1.1. Analysis Setup

To verify the structural integrity of the structure, simulations were done with Finite Element Analysis (FEA) software to simulate the strength of the design under various loading conditions. For these simulations, the mechanical properties of the material need to be input into the FEA software to Analyse how the material will behave. As mentioned in Section 4.3.1, FDM parts behave as orthotropic materials.

The mechanical properties that were used for the analysis were acquired by previous researchers as discussed in Section 4.5.4. The properties used can be seen in Table 6-2. This assumes the printer at CPUT would be able to replicate the printing ability of the researcher from Section 4.5.4. It should be noted that for more accurate results, tensile tests should be conducted on test specimens 3D printed by the CPUT 3D printer.

Table 6-2: ULTEM 9085  
Mechanical Properties

Property	Value
E1	2000
E2	2300
E3	2000
$\nu_{12}$	0.37
$\nu_{13}$	0.39
$\nu_{23}$	0.33
G12	730
G13	719
G23	865

#### 6.1.7.1.2. Structure Finite Element Models

After creating the ULTEM 9085 material and adding it to the NX material library, the FEM for the CubeSat structure was made. When doing advanced FEA, an overly complicated FEM can lead to unnecessary high computation requirements. It is therefore important to simplify the model as far as possible before creating the FEM. The first step is to remove unnecessary components from the assembly. In this case that included the PC104 boards, the solar panels, and all fasteners. The fasteners can be set up as an FEM feature in the model. The second step is to remove unnecessary geometry features such as fillets and chamfers which would complicate the mesh. In this case, the model wasn't too large, so the fillet features were kept having a more accurate FEM.

Once the unnecessary components had been suppressed, an FEM file was created for the assembly. The FEM was created using the structural NX Nastran solver environment. Individual meshes were then created for the various parts of the assembly. This included the main shell, the base plate, the four rails, and four rods.

#### ***Concept 3 FEM***

The first FEM that was set up was for Concept 3 as this concept showed the best potential for practical use. This FEM was set up in the same manner as discussed below for the final FEM however additional detail has been displayed for the setup of the final FEM in the following section. Concept 3's FEM can be seen in Figure 6-16 below.

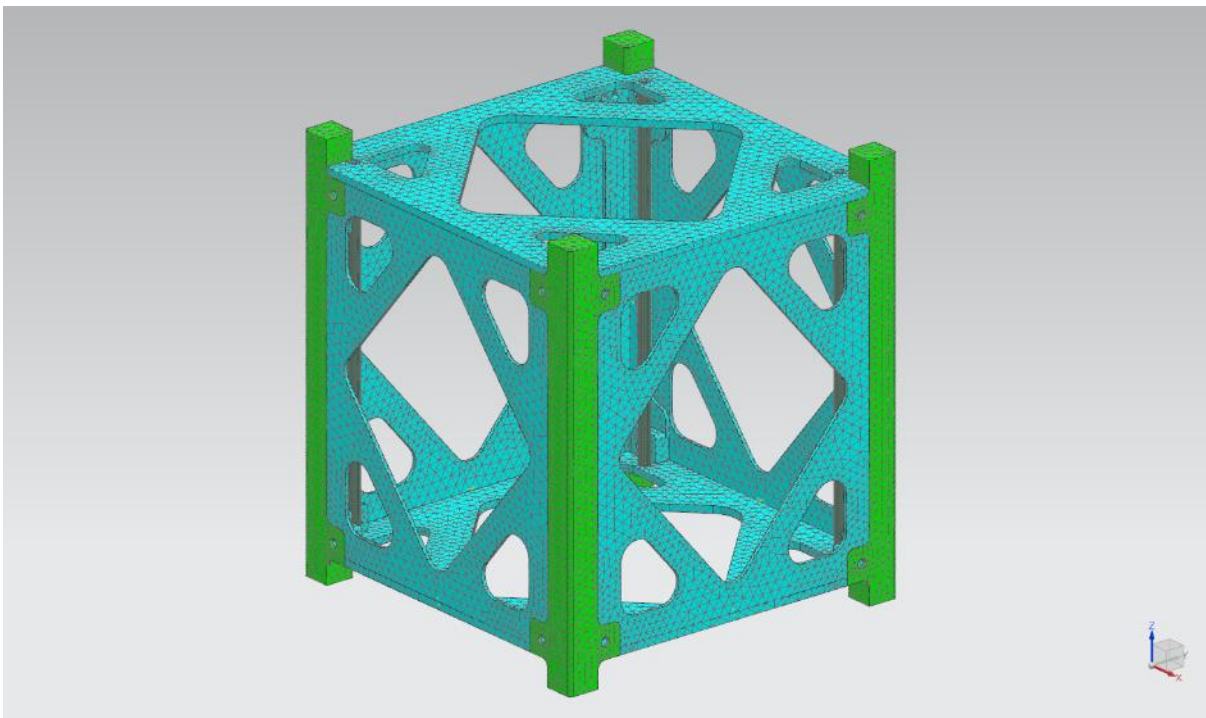


**Figure 6-16: Concept 3 FEM**

The purpose was to obtain simulation results which were then used to further optimise the structure resulting in the final design which was then re-Analysed using the following setup:

### ***Final FEM***

Firstly, the rails were meshed using the CTETRA (10) quadratic 3D tetrahedral mesh type, as seen in Figure 6-17, to allow for meshing on curved based geometry. The initial element size was set to 2.94mm as recommended by the mesher. Curvature bases size variation was set to 80.00 to allow for smaller mesh elements around curved geometry. A mesh control was used under the rail end to reduce the element size to allow for 3 elements through the thickness as this was likely to be a high-stress region. The mesh collector was set to Aluminium 6061.

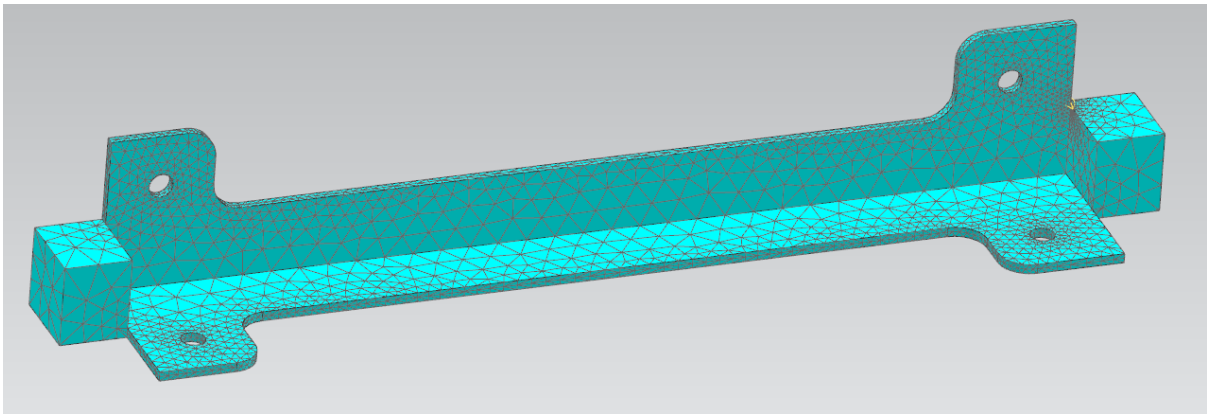


**Figure 6-17: Rail FEM**

Next, the rods were meshed using CHEXA (20) quadratic element types, shown in Figure 6-18, swept through the length of the rods at an element size of 1.5mm. A titanium mesh collector was used for the rods.

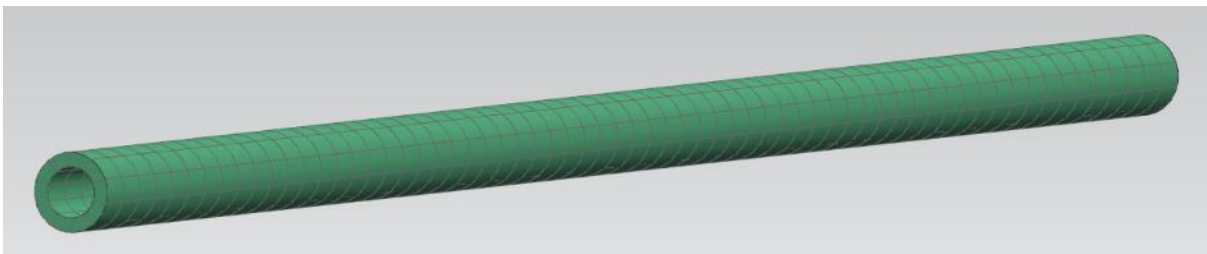


**Figure 6-18: Rods FEM**

For the ULTEM shell structure, again a CTETRA (10) quadratic 3D tetrahedral mesh was used, as shown in Figure 6-19, with the same settings as the rails. This time the mesh collector was set to the ULTEM 9085 material that was created previously.



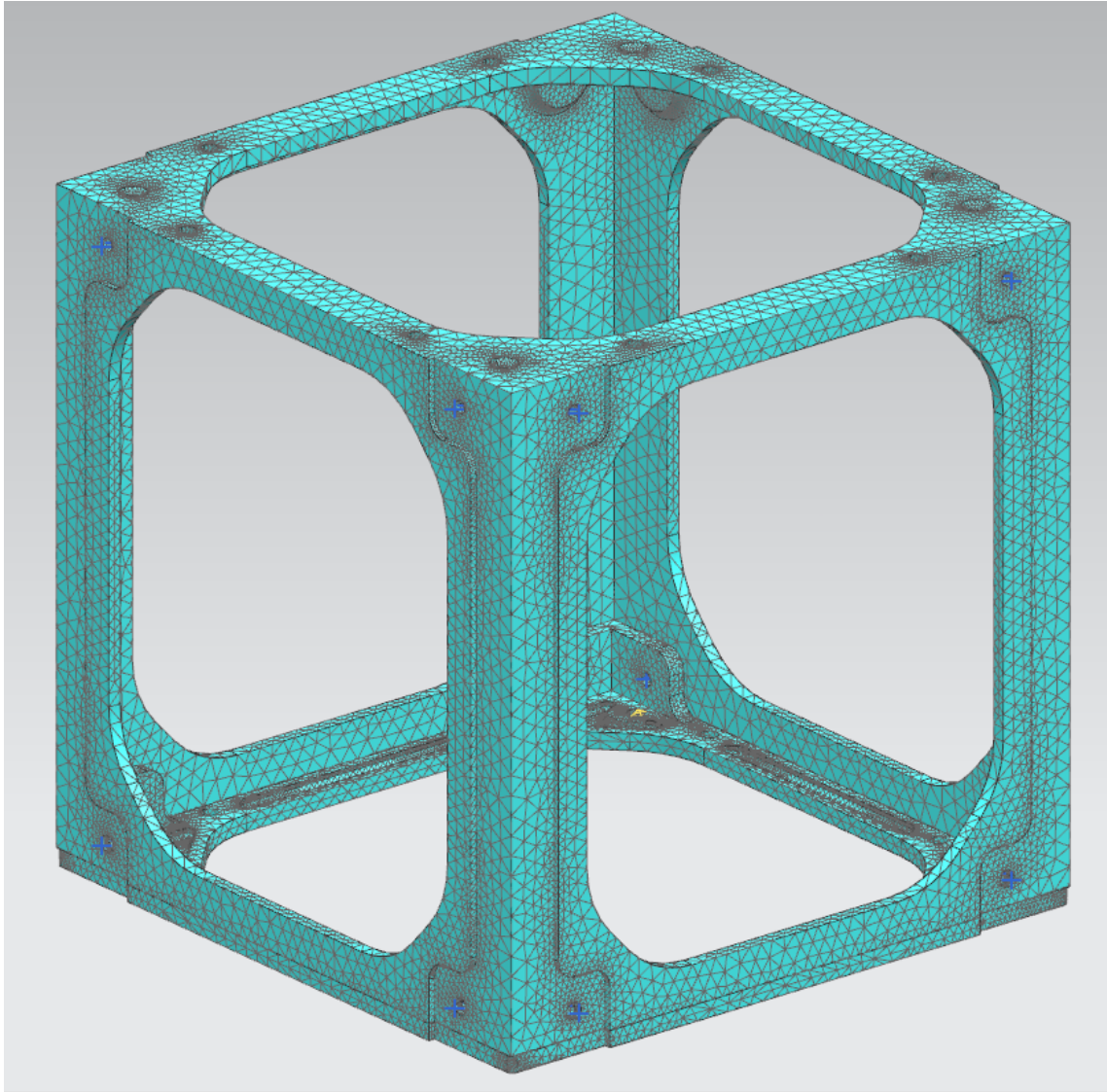


**Figure 6-19: ULTEM shell FEM**

To ensure that the orthotropic material properties are set up in the correct direction, the mesh associated data can be displayed. The red, yellow and blue arrows as seen in Figure 6-20 represent the 1,2 and 3 planer directions respectively. These directions are directly related to the printing orientation within the 3D printer chamber.

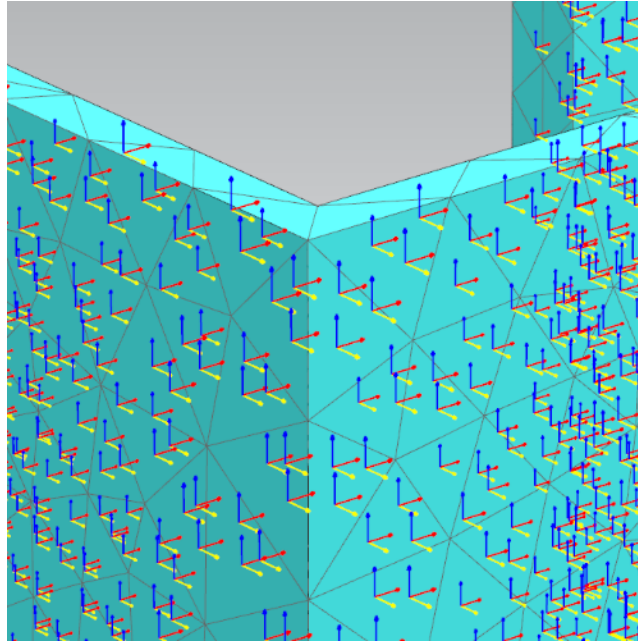


**Figure 6-20: Material orthotropy**

Once all the components of the structure had been meshed, the final step to the FEM was to connect the meshes using one-dimensional RBE3 connectors. These connectors were set up to represent fasteners by creating an RBE3 1D element that was given the fastener's specifications. In this case, the fastener was set up as a stainless steel M2.5 screw as can be seen in Figure 6-21.

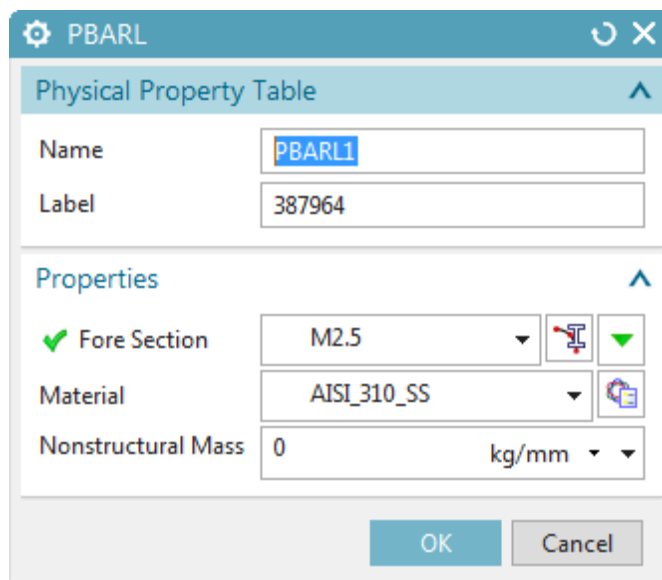


**Figure 6-21: RBE3 element definition**

In Figure 6-22 and Figure 6-23 an example of where the 1D elements were used can be seen. The 1D element connects to elements within a circular region on the outer surface which represents the head of

the screw. The elements on the inner surface of the tapped hole were then connected to the other side of the 1D element.

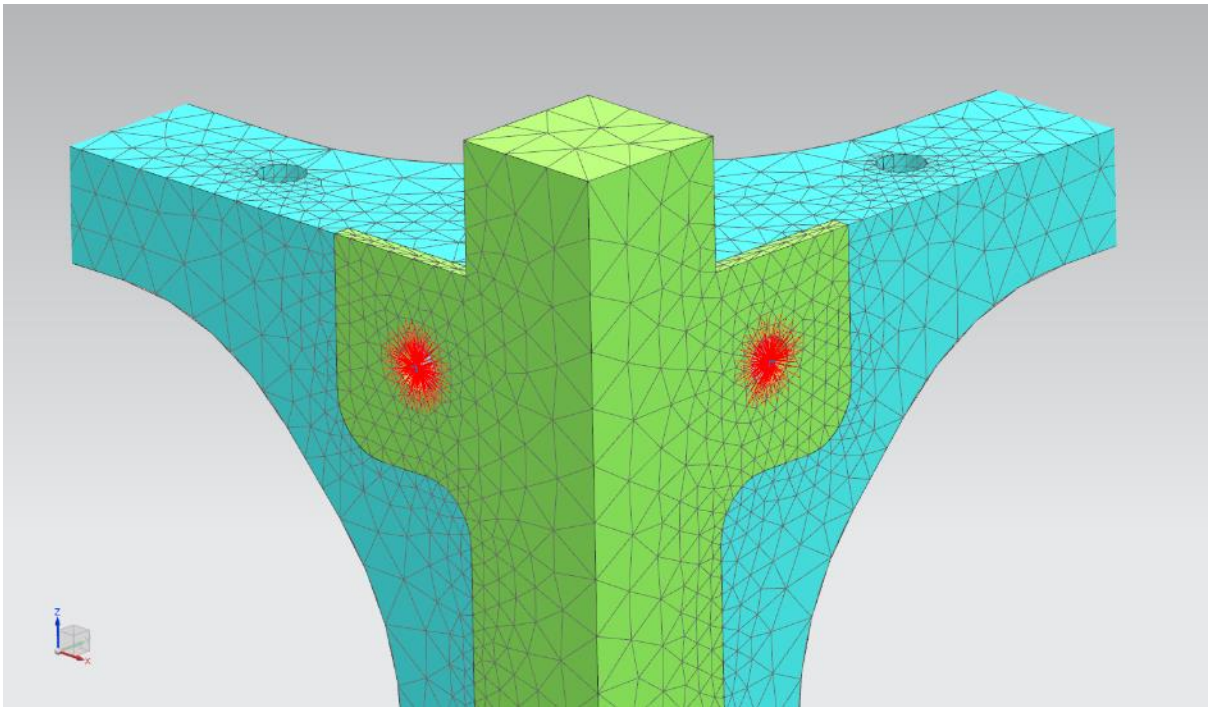


**Figure 6-22: 1D element connector external view**

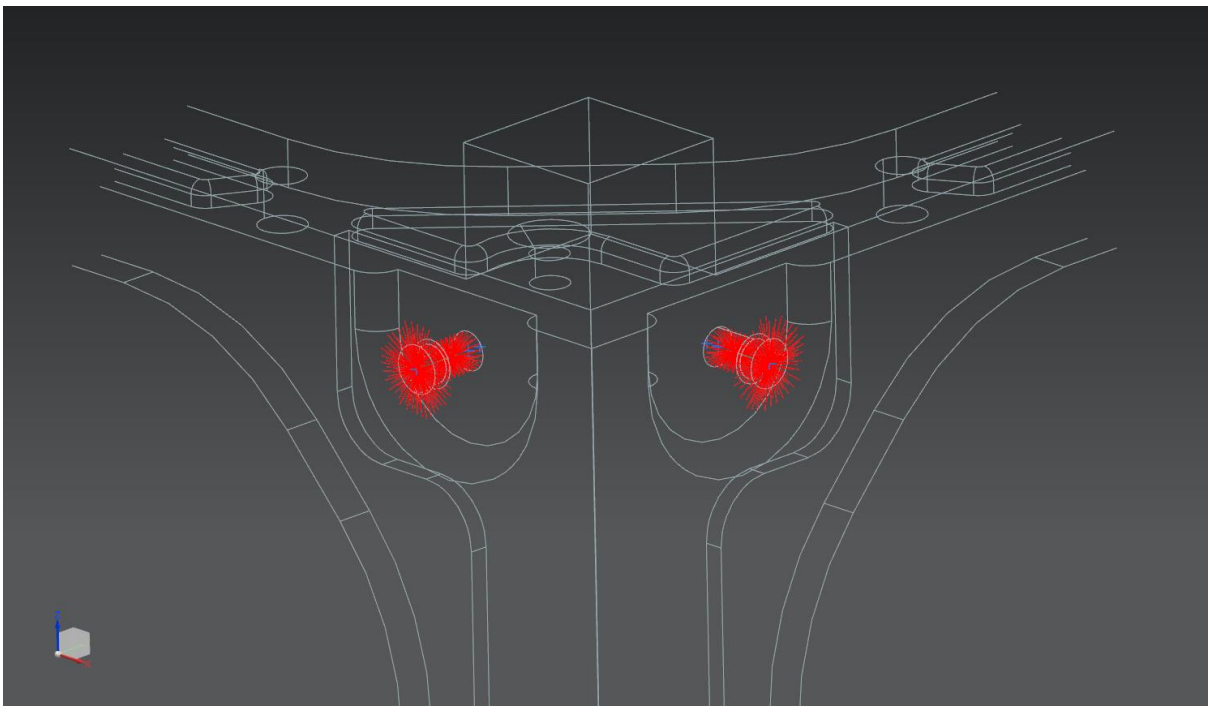


**Figure 6-23: 1D element connector internal view**

Once all the components had been meshed and connected with the 1D connectors, the FEM was completed as displayed in Figure 6-24.

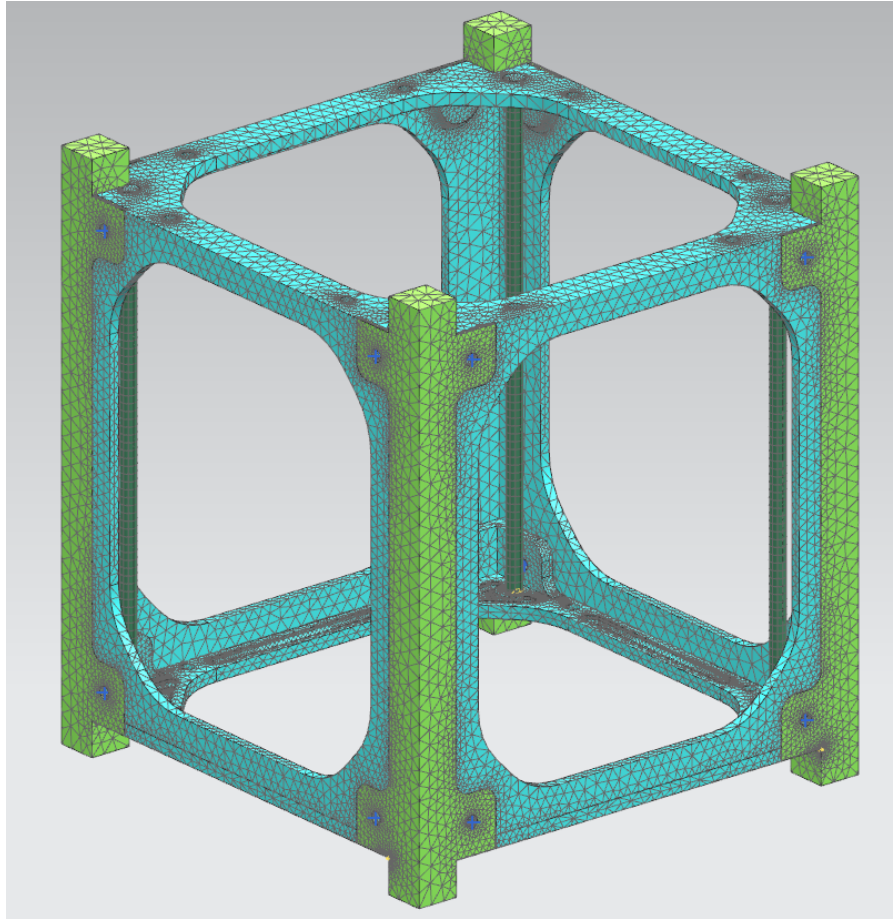


**Figure 6-24: Final FEM**

#### 6.1.7.1.3. Simulation Setup

The first study that was conducted was a static loading of the structure along its longitudinal axis. An SOL 101 Linear Statics solution type of the NX Nastran Solver in NX Pre/Post FEA was used to Analyse the model. The first step was to then define the contacts between the different parts of the assembly. The Surface-to-Surface feature was used which automatically detects parts that are in contact with one another and gives them a *sliding* type of contact. This allows the parts to slide over one another but cannot penetrate each other. Constraints and loads then needed to be applied to the model.

For all structural loading, the qualification requirements as stated by Fortescue et al. in Section 3.2.1 were used. For static loading, the worst case was 5 g. This was however specific for the Ariane 5 launch vehicle. Each structure must be qualified for its specific launch vehicle. For this reason, a factor of safety of 4 was implemented.

### Longitudinal Analysis

For the longitudinal analysis, the rail ends were constrained with a *fixed* constraint. This allows zero displacement to these faces. The fixed constraint is displayed in Figure 6-25 below in orange. A 20g load was applied along its longitudinal axis to the entire model. The loading of an additional two 1U CubeSats pushing down on the structure at 20 gs was also applied to the rail ends. This load was found by taking the maximum allowable 1U mass and multiplying it by 20 times gravity and by 2 to represent two CubeSats. This results in a load of 521.9N being applied across the top of the rail ends.

$$\begin{aligned} \text{Rail Load} &= 1U \text{ Mass} \times 20g \times 2 \\ &\therefore = 1.33 \times 20(9.81) \times 2 \\ &= 521.9 \text{ N} \end{aligned}$$

The third and final load applied to the structure was the internal components of the CubeSat applied to the rails of the structure. This was taken as 1kg of components multiplied by 20 g resulting in 196.2 N applied to the rods. The loading on the structure is displayed in Figure 6-25 in Red.

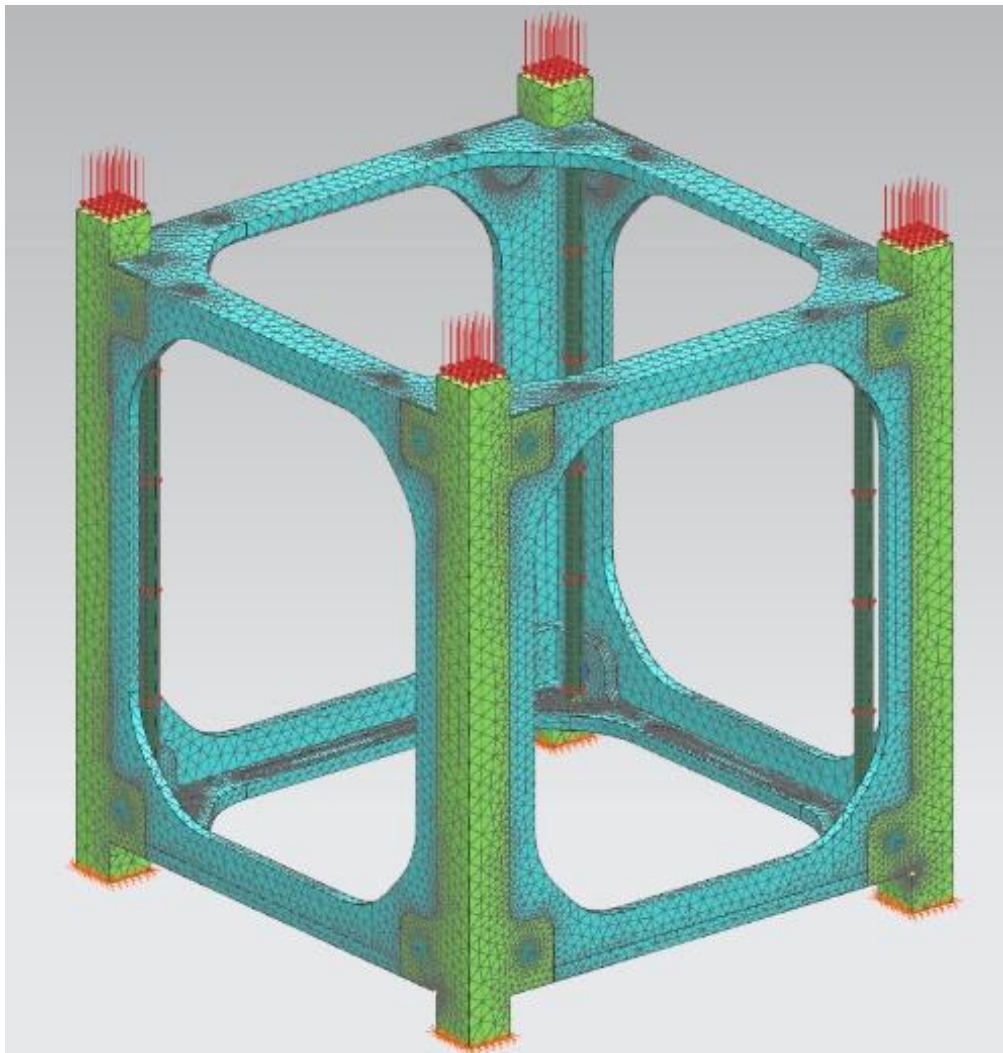


**Figure 6-25: Longitudinal analysis setup**

### Lateral Analysis

For the second analysis, the lateral loading was analysed. For this analysis, a similar setup was done however this time the additional two CubeSats were not required. The gravitational loading was switched to the lateral direction and the fixed constraint was moved to the side of the rails. The lateral loading setup can be seen in Figure 6-26 below.

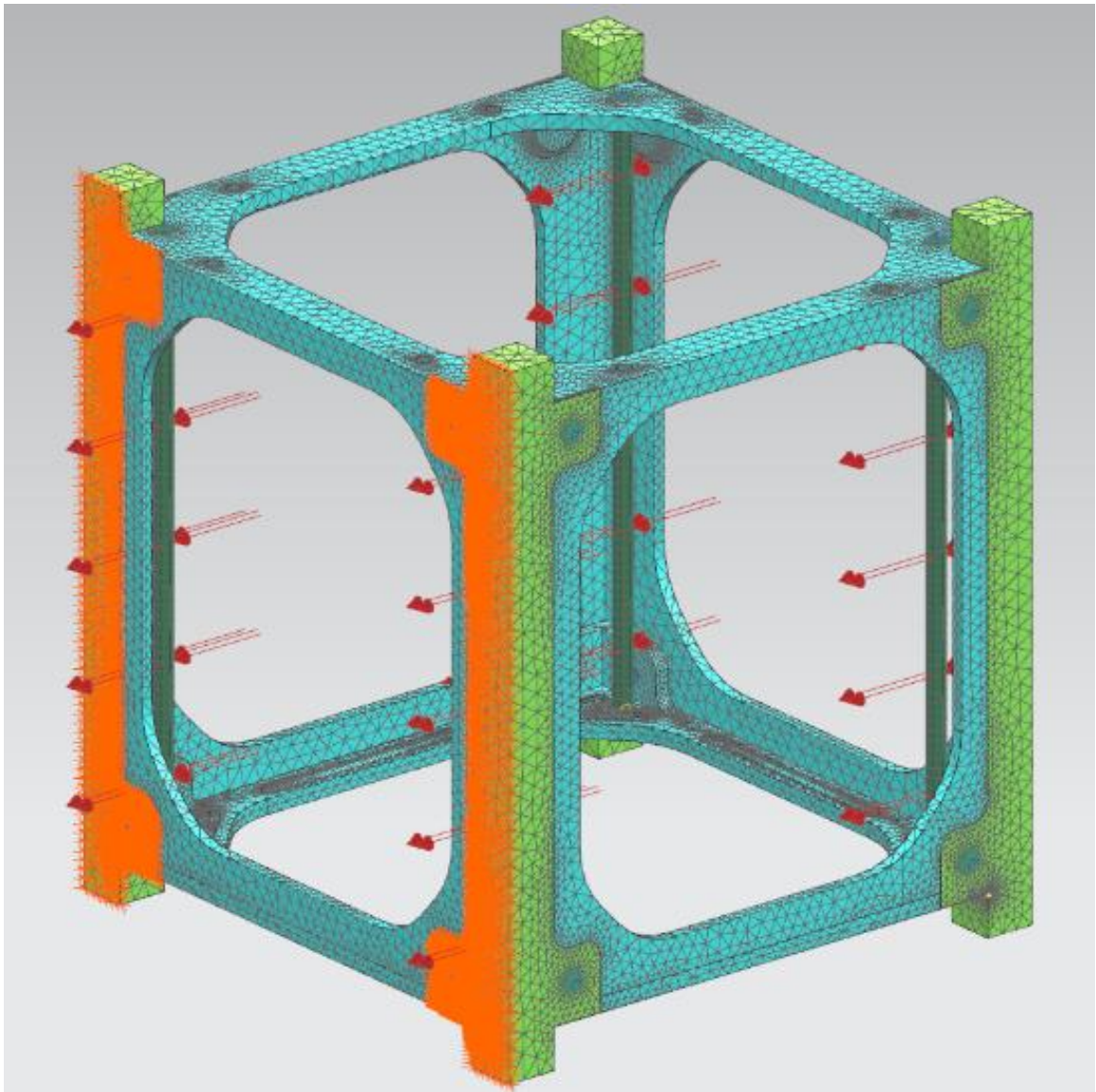


**Figure 6-26: Lateral analysis setup**

### Harmonic Modal Analysis

The third analysis that was conducted was a harmonic modal analysis, this was to identify the structure's first four natural harmonic modes. This is important to ensure that the natural harmonic mode or resonant frequency does not fall within the expected frequency range during launch. The resonant frequency of

the structure should also be at least double that of the launch vehicle frequency as tabulated in Table 3-2 of Section 3.2.1 (Fortescue et al., 2011).

The NX Nastran solver was setup using the SOL103 Real Eigenvalues solution type. The Lanczos eigenvalue method was used as recommended for medium-sized models. By setting the frequency range lower limit to 1 Hz, the structure can be Analysed as an unrestrained structure. This avoids the calculating of rigid body modes. The solution was set up to display the first 10 harmonic modes of the structure as seen in Figure 6-27 below.

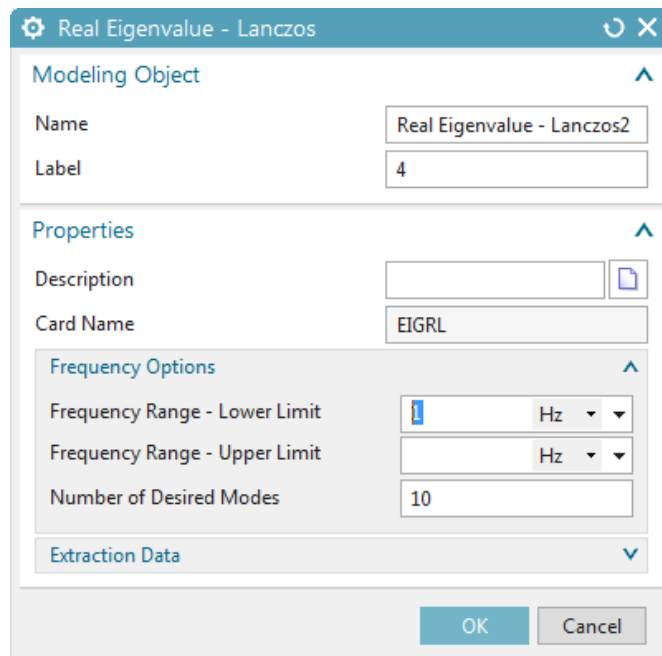


**Figure 6-27: Real Eigenvalue - Lanczos settings**

#### 6.1.7.1.4. Pumpkin 1U Comparative Analysis

A FEM was also set up on a COTS structure made by Pumpkin Inc. This was to run a comparative analysis on a COTS structure using the same loading conditions as the ULTEM structure so that comparisons between the two could be made.

The FEM was setup using 3D tetrahedral elements of 2.7 mm in size with a curvature size variation set to 50. The model was set as Aluminium 6061 T6. The FEM can be seen in Figure 6-28.

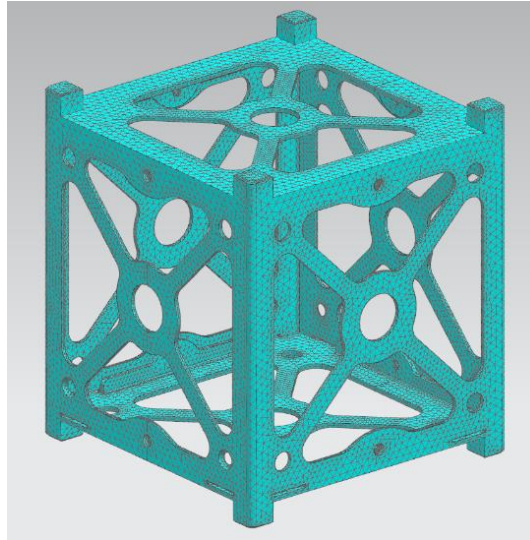


**Figure 6-28: Pumpkin structure FEM**

The loading was set up similarly to that of the ULTEM structure by applying the 3 20 g loads to the structure.

#### 6.1.7.2. FEA Results

##### 6.1.7.2.1. Concept 3 Basic Analysis

The first analysis run was the longitudinal loading of the structure. In Figure 6-29(left) it can be seen how the maximum induced stress in the structure is about 25.5 MPa with a maximum deflection of about 0.16 mm as seen in Figure 6-29(right).

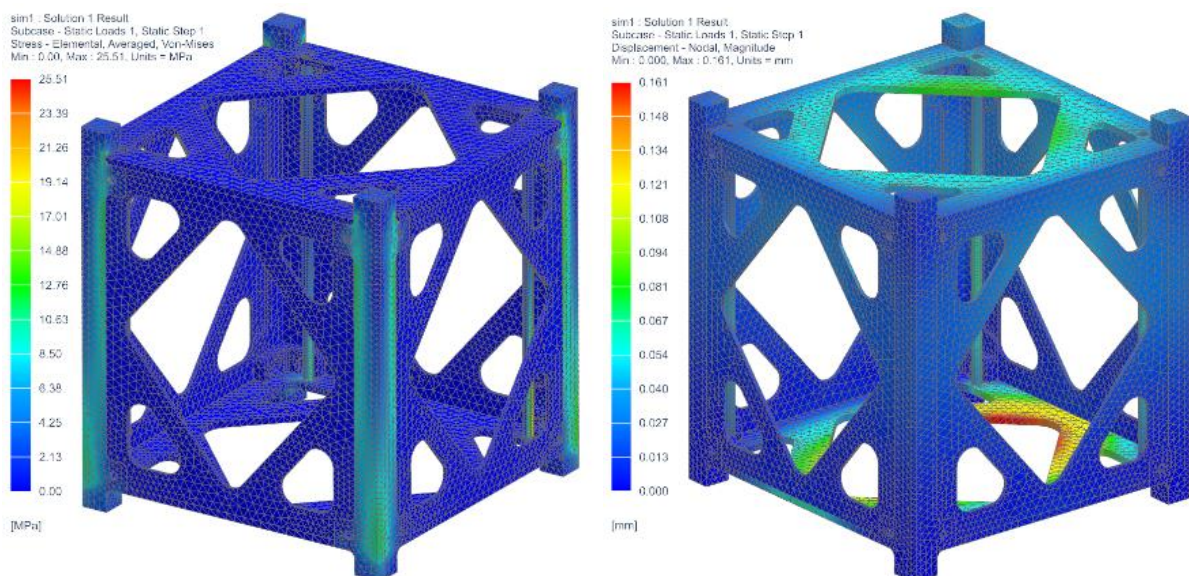


**Figure 6-29: Von Mises stress (left) and displacement (right)**



#### 6.1.7.2.2. Longitudinal Analysis

The first analysis that was conducted on the final structure was a static loading along the longitudinal axis as discussed in Section 6.1.7.1.3. It can be seen, as anticipated that most of the loading was taken up by the rails of the structure. The maximum induced stress in the structure was 40.3 MPa with a maximum deflection of 0.07 mm as can be seen in Figure 6-30 and Figure 6-31.

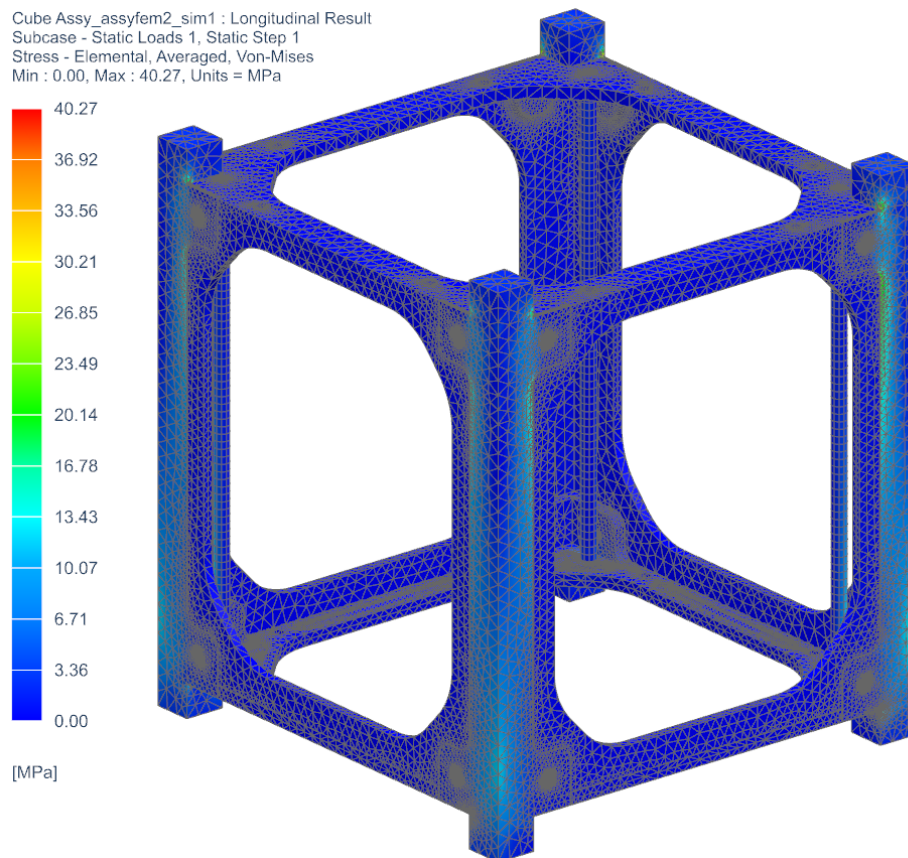


**Figure 6-30: Von-Mises stress under longitudinal loading**

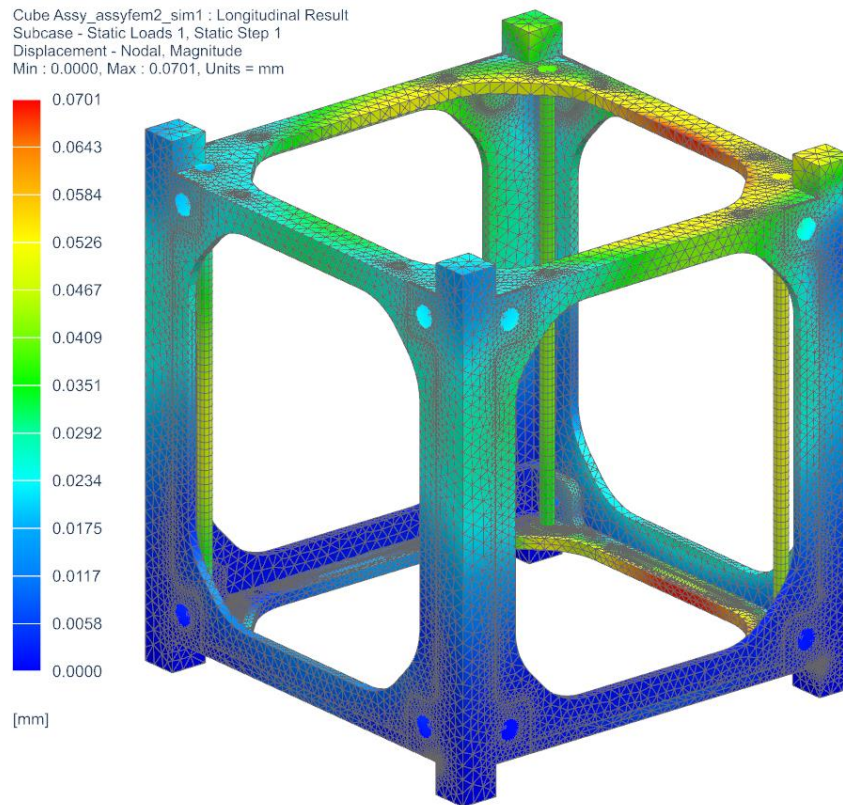


**Figure 6-31: Deflection under longitudinal loading**

The rails showed the highest induced stress with average stress of about 10 MPa through the part. A concentration of stress can be seen in Figure 6-32 near the base of the rail in the corner of the flange. Sharp geometries like this are expected to have high-stress results as it is a weak spot in the part. This can, however, be ignored as the sharp corner will not exist after machining. The tip of the milling machine will have a radius which will ensure that there are no sharp corners in the part. The 6061 T6 aluminium rails have a yield stress of 276 MPa showing that the induced stress in the rails is only approximately 15% of the yield.

The maximum deflection of 0.07 mm is well below the build limit of structure and will not cause any interference with the P-POD.

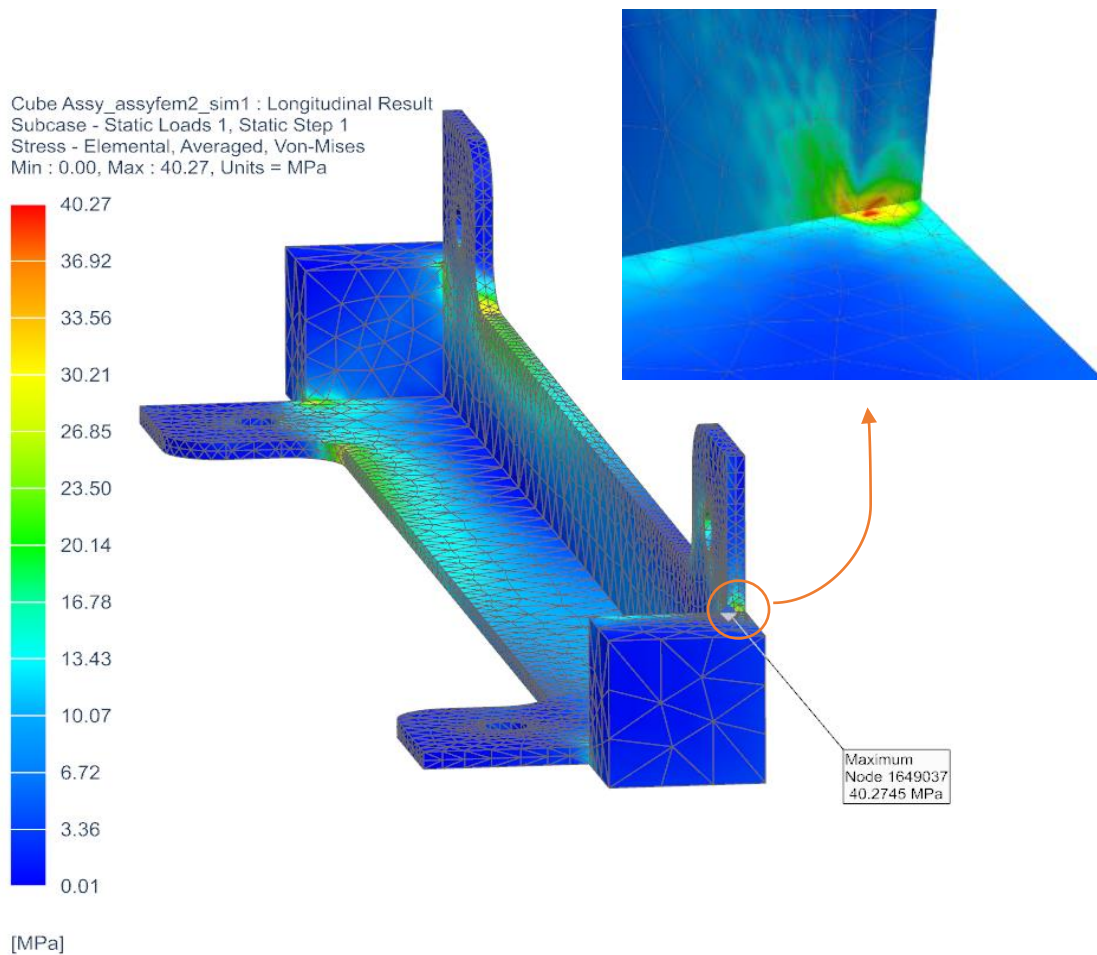


**Figure 6-32: Stress concentration for longitudinal loading**

When analysing the stress induced in the ULTEM structure, it could be seen in Figure 6-33 that the maximum stress was located around the mounting points for the rods. This is due to the loading of the components causing a compressive load on the base. The maximum stress induced around the mounting hole was approximately 10 MPa. The bottom of the base was experiencing tensile stress of also approximately 10 MPa due to the compressive load above. ULTEM 9085 has a vertical compressive and tensile yield stress of 87 MPa and 33 MPa respectively, therefore the stress-induced is approximately 30% of its lowest yield strength.

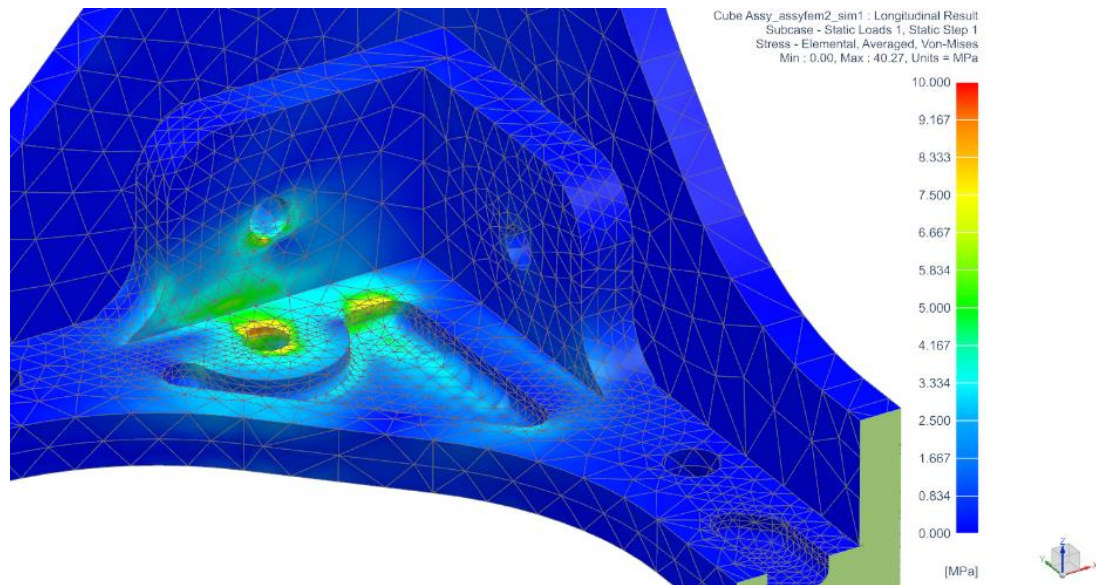


**Figure 6-33: Maximum stress in ULTEM under longitudinal loading**

### 6.1.7.2.3. Lateral Analysis

For the lateral analysis, the overall induced stress was found to be lower than that of the longitudinal analysis. This was since under lateral loading the structure was not subjected to loading of the additional two CubeSats. This resulted in a maximum Von Mises stress of 14.15MPa as can be seen in Figure 6-34 below.

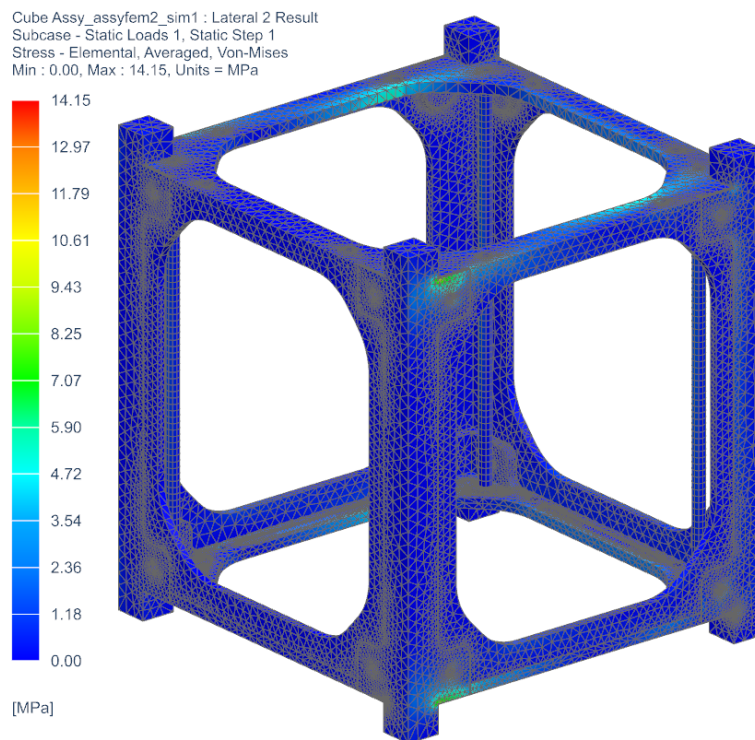


**Figure 6-34: Von Mises stress under lateral loading**

The maximum deflection for the lateral analysis was found to be approximately 0.272 mm of compression along the y-axis. This resulted in an expansion along the x-axis of approximately 0.14 mm on each side of the structure. These deflections can be seen in Figure 6-35.

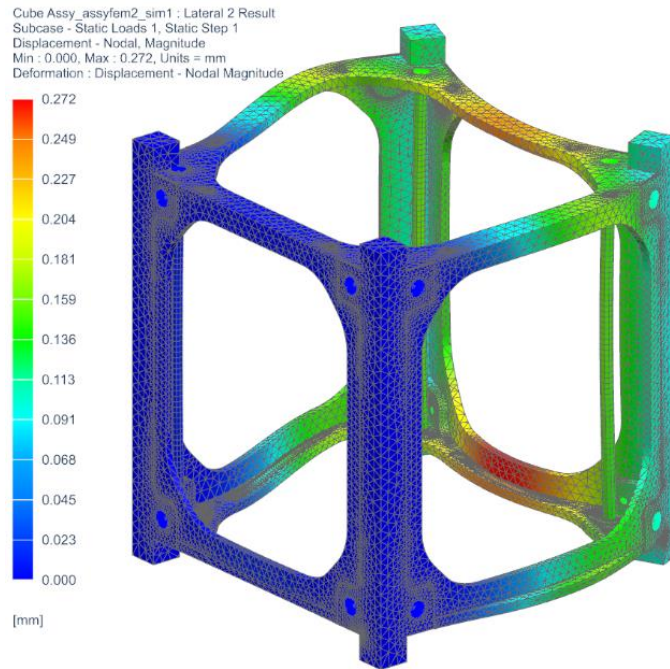


**Figure 6-35: Deflection under Later loading**

The maximum stress again was found in the rail of the structure, again concentrated around the base flange of the rail as can be seen in Figure 6-36. This time only displaying 14.15 MPa which is only 5% of the rail's yield strength.

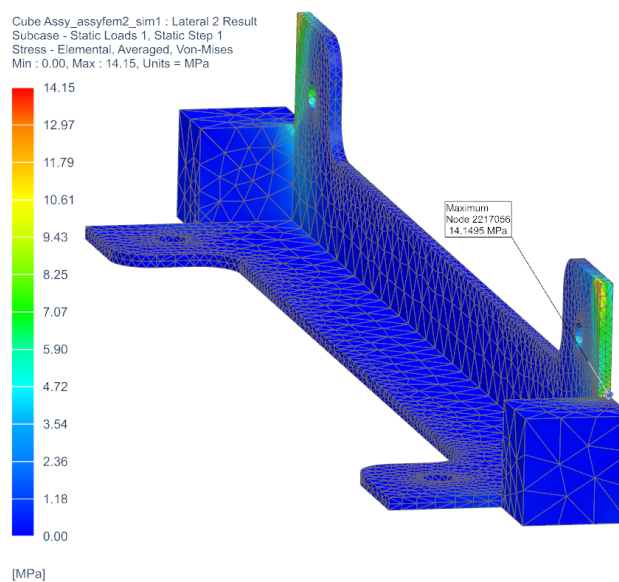


**Figure 6-36: Stress concentration for lateral loading**

For the ULTEM shell, the maximum induced stress was approximately 7 MPa concentrated in the base of the structure as can be seen in Figure 6-37. This time approximately 22% of its yield strength.

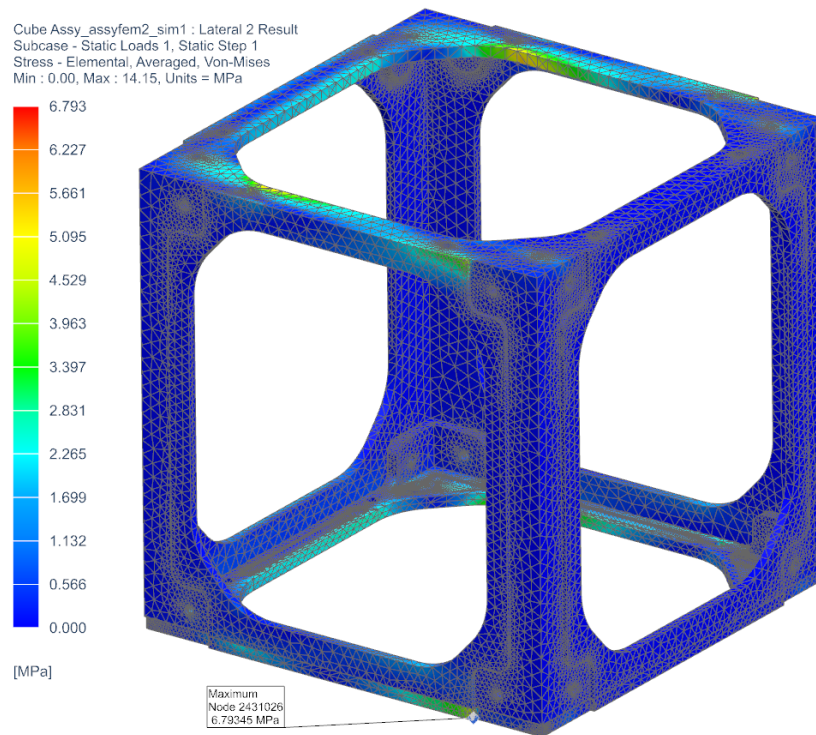


**Figure 6-37: Maximum stress in ULTEM under lateral loading**

#### 6.1.7.2.4. Harmonic Modal Analysis

For the harmonic modal, the first 10 natural harmonic modes for the structure were found to range from 190 through to 411 Hz. With the first four being 193, 235, 243 and 249 Hz. Figure 6-38 shows these first four modes.

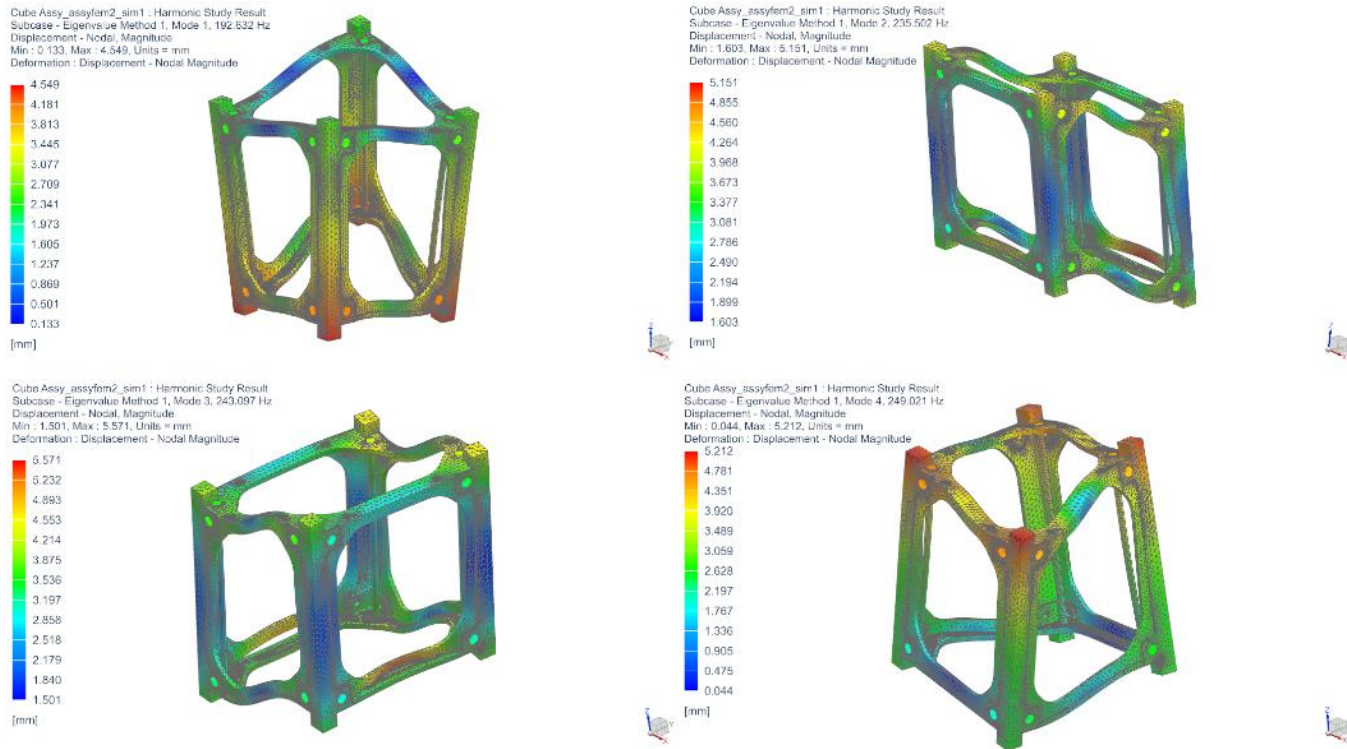


**Figure 6-38: First four harmonic modes**

#### 6.1.7.2.5. Pumpkin 1U Analysis

The COTS Pumpkin structure displayed a maximum induced stress of 33 MPa as can be seen in Figure 6-39 and Figure 6-40. This stress was concentrated in the small gap between the surfaces of the structure. The deflection induced in the structure was found to be very similar to that induced in the ULTEM structure of 0.07 mm as can be seen in Figure 6-41.

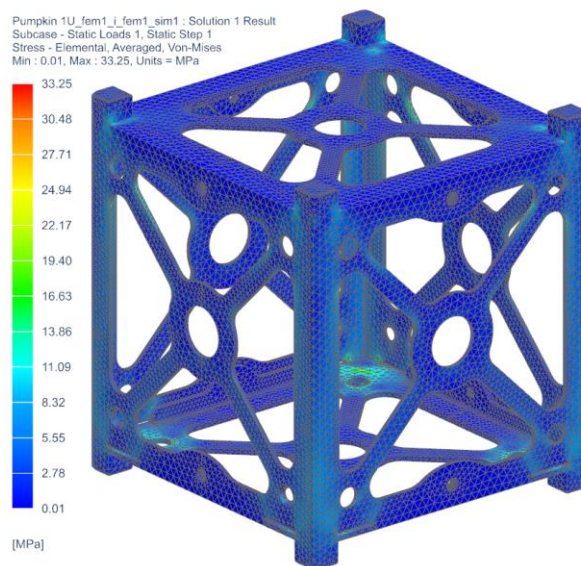


**Figure 6-39: Von Mises stress for Pumpkin structure**

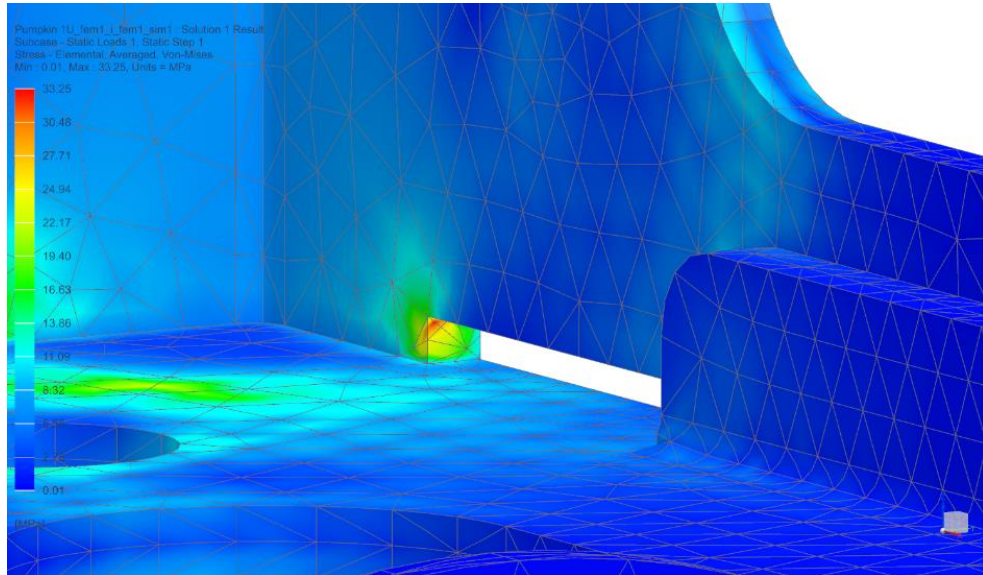


**Figure 6-40: Stress concentration in Pumpkin structure**

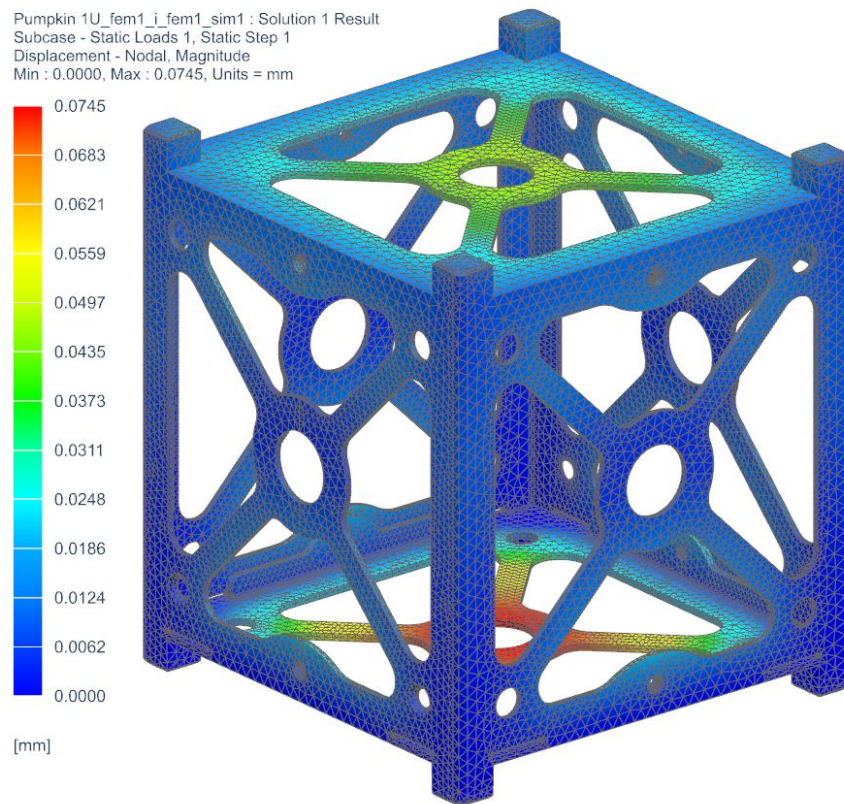


**Figure 6-41: Deflection in Pumpkin structure**



### 6.1.7.1. Finite Element Analysis Discussion

#### 6.1.7.1.1. Concept 3 Analysis

In the previous section, the results of the different analyses were shown. First, the Concept 3 structure was Analysed to identify if it was structurally qualified for use. The results of the analysis were displayed in Section 6.1.7.2.1 which showed maximum stress of approximately 25 MPa and a deflection of 0.16mm. It can be seen that the majority of the deflection was in the diagonal sections of the top and bottom face. It is also clear that there was very little induced stress in the ULTEM structure itself.

At this point, the structure weighed approximately 100 grams. The results showed that more material could be removed, and the structure could be further optimised for weight reduction and ease of access. The structure was then modified to further reduce material and create more space within the structure. The details of these changes are discussed further in the following section, Section 6.1.8.1. Once these changes were made reducing the overall weight by 10% down to 90 grams, the structure was re-Analysed to verify the structure's strength once more.

#### 6.1.7.1.2. Final Design – Longitudinal and Lateral Analysis

The final ULTEM structure was studied in its longitudinal axis, then it's lateral and finally, the harmonic modal analysis was done. For the longitudinal analysis, the maximum induced stress was approximately 40MPa which was situated in the rails resulting in about 15% of the aluminium's yield stress. The ULTEM itself experienced approximately 10 MPa of stress, 30% of its yield.

The longitudinal loading resulted in induced stress, which was much greater than that of the lateral, 40 MPa compared to 14 MPa, this was due to the fact that the loading of the additional two CubeSats above the ULTEM structure was neglected in the lateral direction. While this configuration resulted in a higher overall stress, this stress was located in the aluminium rails with the ULTEM only experiencing about 7 MPa of stress.

This being said, the lateral loading resulted in a higher deflection of about 0.27 mm. This was due to the orientation of the structure. In the longitudinal axis, the loading is supported primarily in the rails, however, under lateral loading, most of the loading is supported by the ULTEM shell. When comparing modulus of elasticity, aluminium 6061 has approximately 69 GPa compared to the ULTEM of about 2 GPa. This means that for the same amount of loading, ULTEM will have a significantly higher deflection. It should be noted however that with the structure fully stacked with the components and payloads, the overall structural rigidity will increase, thus lowering the overall deflection.

#### 6.1.7.1.3. Final Design - Harmonic Mode Analysis

For the harmonic mode analysis, the goal was for the structure's natural harmonic modes to be outside of the launch vibration loading range and to be greater than that of the natural harmonic frequency of the launch vehicle. In Section 3.2.1, it was discussed that the vibrations range up to 100 Hz and the highest natural harmonic frequency of a launch vehicle was 45 Hz. Therefore, for the ULTEM structure to qualify after vibration analysis, the lowest frequency mode must be above 45 Hz. If it fell within the range of 45 and 100 Hz, an additional analysis of an inducing a sine vibration ranging from 5 to 100 Hz would need to be run to check the results of the structure vibrating within that range. For the ULTEM shell, however, the lowest harmonic mode was found to be 193 Hz, well outside of the excitation range and therefore achieved the goal of the harmonic mode analysis.

Analysing the structure using FEA allowed for the qualification of the structure with respect to the structural loading. By running static loading analysis in various orientations as well as vibrational analysis, the structure was not only qualified under loading with a factor of safety of 4 but also allowed for geometry optimisation. This further reduced the weight of the structure as well as improving the ease of access, assembly, and integration of the structure.

### 6.1.8. Final Design Discussion

#### 6.1.8.1. Optimisation

Once finite element analysis was conducted on the structure as could be seen in Section 6.1.7.2.1, the design was then further optimised by removing additional material for weight reduction and ease of access.

The aluminium rails of the structure showed to hold most of the structural loading on the structure as they are in contact with the PPOD and other CubeSats. This meant that the side of the structure shell can have as little material as possible while keeping the shell rigid. The diagonal sections of the side of the structure could be removed, see Figure 6-42.

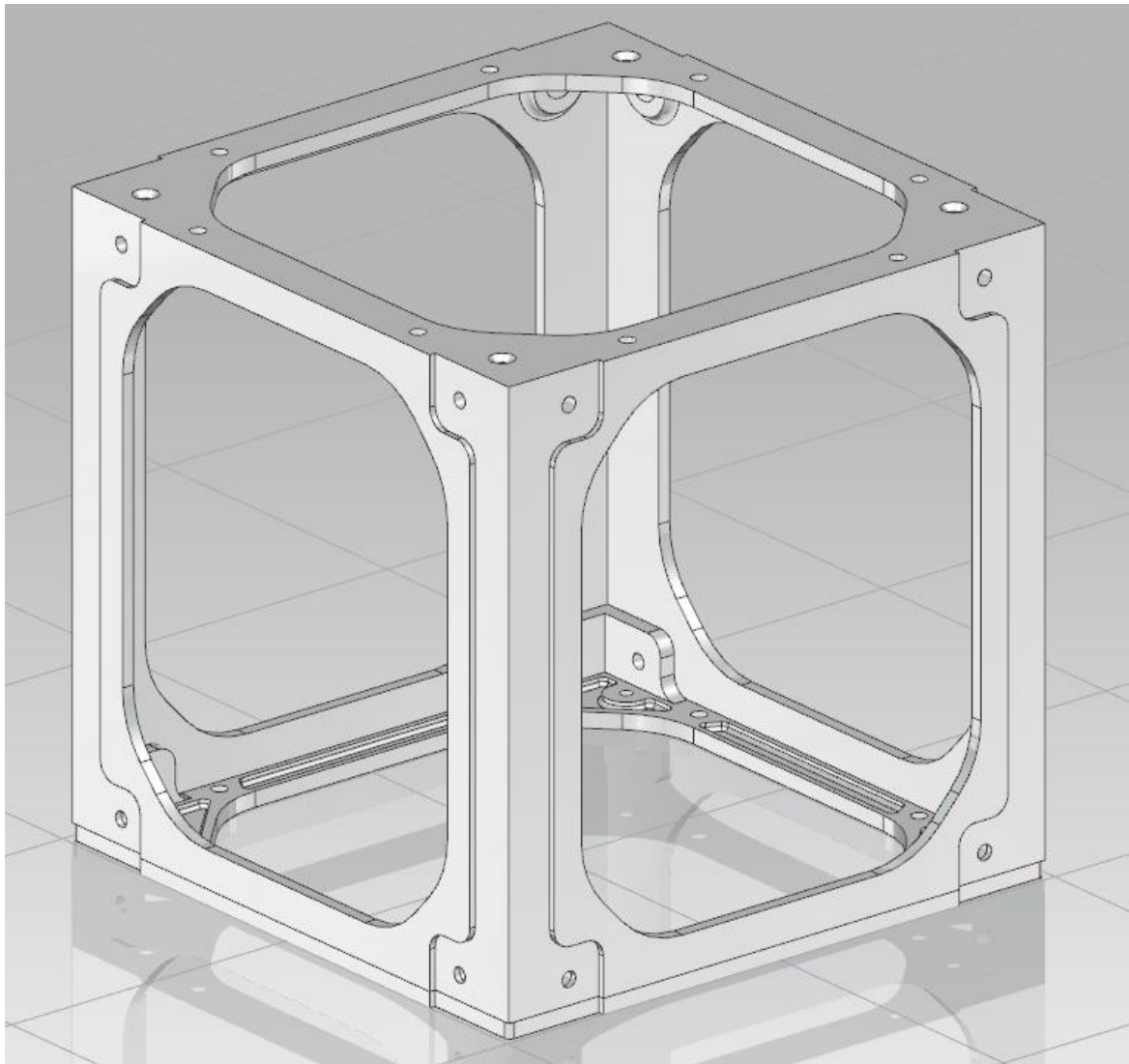


**Figure 6-42: Final design shell**

The structure shell thickness was set to 2.5 mm to fit the M2.5 helical inserts which were 2.5 mm long. Further material, however, was removed in the base and lid of the structure as seen in Figure 6-43 after analysing the FEA results seen in Section 6.1.7.1.2.

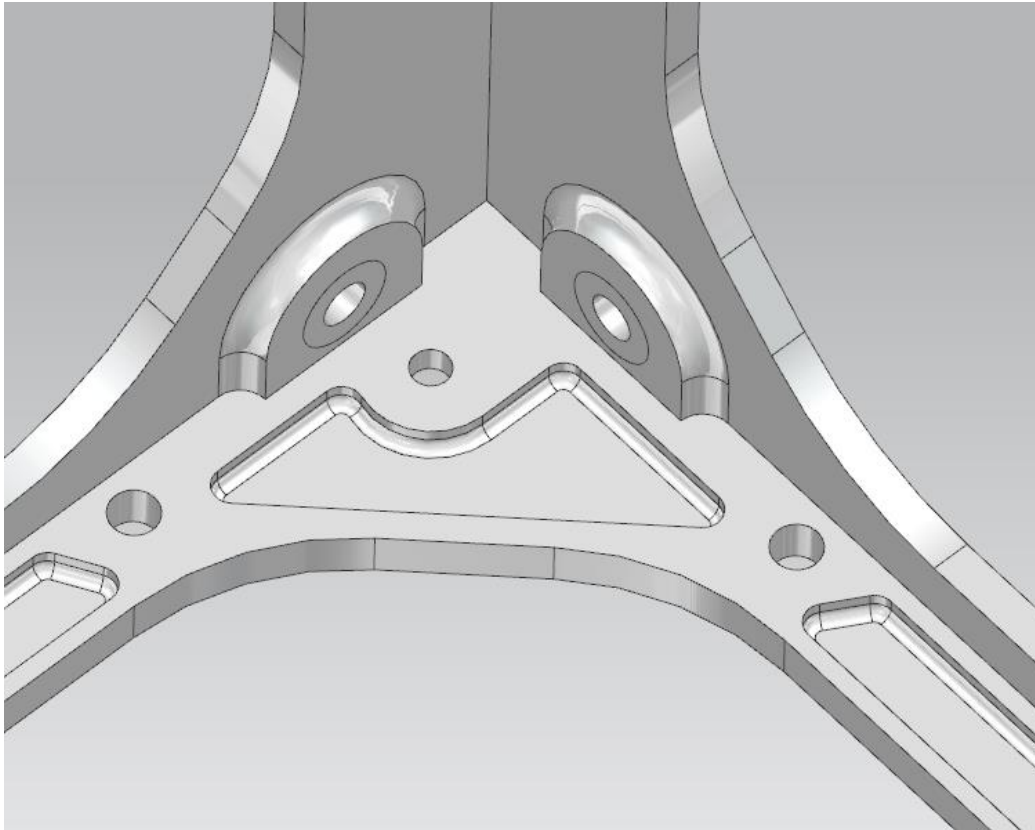


**Figure 6-43: Weight reduction in base and lid**

As discussed in Section 6.1.4.1.3, helical inserts were qualified for use in the structure, therefore changes were made to accommodate for this. This method was a great improvement over the use of inserting nuts in Concept 3. This integrating of the helical inserts over inserting nuts was a much similar process and allowed for less required material around the insert.

The structure was also optimised for 3D printing as the main shell would be impossible to print using conventional subtractive manufacturing methods. Thanks to the ability of printing support material, it would be possible to print a complete shell with open panels. The weight reduction sections in the base and the lid of the shell are also simple for 3D printing and do not require complicated tool changes and cutting paths like that of subtractive manufacturing.

#### 6.1.8.2. Discussion of Design

The core of the structure of the CubeSat consists of only 6 different parts (excluding fasteners, rods and solar panels). This reduces the number of parts from 10 to 6 when comparing to COTS structures such as the Clyde Space structure. This reduces the chance of components vibrating during launch, it reduces

the difficulty and time required to assemble the structure as well as reduces the manufacturing time for the structure. In Figure 6-44, an exploded view of the entire structure with Clyde Space solar panels and PC104 PC boards can be seen.

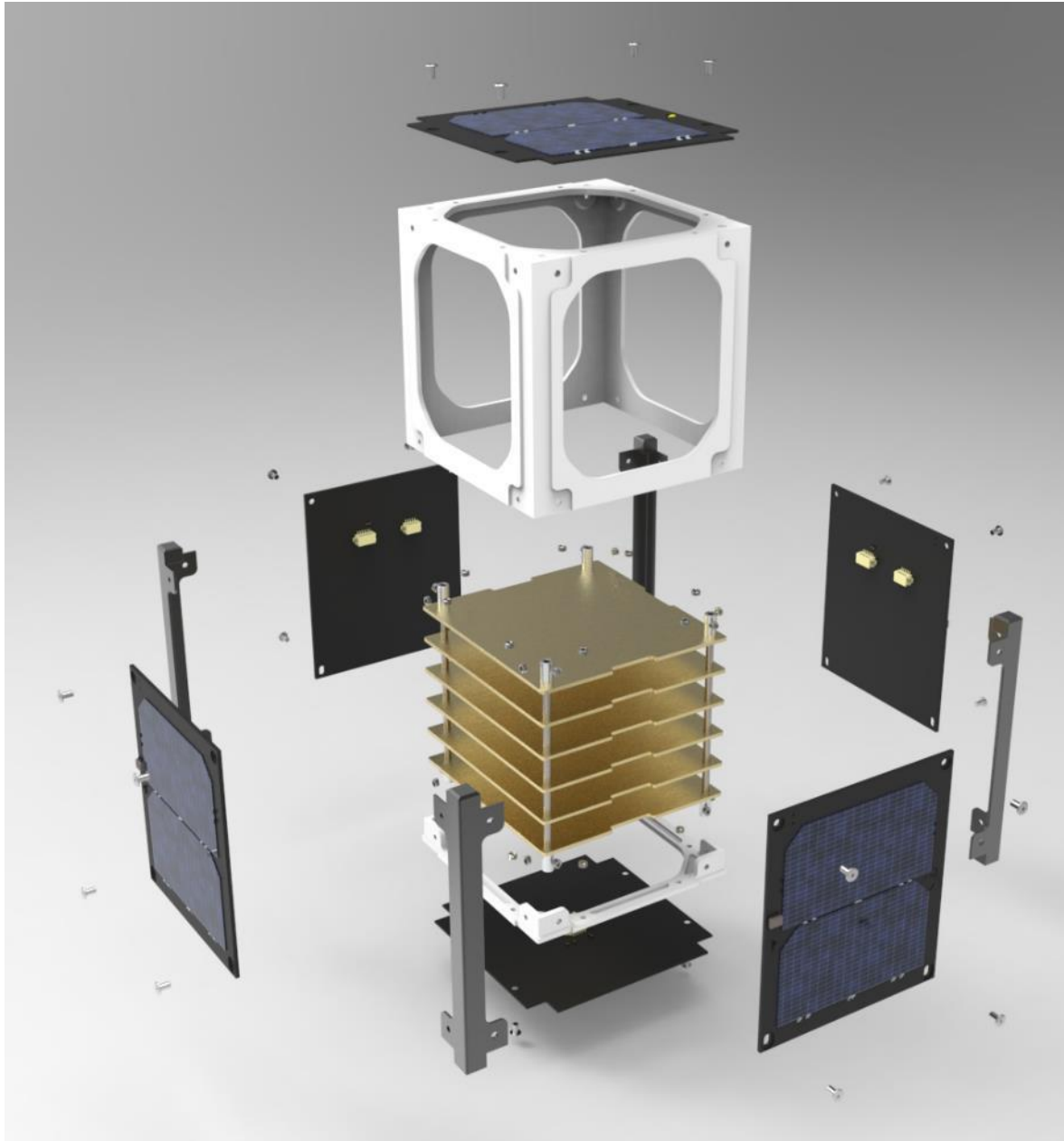


**Figure 6-44: Final design exploded view**

The core of the structure consists of an ULTEM base, a ULTEM shell, and the four aluminium rails. This significantly simplifies the integration and assembly of the components and payloads of the structure.

The final design of the structure resulted in the main core of the structure weighing approximately 81 grams. This consisted of the base, shell, rails and 16 fasteners and helical inserts to hold the structure together. Adding the rods and their fasteners increase the mass to 95 grams. The detailed mass properties

can be found in Appendix B. The final 8 fasteners and helical inserts are on the top and bottom surfaces for fastening solar panels to the structure so are optional. In Figure 6-45 below, a comparison between the ULTEM structure and COTS structure masses can be seen. It can be seen that the ULTEM structure has about a 15.3 gram (14%) weight saving over the next lightest COTS structure of ISIS and a 60.3 gram (39%) weight saving over the Clyde Space structure.

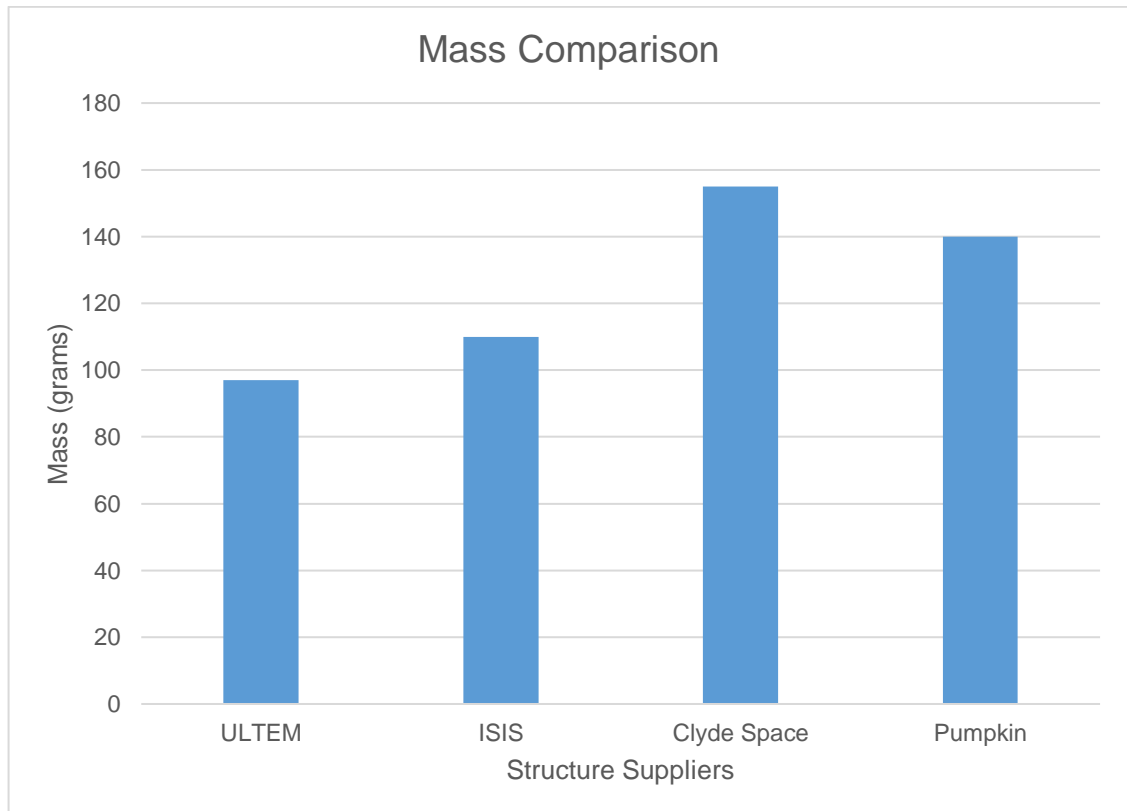


**Figure 6-45: Mass comparison structures**

In Figure 6-46, the ULTEM base, with mounting rods and spacers can be seen. The CubeSat components can now be easily slid down the mounting rods and onto the aluminium spacers. These spacers are to ensure that the PC boards are supported evenly throughout the structure and the bottom PC board does not sit on the base flanges.

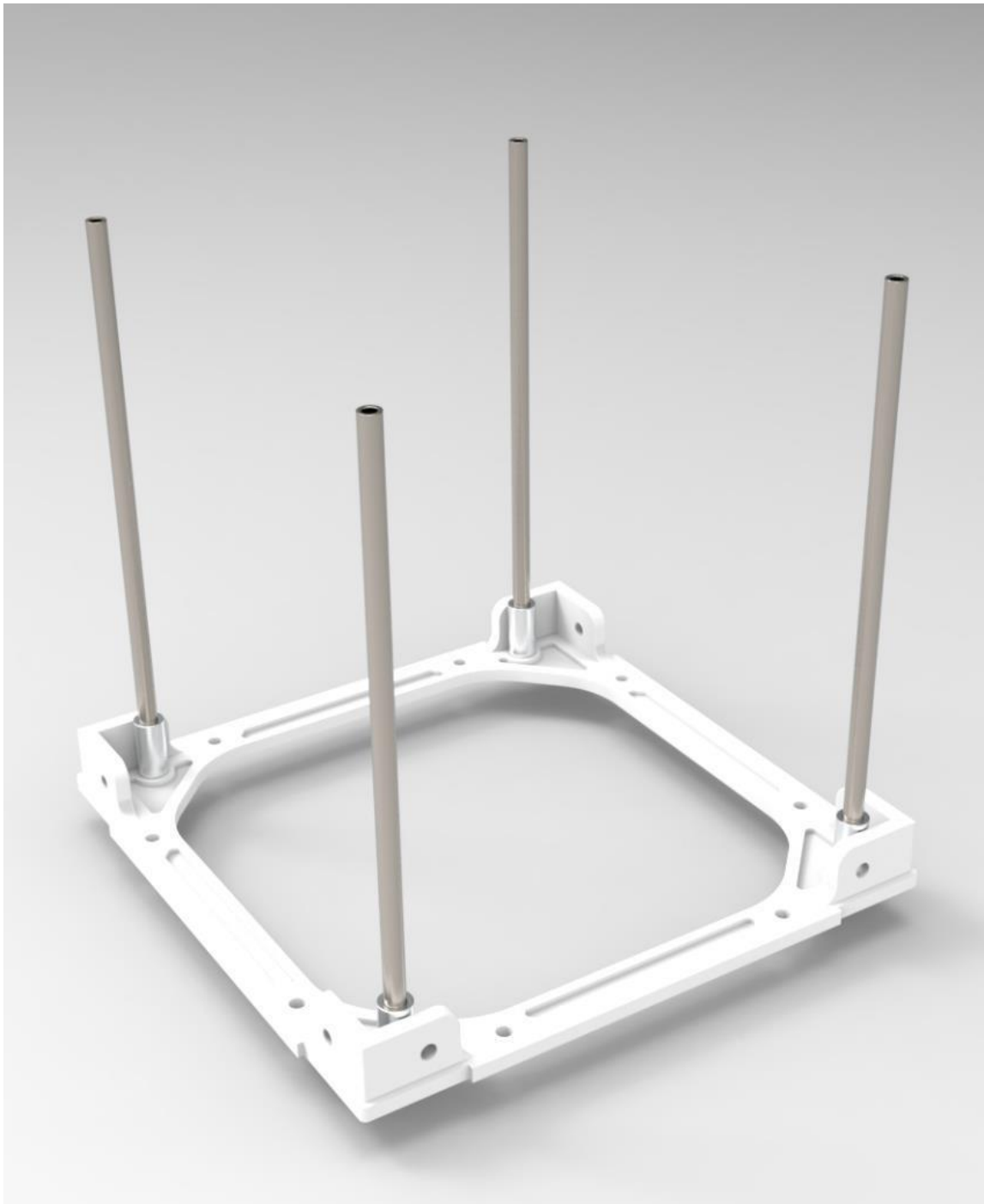


**Figure 6-46: Final design base with rods**

The components can then be stacked upon one another with ease as can be seen in Figure 6-47. Depending on the depth of the component, spacers are stacked between the components (not imaged), again to balance the loading.

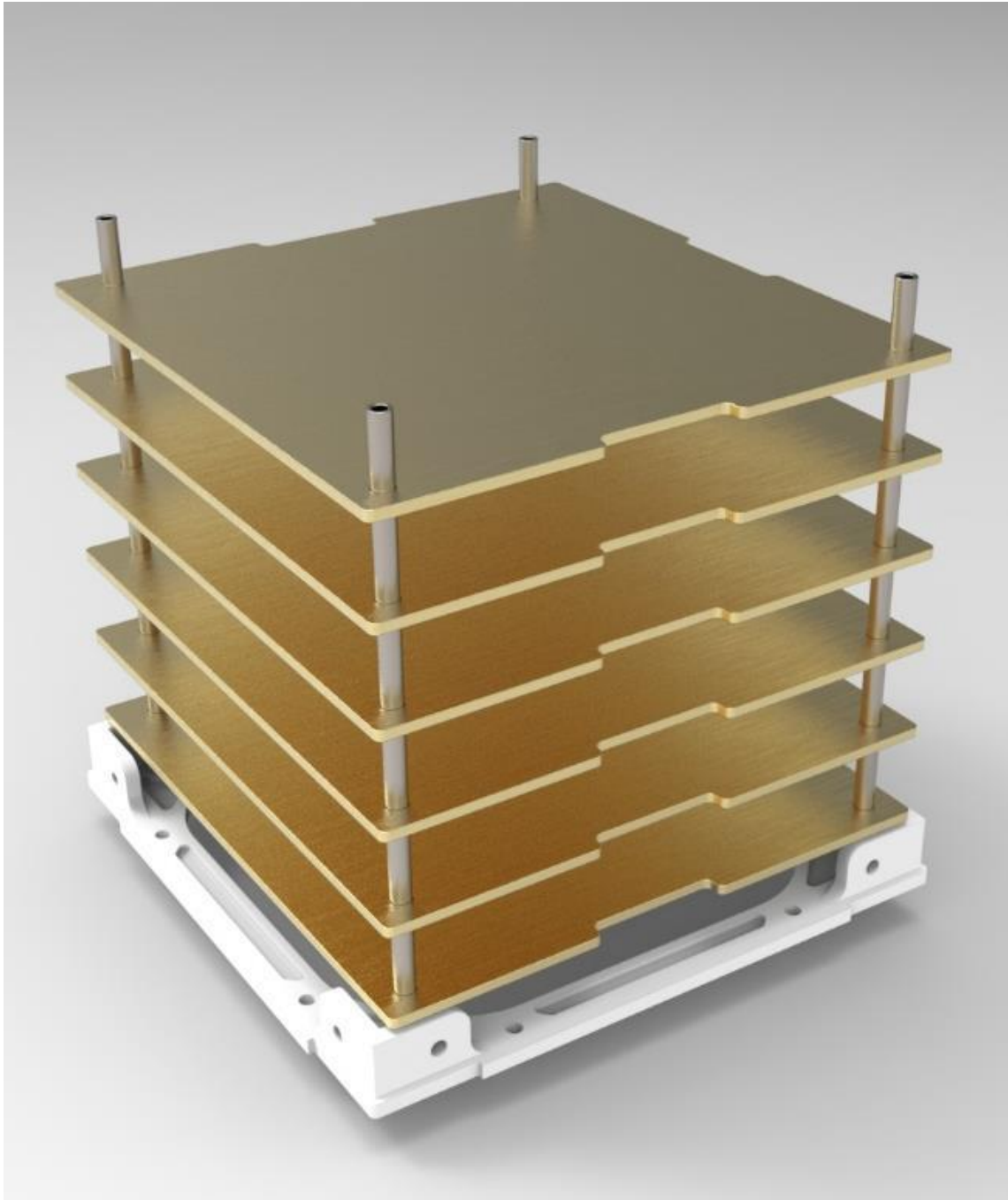


**Figure 6-47: Final design PCB stacking**



Once the CubeSat has been stacked, the shell can be placed over the components. As can be seen in Figure 6-48, once the shell has been placed, it is still very easy to access the components to direct wiring looms and connectors, etc.

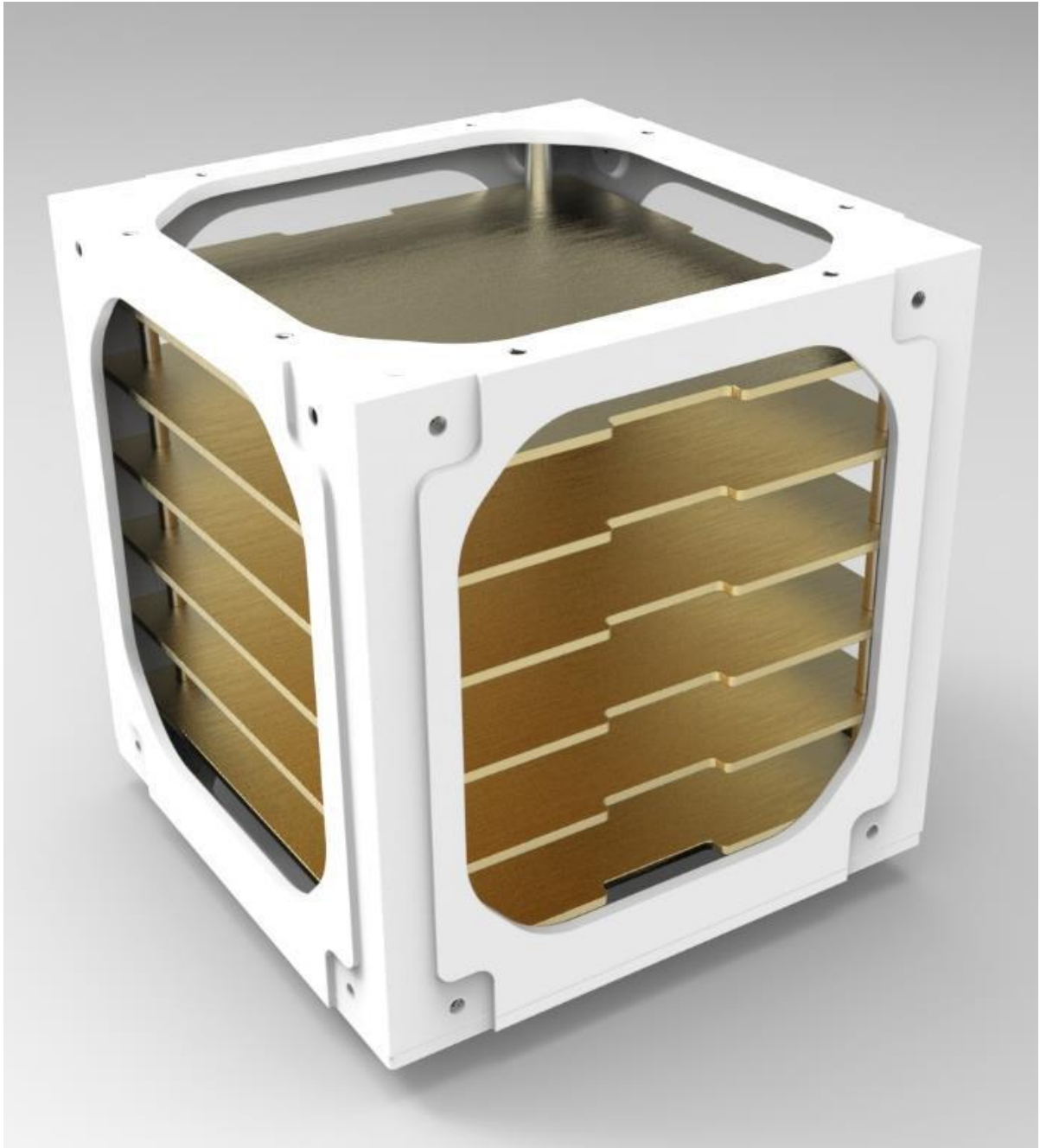


**Figure 6-48: Final design shell mounted**

The four rails can then be mount on the edges of the structure as seen in Figure 6-49.

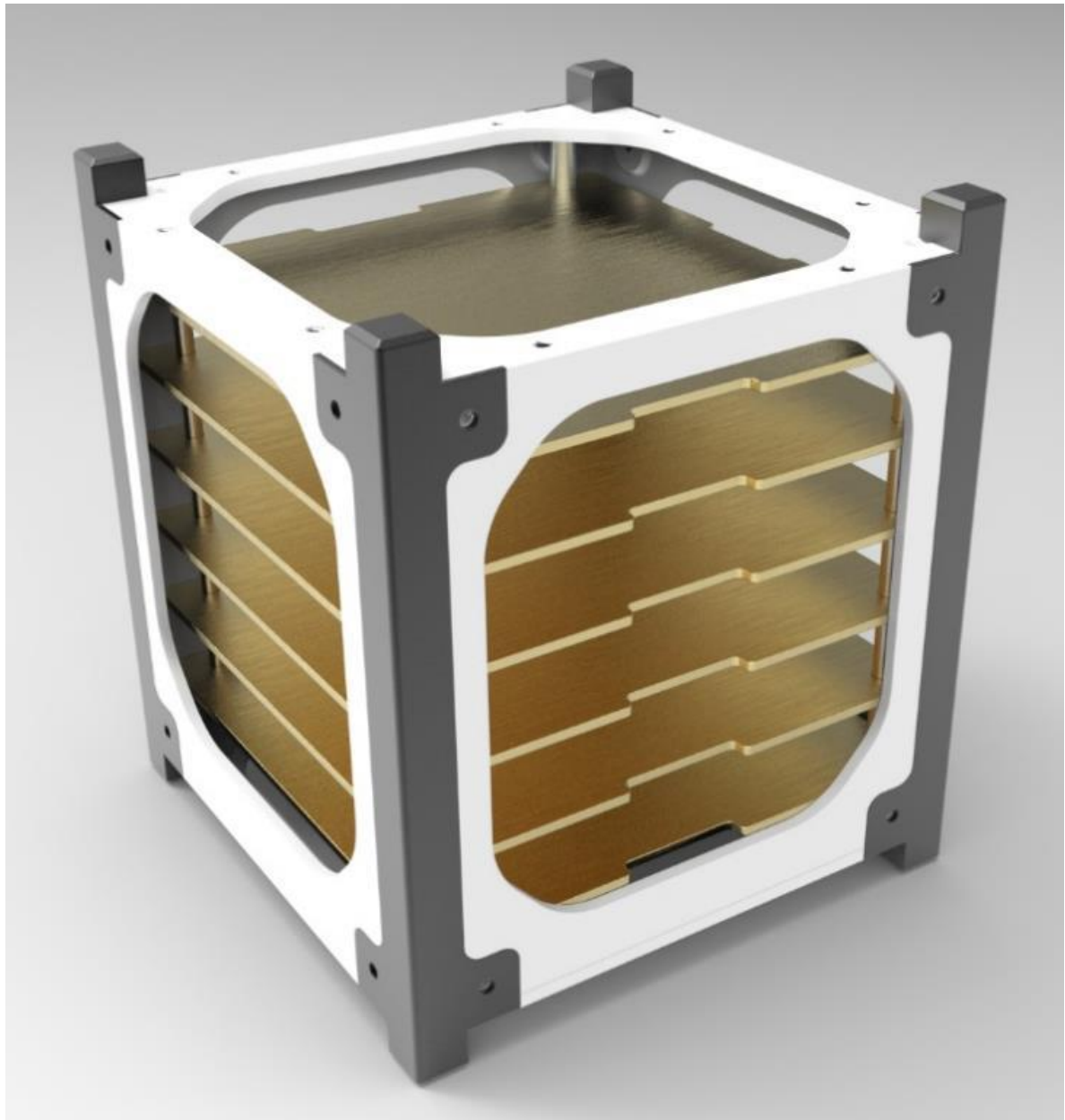


**Figure 6-49: Final design rails mounted**

The solar panels can then be connected and fastened onto the structure, completing the assembly of the structure as seen in Figure 6-50.

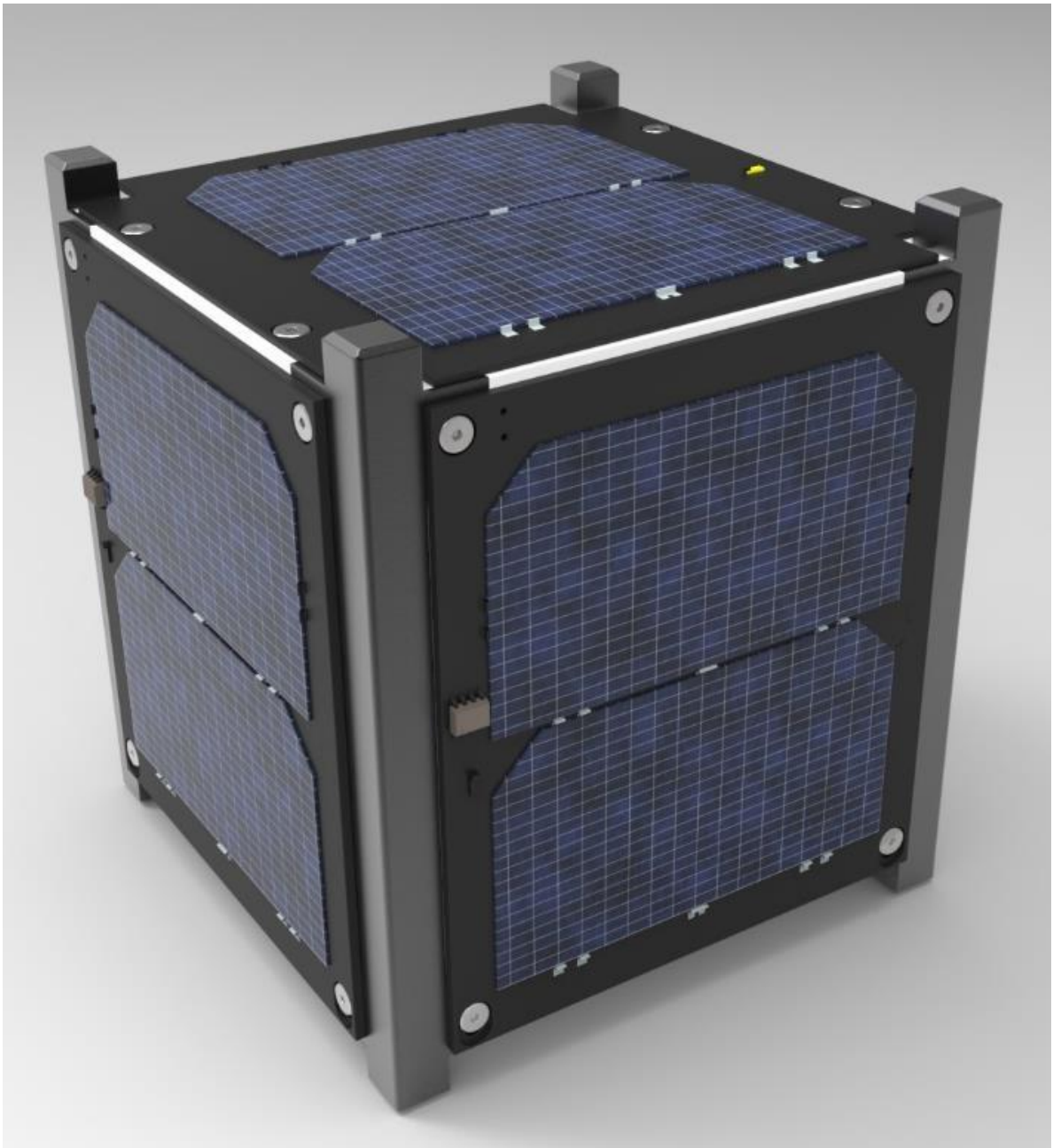


**Figure 6-50: Final design assembled**

### 6.1.9. Manufacturing

Due to insufficient funding, a structure could not be manufactured for this research. The following section, however, discussed the procedure that would have been followed for the manufacturing of the CubeSat structure.

#### 6.1.9.1. ULTEM Structure

The ULTEM 9085 structure could be manufactured at CPU T's manufacturing lab using their Stratasys Fortus 400mc 3D printer seen in Figure 6-51 below. This printer is reputable as a commercial-grade 3D printer as is widely used around the world. First, the printer is set up for printing using ULTEM 9085. This requires the printer to a T16 tip which produces a slice height of 0.254 mm. The support material must also be loaded for the print. The support material for ULTEM is called ULT\_S and is the breakout type support material.



**Figure 6-51: Fortus 400mc 3D printer**

Once the printer had been set up, the geometry of the models could be imported into the slicing software to generate the code for the 3D printer to print the parts. Fortus uses a slicing software named Insight to generate the code for the printer. A free slicing software called Repitier Host was used to set up a dummy slice of the geometry as seen in the Figures below.

First, the model is imported into the software as an .STL file as seen in Figure 6-52. It is important then to orientate the part keeping in mind that the orientation determines the ease of printing the structure as well as the strength of the structure.

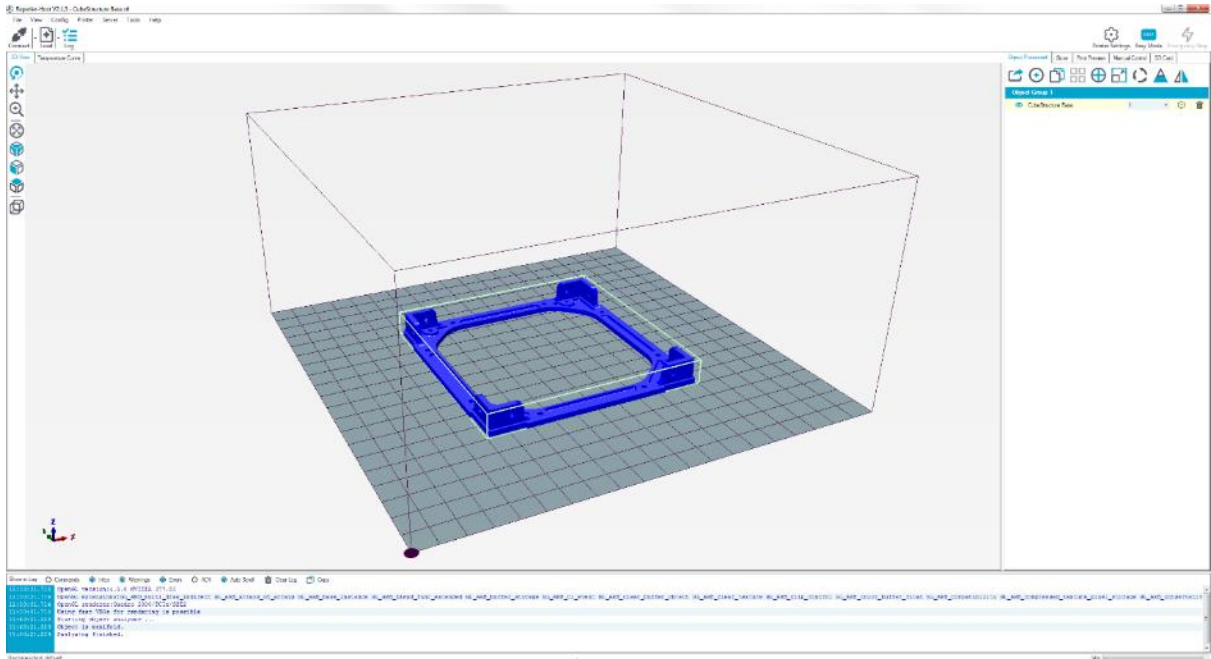


**Figure 6-52: STL import into Repitier Host**

The model is then sliced using a layer height of 0.25 mm. Figure 6-53 below shows the first layer of the print. It can be seen how the standard infill setting of 45° infill raster orientation is used. The second layer will then infill in the opposite direction. This allows for the material to have partial isotropy along the horizontal plane.

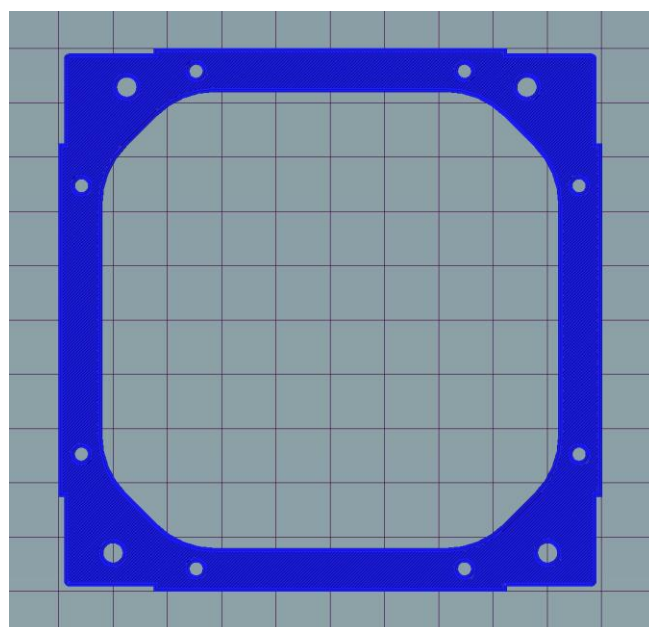


**Figure 6-53: Layer 1 of sliced 3D Print**

In Figure 6-54 below, a close-up view showing the sliced detail of the layers of filament for the part can be seen.

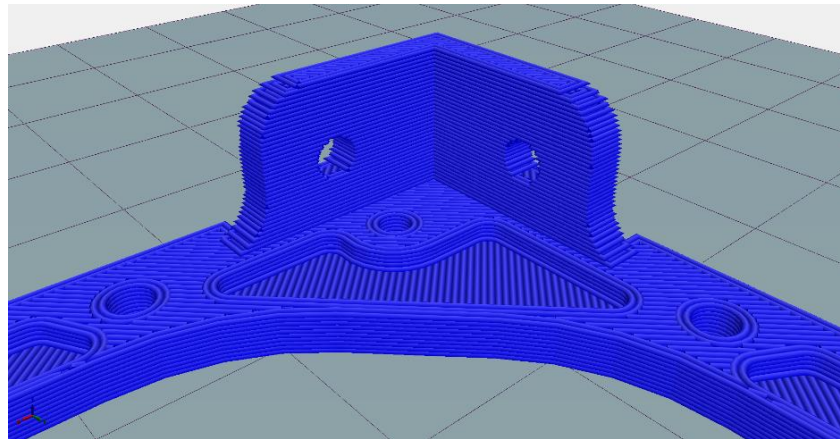


**Figure 6-54: Sliced 3D model**

The second ULTEM part to be printed would be the shell. For the shell, the print is much larger and has areas that overhang and therefore require a support structure. The entire sliced model can be seen in Figure 6-55 below.

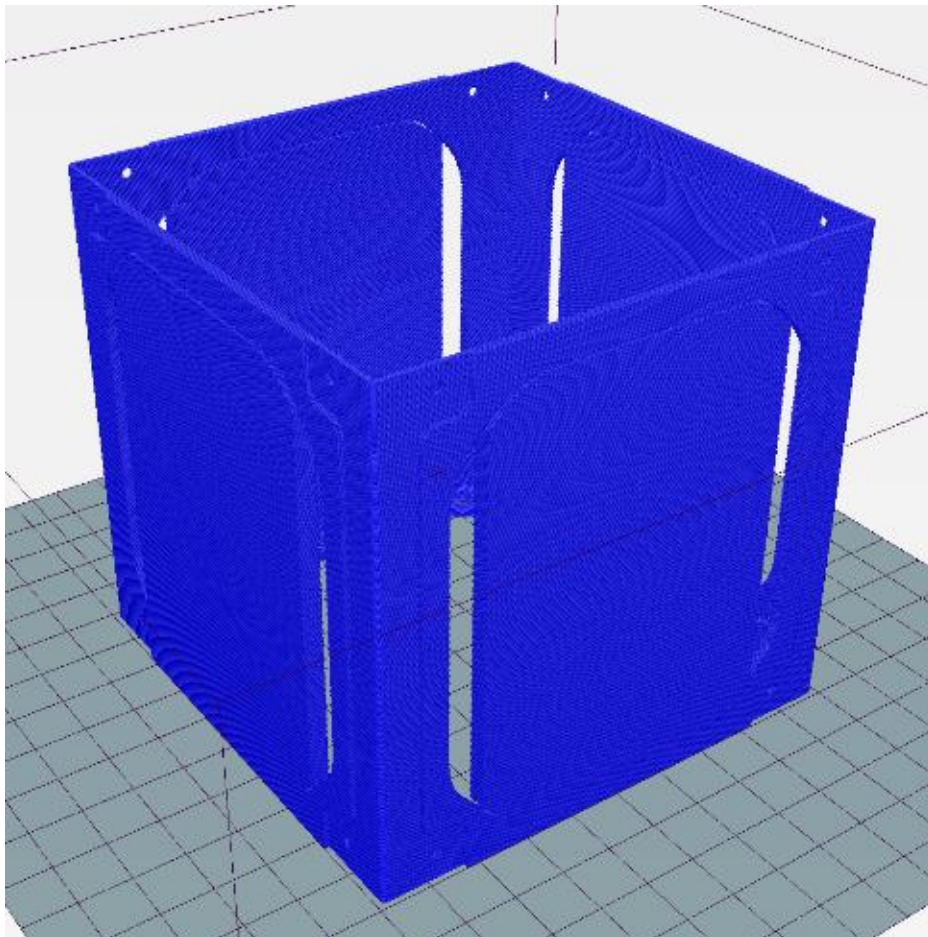


**Figure 6-55: Sliced ULTEM shell**

In Figure 6-56 below, the sliced shell can be seen up to layer 150. It can be seen how the support structure is being generated to support the top region of the shell. This support structure is easily broken out later once the 3D print has been completed.

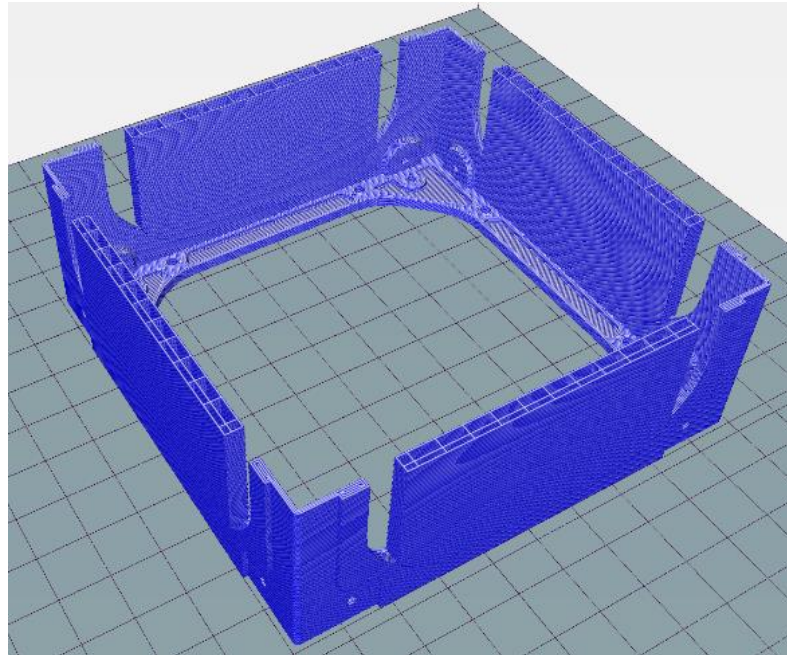


**Figure 6-56: Sliced ULTEM shell up to layer 150**

The estimated total printing time for both parts is approximately 5 hours with a total filament length of approximately 24.5 m used as can be seen in Table 6-3. These estimations were based on a layer height of 0.25 mm at a print speed of 50 mm/min with 100% infill density. The print time would, however, be different for various 3D printers.

**Table 6-3: 3D printing build details**

	<b>Filament used</b>	<b>Estimated printing time</b>
ULTEM Base	4.811 m	54 min
ULTEM Shell	19.637 m	3h,53 min
<b>Total</b>	<b>24.448 m</b>	<b>4h, 47 min</b>

#### 6.1.9.2. Aluminium Rails

The aluminium rails could also be manufactured at the university’s manufacturing lab making use of the 5-axis CNC milling machine. These rails would be manufactured out of aluminium 6082 T6 and then sent for anodizing. Anodizing could be done by Cape Anodizing once the parts had been machined. It should be noted that South Africa only supplies aluminium 6082 T6 and not 6061 so costing has been done based on the supply of 6082 T6 aluminium. The stock size required per rail is 114x17.5 mm excluding the clamping area.

### 6.1.9.3. Fasteners and Others

M2.5x5 Ultra-low-profile socket screws, like shown in Figure 6-57, and M2.5x2.5 helical inserts would be used for fastening the structure together. M2x5 countersunk socket screws would be used for the fastening of the rods within the structure. The titanium rods would be supplied by SAETRA Ltd and the fasteners could be supplied by any local fasteners store. The rods ends would have their threads tapped using a lathe to ensure alignment of the thread.



**Figure 6-57: Ultra-low profile screws**

### 6.1.9.4. Bill of Materials and Costing

In Table 6-4 below the bill of materials for the entire structure and the manufacturing/supply cost can be seen. The costs of all the components are based on industry quotes acquired in 2017 from around South Africa. It should be noted that these costs would be significantly lower if manufactured in-house.

**Table 6-4: Bill of Materials**

Description	Material	Mass	Number of	Cost
ULTEM Base	ULTEM 9085	12.1 grams	1	R13,400 (\$868)
ULTEM Shell	ULTEM 9085	36.5 grams	1	
Aluminium Rails	Aluminium 6082 T6	6.7 grams (each) 26.8 grams (total)	4	R2,800 (\$181)
M2.5x5 Ultra-Low Socket screws	Stainless Steel	0.2 grams (each) 4.8 grams (total)	24	R100 (\$6)
M2x5 countersunk socket screws	Stainless Steel	0.2 grams (each) 1.6 grams (total)	8	



M2.5x2.5 Helical Inserts	Stainless Steel	0.14 grams (each) 3.36 grams (total)	24	
Rods	Titanium	2.4 grams (each) 9.6 grams (total)	4	R700 (\$45)

The core of the structure which consists of the ULTEM Base, Shell and Aluminium rails come to a total mass of 75.34 grams and cost approximately R16,200 (\$1050). The 3D printing of the ULTEM structure was quoted by Adaptronics AMTL, the manufacturing lab at CPUT. The manufacturing of the rails was quoted by Theo Marnewick Engineering cc, the anodizing cost was included in the cost displayed in the table and quoted by Cape Anodizing.

The fasteners were not quoted for but prices were found from online databases and stores while the rods were quoted from SAETRA Ltd and also to be machined by Theo Marnewick Engineering cc. Adding these auxiliary components take the mass to approximately 95 grams and increasing the total cost to R17,000 (\$1100).

#### **6.1.10. Prototype**

To test the fitment of the structure, inserting of helical inserts, and fastening with fasteners, a PLA prototype was 3D printed using the ASIC TronXY X5 SA 3D printer.

##### **6.1.10.1. 3D Printing**

Repetier Host software was used for the slicing of the structure model. The slicer properties were set to a layer height of 0.15 mm, a print speed of 50 mm/s and an infill density of 100%. The printing time to print the base and shell of the structure took a total print time of 7 hours and 35 min with about 20 min spent on post processing.

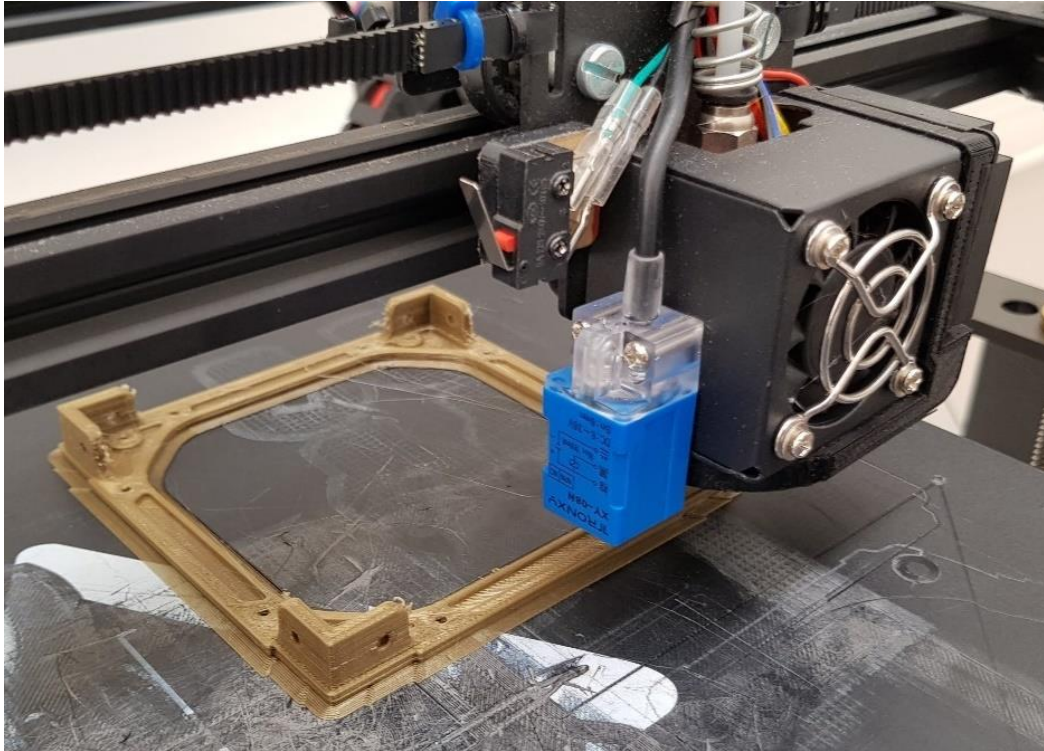


**Figure 6-58: 3D printed prototype base**

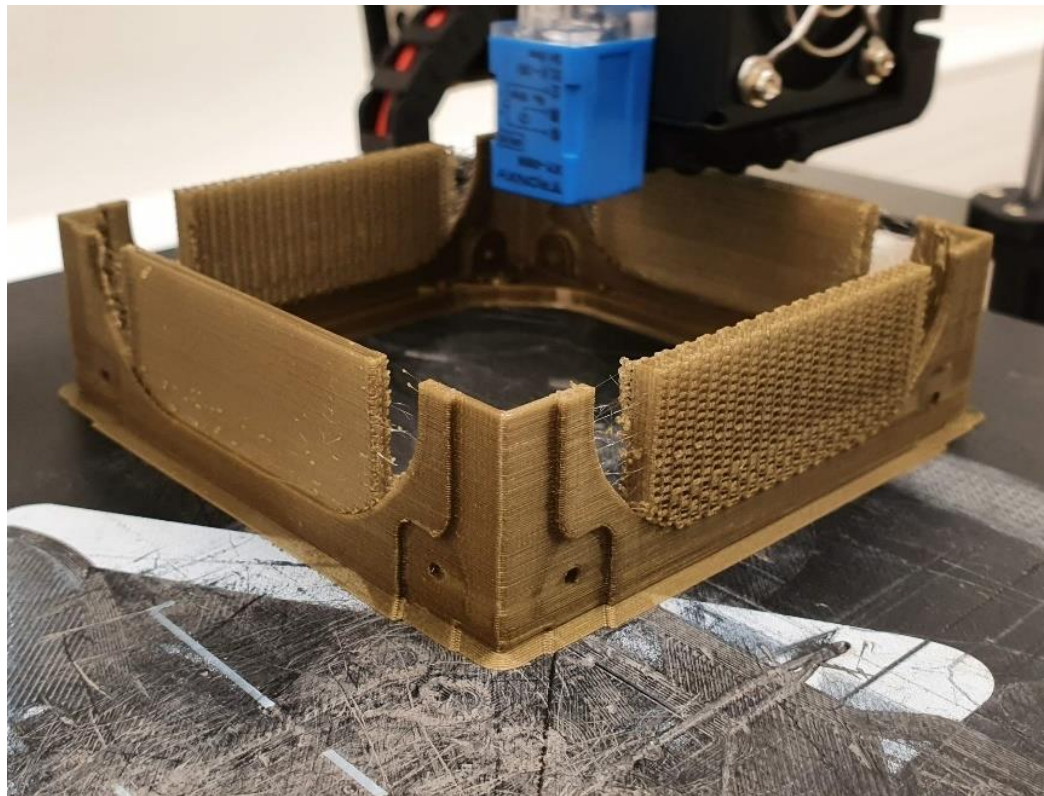


**Figure 6-59: Prototype shell 3D print in progress**

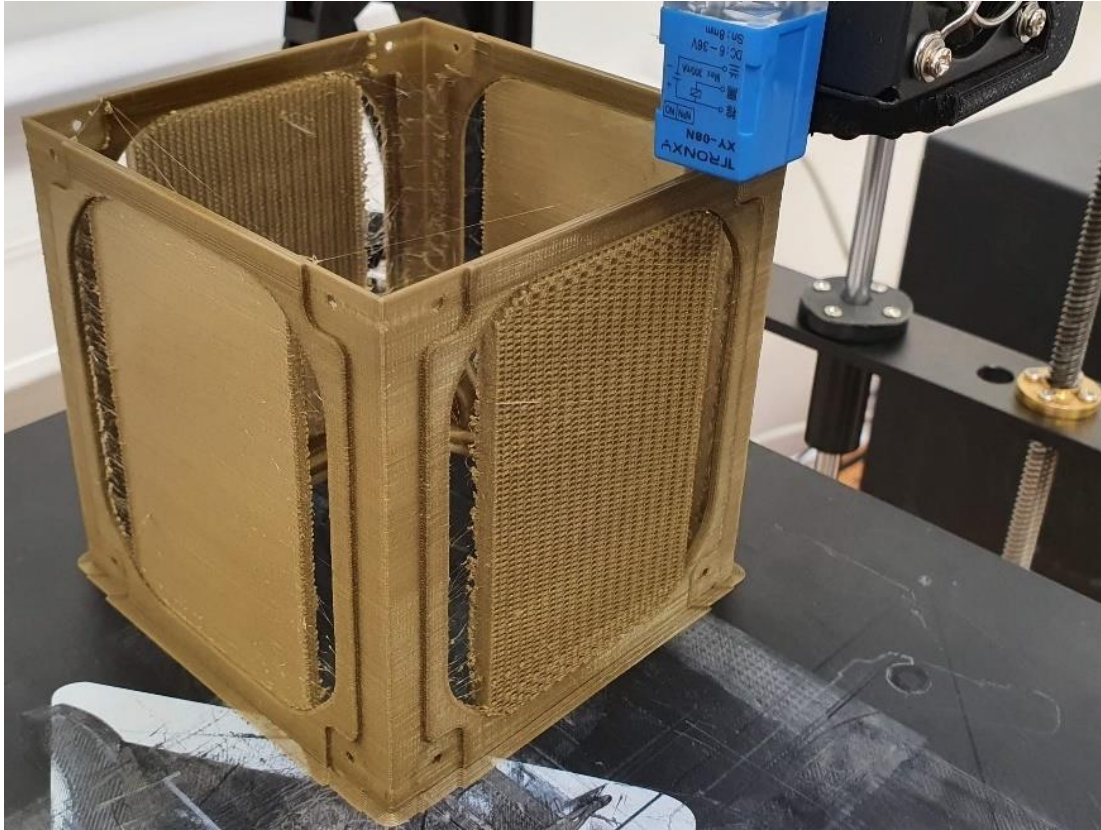


**Figure 6-60: 3D printed prototype shell**

Figure 6-58 shows the completed prototype base cooling before post processing. In Figure 6-59, the print progress can be seen, clearly showing the support material being printed to support the top section of the shell. In Figure 6-60, the completed shell can be seen, showing the effect the support material had. It can be seen how the support material successfully held the top layers of the shell retaining its flat surface. Excessive filament strings can be seen in the final product which could be due to over extrusion due to a filament temperature set too high. While this did not influence the shell itself, it did result in additional time required for post processing.

#### 6.1.10.2. Helical Inserts

Figure 6-61 shows the threaded helical inserts fitted into the prototype structure shell. The process of inserting the helical inserts was easy and completed successfully.

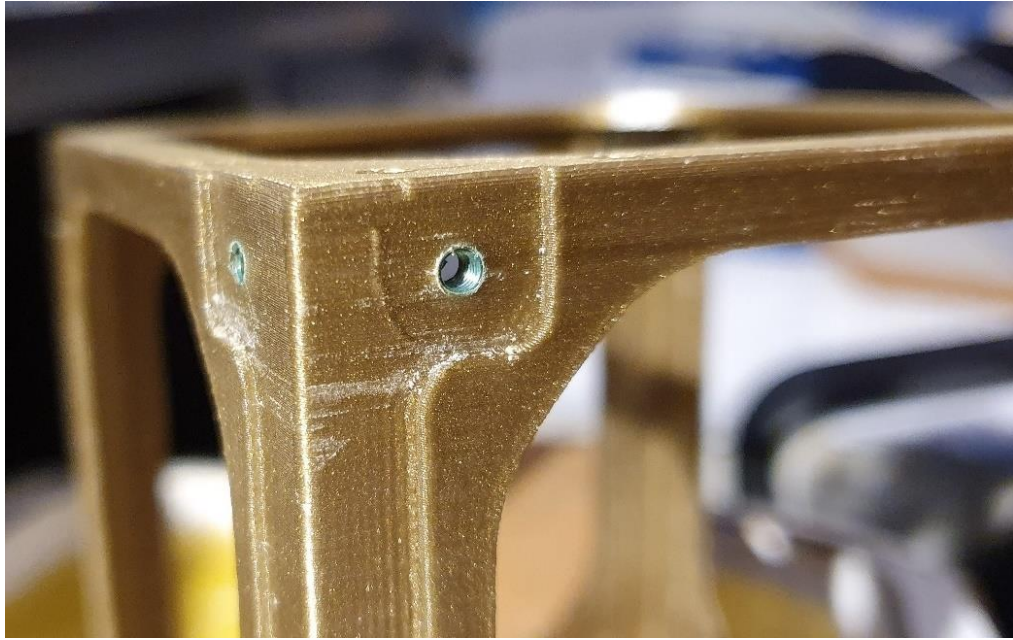


**Figure 6-61: Helical inserts in 3D printed prototype**

The assembled structure prototype can be seen in Figure 6-62 including the rails and fasteners. The rails were 3D printed and not milled out of aluminium due to a lack of budget. The fasteners that were used were M2.5 torx pan head screws. The rods were also excluded due to a lack of budget.

#### 6.1.10.3. Assembly

Assembling the prototype, one issue was encountered due to tolerance issues. With the basic ASIC 3D printer that was used, tolerance for the 3D print cannot be implemented which would require the model itself to have manufacturing tolerances added to the models. This resulted in a very tight fit of the parts, requiring some filing in some places to allow for proper fitment. It should be noted however that while these issues were experienced with the basic ASIC 3D printer, both Fortus 3D printer and CNC mills have tolerance tests and settings which accommodate for manufacturing tolerances to ensure perfect fitment so similar issues should not be experienced using the intended manufacturing machines.

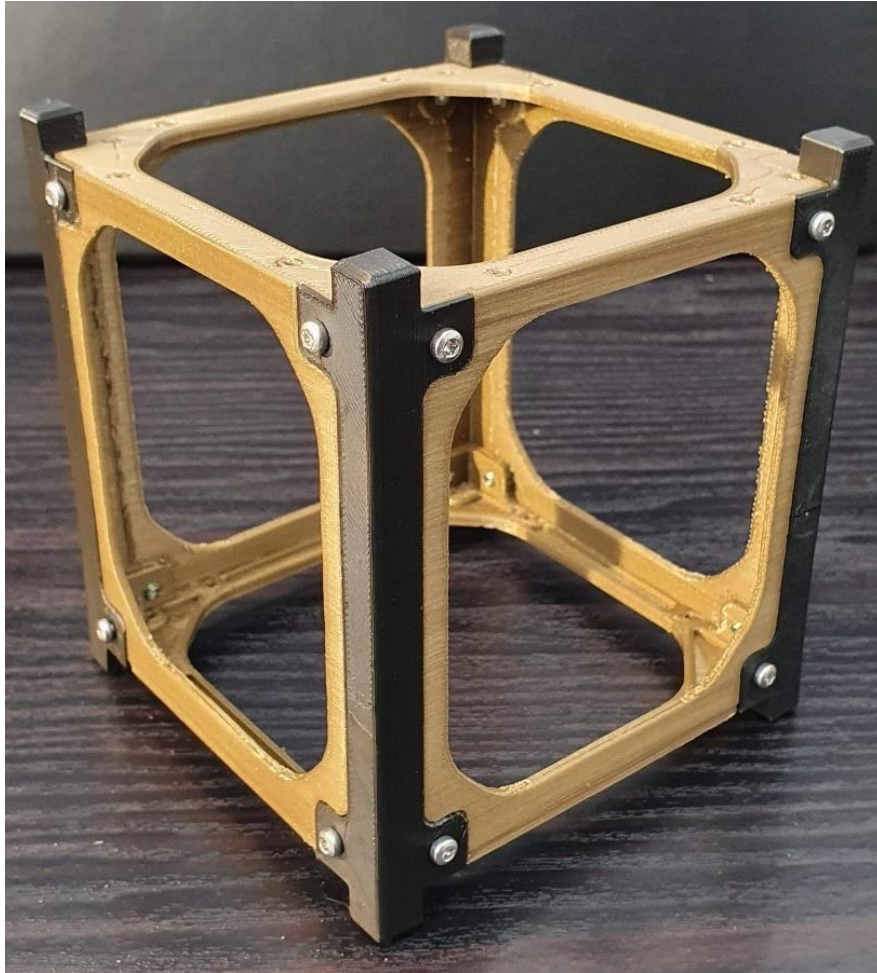


**Figure 6-62: Assembled prototype structure**

## **6.2. AM Applications for CubeSat Development**

### **6.2.1. Rapid Prototyping for SMAD**

In section 1.1.3, the project phases for space missions were discussed and how different phases have reviews and deliverables.

ASIC have two major deliverables when it comes to satellite development, the EQM at the end of phase C and the FM at the end of phase D. This has its drawbacks as when building the EQM, the assembly and integration methods are being tested. At this point, it is crucial that all components integrate perfectly as it is too late to make changes. It is therefore also crucial that the CAD is extremely accurate so that the assembly and integration can be set up within the CAD software.

Developing a CAD model of an assembly has its benefits, however errors may occur in the CAD and not be noticed. For example, certain parts penetrating others without being noticed. That is why it is safer to test assembly and integration with physical models.

By introducing a new deliverable to the ASIC phases, a Concept Model (CM) at the end of phase B, integration and assembly can be tested before procurement and production commence in the further phases. By making use of additive manufacturing to rapidly-produce a concept prototype of the design, a cheap, quick model can be made. Figure 6-63 below, shows the CAD model for the ZACube-2 concept (left) and the 3D printed model of the Zacube-2 concept (right).

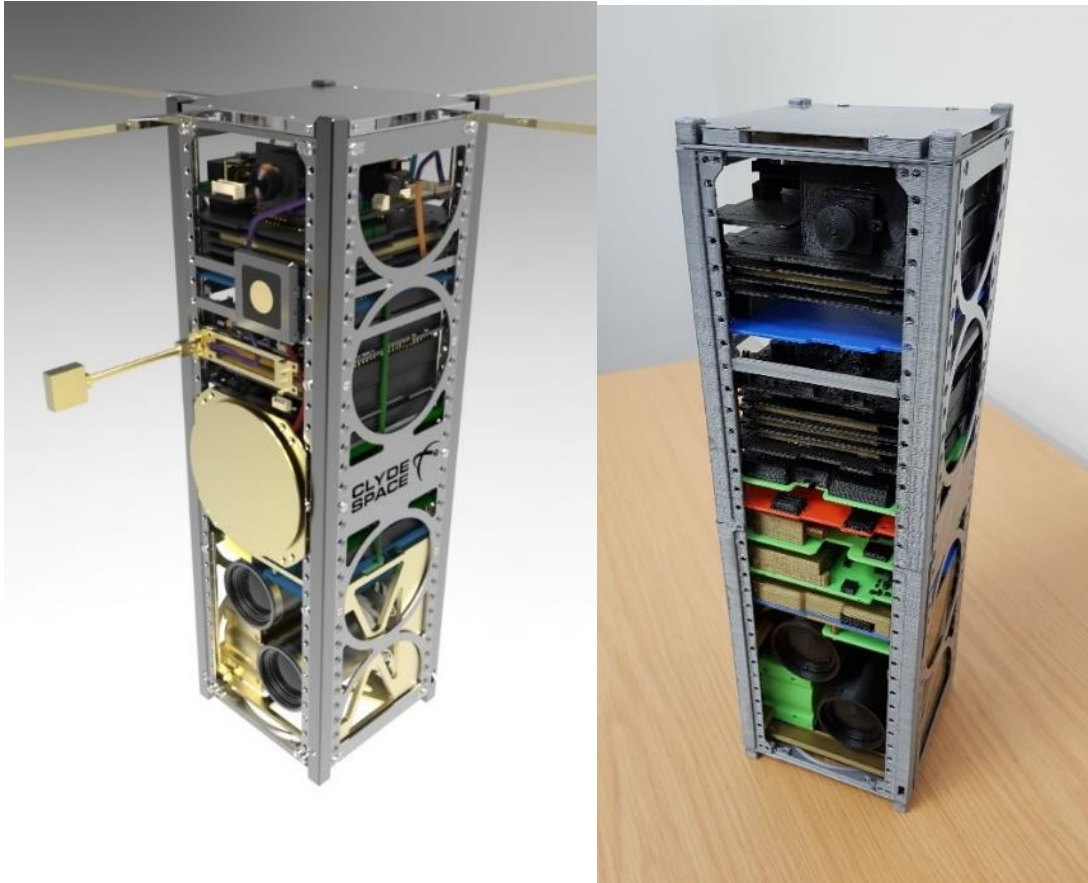


**Figure 6-63: ZACube-2 CAD concept (left) and ZACube-2 3D printed concept**

The CM will be a rapid prototype of the CubeSat concept making use of additive manufacturing, fasteners, connectors and harnesses. Each component of the CubeSat will be simplified and then 3D printed using FDM. Actual connectors such as headers, SMA's, etc. will be glued or fastened onto the components. Harnesses will be made using non-space grade wiring. Once all components have been made the entire model can be assembled as it would for the EM and FM. This includes fasteners and the connectors and harnesses mentioned previously.

The rapid-prototyped CM allows for a cheap and quick method of creating a physical model that can be used to better visualize the concept of the design. This model can also be used to test assembly and integration by making use of the harnessing and connectors embedded into the 3D printed components. The development process of the CM can be seen in Figure 6-64.

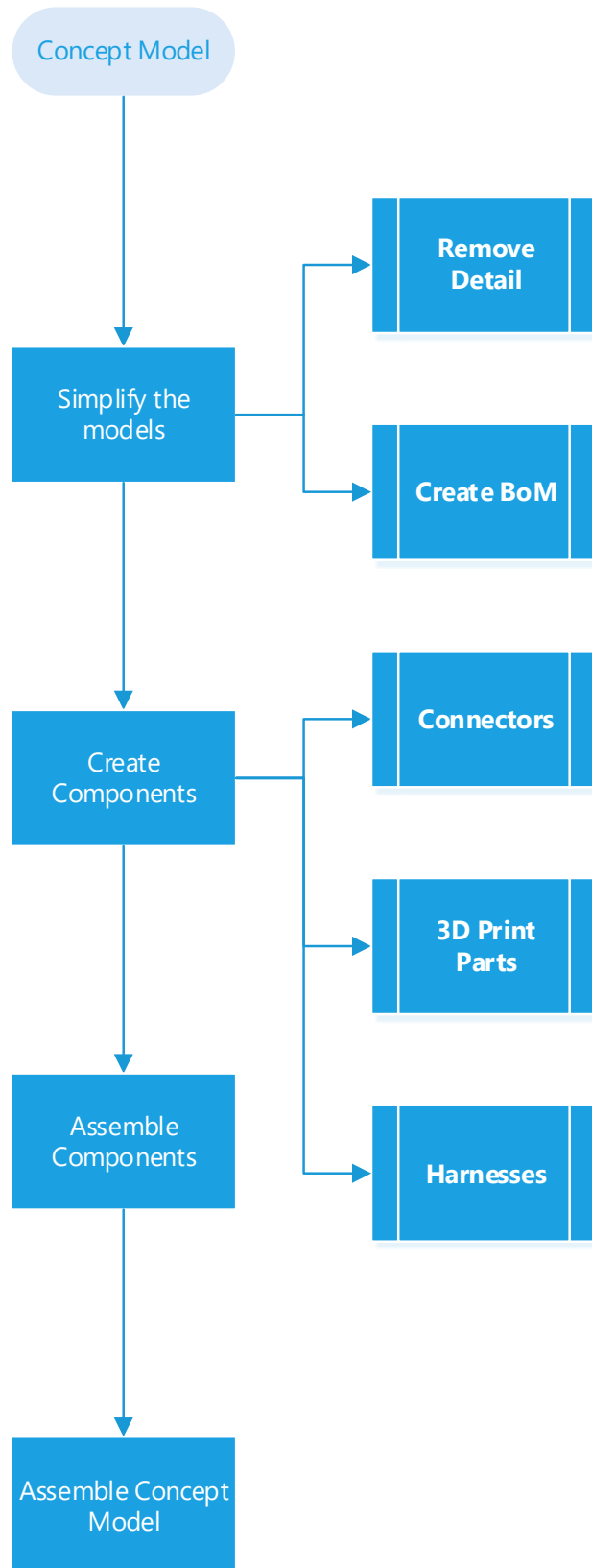


**Figure 6-64: Concept Model development process**

### 6.2.1.1. Simplifying the Models

As mentioned previously it is important to simplify the models to reduce the time required for 3D printing. Figure 6-65 (left) shows a photo of the F'SATI CMC/UTRXC and on the right the simplified model can be seen ready for 3D printing and assembling.

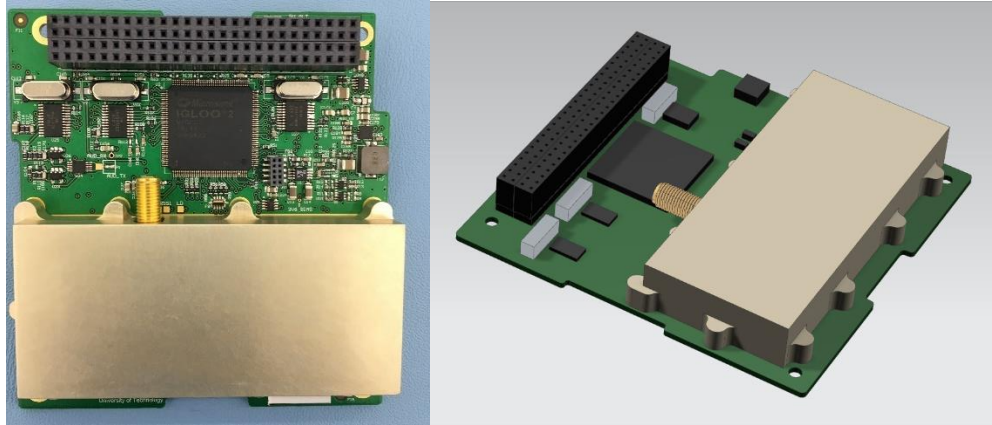


**Figure 6-65: Real vs simplified CAD of UTRXC**

The UTRXC is made up of two 3D printed components, the board and the cover. The two connectors for this component are the Samtec ESQ39 doubleheader and the straight SMA connector. The SMA is glued into the cover which is then glued onto the 3D printed board along with the header. This can be seen in Figure 6-66 below:

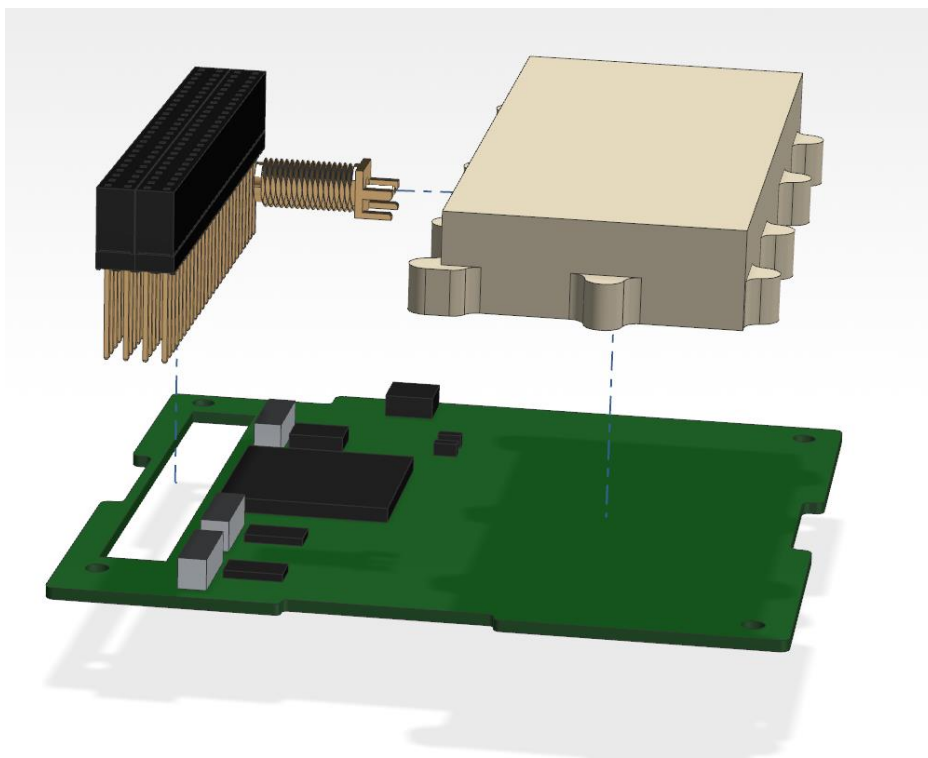


**Figure 6-66: UTRXC Concept Model**



An overall BoM should be created for all components and sub-components that are required for the model. This BoM will be used later for assembling of the various components.

#### 6.2.1.2. Create Components

##### 6.2.1.2.1. Connectors and Harnesses

Refer to the BoM that has been generated listing all connectors and harnesses. Most CAD software such as Siemens NX has harnessing features that allow the user to connect connectors with specific harnesses. A technical drawing can then be generated showing the straight length of the harness with sufficient tolerance for bends and soldering. From these drawings, the various harnesses can be made.

In Figure 6-67 below various connectors and harness wiring can be seen required for the MDASat CM.



**Figure 6-67: Concept Model connectors**

##### 6.2.1.2.2. 3D Print Parts

Once the various components of the model had been simplified, they can be 3D printed. The 3D can models can be imported into the slicing software and sliced to generate the g-code for the 3D printer. Using a layer height of 0.15 mm allows for accurate prints while still being fast. In Figure 6-68, the

sliced model for the UTRXC PCB can be seen. This slicing software estimated a printing time of 1h 20min.

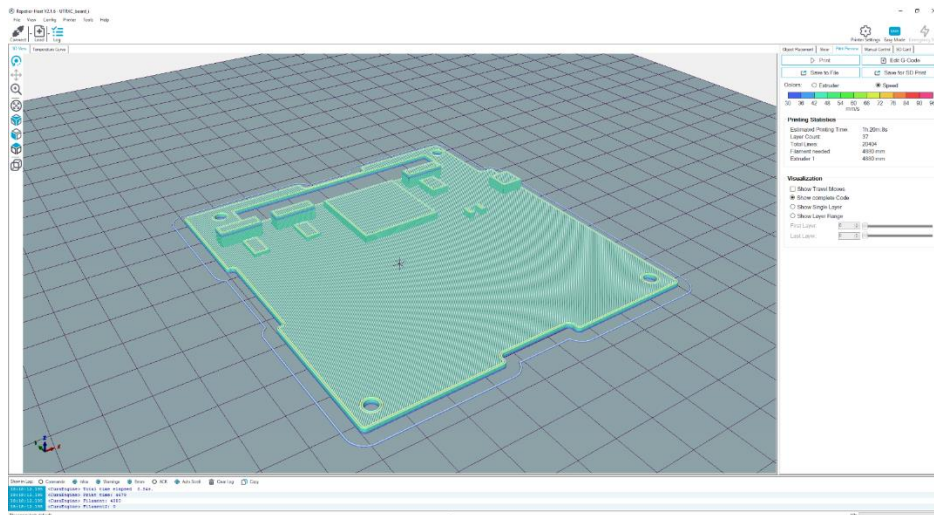


**Figure 6-68: Sliced UTRXC board**

The 3D printer used for the printing of the MDASat components was a TronXY X5 SA which has a printing volume of 350x350x400 mm. This 3D printer is a basic desk FDM printer which only cost the equivalent of \$972. Prints were printed using PLA, which is also biodegradable, thus environmentally friendly. One of the boards being printed can be seen in Figure 6-69.

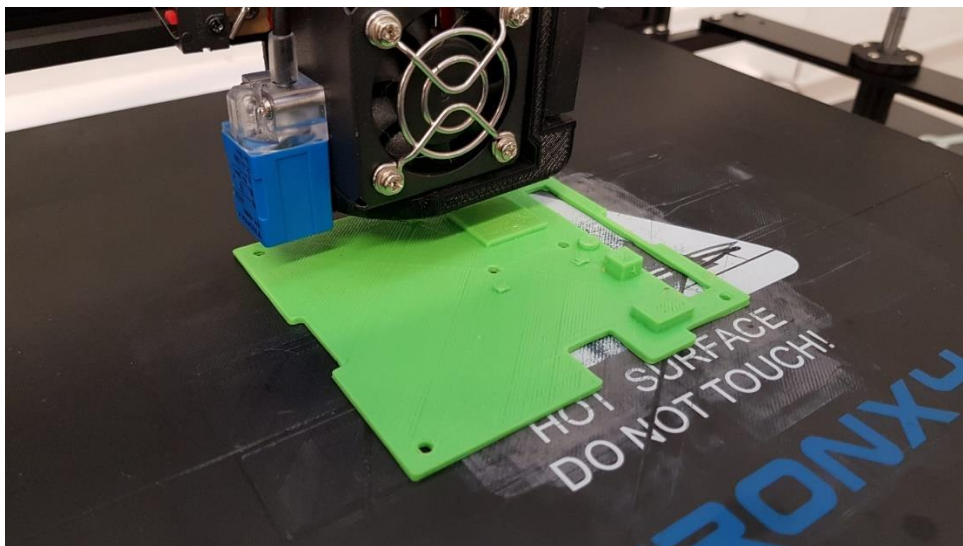


**Figure 6-69: 3D printed UTRXC**

### 6.2.1.3. Assemble Components

Once all the parts have been printed, the components can be assembled, as shown in Figure 6-70, with their associated connectors as listed in the BoM. The different 3D printed parts and connectors can be glued together using epoxy or superglue where fasteners are not used.

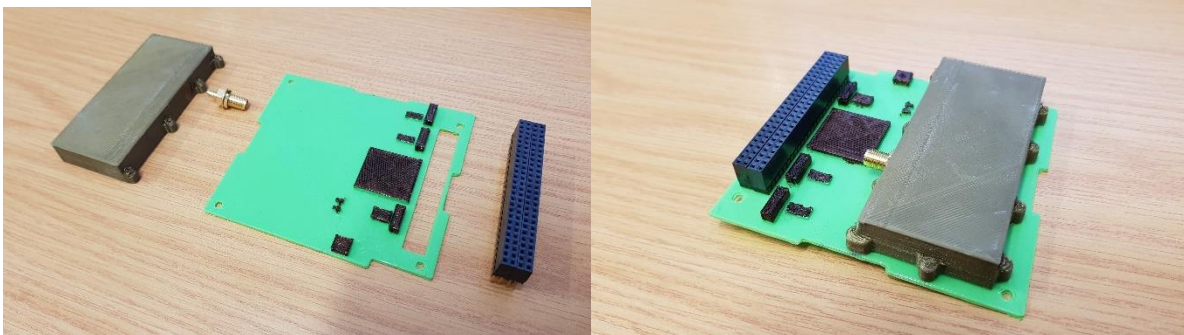


**Figure 6-70: Assembly of UTRXC CM**

In cases where fasteners are used for the final assembly, for example, the structure, helical inserts, as shown in Figure 6-71, can be inserted into the plastic to improve the longevity of the threads.



**Figure 6-71: Helical insert tool**

### 6.2.1.4. Assemble Concept Model

Once each of the components of the assembly has been assembled, the entire CM assembly can be assembled. The CM can then be used to test how each component integrates with each other, check harness lengths and connections. The CM can be used to test and plan the assembly procedure that will

be used for the later EM and FM. This allows the users the physically try different assembly methods which are difficult to simulate accurately using software.

Figure 6-72 below shows the assembly sequence of the MDASat CM.

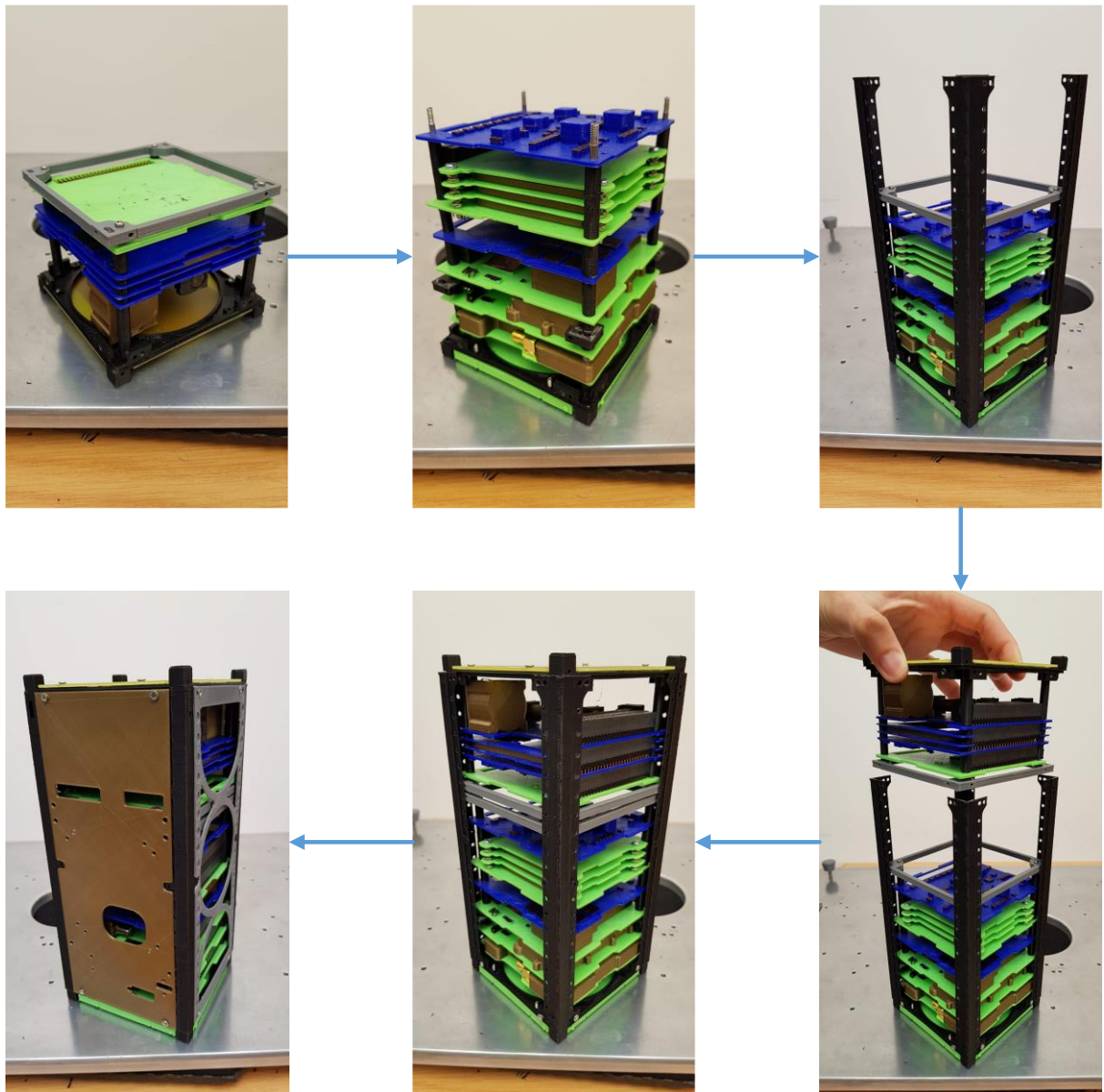


**Figure 6-72: Concept Model assembly process**

Figure 6-73 below shows an image of an assembled CM of MDASat with all connectors and harnesses attached. The model is used for checking harness lengths compared to CAD data, checking fitment of the harnessing and connectors so ensure that all connectors are easily accessible, and harnesses have sufficient room to be routed. It is also used to practice the integration and assembly procedure of the satellite.



**Figure 6-73: Assembled Concept model**

### 6.2.2. Infill Effects on Cost vs Performance

While 3D printed parts used in space would be printed at 100% infill to prevent outgassing, parts that are used on the ground can have varying infill densities that will reduce the material usage and print time but at the cost of tensile strength.

An experiment was conducted using PLA to determine what the effect of reducing the infill density to 80% has on parts. These experiments were conducted using a Tronxy X5 SA 3D printer using PLA rather than the Fortus 400mc due to financial constraints. Although the printer and material is different the hypotheses is applicable to other FDM 3D printers.

The following sections discuss the methods to be followed when conducting tensile testing on plastics as defined in the ASTM standard D638 (ASTM International, 2003).

#### 6.2.2.1. Apparatus

The Hounsfield Tinius Olsen tensile test machine will be used for the testing as it meets the testing machine requirements and has its calibration certificate. Strain measurement on the Hounsfield is acquired by strain-by-displacement. The machine must be of the constant-rate-of-crosshead-movement type where one member and grip are stationary while the second member and grip are movable. The grips used can be either fixed or self-aligning.

When fixed grips are used, extreme care must be used to ensure that the test specimen is aligned so that the long axis of the test specimen is aligned with the direction of the pull of the centreline of the grip assembly.

The self-aligning grips are attached so that once the load is applied to the moving member, the grips will freely move into alignment with the centreline of the grip assembly.

To avoid slippage of the test specimen the grip surface should have a serrated pattern like that of a coarse single-cut file. The serrations should be about 2.4mm apart and about 1.6mm deep. If grips are smooth-faced, interposing a piece of cloth, paper or fabric between the grip and test specimen can be effective.

For the measurement of the modulus of elasticity, and extensometer with a maximum strain error of 0.0002 mm/mm shall be used. The extensometer must be set at the full gage length of the specimen of 50mm. Bi-axial or an axial in combination with a transverse extensometer will be needed to measure Poisson's Ratio.

#### 6.2.2.2. Test Specimens

For 3D printed thermoplastics, Type I specimen dimensions should be used. In Figure 6-75 below the profile for the test specimens can be seen. The overall length (LO) to be 165 mm, a major width (WO)

of 19mm, a minor width ( $W$ ) of 13mm and a thickness ( $T$ ) of 3.2 mm. Appendix C shows more detailed dimensions for the specimens.

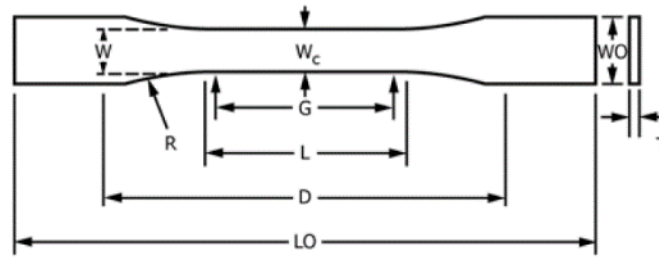


**Figure 6-75: Type I specimen profile**

#### 6.2.2.3. Method

- Measure the width and thickness of the specimen to the nearest 0.025 mm. Measurements must be taken at the centre and within 5 mm of each end of the specimen.
- Place the specimen in the grips ensuring correct alignment. The distance between the grip ends is to be 115 mm. Tighten the grips evenly and sufficiently to prevent slippage but not to the point where the specimen will be crushed.
- Attach the biaxial extensometer for modulus and Poisson's Ratio measurement.
- Apply a small pre-loading force of less than 5 N at a speed of 0.1 mm/min to eliminate any bending in the specimen. Rebalance the extensometers back to zero.
- Set the speed of the testing to 5 mm/min  $\pm$  25%.
- Record the load-extension curve of the specimen.
- Record the load and extension at the yield (if there is one) and rupture point.

#### 6.2.2.4. Calculation

- Toe compensation must be considered for all stress-strain calculations. Toe compensation will be discussed in Section 6.2.2.4.1 below.
- The tensile strength can be calculated by dividing the maximum load by the average original cross-sectional area of the gage section. The results can be expressed in Pascals to three significant figures.
- Percentage elongation can be found by the change in gage length relative to the original specimen gage length expressed as a percentage.
- Modulus of elasticity can be found by extending the initial linear section of the curve and divide the difference in stress along any segment of the straight line by the corresponding difference in strain.
- Secant Modulus is calculated when no proportionality is evident. This is done by drawing a tangent as directed in the following section and mark off the strain from the yield point where the tangent line goes through zero stress.

- Poisson's Ratio can be determined within the linear portion of the curve below the proportional limit. If the material does not exhibit linear stress to strain relationship the Poisson's Ratio within the axial strain range of 0.0005 to 0.0025 mm/mm (0.05 to 0.25 %):
  - The axial ( $E_a$ ) and transverse strains ( $E_t$ ) as indicated by the respective extensometers are plotted against the applied load ( $P$ ). See Figure 6-76 below,

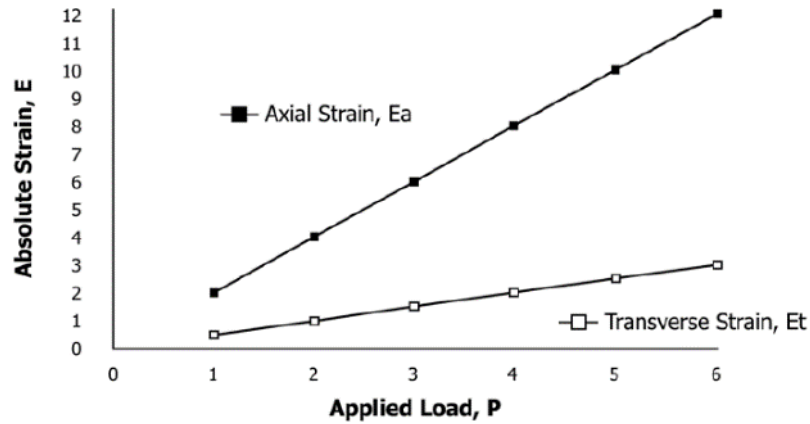


Figure 6-76: Axial and transvers strains for applied load

- For materials that have proportionality and it is possible to determine the modulus of elasticity, the slopes of  $d\varepsilon_a/dP$  and  $d\varepsilon_t/dP$  of the proportionality lines can be determined. Using the least-squares method will reduce errors resulting from drawing lines. Poisson's Ratio,  $|\mu|$ , is calculated from the following:

$$|\mu| = (d\varepsilon_t/dP)/(d\varepsilon_a/dP)$$

Where

$d\varepsilon_t$  = change in transverse strain

$d\varepsilon_a$  = changing in axial strain, and

$dP$  = change in applied load;

$$|\mu| = (d\varepsilon_t)/(d\varepsilon_a)$$

For materials where there is no proportionality, determine the ratio of  $d\varepsilon_t/d\varepsilon_a$  when  $d\varepsilon_a = 0.002$  (based on the axial strain range of 0.0005 to 0.0025 mm/mm) and after toe compensation has been made.

$$|\mu| = d\varepsilon_t/0.002$$



- Determine the standard deviation to two significant figures for each observation using the following formula:

$$s = \sqrt{(\sum X^2 - n\bar{X}^2)/(n - 1)}$$

Where

$s$  = estimated standard deviation

$X$  = value of single observation

$n$  = number of observations, and

$\bar{X}$  = arithmetic mean of the set of observations

#### 6.2.2.4.1. Toe Compensation

In a typical stress and strain curve, as can be seen in Figure 6-77 below, there is a portion of the curve called the toe region, AC, that does not represent the material property. This region is due to the take up of slack or the alignment or seating of the specimen. To obtain accurate data from the curve, compensation must be made for this region.

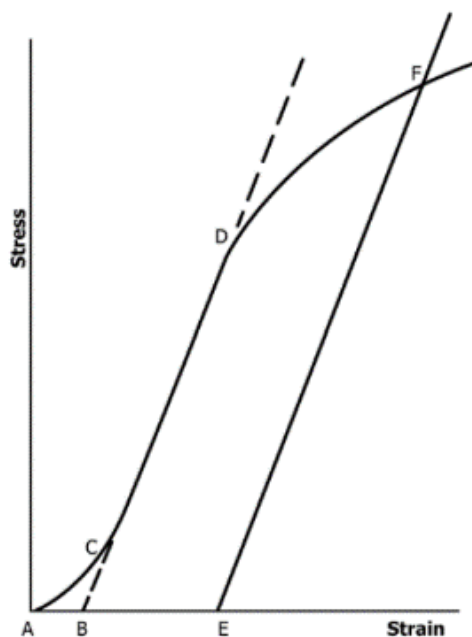


**Figure 6-77: Typical stress-strain curve**

When a material exhibits a linear region of the stress-strain curve as can be seen at CD, this linear curve can be extended to intersect the zero-stress axis at point B. This intersection point will be the corrected zero-strain point. All strain measurements must be taken from this point.

When a material does not exhibit any linear region as seen in Figure 6-78 below, the toe can be compensated for by constructing a tangent to the maximum slope at the inflection point (H'). This tangent can be extended to intersect the zero-stress axis at point B' to create the corrected zero-strain point. The secant modulus can be found by taking the stress at any point on the curve (G') and dividing it by its corresponding strain to create the slope of line B'G'.

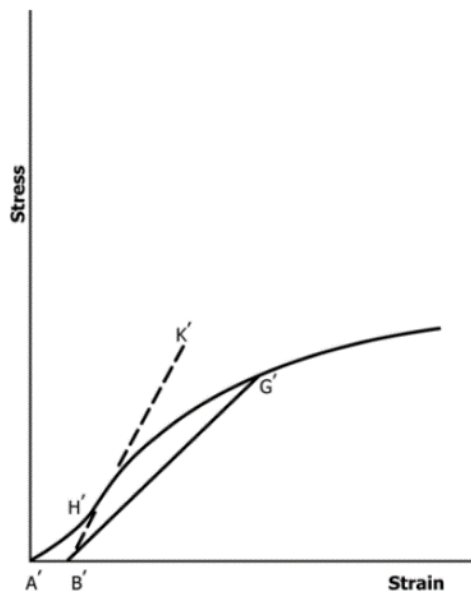


**Figure 6-78: Toe compensation**

#### 6.2.2.5. Testing

##### 6.2.2.5.1. Setup

Repetier-Host slicing software was used to slice the test specimens for 3D printing. The print quality was set to 0.15 mm, printing at a speed of 55mm/s. The first three specimens were printed at 100% infill, and the second three at 80% infill. Both were printed flat, along the X-axis. Figure 6-79 below shows the 100% infill 3D print in progress.



**Figure 6-79: PLA 100% printing**

6.2.2.5.2. Testing

The tensile tests were conducted on a Hounsfield Tinius Olsen tensile tester, using the ASTM D638 testing methodology. The strain was measured by position as there were no facilities available for measuring by strain gauge. Figure 6-80 shows one of the strain gauges gripped, ready for testing.



**Figure 6-80: PLA tensile test**

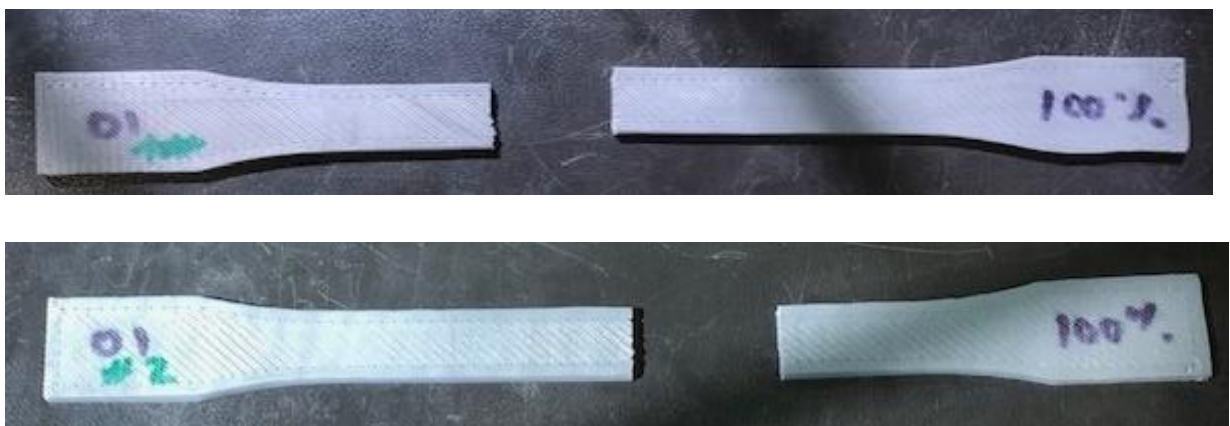
6.2.2.6. Results

All three 80% infill test specimens failed within their gauge region, as shown in Figure 6-81, which account to a successful test. Each specimen failing at around 40% of its total length. It can be seen in the figures that the 80% infill specimens experienced a small amount of delamination. This is expected for a lesser infill density as there is less material held together, allowing the layers to separate easier.



**Figure 6-81: Three broken 80% PLA tensile test specimens**

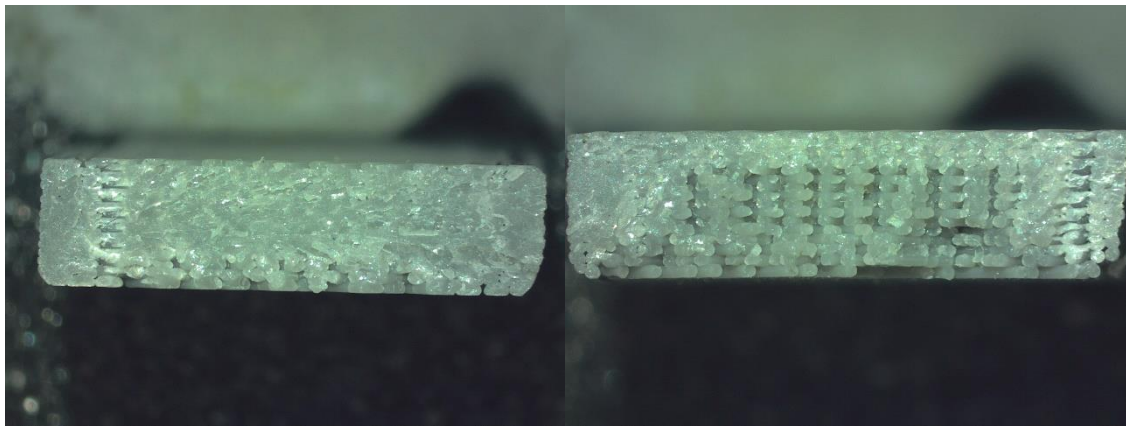
The three 100% infill specimens also all broke within their gauge region, as shown in Figure 6-82, again failing at about 40% of their total length. It can be seen from the figures below that the break is much cleaner than that of the 80% infill, this is due to the better bonding between the layers.





**Figure 6-82: Three broken 100% PLA tensile test specimens**

Looking at the cross section of the break point for the 80% versus 100% infill specimens in Figure 6-83, it can clearly be seen how the 80% infill cross section has gaps between the filament while the 100% infill is much more solid.



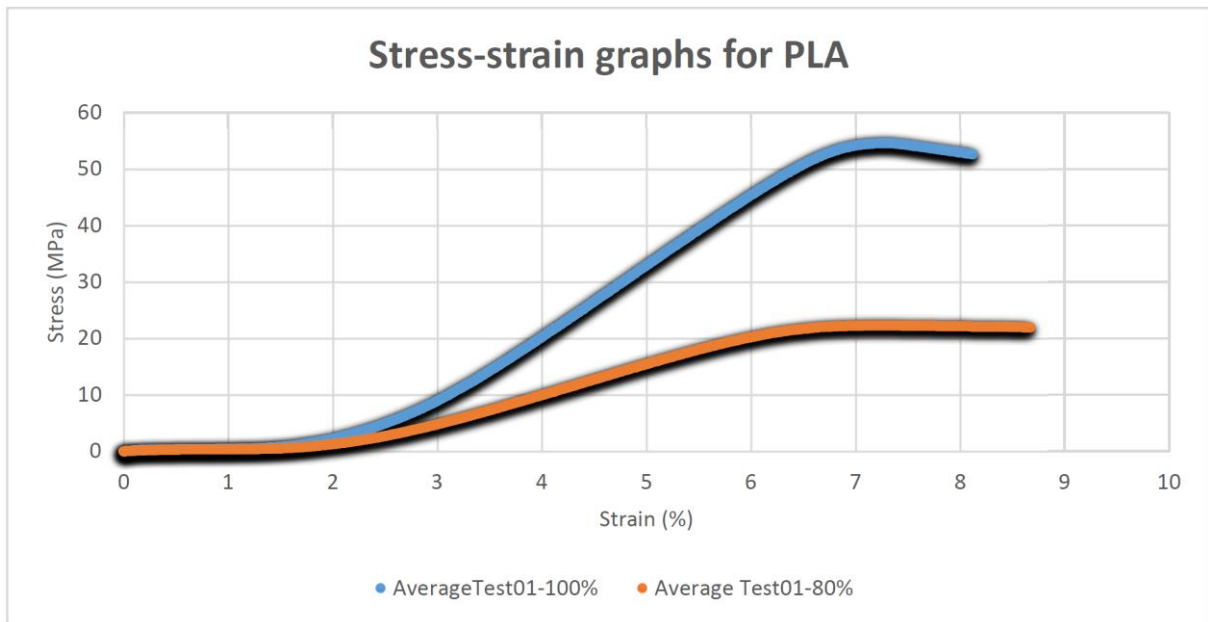
**Figure 6-83: PLA Specimen cross section view 100% (left) 80% (right)**

Table 6-5 and Figure 6-84 show the results of the tensile tests on the two different specimens. As expected, the 100% infill specimens had a higher average tensile strength of 55 MPa compared to 22 MPa of the 80% infill specimens.

The modulus of elasticity for each specimen was determined from the linear section of the stress-strain graphs resulting in a modulus of elasticity of 559 MPa and 1244 MPa for 80% and 100% respectively. As expected, the lower density specimen was much more brittle in comparison to the solid specimen.

**Table 6-5: PLA Tensile Test Results**

	<b>01-4(80%)</b>	<b>01-5(80%)</b>	<b>01-6 (80%)</b>	<b>Average</b>
<b>Yield strength [MPa]</b>	22.4	21.9	22.6	22.30
<b>Strain</b>	6.77	6.85	7.6	7.07
<b>Modulus of elasticity [MPa]</b>	544.81	597.60	534.76	559.10
	<b>01-1(100%)</b>	<b>01-2(100%)</b>	<b>01-3(100%)</b>	<b>Average</b>
<b>Yield strength [MPa]</b>	53.6	55	56.5	55.03
<b>Strain [%]</b>	7	7.09	6.94	7.01
<b>Modulus of elasticity [MPa]</b>	1224.48	1240.60	1265.8	1243.63



**Figure 6-84: Stress-strain graph for PLA**

Table 6-6 below shows the statistics for each specimen. It can be seen how the 100% infill print took about 14 min longer to print, used 250 mm more filament which increased the overall mass by 0.4 g and brought the material cost up by the equivalent of \$0.065. Material costs are equivalent to \$4.5/100g, based on the cost for a roll of PLA filament in South Africa.

**Table 6-6: Specimen printing statistics**

	Printing Time	Mass	Material Cost
<b>80% Infill</b>	56m 42s	8.93 grams	\$0.4
<b>100% Infill</b>	1h 10min 52s	10.37 grams	\$0.47

#### 6.2.2.7. Discussion

The tests that were conducted all failed within their gauge length, at approximately 40% of the specimen's total length. This shows that not only was the testing conducted consistently for each specimen but also shows the repeatability of the 3D printer. Each specimen reacted to the applied stress similarly, this could be seen for both 80% and 100% infill. The consistency of the data acquired from the test results is also evidence of this.

While it was clear that by reducing the infill density the printing time and material cost improved, there was a significant reduction in tensile strength of the specimen. Reducing the infill density to 80% reduced the printing time by 20% and the material costs by 14% while the tensile strength of the material reduced by about 60%. This results in an unfavourable reduction in the 3D printer's performance as the

strength-weight ratio drops from 5.3 by less than half to 2.5. Finally, the cost-performance ratio can be seen in Figure 6-85 as 1.4 for 100% versus 2.5 for 80% (where a lower cost-performance is more favourable)

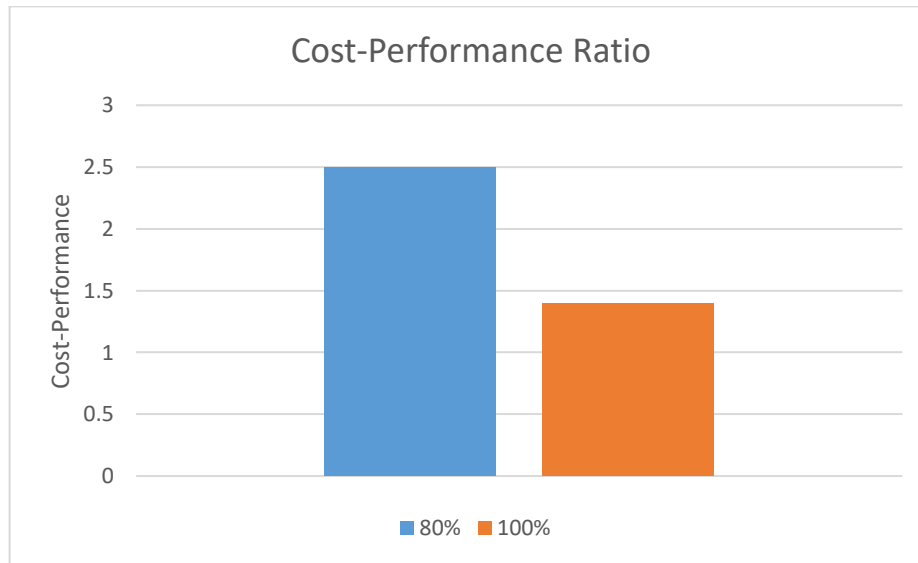


**Figure 6-85: Cost-performance ratio comparison for PLA**

This shows that to get the most performance out of a part for a given price, it is more efficient to use 100% infill. Even for parts that do not experience direct structural loading, by using 100% infill, it will increase the lifespan of the part.

There are two exceptions to this conclusion; the first is when a large part needs to be printed as a closed object. To print this at 100% infill will of course take significantly longer and use much more material, for these parts, if they are not experiencing direct structural loading, a low infill density of 20% can be used to reduce the print time and cost of the part. The second exception is when a flexible part needs to be made. By reducing the infill density, the overall stiffness of the part reduces, allowing for flex in the part.

### 6.2.3. Functional parts

Additive manufacturing has also introduced the ability to easily and cost effectively create parts on demand to assist with CubeSat integration and assembly.

#### 6.2.3.1. 3D printed adhesive dispenser

During assembly and integration of the CubeSats, all loose components such as fasteners and connectors are “potted” with an adhesive to ensure that they do not vibrate loose during launch, see Figure 6-86. It is very important that the amount of adhesive used is correct and not over applied, adding unnecessary weight. Using a syringe and needle for the application allows for small accurate “potting” to be applied. The problem with using a syringe however is that controlling the amount of adhesive with the depressor can be difficult and result in inconsistencies.

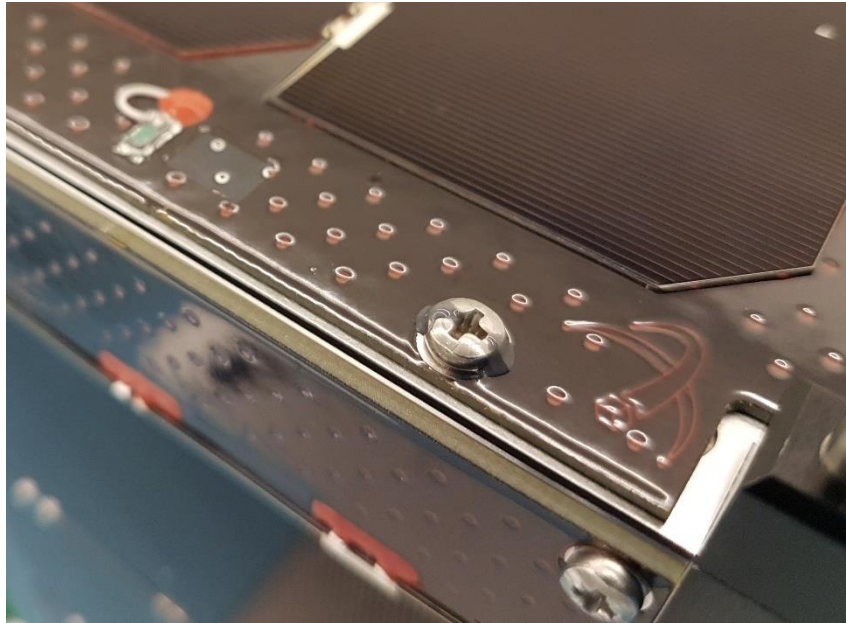


**Figure 6-86: "Potted" fastener**

Figure 6-87 shows the CAD of a dispenser design that can be 3D printed and used with an M6 screw and nut to accurately and precisely dispense adhesive for potting. By turning the screw, 0.086 ml of adhesive is dispensed for each revolution. This makes it possible for the exact amount of adhesive to be used for each “potting”.

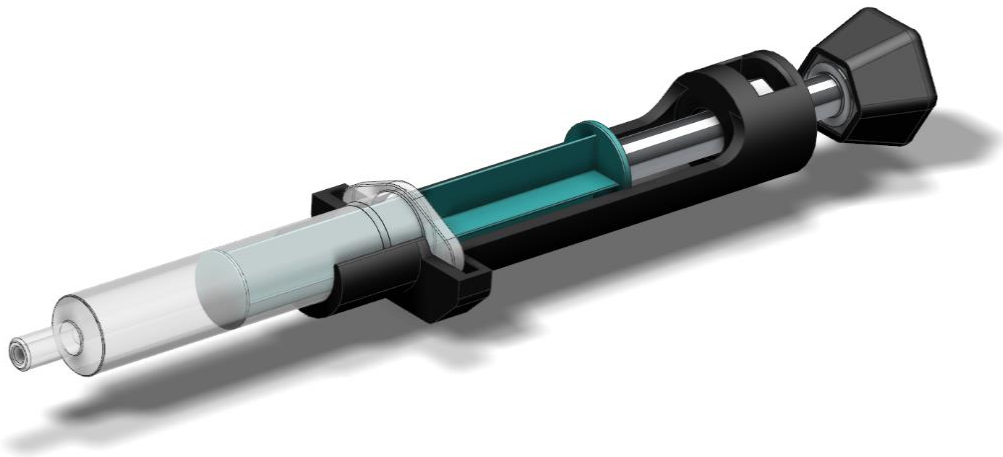


**Figure 6-87: Adhesive dispenser CAD**

Figure 6-88 shows the PLA dispenser 3D printed with a syringe mounted in position. The 3D print took 45 min to print at 100% infill with 0.15 mm layer height. These settings were selected based on the findings discussed in Section 6.2.2.7 to ensure optimal strength vs cost. 2.7 m of filament would be required which would cost approximately the equivalent of \$0.32 in material costs.





**Figure 6-88: 3D printed adhesive dispenser**

#### 6.2.3.2. Solar panel integration mount

During integration and assembly of CubeSats the mechanical ground support equipment (MGSE) plays a large role in ensuring that the satellite is securely held in place and is easily accessible for assembly. One problem identified by F'SATI engineers during the assembly of ZACube-2 was when it came to assembling the solar panels to the structure. First the harnesses needed to be connected and potted before fastening onto the structure. During harnessing and potting, positioning the solar panel became tricky as the harness length is very short and to have someone holding the panel would result in too many engineers working on assembly at once. By designing a simple, 3D printed solar panel mount, the engineers would be able to let the solar panel rest within the mount, move it as desired and conduct harnessing and potting, see Figure 6-89.



**Figure 6-89: Solar panel mount in position**

The mount is a simple slot-in type where the solar panel can easily slot into the groove and be securely held in place. The legs extend out equally spaced for optimum stability. Countersunk screws with nuts have been placed at the end of the legs for additional stability and balance, see Figure 6-90.

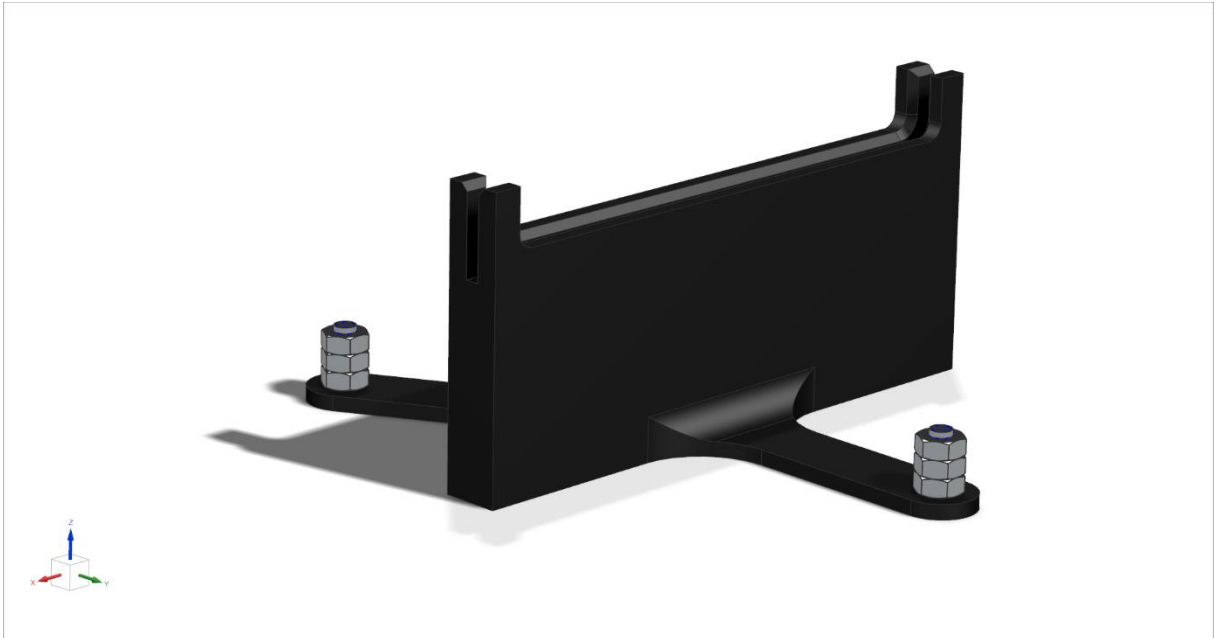


**Figure 6-90: Solar panel mount**

In Figure 6-91 the 3D printed mount can be seen with a dummy solar panel inserted for testing. The mount was sufficiently stable and strong, even with a 3U side solar panel dummy tested. The mount was 3D printed with PLA at 100% infill density and at a layer height of 0.15 mm. Kapton tape will be taped on the inside surface of the mount to protect the solar panels from the rough 3D printed material.



**Figure 6-91: 3D printed solar panel mount**

#### 6.2.4. Discussion of AM applications for CubeSat development

In this section we have seen how making use of additive manufacturing in the form of a novice 3D printer has a significant impact on CubeSat development. Using a TronXY X5 SA novice 3D printer with PLA filament has produced concept models of CubeSats, as well as functional parts to aid in the integration and assembly process of the satellite. The study on infill effects has also shown how these functional parts can be optimally printed to gain the best performance versus the cost. Making use of the Concept Model, integration engineers at ASIC identified several harness lengths that were too short for the planned route. Fitment and accessibility issues were also identified, including incorrect spacer lengths. These issues were then implemented back into the CAD model saving significant time and money by avoiding finding these issues with the full EM of the CubeSat.

Table 6-7 below shows the breakdown of the costs involved for each harness used in the CubeSat. This example is for a 300mm harness with two DF13-6 connectors. The parts for the harness are priced from RS Components. It can be seen how it costs approximately the equivalent of R1274 (\$82.55) per harness in the CubeSat. The CM harnesses, however, would be significantly cheaper. Only one single wire would need to be used per harness, reducing the assembly time significantly. The CM harnesses could also be assembled and routed by lower level engineers or interns which have a much lower per hour rate. An estimation considering these reductions in cost would value a CM harness at about 12% of an EM/FM harness. This shows that by discovering a CM harness that is an incorrect length at this early phase would save 88% from the mission costs per harness. Similarly, the CM 3D printed spacers cost only 5% of the aluminium equivalents, further increasing the savings.

**Table 6-7: Harness costs**

Description	Number of	Unit price	Total price
DF13-6 Connectors	2	R5	R10
44A0111-24-2 wire	6 x 0.3 m	R9.8 / m	R18
Assembly time	12 connections	R83 / connection <sup>1</sup>	R996
Routing time	15 min	R250	R250
<b>Total cost</b>			<b>R1274 (\$82.55)</b>

With 3D printing being one of the major fourth industrial revolution developments, it can be seen how the revolution has allowed for cheap, easy solutions to issues that previously would not have been addressed due to their high cost. In comparison, to create any of the functional parts or concept model as discussed, using traditional manufacturing methods would have long lead times and high cost.

---

<sup>1</sup>Based on ASIC AIT engineer rates of R1000/hr at 5min per connection.

### 6.3. CubeSat Thermal Digital Twin

Creating an accurate digital twin of the 3-unit CubeSat, ZACube-2 in a form of a thermal model will allow not only troubleshooting of potential thermal issues on the satellite but also allow for the predicting of the thermal performance of future CubeSat missions. This study focuses on the thermal modelling of ZACube-2, but the methods and results can be applied to other Cube or nanosatellites. The digital twin will be created by creating a finite element model and simulating the orbital thermal conditions and comparing the results to actual data taken from ZACube-2 telemetry. This will validate the accuracy of the methods and models used. The FEA software to be used is Siemens SimCentre, Space Systems Thermal which is a specific thermal solver that specializes in analysing, orbital heating, radiation and the transient effect during orbit.

#### 6.3.1. Thermal Design and Analysis

Thermal analysis during the design phase of a mission considers the internal and external heat sources and predicts the temperature ranges and thermal conditions the satellite will experience during orbit. This is important to ensure that subsystems and payloads remain within their allowable temperature range during operation as well as checking for any potential thermal strain being induced. If the requirements are not met, alternative sub-systems must be selected, or design changes must be made to ensure the safe functioning of the satellite once launched. In Table 6-8 the minimum and maximum allowable temperature ranges for the various subsystems can be seen. These temperature ranges were acquired from ASIC databases for the various subsystems.

**Table 6-8: ZACube-2 minimum and maximum subsystem temperatures**

Subsystem	Min temp (°C)	Max temp (°C)
VHF/UHF antenna	-20	60
Structure	-40	80
Solar panels	-40	80
Electronic power system (EPS)	-40	85
Battery	-10	50
On-board computer (OBC)	-40	80
ADCS	-10	60
S-Band transmitter (STX)	-25	60
Interface adapter board (IAB)	-25	60
UTRX	-25	60
XTX	-25	60
SDR	-25	60

### 6.3.2. Material Properties

The thermal characteristics of a material can be defined by the following properties; density,  $\rho$ , thermal conductivity,  $k$ , specific heat,  $C$ , absorptance,  $\alpha$  and emittance,  $\epsilon$ . Some of these properties were available within the FEA software but in some cases the properties were taken from published data (Siemens, 2020; Matweb, 2020; Spectrolab, 2018). The materials and their properties used for the various subsystems can be seen in Table 6-9. Wendland, et. al. determined a simplified material combination for PCB boards that can be used the material properties for the PCBs which can be seen in Table 6-10 (Wendland et al., 2020).

**Table 6-9: Thermal material properties**

Subsystem	Material	Density (g/cc)	Thermal conductivity (W/m.k)	Specific heat (J/kg.k)	$\alpha$	$\epsilon$
Structure – rails	Aluminium 6061 (Anodized)	2.7	154	896	0.95	0.85
Nadir panel	Aluminium 6061 (Chromate)	2.7	154	896	0.6	0.2
Structure	Aluminium 6061 (Polished)	2.7	154	896	0.09	0.05
Solar panel PCB	Multi-layer	2.6	36.54	1126	0.82	0.8
Solar cell	Silicon	2.33	124	713	0.88	0.85
Subsystem PCB	Multi-layer	2.6	36.54	1126	0.85	0.85
Spacers	Aluminium 6061 (Dull)	2.7	154	896	0.6	0.2
Lenses	Stainless Steel	7.7	24.3	460	0.88	0.88
Rods	Titanium	4.43	6.7	526	0.55	0.3
Chips	Silicon	2.33	124	713	0.88	0.85

**Table 6-10: PCB material properties**

Material	Thickness (mm)	Thickness (%)	Specific Heat (J/kg.K)	Thermal Conductivity (W/m.K)	Density (g/cc)
Dielectric	1.427	91	1200	0.5	1.97
Copper	0.146	9	385	401	8.96
Resultant material	1.573	100	1126.65	36.54	2.6

### 6.3.3. Finite Element Model

#### 6.3.3.1. Geometry

To create the thermal digital twin of ZACube-2, the first step was to create geometry that represented the CubeSat sufficiently. The orbital thermal analysis is extremely complex, and it was therefore important to create a finite element model (FEM) that was simple enough for the simulation to run while still being sufficiently accurate.

The overall geometry was shaped as a rectangular prism with the outer dimensions of 100x100x326.5 mm, the size of a 3U CubeSat. 5 of the 6 faces were divided to represent the solar panels with their solar cells. The 6<sup>th</sup> face was blank, representing the nadir panel. 7.5 mm of the edges were divided to represent the anodized rails of the satellite. The imager within the prism, was modelled with two-dimensional (2D) surfaces for the frame of the imager while 1D elements were used for the lenses. The geometry linked to the lenses was defined when defining the 1D element.

#### 6.3.3.2. Exterior Mesh

As previously mentioned, it was important to create a FEM that was simple, yet accurate. The exterior mesh was therefore modelled using 2D, 4-node quadrilateral thin shell elements. The elements average size was 8mm. To still represent accuracy within the model, the thin shell elements were defined using multi-layer shells, with different materials for each layer as can be seen in Figure 6-92. The red region represents the solar cells, the yellow region represents the solar panel, which is simplified as a PCB and only contains the PCB and aluminium layers, and the blue section represents aluminium. The exposed sections on the rails has hard anodizing. Finally, the green section represents aluminium again, but for the nadir panel, which is chromate conversion coated.

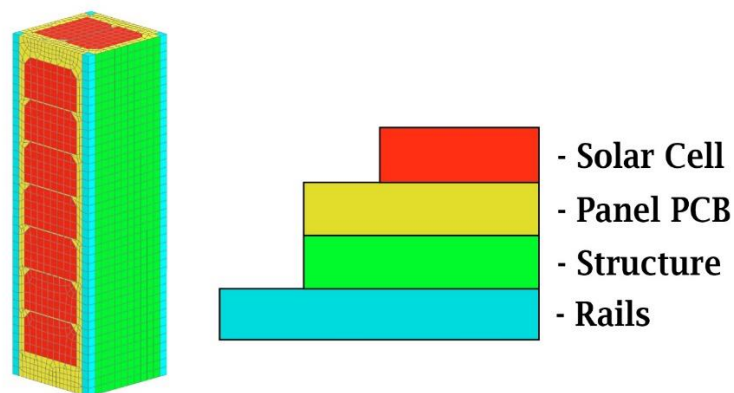


**Figure 6-92: ZACube-2 exterior mesh**

#### 6.3.3.3. Interior Mesh

To simplify the internal subsystems of the satellite as seen in Figure 6-93, the PCB boards (blue) are meshed as 2D shell elements with PCB material properties. The two aluminium structure interface ribs

(pink) are also added to the inside of the structure to accurately represent the heat conduction path within the satellite. One-dimensional (1D) line elements are used to represent the aluminium spacers and titanium rods (orange) to further extend the conductive path between the boards. Regions on the PCB boards are meshed with layer properties of silicon on top of PCB (red) to represent the component chips that are generating heat. Finally, the imager assembly is modelled with aluminium 2D shells (green) and 1D line elements to represent the lenses (purple).

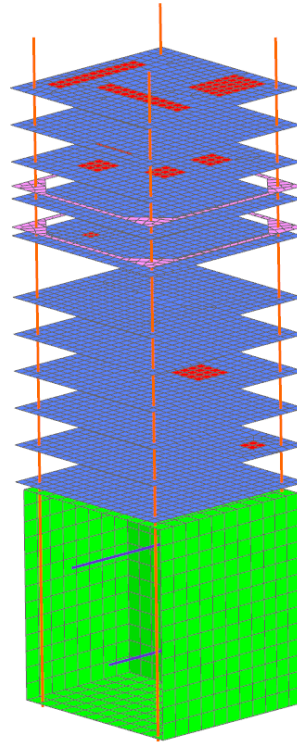


**Figure 6-93: ZACube-2 interior mesh**

Each PCB board is set up with its own mesh collector which allows for additional 'non-structural mass' to be added to each board. This is to compensate for the thermal inertia that a subsystem would have if it has a higher mass. Each PCB board had mass added to achieve the actual subsystems' mass as listed in Table 6-11.

**Table 6-11: ZACube-2 subsystem masses**

Subsystem name	ADCS	IAB	EPS	BAT	XTX	OBC	HSTX	UTRX	SDR	Imager
<b>Mass (grams)</b>	285	56	93	271	118	70	84	98	128	1022

#### 6.3.3.4. Numerical Method

Siemens NX is used to create the geometry for the solid model and Simcentre Space Systems Thermal to create the FEM and set up and execute the simulation.

The simulation is set up as a transient analysis to run for 15 orbits at an interval of 3 minutes per simulation step, which covers approximately one full day of orbit. The solution is set with a radiative environment temperature of 3K (ECSS, 2008).

The default method for defining boundary conditions in Simcenter Space Systems Thermal is to apply them directly to the geometry of the model, not on to the mesh. The software resolves the associated elements during the solve.

The conjugate gradient algorithm used by the thermal solver provides high performance for large, complex-condition systems by using the Newton-Raphson method for non-linear terms. The solver also simulates diffuse radiative exchange with automatic view calculations for enclosures and shadowing surfaces (Siemens, 2020).

#### 6.3.3.5. Simulation Setup

The simulation was setup using the orbital parameters as shown listed in Section 1.1.2.1 for a LEO sun-synchronous orbit. The orientation of the model corresponds with the attitude of ZACube-2, which is with its long axis along the velocity vector. The sun-planet characteristics are set to the default planet data that adheres to that of the ECSS standard (ECSS, 2008). For the solar data, the sun position is set to the same date of the recorded temperature data from ZACube-2, which computes a solar flux value of  $1379.7 \mu W/mm^2$ .

Thermal couplings have been added between each board and their adjacent spacers with a thermal conductivity of aluminium to represent the transfer of heat through the aluminium spacers. A thermal coupling has also been added to the structure interface ribs and imager to couple to the aluminium rails. Finally, a thermal coupling has been applied to represent the header connections between the boards. The coupling conductivity value is determined to represent the effective conductivity of the copper pins of the headers.

The radiative environment of the satellite was defined using the simulation functions; where 'Enclosure radiation' is applied to the outer surface of the satellite while 'all radiation' is applied to allow radiation between subsystems within the satellite.

Heat loads are applied to the individual subsystems on the chip meshes at magnitudes as defined in Table 6-12. The location of the heat loads are based on known or expected positions of processors, power-amplifiers and other high-heat components. The SDR, X-Band transmitter and imager payload were in the off state for this scenario to match that of the actual satellite conditions.

**Table 6-12: Subsystem heat loads**

<b>Subsystem name</b>	<b>ADCS</b>	<b>EPS</b>	<b>BAT</b>	<b>OBC</b>	<b>STX</b>	<b>UTRX</b>	<b>Reaction wheel</b>
<b>Heat load (W)</b>	0.69	0.2	0.6	0.35	0.05	0.22	0.085



The 0.6W heat load of the battery is activated as a battery heater to prevent the battery from cooling below its allowable operating temperature. The heater is enabled by a temperature sensor in the centre of the board at 1° C and disabled at 6° C (AAC-CS, 2018). The heat loads were applied to the region on the board where the battery cells were located.

### **6.3.4. Thermal Results<sup>2</sup>**

#### **6.3.4.1. Computation**

The simulation was conducted on a single workstation with parallel processing enable for both view-factors (8 processes and solvers). The simulation also made use of the Hemicube Rendering method to calculate shadowed view factors for the radiation requests. This method makes use of the computer's graphics card rendering capabilities for these view factors. The workstation that the simulation was run on has two Intel Xeon E5-2670, 2.6 GHz processors, 128 GB of RAM and a Nvidia Quadro K5000. The simulation took 1 hour, 18 min and 33 seconds to complete with a FEM of 8606 elements at an average element size of 8 mm.

#### **6.3.4.2. Hottest State**

During idle conditions the hottest temperature the satellite experiences, is when it enters eclipse after having sunlit conditions for the longest period of time. This can be seen in Figure 6-94. The last face to be visible to the sun experiences the highest temperature of about 22° C, while within the satellite most of the subsystems are at a similar temperature of between 7° C and 10° C. The hottest subsystem is the OBC which can be seen with its concentration of heat around the chip that has a heat load. The coldest being the battery, with a temperature of about 7° C, which is not low enough however to activate the internal battery heater.

---

<sup>2</sup> The temperature gradient results from the two payloads, namely the SDR and Imager, have been removed from the figures due to intellectual property protection measures.

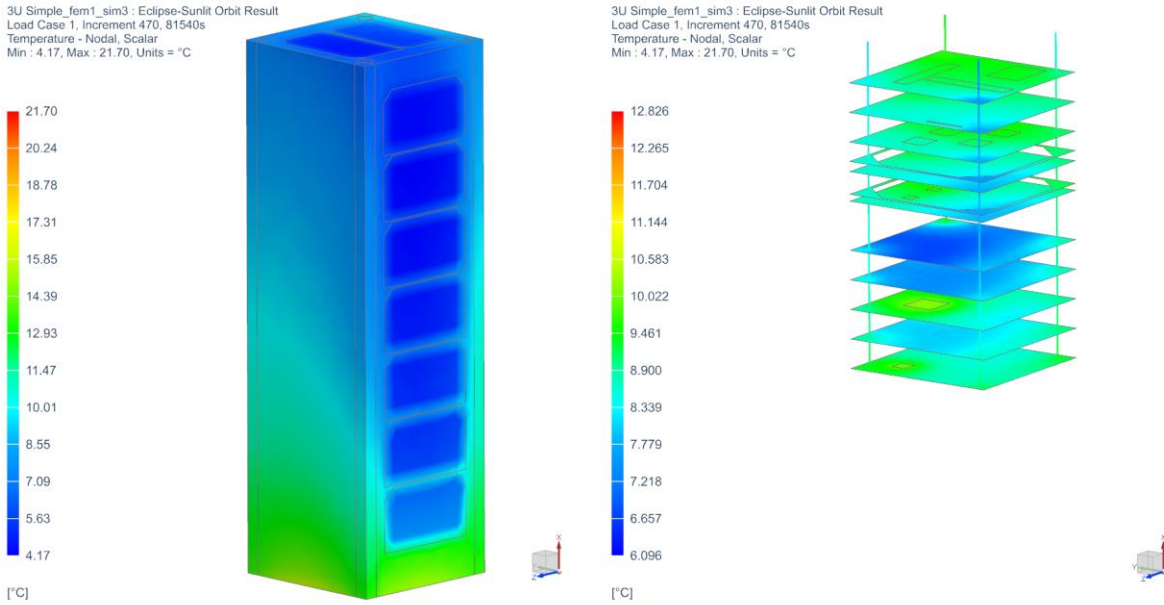


**Figure 6-94: Simulation results – hot**

6.3.4.3. Coldest State

During idle conditions, the coldest temperature the satellite experiences is when it enters sunlit conditions after being in eclipse for the longest period of time. This can be seen in Figure 6-95. The outer surface of the satellite has the lowest temperature of about  $-15^{\circ}\text{C}$  as it has radiated its heat out into the space environment. Within the satellite, the subsystems temperatures vary from about  $-8^{\circ}\text{C}$  to about  $-2^{\circ}\text{C}$ , with the warmest subsystem being the battery with its heaters in full operation.

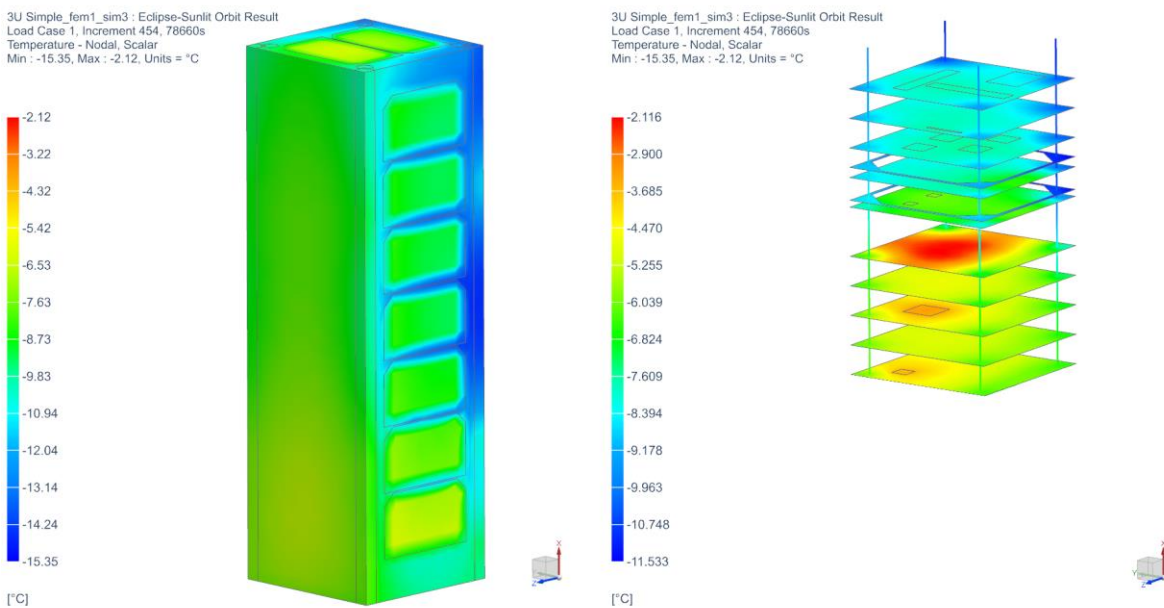


**Figure 6-95: Simulation results – cold**

6.3.4.4. Simulated versus Actual Temperatures

The three subsystems that had continuous temperature telemetry data from ZACube-2 are the UHF TRX, EPS and Battery. Sensors have been placed on the subsystems in the simulation corresponding to the location of sensors on the actual subsystems. Figure 6-96, Figure 6-97 and Figure 6-98 show the comparison of the simulated vs actual data; the dotted lines (polynomial trendline) show the average temperature throughout the analysis period.

The simulated results for the UHF TRX subsystem show an average temperature of 5° C higher initially, and then converging to a difference of 2° C after 2 hours of orbital time, and further converging and remaining within 1° C for the next 8 hours. The results then diverge again, increasing the difference to about 2° C. Comparing the peak maximum and minimum temperatures, it is evident that the minimum experienced temperature for the UHF TRX is almost identical, while the maximum experienced temperature deviates by approximately 1° C.

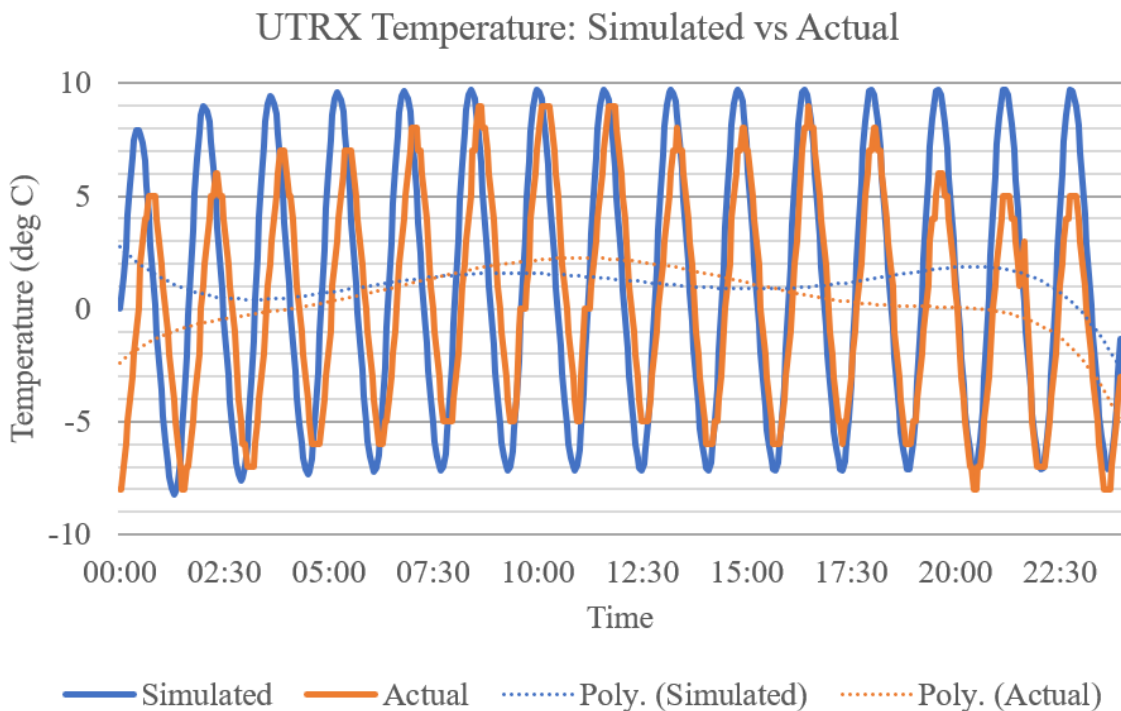


**Figure 6-96: Simulated vs actual UTRX temperatures**

The EPS exhibits almost identical simulated and actual temperature levels with a maximum divergence in average temperature of about 2.5° C near the end of the cycle. Deviations between the simulated and actual peak maximum and minimum temperatures range between 1.5° C (maximum) and 2.5° C (minimum).

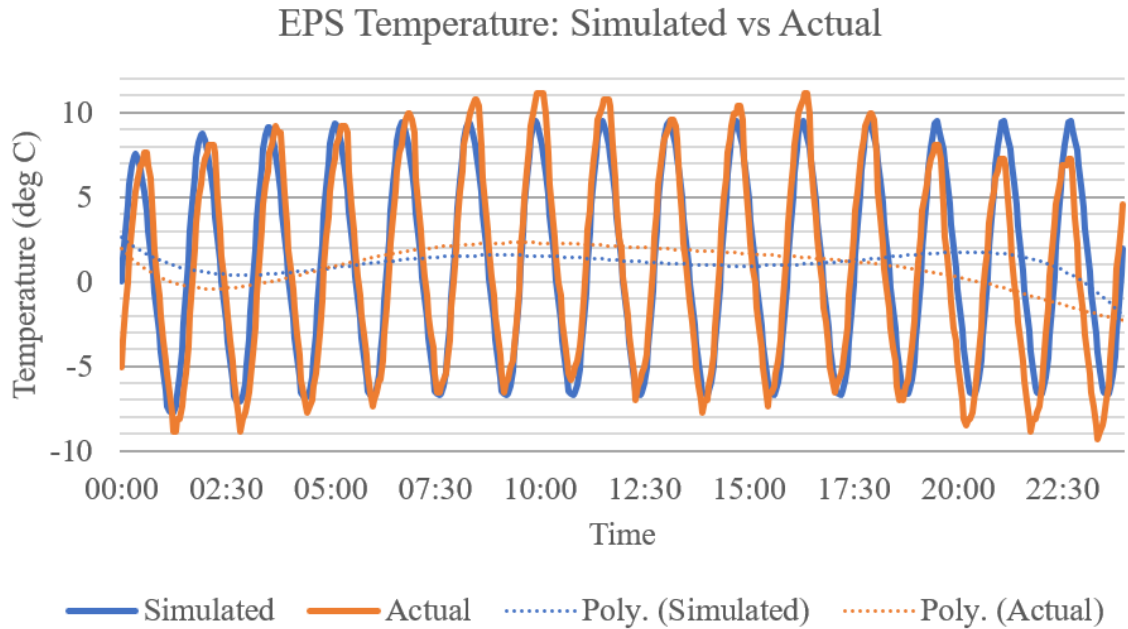


**Figure 6-97: Simulated vs actual EPS temperatures**

The Battery exhibits a deviation in average temperature of approximately 2° C for most of the cycle. While the deviation between the maximum simulated and actual temperature is of the order 0.5° C, the deviation in the minimum temperature is about 1.5° C.

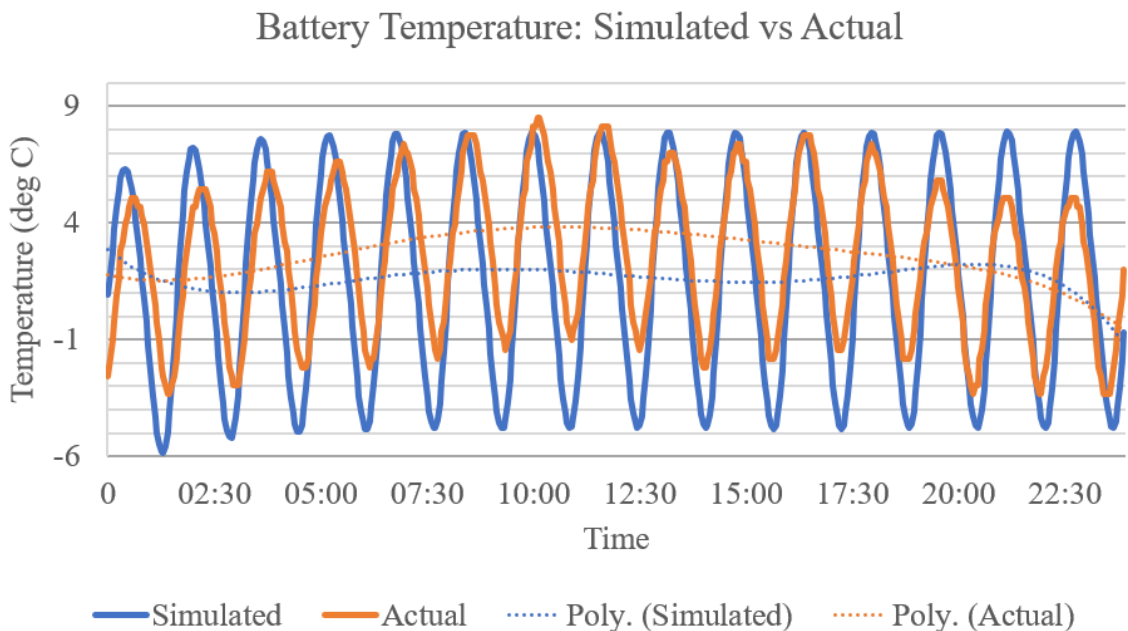


**Figure 6-98: Simulated vs actual BAT temperatures**

### 6.3.4.5. Temperature Limits

As discussed in Section 6.3.1 the satellite subsystems have maximum allowable temperature limits. It was seen in from the results that the subsystem that was closest to its allowable limits was the battery, with specified minimum and maximum temperature limits of -10 °C and 50 °C, respectively.

Figure 6-99 shows the coldest and hottest temperatures that the battery experiences during orbit. It can be seen how in the coldest state, the battery board temperature ranges from -8.4° C to -3.7° C, where the cold regions are focused around the corners where the board connects to the spacers. The battery sensor itself, which would be placed near the battery cells that are positioned in the centre of the board, exhibits the highest temperature. For the hottest state, the temperature ranges from a lowest temperature of 6.7° C near the centre of the board to 9.2° C around the corners, which have the highest heat concentration around the spacers. It can also be seen how in the coldest state, the heat is concentrated in the centre of the board while the battery heaters are activated. In the hottest state, the battery heaters can be seen to be in the off state, while the maximum heat is being conducted through the spacers from adjacent boards. Importantly, the battery remains within its operating temperature limits with an average minimum temperature of -6° C and maximum of 8° C.

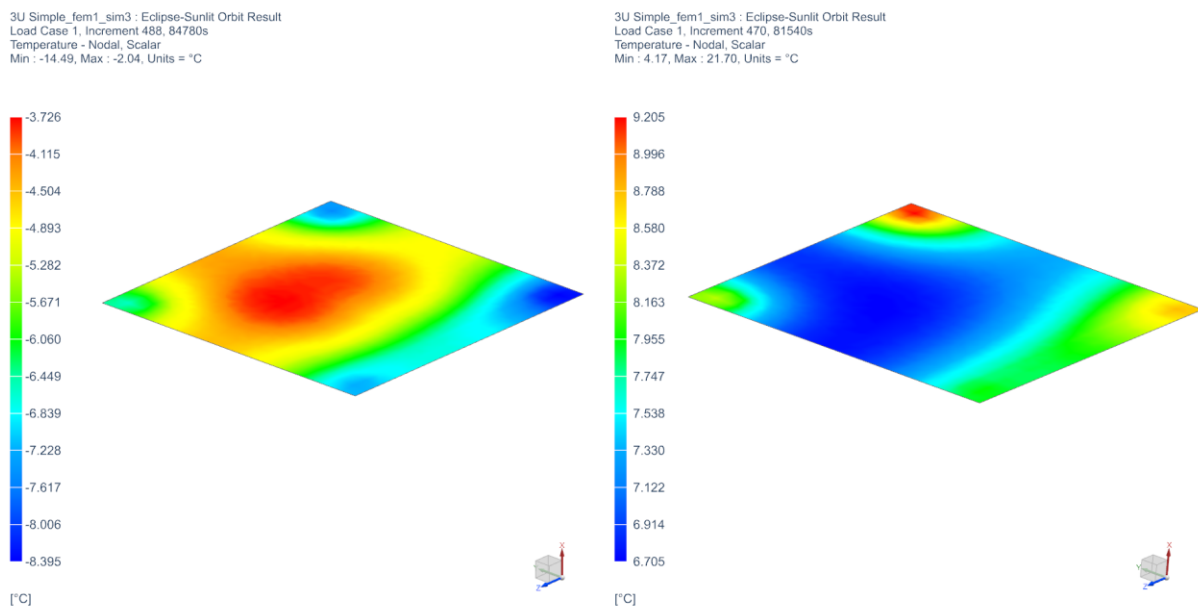


**Figure 6-99: Battery cold (left) and hot (right) results**

### 6.3.5. Thermal Discussion

#### 6.3.5.1. ZACube-2 Thermal Model

In section 6.3.4.4, the simulated results reach as steady transient state<sup>3</sup> during the analysis period, while the actual results also exhibit a slower cyclic variation superimposed on the variation associated with the orbital movement of the satellite. This is believed to be due to the battery heaters turning on and off.

Figure 6-100 shows the battery heater telemetry, as well as the EPS board temperature and solar array current. It can be seen how that, while the battery heaters (red, green and yellow) are fully active, there is a higher current (blue) being drawn from the solar arrays than when the heaters are inactive. A higher current drawn from the solar arrays results in more thermal energy being converted to power than into heat. Therefore, during the period of low solar array current, the satellite heats up more due to the solar energy being converted to heat (purple) instead of power. The complexity of the power use of the battery, EPS and solar cells is difficult to model in the simulation context, which explains the deviation in the results.

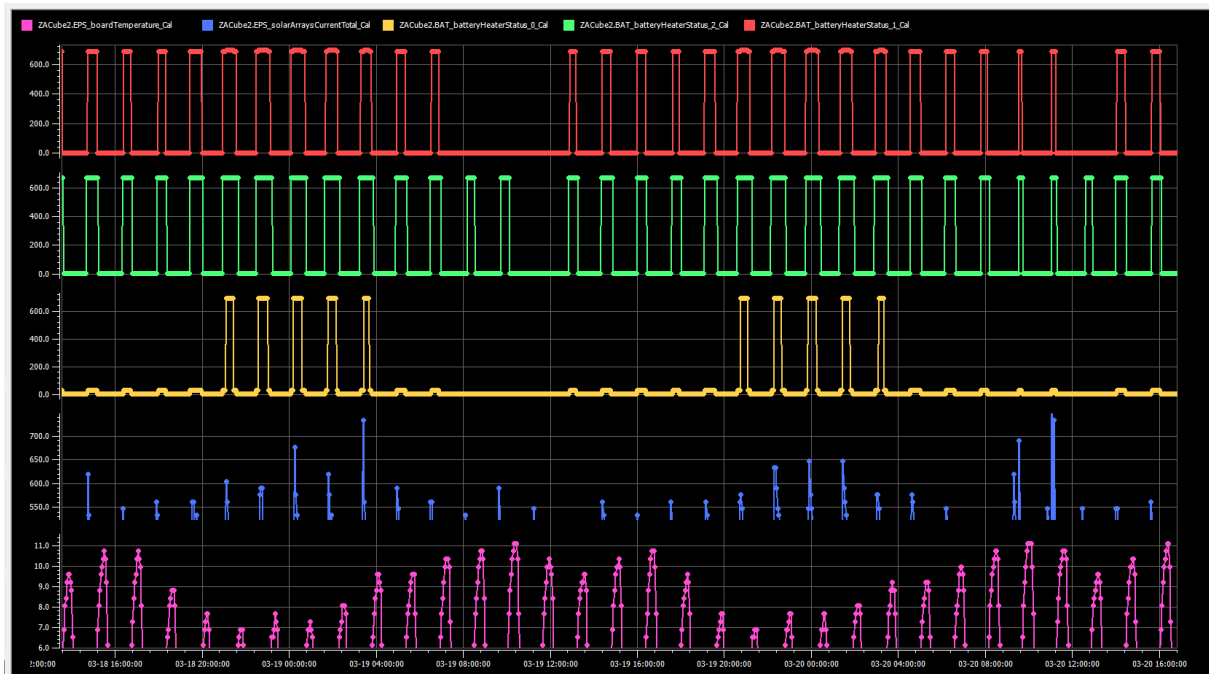


**Figure 6-100: Battery heater telemetry**

Another noticeable difference between the simulated vs actual temperature plots is the periods of the cycles. This is most noticeable in Figure 6-96 where the cycle is out of sync initially. This is most likely due to a slightly inaccurate LTAN and period being used versus that of the actual satellite orbit. This,

<sup>3</sup> The initial increase in temperature is due to the iterating from the simulation starting temperature of 0° C

however, has little impact on the temperature results themselves; it merely manifests as a de-synchronisation between the orbital periods.

#### 6.3.5.2. Dusk-Dawn Scenario

After validating the accuracy of the methodology used for creating a CubeSat thermal model, the methods can be used for further predictions and designs. An example of which would be determining the effect of selecting an alternative orbit. A simulation was run on the same thermal model; only changing the orbit LTAN to 6 am, resulting in what is known as a dusk-dawn orbit. This orbit experiences the most sunlit conditions because it orbits perpendicular to the solar vector, as can be seen in Figure 6-101.

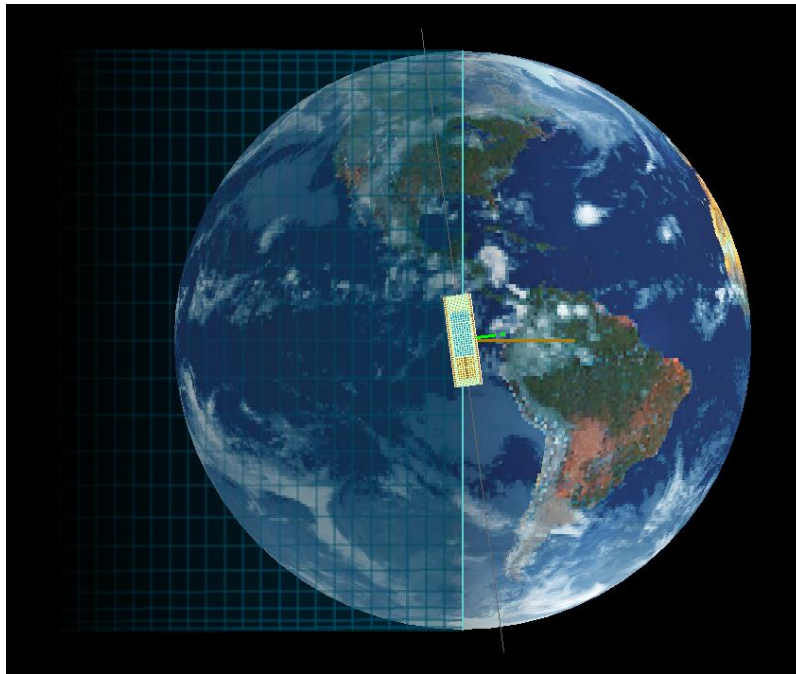


**Figure 6-101: Dusk-dawn orbit**

As can be expected with a dusk-dawn orbit, the change in temperature is minimal during its orbit as it does not experience a full eclipse. This can be seen in Figure 6-102 where the satellite temperature only varies by about 1° C between orbits. Furthermore, its overall average temperature is higher than that of a midday LTAN orbit.

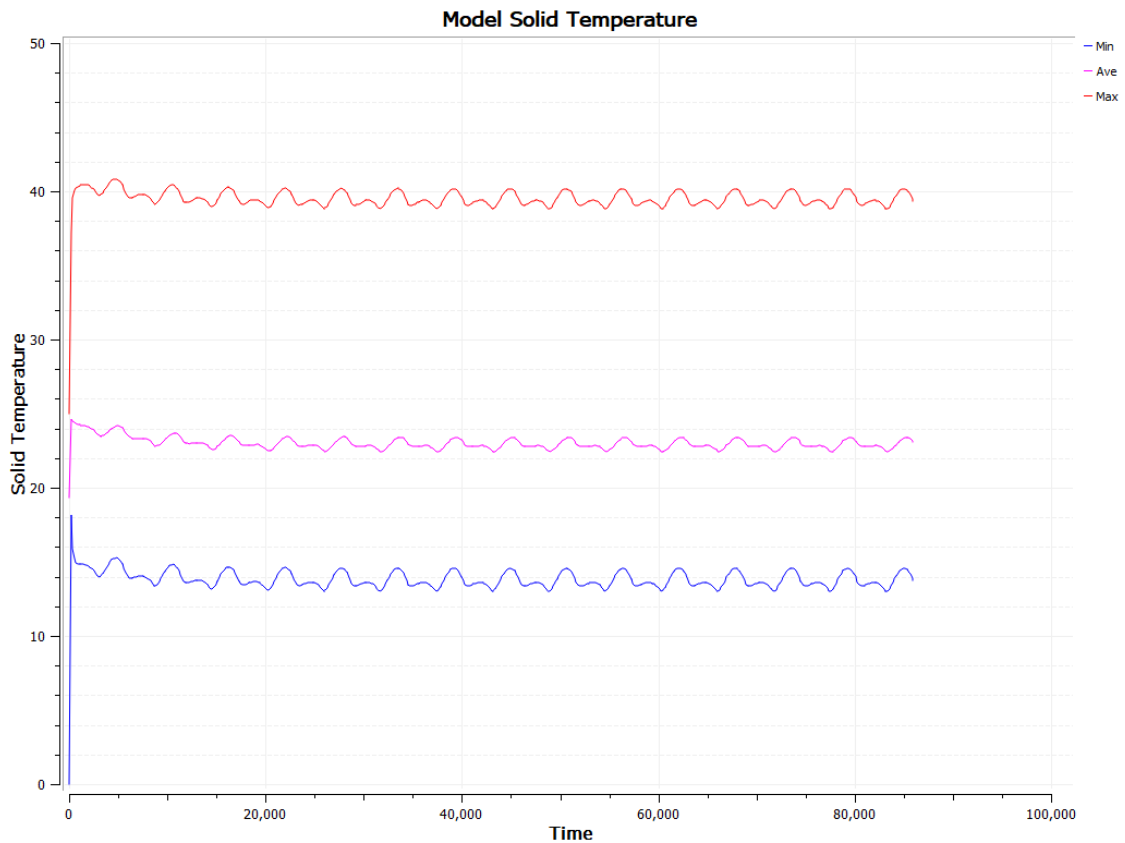


**Figure 6-102: Dusk-dawn temperature over time - entire satellite**

In Figure 6-103 the internal boards' temperatures are shown. A temperature gradient across the board from the sunlit side to the shadowed side can be seen. The internal subsystems of the satellite vary from 18.5° C on the shadow side to 28.7° C on the sunlit. This temperature gradient of 10° C can result in thermal stresses within the boards and, in the case of a satellite with an imager payload, defocus of the lenses.

These results show that, should a dusk-dawn orbit have been selected for the ZACube-2 mission, the satellite would have suffered from the issues mentioned above, and hence, the significance and importance of thermal simulations. For a scenario such as this, a form of heat controlling would need to be implemented. For CubeSats, this would most likely be passive heat control, such as heat pipes or straps. These can act as conductive paths to conduct heat from a hot to a cold source (Fortescue et al., 2011).



3U Simple\_fem1\_sim3 : Dusk-Dawn Result  
Load Case 1, Increment 468, 81900s  
Temperature - Nodal, Scalar  
Min : 13.69, Max : 38.98, Units = °C

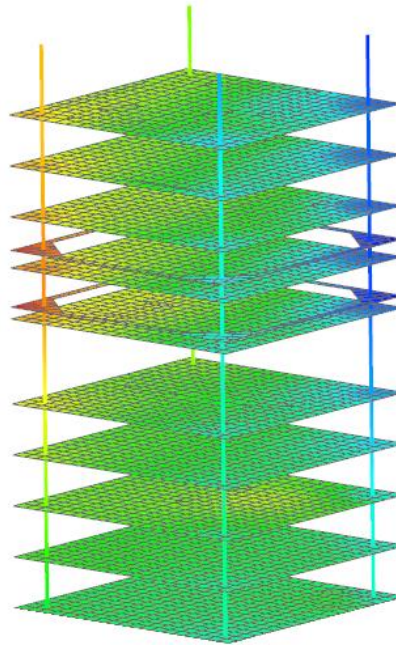


**Figure 6-103: Dusk-dawn temperatures**

#### 6.4. Final workflow chart

In Figure 6-104 a flow chart is shown for the workflow as a result of the experience gained conducting the research for improvements made to CubeSat development for missions by integrating the current state-of-the-art in manufacturing techniques and engineering analysis software. This flow chart can be seen to link to different sections in the research and is described more in Table 6-13 below.

**Table 6-13: Workflow details**

<b>Workflow step</b>	<b>Reference section</b>	<b>Details</b>
1 CubeSat mission	1	This is the top level representing the start of a CubeSat mission.
2 Identify the problem: Technology limitations	1.2	Identifying how additive manufacturing, and orbital thermal simulations can be implemented to improve CubeSat development.
2.1 Advanced Manufacturing	2	Looking into what current methods of manufacturing are for CubeSat development and what advanced methods have been used.
2.2 Engineering analysis software	2, 5	Studying the current engineering analysis software capabilities and how they can be used for CubeSat development.
3.1 Additive Manufacturing	4	Additive manufacturing as an advanced manufacturing method and its current capabilities, limitations and design considerations
3.2 CubeSat Structures	3	Studying the requirements for CubeSat structures and what is currently available. Including what design considerations need to be made.
3.3 Space Environment	3	The conditions that a CubeSat will experience both during launch (3.3.1) and once in orbit (3.3.2).
4.1 “Concept Model”	6.2	Implementing the above steps results in one of the outcomes of the research, a “Concept Model” as a phase deliverable during the CubeSat mission lifecycle to save costs and improve assembly efficiency.
4.2 Functional parts	6.2	Another outcome of the research is the ability to rapidly manufacture functional parts for the CubeSat integration process that also reduces costs and improves integration and assembly efficiency.
4.3 3D printed structure	6.1	The third outcome of the research is the 3D printed structure as an alternative to COTS aluminium structures to reduce weight, improve integration by reducing number of parts, reduce cost and lead time as well as introducing versatility into the design.
4.4 ZACube-2 digital twin	6.3	The thermal modelling of a digital twin of ZACube-2 CubeSat, to validate against actual data, to then implement methodologies used to create digital twins of future CubeSat designs to predict the orbital thermal effects for better bus and mission design.

5.1 Design	6.1, 6.2	To achieve the outcomes of 4.1, 4.2 and 4.3, design is conducted using CAD.
5.2 Thermal model	6.3	Like 5.1 but for the thermal digital twin of the CubeSat a thermal model is created using FEM.
6.1 Structural FEA	6.1.3	After the design is completed, FEA is conducted to simulate the launch conditions. A decision is then made (6.1.1) based on whether the design passes the launch conditions loading or not. An iterative process is then conducted between design and FEA until the design passes the launch conditions.
6.2 Thermal FEA	6.3.4	Like that of 6.1, analysis is run on the thermal model of the CubeSat. The results are then validated (9.4) against that of the actual data from the CubeSat. Again, an iterative process is followed until the thermal model is accurate against the actual data.
7 Manufacture	6.1.5, 6.1.6.1, 6.2.1.2, 6.2.3	Once the design has been completed and validated, they can then be manufactured using the appropriate 3D printer.
8 Assemble	6.1.4.2, 6.1.6.3, 6.2.3,6.2.1.4	Once the parts are manufactured, they can be assembled.
9.1 Decision for 4.1	6.2.1	Does the “Concept Model” meets its requirements for improving CubeSat development by reducing costs and improving assembly efficiency, if not, the process must return to the design.
9.2 Decision for 4.2	6.2.3	Do the functional parts serve as a better alternative to COTS options? This could be by reducing costs, lead time or improving functionality of the part required. If not, the process must return to the design.
9.3 Decision for 4.3	6.1	Does the structure pass environmental testing of manufacturing and does it improve the integration process of the structure or generally improve the structure performance? This could be from lower weight, less parts, more versatility, cheaper to manufacture, lower lead time. If not, the process must return to the design.
9.4 Decision for 4.4	6.3	As mentioned in 6.2, the thermal simulation results must meet those of the actual data, if not, the process must return to the thermal modelling.
10 Implement for CubeSat development	7	Once all the previous 4 workflows have been achieved, these methods can be implemented for CubeSat mission development optimizing the CubeSat and mission design.

---

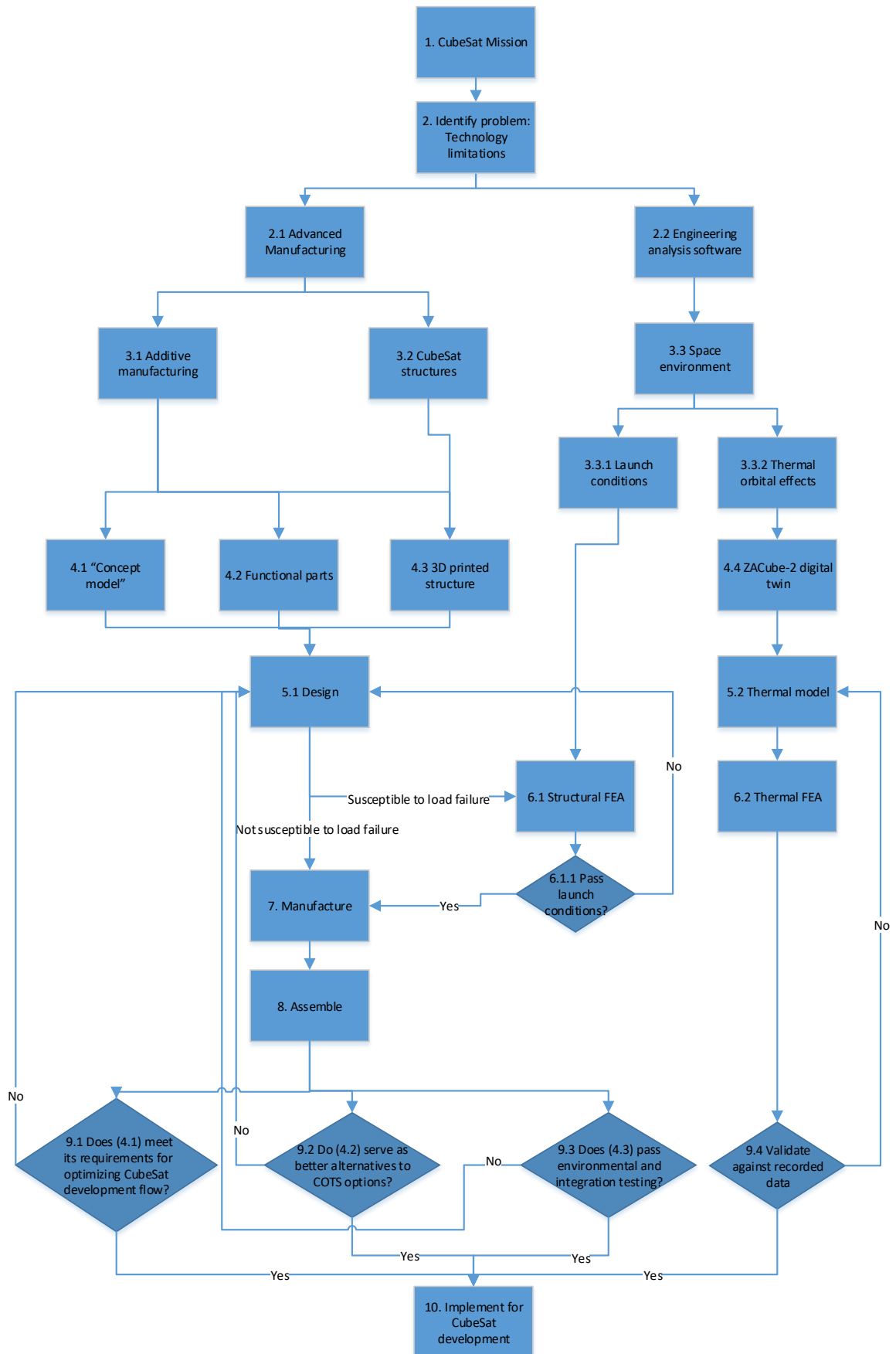


Figure 6-104: Flow chart for improved CubeSat development by integrating the current state-of-the-art in manufacturing techniques and engineering analysis software

## ***CHAPTER SEVEN***

### **7. CONCLUSION**

#### **7.1. Structural Design for AM**

In Section 6.1 a CubeSat structure was designed to be suitable for additive manufacturing. This design met the design objectives as listed in Section 6.1.1, this included the first design objective, meeting the dimensional constraints, using aluminium corners and using the ULTEM 9085 material that was already approved by the CDS.

The structural FEA qualified the structure for survivability during the launch with a safety factor of 4. The ULTEM 9085 3D printed satellite structure moreover achieved a reduced launch weight. The finite element model used orthotropic material properties to account for the characteristics of the 3D printed material which is affected by the print directions. Modal analysis was also performed to ensure that the first harmonic mode was above 100Hz as required for launch.

Analysis was also conducted to determine the radiation protection effect of the material while in orbit. It was determined that ULTEM 9085 provided 26% less protection against radiation than aluminium. The 3D printed structure, and indeed the aluminium structure it replaces, does not have a significant enough surface area for the protection of components against radiation so it should not be relied on as a radiation protector therefore it does not disqualify it for use in a CubeSat in terms of the current design but this needs to be borne in mind for any future design where radiation protection is incorporated into the supporting structure. The available thermal properties for ULTEM 9085 3D printed material was not sufficient to conduct an accurate thermal radiation analysis so producing the missing properties and doing the analysis is recommended for further research.

The second design objective was met with the final design of the structure weighing a total of 94.7 grams. For space applications, this 14-39% weight saving compared to COTS structures is significant as this allows for cheaper launch costs or allows for more weight to be allocated to the development of the primary payload.

The third design objective was met by showing the benefit of using an AM structure compared to COTS alternatives in terms of the number of components to assemble. The structure only consists of 6 parts (excluding fasteners and rods) compared to 10 of the Clyde Space 1U structure reducing the time and effort required for assembly as well as the possibility of making assembly errors. There are no obstructions when stacking the components and minimal preparation is required. In Section 6.1.10 a prototype of the structure was printed and assembled using PLA material on the ASIC 3D printer. It was found that the tolerances needed for the helical inserts used in assembly requires the 3D printer to be of a certain precision which a 3D printer capable of using ULTEM 9085 will meet. AM also significantly

reduces the lead time for manufacturing when compared to conventional manufacturing methods from about 2 weeks to 2 days if the facility is in-house.

Further meeting the third design objective, design versatility and customizability is possible. The fact that the main shell of the structure is a 3D printed part allows for easy design changes. If a client requires additional structural rigidity on one of the side or bottom panels, the design can be easily changed and printed accordingly without changes to the rails and fastening points.

Taking all of the above into account we can conclude that it is possible to produce CubeSat structural designs suitable for AM that meet the mission requirements and offer performance advantages when using a 3D printer that is capable of printing with the required precision and in materials that have been qualified by the CDS.

## **7.2. AM Applications for CubeSat Development**

Several significant methods were determined and implemented using additive manufacturing to improve general CubeSat development. On a systems level, implementing a Concept Model (CM) deliverable at the end of Phase B of the project allowed for the testing and optimising of assembly and integration methods, further improving the efficiency of the assembly process when it comes to the flight models.

Byeloborodov, 2017 in Section 2.3.1 discusses how a 3D printed model of their CubeSat design was used for fitment checks. A similar method was used in developing the Concept Model, proving its functionality and benefit. In Section 6.2.4 it was discussed how the Concept Model saved significant time and costs by identifying issues with the CAD design that were picked up in the early phases of the design rather than once the highly expensive EM CubeSat was built. Fitment issues such as incorrect harness lengths and spacers can be identified early on in the process avoiding expensive delays in assembly that have been experienced without employing this approach.

A study was conducted in Section 6.2.2 to determine the most efficient infill density to print PLA parts. The study showed that printing at 100% infill is a more efficient method of part manufacturing as its performance versus cost is higher than that of using a less dense infill. It was also clear how the test specimens that were tested were printed with consistent repeatability which was evidenced by the consistent test results as well as break location.

This method of printing was then used for the printing of functional parts, as discussed in Section 6.2.3, to aid in the integration and assembly of the MDASat-1 constellation. Making use of 3D printed parts such as the adhesive dispenser and solar panel integration mount saves significant time and money compared to having similar components manufactured using traditional manufacturing methods. The adhesive dispenser was created to solve an issue discovered by ASIC where it was difficult to apply a consistent amount of adhesive when potting the fasteners of the satellite. It is important to be consistent

with the adhesive as adding too much would result in unnecessary added weight. The dispenser mitigated this issue by being able to accurately dispense the exact amount of adhesive required, repetitively. The dispenser was also cheap and easy to manufacture, taking only 45 min and costing about \$0.32. This meant that multiple dispensers could be printed for multiple users to use. The 3D printed solar panel mount was also an easy, cheap solution to safely hold the solar panels in place during integration. This meant that one less engineer was required, as they were not required to hold the panel by hand and could focus on other tasks. Thus we have shown that AM should be considered not only for the CubeSat structure but for tooling to produce the satellite as a way of saving cost.

### **7.3. The Effect of AM on Cost**

Several AM methods were determined to have a cost saving effect on CubeSat development and production.

The Concept Model resulted in significant time and cost savings to the MDASat-1 project at ASIC. It was shown in Section 6.2.1 how 88% can be saved on cost per harness identified to be the incorrect length and 95% saved per spacer set by identifying the incorrect spacer length. This was identified when two harnesses and one set of spacers were identified to be the incorrect length during the assembly of the CM. These changes could then be rectified in the CAD, ensuring that when EM assembly commences, there are no errors or delays.

An ULTEM 9085 AM structure for a CubeSat showed a cost to be 57% greater than that of a similar aluminium structure. To 3D print the structure, it would take approximately 23.5 m of filament and a total of about 5 hours of printing time to complete the two parts. The total cost for the manufacturing of the structure was estimated at R16,200 (\$1050) compared to an estimated cost for manufacturing a similar aluminium structure at R10,350 (\$670.65). The aluminium structure, however, would not have the advantages as discussed in Section 7.1, like the AM structure would. It should be noted that the manufacturing cost of \$1050 is for outsourcing the 3D printing. Should an inhouse 3D printer be used the costs would be significantly less if neglecting the capital outlay cost. The materials costs for 23.5 m of filament would be only \$27 based on the rates given in Table 4-3, showing that using AM for a CubeSat structure would have a significant cost savings if the user has an in-house 3D printer compatible with ULTEM 9085.

### **7.4. CubeSat Thermal Digital Twin**

In Section 6.3 a thermal digital twin of ZACube-2 was developed in the form of a finite element model. Orbital thermal simulations were conducted on the digital twin to replicate the orbital parameters of ZACube-2 in orbit. A combination of 1D and 2D elements were used when meshing the FEM. The 2D mesh used for the outer surfaces and internal components of the CubeSat with 1D elements being used to connect the boards. When defining the mesh properties, it was important to define the material properties as accurately as possible ensuring that the correct thermal and thermo-optical properties were used

to represent each component and surface. The transient simulation simulated 15 orbits around Earth, following the same orbital parameters of that of ZACube-2, calculating the thermal radiation being experienced by the satellite every 3 minutes. Analysing the results of the thermal digital twin showed that the methods and model developed accurately replicated that of ZACube-2. This was evident by the average temperature of the subsystems that was very similar to that of the actual values with a minimal deviation. The battery subsystem showed the greatest deviation between the simulated and actual results. This is believed to be due to the current being produced by the solar panels when charging and the battery heaters being toggled on and off. When considering maximum and minimum temperatures for the UTRX and EPS, the variance between simulated and actual temperatures is only 1-2° C. This shows that the methods used in creating this thermal model can be used to replicate the thermal environment that CubeSats experience in low Earth orbit.

The simulated results showed that all subsystems remained within their allowable temperature range. It is critical that subsystems remain within these temperature ranges to ensure survivability throughout the mission. A subsystem that exceeds these limits is vulnerable to damage which could cause a mission failure. In the results it was seen that the battery subsystem was the closest to its allowable minimum temperature limit of -10° C at a temperature of -6° C. If the battery was to fail from exceeding its temperature limits, this would cause catastrophic failure, losing complete functionality of the CubeSat. It should be noted however that the simulation was for idle conditions, so operating the CubeSat would increase the average temperature throughout the CubeSat. The battery also has heaters to prevent the batteries from becoming too cold. This shows however why it is critical to be able to accurately predict each subsystem's operating temperature to ensure none fail by exceeding their allowable operating temperature ranges.

Other researchers such as Dinh, 2012 and Chandrashekar, 2017 have conducted thermal analysis of nanosatellites using various software packages as discussed in Section 2.4.1. What is unique to the results in this research, is the comparison of these results to actual temperature data from a CubeSat in orbit. This validates the accuracy of the thermal model, proving that its methodologies and procedures are reliable for implementation into other nanosatellite thermal-orbital simulations.

This research has also shown that using simplified 2D and 1D elements to create a digital twin of the satellite in the form of a FEM for use with the Space Systems Thermal package of Siemens NX, has shown to be sufficiently accurate in designing CubeSats for a particular orbital mission. It was seen that, by changing the orbit for ZACube-2 to a theoretical, dusk-dawn orbit, resulted in a significant impact on the satellite's temperature distribution and the overall average satellite temperature, raising the average temperature by 15° C when compared to ZACube-2's hottest state of its 11:30am LTAN orbit. This shows how predicting the thermal environment is crucial for orbit selection, stack layouts and thermal control design within CubeSats to ensure a safe thermal balance.



### **7.5. Flow Chart for Managing CubeSat Development**

In Section 1.7, Figure 1-11 showed a basic flow chart for CubeSat development. The research built on these workflow processes, implementing AM methods and advanced simulation software resulting in a detailed flow chart which was displayed and explained in Figure 6-104 and Table 6-13. The flow chart showed methodologies and processes that were followed in this research to successfully improve CubeSat development using AM. These can be replicated for future missions and by other researchers to achieve the same outcomes.

In Section 6.4 the developed workflow processes for improving CubeSat development showed how the Digital Twin workflow processes can be implemented into CubeSat missions and projects to optimise the system design by being able to predict the thermal behaviour of a CubeSat in orbit and use that for optimising the CubeSat design for a given mission.

## ***CHAPTER EIGHT***

### **8. RECOMMENDATIONS**

Where the use of ULTEM for CubeSat structures has shown to be a promising alternative to COTS options, more thorough research into the material properties should be conducted. Specifically, its detailed mechanical properties and how the 3D printed material will react in the space environment. For example, how will the material react to the extreme thermal conditions in space, will solar radiation have a long-term effect on the material. Additional research could be done focusing on the detailed structural behaviour and properties of 3D printed materials, specifically ULTEM 9085 for structural aerospace use. This could include the effect of controlling the 3D printed raster orientation during the 3D print. Furthermore, an investigation could be conducted to determine the effect heat has on the helical inserts within the structure. There is enough scope here for an entire research topic. The findings could be used to further improve the validity of the CubeSat structure design. Due to inadequate tensile testing facilities at the university and lack of budget, tensile testing of ULTEM specimens were not conducted. Therefore, for future research, the test specimens should be tested to determine the tensile and shear properties to identify the mechanical properties of ULTEM 9085. A working prototype can also be manufactured using intended machines and materials and assembled to test the integration process as well as running additional tests on the structure. This would include quasi-static, vibration and shock testing on the structure. These tests would not only validate the survivability of the structure but also the FEM and simulation results conducted previously. Before implementing into use, end feet switches and separation springs would also need to be added for full CubeSat functionality. In Section 4.2, literature about embedding electronics into 3D printed parts was discussed. The potential of including embedded electronics within a CubeSat structure could further improve the structural design. An additional study could be conducted on how one would integrate the circuitry into the various 3D printed structure sides and how it could be used to connect payloads and components.

While significant uses of affordable 3D printing for CubeSat development was found, the ability to 3D print metals using a laser sintering type of 3D printer could significantly further the potential for additive manufacturing applications for CubeSat development. This could include complex camera housing structures, antennas, and complex heat strapping/piping routes.

Using the methods developed in creating the CubeSat thermal digital twin, passive heat control solutions such as heat strapping and heat piping for hot orbits such as a dusk-dawn orbit could be analysed. This will allow for an accurate representation of the effectivity of the passive heat control device.

## 9. BIBLIOGRAPHY

- 3DXTech Advanced Materials. 2019. <https://www.3dxtech.com/>.
- AAC-CS. 2018. *30 whr Battery Specification sheet*.
- Ahn, S., Montero, M., Odell, D., Roundy, S. & Wright, P.K. 2002. Anisotropic material properties of fused deposition modeling ABS. *Rapid Prototyping Journal*, 8(4): 248–257. <http://www.emeraldinsight.com/doi/10.1108/13552540210441166>.
- Anon. Class of material: Polyamide based material. [http://www.windform.com/PDF/SCHEDA\\_WF\\_XT\\_ENG.pdf](http://www.windform.com/PDF/SCHEDA_WF_XT_ENG.pdf) 20 July 2017.
- Anon. 2017. French South African Institute of Technology. <http://www.cput.ac.za/blogs/fsati/> 20 July 2017.
- Anon. 2016. Tomsk-TPU-120 CubeSat celebrates University anniversary | AMSAT-UK. <https://amsat-uk.org/2016/04/30/tomsk-tpu-120-cubesat/> 19 July 2017.
- ASTM International. 2003. Standard test method for tensile properties of plastics. *ASTM International*, 08: 46–58. <http://scholar.google.com/scholar?hl=en&btnG=Search&q=intitle:Standard+Test+Method+for+Tensile+Properties+of+Plastics#0>.
- Australian Centre for Space Engineering Research. UNSW EC0 Satellite Educational Cubesat 0. [http://www.acser.unsw.edu.au/sites/acser/files/uploads/files/QB50-UNSWEC0-EducationalPoster\\_A1\\_2017.pdf](http://www.acser.unsw.edu.au/sites/acser/files/uploads/files/QB50-UNSWEC0-EducationalPoster_A1_2017.pdf) 24 July 2017.
- Ball, J. & Oliver, P.G. 2017. Cape Peninsula University of Technology A design and analysis of a multifunctional composite structure for nano-satellites by requirements for Master 's thesis in Mechanical Engineering MEng in Mechanical Engineering. , 2017.
- Bathe, K.-J. 2016. *Finite Element Procedures*. [http://web.mit.edu/kjb/www/Books/FEP\\_2nd\\_Edition\\_4th\\_Printing.pdf](http://web.mit.edu/kjb/www/Books/FEP_2nd_Edition_4th_Printing.pdf).
- CalPoly. 2014. Cubesat design specification (CDS). *The CubeSat Program, California Polytechnic State ...*, 8651(June 2004): 42. [http://www.cubesat.org/images/developers/cds\\_rev12.pdf%5Cnhttp://scholar.google.com/scholar?hl=en&btnG=Search&q=intitle:CubeSat+Design+Specification#0](http://www.cubesat.org/images/developers/cds_rev12.pdf%5Cnhttp://scholar.google.com/scholar?hl=en&btnG=Search&q=intitle:CubeSat+Design+Specification#0).
- Chandrashekar, S. 2017. Thermal Analysis and Control of MIST CubeSat. : 1–26. <http://www.diva-portal.org/smash/get/diva2:1071655/FULLTEXT02>.

Clyde Space Ltd. Clyde Space Products.

- Clyde Space Ltd. 2017. CS 1U CubeSat Structure. <https://www.clyde.space/products/4-cs-1u-cubesat-structure>.
- CubeSat\_Shop. CubeSat Shop Products.
- Davies, S. 2017. Made In Space to use PEI/PC polymer on International Space Station 3D printing platform.
- Dilberoglu, U.M., Gharehpapagh, B., Yaman, U. & Dolen, M. 2017. The Role of Additive Manufacturing in the Era of Industry 4.0. *Procedia Manufacturing*, 11(June): 545–554. <http://dx.doi.org/10.1016/j.promfg.2017.07.148>.
- Dinh, D. 2012. *Thermal modeling of a nanosat*. San Jose State University. [http://scholarworks.sjsu.edu/etd\\_theses/4193](http://scholarworks.sjsu.edu/etd_theses/4193).
- Dr.Wahidurni. 2017. 2U Cubesat Structural Design and Integration. *Thesis*: 1–14.
- Duann Scott. 2017. Add It Up: 5 Industrial Additive Manufacturing Trends for 2017. <https://www.autodesk.com/redshift/industrial-additive-manufacturing-trends/> 27 September 2017.
- ECSS. 2008. *Space engineering: Space environment*. Noordwijk, The Netherlands,.
- El-Gizawy, A.S., Corl, S. & Graybill, B. 2011. Process-induced Properties of FDM Products. *International Conference on Mechanical Engineerings and Technology Congress and Exposition*.
- Espalin, D., Muse, D.W., MacDonald, E. & Wicker, R.B. 2014. 3D Printing multifunctionality: Structures with electronics. *International Journal of Advanced Manufacturing Technology*, 72(5–8): 963–978.
- Eurosteel. 2017. Aluminium Technical Data. <https://www.eurosteel.co.za/wp-content/uploads/2017/12/Euro-Steel-Aluminium-Technical-Data.pdf>.
- Forster, A.M. 2015. *Materials Testing Standards for Additive Manufacturing of Polymer Materials: State of the Art and Standards Applicability*. Gaithersburg, MD. <http://nvlpubs.nist.gov/nistpubs/ir/2015/NIST.IR.8059.pdf>.
- Fortescue, P.W., Stark, J.P.W. & Swinerd, G. 2011. *Spacecraft systems engineering*. Wiley. <http://library.books24x7.com/libproxy.cput.ac.za/toc.aspx?bookid=44428> 10 August 2017.
- Gibson, I., Rosen, D. & Stucker, B. 2015. *Additive Manufacturing Technologies*. <http://www.scopus.com/inward/record.url?eid=2-s2.0-84944216444&partnerID=tZOtx3y1%5Cnhttp://link.springer.com/10.1007/978-1-4939-2113-3>.
- Grunewald, S. 2015. Stratasys 3D Printers Helping to Launch Rockets into Space. <https://3dprint.com/59428/united-launch-alliance-rockets/> 2 September 2019.

- ISISpace. 2015. CubeSat Structures. *Online Store*: 2012–2014.  
[http://www.isispace.nl/brochures/ISIS\\_CubeSat\\_Structures\\_Brochure\\_v.7.11.pdf](http://www.isispace.nl/brochures/ISIS_CubeSat_Structures_Brochure_v.7.11.pdf).
- Jones, J. & Coates, P. 2015. 7 Families of Additive Manufacturing (ASTM F2792).  
*Www.Hybridmanutech.Com*: 1–2.  
[https://www.additivemanufacturing.media/cdn/cms/7\\_families\\_print\\_version.pdf](https://www.additivemanufacturing.media/cdn/cms/7_families_print_version.pdf).
- Keane, P. Functional CubeSat Structure- &quot;The Mk III&quot; - STL - 3D CAD model - GrabCAD.  
<https://grabcad.com/library/functional-cubesat-structure-the-mk-iii-1> 15 January 2018.
- Liu, Y. 2002. *Introduction to Finite Element Method ( Stress Analysis )*.
- M, A. 2020. A futuristic reality: 3D printed SpaceX helmets. <https://www.3dnatives.com/en/3d-printed-spacex-helmets-090620206/>.
- Martin, S.A.H., Cogan, D.J., Zyl, R. Van & Africa, S. 2020. *CubeSatellite Thermal Modelling with On-Orbit Validation*. Cape Town.
- Matweb. 2020. Silicon, Si Material Properties.  
<http://www.matweb.com/search/DataSheet.aspx?%0AMatGUID=7d1b56e9e0c54ac5bb9cd433a0991e27&ckck=1>.
- Piattoni, J., Candini, G.P., Pezzi, G., Santoni, F. & Piergentili, F. 2012. Plastic Cubesat: An innovative and low-cost way to perform applied space research and hands-on education. *Acta Astronautica*, 81(2): 419–429.
- Poghosyan, A. & Golkar, A. 2017. CubeSat evolution: Analyzing CubeSat capabilities for conducting science missions. *Progress in Aerospace Sciences*, 88(November 2016): 59–83.
- Pumpkin, I. 2015a. Pumpkin CubeSat Kit Models. <http://www.cubesatkit.com/content/design.html> 20 July 2007.
- Pumpkin, I. 2015b. Pumpkin CubeSat Kit Structures.  
[http://www.pumpkinspace.com/store/c4/CubeSat\\_Kit<sup>TM</sup>\\_Structures.html](http://www.pumpkinspace.com/store/c4/CubeSat_Kit<sup>TM</sup>_Structures.html) 1 July 2017.
- Pumpkin Inc. 2003. CubeSat Kit PCB Specification.
- Rodič, B. 2017. Industry 4.0 and the New Simulation Modelling Paradigm. *Organizacija*, 50(3): 193–207.
- Rogers, T. 2015. Everything You Need To Know About Polylactic Acid (PLA).  
<https://www.creativemechanisms.com/blog/learn-about-polylactic-acid-pla-prototypes>.
- Roylance, D. 2000. Laminated Composite Plates and Shells. : 1–18.  
<http://www.springerlink.com/index/10.1007/978-1-4471-0095-9>.

- Salmi, B. 2019. The World's Largest 3D Metal Printer Is Churning Out Rockets. <https://spectrum.ieee.org/aerospace/space-flight/the-worlds-largest-3d-metal-printer-is-churning-out-rockets>.
- Schiller, G.J. 2015. Additive manufacturing for Aerospace. *IEEE Aerospace Conference Proceedings*, 2015-June.
- Sher, D. 2019. SpaceX's Crew Dragon spacecraft with 3D printed SuperDraco engines is now officially flying. <https://www.3dprintingmedia.network/spacexs-dragon-spacecraft-with-3d-printed-superdraco-engines-will-take-astronauts-around-moon-in-2018/>.
- Siemens. 2020. Siemens NX Material Properties Library. <https://www.plm.automation.siemens.com/global/en/%0Aproducts/nx/>.
- Skrzypek, J.J. & Ganczarski, A.W. eds. 2015. *Mechanics of Anisotropic Materials*. Cham: Springer International Publishing. <http://link.springer.com/10.1007/978-3-319-17160-9>.
- Spectrolab. 2018. XTJ Prime Data Sheet. [https://www.spectrolab.com/photovoltaics/XTJ-Prime\\_Data\\_%0ASheet.pdf](https://www.spectrolab.com/photovoltaics/XTJ-Prime_Data_%0ASheet.pdf).
- Stratasys Ltd. 2017. Stratasys - Our Materials.
- Swartwout, M. 2015. CubeSat DataBase. *Saint Louis University*. <https://sites.google.com/a/slu.edu/swartwout/home/cubesat-database> 1 July 2017.
- Swartwout, M. 2013. The first one hundred CubeSats : A statistical look. *Journal of Small Satellites*, 2(2): 213–233. <http://www.jossonline.com/>.
- The Australian Centre for Space Engineering Research. 2016. The UNSW-EC0 QB50-AU02 CubeSat | The Australian Centre for Space Engineering Research (ACSER). <http://www.acser.unsw.edu.au/QB50> 24 July 2017.
- Tomsk Polytechnic University. 2017. Tomsk-TPU-120 CubeSat deployed in outer space / TPU. [https://tpu.ru/en/about/tpu\\_today/news/view?id=3188](https://tpu.ru/en/about/tpu_today/news/view?id=3188) 8 March 2018.
- Villiers, D. De & Zyl, R. Van. 2015. ZACube-2: The successor to Africa's first nanosatellite. *Southern African Amateur Radio Satellite Association Space Symposium*.
- Wendland, A., Bumann, M., Martin, S., Niemann, J. & Bosman, S. 2020. Optimizing System Design Through Thermal Analysis with Cubesatellite as Case Study. In 408–420. [http://link.springer.com/10.1007/978-3-030-56441-4\\_30](http://link.springer.com/10.1007/978-3-030-56441-4_30).
- Wertz, J.R. & Larson, W. 1999. *B3 - Space Mission Analysis and Design*. <http://www.amazon.ca/Space-Mission-Analysis-Design->

James/dp/0792359011/ref=sr\_1\_1?s=books&ie=UTF8&qid=1430653992&sr=1-  
1&keywords=9780792359012.

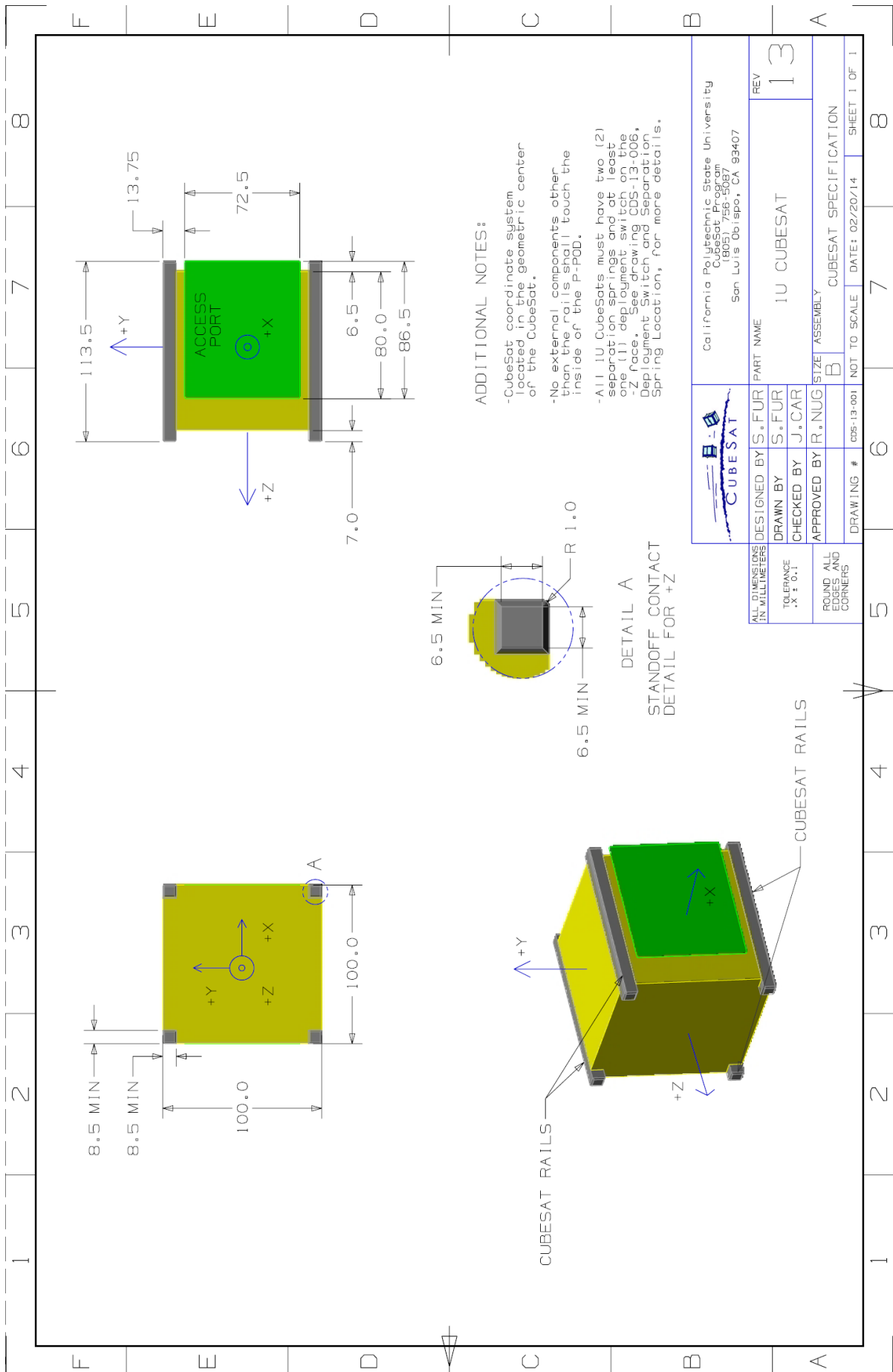
Zaidi, Y. 2017. Engineering for the Space Environment Module II – Spacecraft Mechanical Load Analysis.

Zaldivar, R.J., Witkin, D.B., McLouth, T., Patel, D.N., Schmitt, K. & Nokes, J.P. 2017. Influence of processing and orientation print effects on the mechanical and thermal behavior of 3D-Printed ULTEM?? 9085 Material. *Additive Manufacturing*, 13: 71–80. <http://dx.doi.org/10.1016/j.addma.2016.11.007>.

Ziemian, C., Sharma, M. & Ziemian, S. 2012. Anisotropic mechanical properties of ABS parts fabricated by fused deposition modelling. *Mechanical Engineering*: 159–180. [http://cdn.intechopen.com/pdfs/35261/InTech-Anisotropic\\_mechanical\\_properties\\_of\\_abs\\_parts\\_fabricated\\_by\\_fused\\_deposition\\_modelling.pdf](http://cdn.intechopen.com/pdfs/35261/InTech-Anisotropic_mechanical_properties_of_abs_parts_fabricated_by_fused_deposition_modelling.pdf).

Van Zyl, R.R., Visser, D.F., Cilliers, P.J. & Opperman, B.D.L. 2013. ZACUBE-1 space weather mission: Characterize the superDARN HF radar antenna array at SANAE-IV. *Space Weather*, 11(2): 52–54. <http://doi.wiley.com/10.1002/swe.20018> 20 July 2017.

APPENDIX A



ADDITIONAL NOTES:

- CubeSat coordinate system located in the geometric center of the CubeSat.
- No external components other than the rails shall touch the inside of the P-PQD.
- All IU CubeSats must have two (2) separation springs and at least one (1) deployment switch on the -Z face. See drawing CDS-13-006, Deployment Switch and Separation Spring Location, for more details.

	DESIGNED BY	S.FUR	PART NAME	REV
	DRAWN BY	S.FUR	IU CUBESAT	13
	CHECKED BY	J.CAR		
	APPROVED BY	R.NUG	SIZE ASSEMBLY	
	DRAWING #	CDS-13-001	NOT TO SCALE	DATE: 02/20/14
			CUBESAT SPECIFICATION	
				SHEET 1 OF 1

California Polytechnic State University  
 CubeSat Program  
 (805) 756-5087  
 San Luis Obispo, CA 93407



## APPENDIX B

**Information**

Density = 0.000001735 kg/mm<sup>3</sup>  
 Area = 79239.013838414 mm<sup>2</sup>  
 Volume = 54603.613226524 mm<sup>3</sup>  
 Mass = 0.094755171 kg

**Center of Mass**  
 Xcbar = 9.761056408 mm  
 Ycbar = 0.401057298 mm  
 Zcbar = 18.024829746 mm

**First Moments**  
 Mxc = 0.924910570 kg·mm  
 Myc = 0.038002253 kg·mm  
 Mzc = 1.707945826 kg·mm

**Moments of Inertia (Work)**  
 Ixxw = 353.924628972 kg·mm<sup>2</sup>  
 Iyyw = 360.166223035 kg·mm<sup>2</sup>  
 Izzw = 356.246403002 kg·mm<sup>2</sup>

**Moments of Inertia (Centroidal)**  
 Ixx = 323.123955164 kg·mm<sup>2</sup>  
 Iyy = 320.352686065 kg·mm<sup>2</sup>  
 Izz = 347.203057678 kg·mm<sup>2</sup>

**Moments of Inertia (Spherical)**  
 = 495.339849453 kg·mm<sup>2</sup>

**Products of Inertia (Work)**  
 Pyzw = 0.619229428 kg·mm<sup>2</sup>  
 Pxz = 16.662459213 kg·mm<sup>2</sup>  
 Pxyw = 0.263867145 kg·mm<sup>2</sup>

**Products of Inertia (Centroidal)**  
 Pyz = -0.065754710 kg·mm<sup>2</sup>  
 Pxz = -0.008896336 kg·mm<sup>2</sup>  
 Pxy = -0.107074989 kg·mm<sup>2</sup>

**Principal Moments of Inertia**  
 Ixxp = 347.203222189 kg·mm<sup>2</sup>  
 Iyyp = 323.128080697 kg·mm<sup>2</sup>  
 Izzp = 320.348396020 kg·mm<sup>2</sup>

**Radii of Gyration (Work)**  
 Rgxw = 61.115860756 mm  
 Rgyw = 61.652406155 mm  
 Rgz = 61.315995549 mm

**Radii of Gyration (Centroidal)**  
 Rgx = 58.396002446 mm  
 Rgy = 58.145046867 mm  
 Rgz = 60.532736936 mm

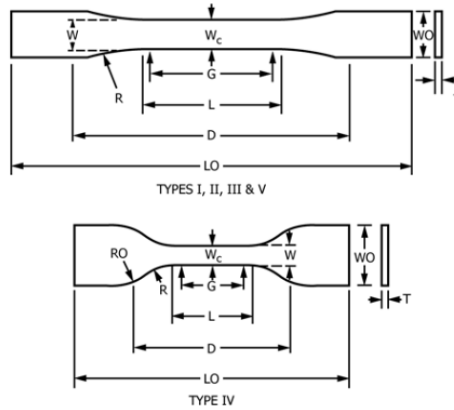
**Radii of Gyration (Spherical)**  
 = 72.301977213 mm

**Principal Axes**  
 Xp(X) = 0.000380359  
 Xp(Y) = 0.002450425  
 Xp(Z) = 0.999996925  
 Yp(X) = 0.999256508  
 Yp(Y) = 0.038551336  
 Yp(Z) = -0.000474545  
 Zp(X) = -0.038552380  
 Zp(Y) = 0.999253616  
 Zp(Z) = -0.002433940

Warnings Generated by the Weight Calculation:  
 -----

APPENDIX C

D638 - 14



Specimen Dimensions for Thickness,  $T$ , mm (in.)<sup>A</sup>

Dimensions (see drawings)	7 (0.28) or under		Over 7 to 14 (0.28 to 0.55), incl		4 (0.16) or under		Tolerances
	Type I	Type II	Type III	Type IV <sup>B</sup>	Type V <sup>C,D</sup>		
$W$ —Width of narrow section <sup>E,F</sup>	13 (0.50)	6 (0.25)	19 (0.75)	6 (0.25)	3.18 (0.125)	$\pm 0.5$ ( $\pm 0.02$ ) <sup>B,C</sup>	
$L$ —Length of narrow section	57 (2.25)	57 (2.25)	57 (2.25)	33 (1.30)	9.53 (0.375)	$\pm 0.5$ ( $\pm 0.02$ ) <sup>C</sup>	
$W_O$ —Width overall, min <sup>G</sup>	19 (0.75)	19 (0.75)	29 (1.13)	19 (0.75)	...	+ 6.4 (+ 0.25)	
$W_O$ —Width overall, min <sup>G</sup>	...	...	...	...	9.53 (0.375)	+ 3.18 (+ 0.125)	
$L_O$ —Length overall, min <sup>H</sup>	165 (6.5)	183 (7.2)	246 (9.7)	115 (4.5)	63.5 (2.5)	no max (no max)	
$G$ —Gage length <sup>I</sup>	50 (2.00)	50 (2.00)	50 (2.00)	...	7.62 (0.300)	$\pm 0.25$ ( $\pm 0.010$ ) <sup>C</sup>	
$G$ —Gage length <sup>I</sup>	...	...	...	25 (1.00)	...	$\pm 0.13$ ( $\pm 0.005$ )	
$D$ —Distance between grips	115 (4.5)	135 (5.3)	115 (4.5)	65 (2.5) <sup>J</sup>	25.4 (1.0)	$\pm 5$ ( $\pm 0.2$ )	
$R$ —Radius of fillet	76 (3.00)	76 (3.00)	76 (3.00)	14 (0.56)	12.7 (0.5)	$\pm 1$ ( $\pm 0.04$ ) <sup>C</sup>	
$R_O$ —Outer radius (Type IV)	...	...	...	25 (1.00)	...	$\pm 1$ ( $\pm 0.04$ )	

<sup>A</sup>Thickness,  $T$ , shall be  $3.2 \pm 0.4$  mm ( $0.13 \pm 0.02$  in.) for all types of molded specimens, and for other Types I and II specimens where possible. If specimens are machined from sheets or plates, thickness,  $T$ , shall be the thickness of the sheet or plate provided this does not exceed the range stated for the intended specimen type. For sheets of nominal thickness greater than 14 mm (0.55 in.) the specimens shall be machined to  $14 \pm 0.4$  mm ( $0.55 \pm 0.02$  in.) in thickness, for use with the Type III specimen. For sheets of nominal thickness between 14 and 51 mm (0.55 and 2 in.) approximately equal amounts shall be machined from each surface. For thicker sheets both surfaces of the specimen shall be machined, and the location of the specimen with reference to the original thickness of the sheet shall be noted. Tolerances on thickness less than 14 mm (0.55 in.) shall be those standard for the grade of material tested.

<sup>B</sup>For the Type IV specimen, the internal width of the narrow section of the die shall be  $6.00 \pm 0.05$  mm ( $0.250 \pm 0.002$  in.). The dimensions are essentially those of Die C in Test Methods D412.

<sup>C</sup>The Type V specimen shall be machined or die cut to the dimensions shown, or molded in a mold whose cavity has these dimensions. The dimensions shall be:

- $W = 3.18 \pm 0.03$  mm ( $0.125 \pm 0.001$  in.),
- $L = 9.53 \pm 0.08$  mm ( $0.375 \pm 0.003$  in.),
- $G = 7.62 \pm 0.02$  mm ( $0.300 \pm 0.001$  in.), and
- $R = 12.7 \pm 0.08$  mm ( $0.500 \pm 0.003$  in.).

The other tolerances are those in the table.

<sup>D</sup>Supporting data on the introduction of the L specimen of Test Method D1822 as the Type V specimen are available from ASTM Headquarters. Request RR:D20-1038.

<sup>E</sup>The tolerances of the width at the center  $W_c$  shall be  $+0.00$  mm,  $-0.10$  mm ( $+0.000$  in.,  $-0.004$  in.) compared with width  $W$  at other parts of the reduced section. Any reduction in  $W$  at the center shall be gradual, equally on each side so that no abrupt changes in dimension result.

<sup>F</sup>For molded specimens, a draft of not over 0.13 mm (0.005 in.) is allowed for either Type I or II specimens 3.2 mm (0.13 in.) in thickness. See diagram below and this shall be taken into account when calculating width of the specimen. Thus a typical section of a molded Type I specimen, having the maximum allowable draft, could be as follows:

<sup>G</sup>Overall widths greater than the minimum indicated are used for some materials in order to avoid breaking in the grips.

<sup>H</sup>Overall lengths greater than the minimum indicated are used for some materials to avoid breaking in the grips or to satisfy special test requirements.

<sup>I</sup>Test marks or initial extensometer span.

<sup>J</sup>When self-tightening grips are used, for highly extensible polymers, the distance between grips will depend upon the types of grips used and may not be critical if maintained uniform once chosen.

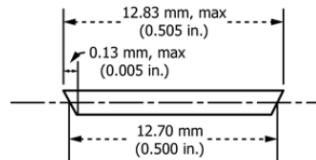


FIG. 1 Tension Test Specimens for Sheet, Plate, and Molded Plastics